

Graduate School for Cellular and Biomedical Sciences
University of Bern

Quantifying bone extracellular matrix properties for improved clinical fracture risk prediction

PhD Thesis submitted by

Tatiana Kochetkova

for the degree of

PhD in Biomedical Engineering

Supervisor

Prof. Dr. Philippe Zysset

ARTORG Center for Biomedical Engineering Research

University of Bern, Switzerland

Co-advisor

Dr. Jakob Schwiedrzik

Empa, Swiss Federal Laboratories for Materials Science and Technology,
Laboratory for Mechanics of Materials and Nanostructures, Switzerland

Accepted by the Faculty of Medicine, the Faculty of Science and the Vetsuisse Faculty of the University of Bern at the request of the Graduate School for Cellular and Biomedical Sciences

Bern,

Dean of the Faculty of Medicine

Bern,

Dean of the Faculty of Science

Bern,

Dean of the Vetsuisse Faculty Bern



This work is licensed under a Creative Commons Attribution 4.0 International License except where otherwise noted.

Exam Committee

Accepted by the exam committee for the degree of PhD in Biomedical Engineering from the University of Bern.

Supervisor

Prof. Dr. Philippe Zysset
ARTORG Center for Biomedical Engineering Research,
University of Bern, Switzerland

Co-advisor

Dr. Jakob Schwiedrzik
Empa, Swiss Federal Laboratories for Materials Science and Technology,
Switzerland

Mentor

Prof. Dr. Dominik Obrist
ARTORG Center for Biomedical Engineering Research,
University of Bern, Switzerland

External Co-referee

Prof. Dr. Jeffry S. Nyman
Vanderbilt Center for Bone Biology,
Vanderbilt University Medical Center, Nashville, TN, USA

External Co-referee

Prof. Dr. Ralph Müller
Institute for Biomechanics,
Department of Health Sciences and Technology, ETH Zürich, Switzerland

Abstract

Metabolic bone diseases like osteoporosis lead to increased bone fragility and consequent implications for the patient lifestyle and health expenses. In the present aging society, fragility fractures pose significant health and economic burden. Current clinical methods to assess bone health status (dual-energy X-ray absorptiometry, FRAX, quantitative computed tomography variations) depend mostly on bone mineral density (BMD) measurements. However, BMD alone only accounts for about 70% of the variance in bone strength. It is therefore of high interest and potential societal impact to investigate bone quality, i.e. measures other than BMD influencing bone strength and toughness.

In the present thesis, novel laboratory methods were developed for high-throughput investigation of bone properties, with the ultimate goal to define combinations of measurements that can be used as a proxy for bone quality in a fracture risk analysis. Firstly, a novel method for quantifying mineralized collagen fibril orientation based on polarized Raman spectroscopy (qPRS) was calibrated and validated on a natural material (mineralized turkey leg tendon). This method enables the quantitative estimation of the local degree of mineralization and 3D collagen fibril orientation non-destructively at submicron resolution. It was then applied to the cortex of bovine bone samples in combination with micropillar compression, allowing to reliably determine structure-property relationships of bone at the microscale. Later, a multimodal framework for bone characterization was developed in another animal bone model (minipig jawbone). This included the development of a novel femtosecond laser ablation protocol for bone micropillar fabrication allowing high-throughput and site-matched testing without exposure to high vacuum.

The key part of the research was then carried out on a set of femoral neck samples collected from patients who underwent the hip arthroplasty due to osteoarthritis or fragility fracture. The femoral neck cortex from the inferomedial region was analyzed *ex vivo* in a site-matched manner using a combination of micromechanical testing (nanoindentation, micropillar compression) together with micro-computed tomography and quantitative polarized Raman spectroscopy for both morphological and compositional characterization. The output bone properties were correlated with the clinical information about age, gender, and primary diagnosis (coxarthrosis or hip fracture) of the participating patients.

Patient gender and diagnosis did not influence any of the investigated bone properties. Moreover, all mechanical properties as well as the tissue-level mineral density were nearly

constant over all ages (45-89 y.o.). Only local tissue composition was found to change significantly with age: decline in mineral to matrix ratio and increase in collagen cross-link ratio. Site-matched microscale analysis confirmed that all investigated mechanical properties except yield strain demonstrate a positive correlation with the mineral fraction of bone. The large dataset of experimentally assessed microscale bone properties together with the available clinical information of the patients allowed the application of machine learning algorithms for fracture prediction *in silico*. Logistic regression classification suggests that indentation hardness, relative mineralization and micropillar yield stress are the most perspective parameters for bone fracture risk prediction.

As a result of this thesis, the output database of experimental measurements is the first to integrate microscale mechanical, chemical, morphological, and clinical information about the patients. In future, it can be used to compare existing methods of bone quality assessment. Moreover, the presented data and analysis approaches may be used to improve the prediction of fracture risk in the elderly.

Zusammenfassung

Stoffwechselerkrankungen des Knochens wie Osteoporose führen zu einer erhöhten Knochenbrüchigkeit und haben Auswirkungen auf den Lebensstil und die Gesundheitskosten der Patienten. In der heutigen alternden Gesellschaft stellen Fragilitätsfrakturen eine erhebliche gesundheitliche und wirtschaftliche Belastung dar. Die derzeitigen klinischen Methoden zur Beurteilung des Gesundheitszustands der Knochen (Dual-Röntgen-Absorptiometrie, FRAX, Quantitative Computertomographie Variationen) hängen hauptsächlich von der Messung der Knochenmineraldichte (BMD) ab. Die BMD allein macht jedoch nur etwa 70 % der Varianz in der Knochenstärke aus. Es ist daher von grossem Interesse und potenzieller gesellschaftlicher Bedeutung, die Knochenqualität zu untersuchen, d. h. andere Parameter als die BMD zu finden, welche die Knochenfestigkeit und -zähigkeit beschreiben.

In der vorliegenden Arbeit wurden neuartige Labormethoden für die Hochdurchsatzuntersuchung von Knocheneigenschaften mit dem Ziel entwickelt, neue Messkombinationen zu definieren, die als Parameter für die Knochenqualität in einer Frakturrisikoanalyse verwendet werden können. Zunächst wurde eine neuartige Methode zur Quantifizierung der Orientierung mineralisierter Kollagenfibrillen auf der Grundlage der polarisierten Raman-Spektroskopie (qPRS) kalibriert und an einem natürlichen Modellmaterial (mineralisierte Sehne des Putenbeins) validiert. Dieser Ansatz ermöglicht die quantitative Abschätzung des lokalen Mineralisierungsgrades und der 3D-Kollagenfibrillenorientierung zerstörungsfrei mit einer Auflösung im Submikrometerbereich. Die Methodik wurde, in Kombination mit der Kompression von Mikrosäulen, zur Untersuchung der Rinderknochenrinde angewandt. Dadurch konnte die Struktur-Eigenschafts-Beziehungen des Knochens auf der Mikroskala zuverlässig bestimmt werden. Anschliessend wurde ein multimodaler Rahmen für die Knochencharakterisierung in einem anderen Tierknochenmodell (Minischwein-Kieferknochen) entwickelt. Dazu gehörte auch die Entwicklung eines neuartigen Femtosekunden-Laserabtragungsprotokolls für die Herstellung von Knochenmikrosäulen, das einen hohen Durchsatz und lokal angepasste Tests ohne Hochvakuum ermöglicht.

Der wichtigste Teil der Forschung erfolgte an einer Reihe von Oberschenkelhalsproben, die Patienten mit Osteoarthritis und Fragilitätsfrakturen während der Implantation einer Hüfttotalendoprothese entnommen wurden. Die Schenkelhalskortikalis aus dem inferomedialen Bereich wurde ex vivo mittels einer Kombination aus mikromechanischen Tests (Nanoindentation, Mikrosäulenkompression), Mikro-Computertomographie und quantitativer polarisierter Raman-Spektroskopie zur morphologischen und kompositorischen Charakterisierung

analysiert. Die ermittelten Knocheneigenschaften wurden mit den klinischen Informationen über Alter, Geschlecht und Primärdiagnose (Coxarthrose oder Hüftfraktur) der teilnehmenden Patienten korreliert.

Geschlecht und Diagnose der Patienten hatten keinen Einfluss auf die untersuchten Knocheneigenschaften. Darüber hinaus waren alle mechanischen Eigenschaften sowie die Mineraldichte auf Probenebene über das Alter (45-89 Jahre) nahezu konstant. Lediglich die lokale Gewebezusammensetzung veränderte sich mit zunehmendem Alter signifikant, das Verhältnis von Mineralien zu Matrix nahm ab und das Verhältnis von Kollagenvernetzungen zu. Eine lokale Analyse auf der Mikroskala bestätigte, dass alle untersuchten mechanischen Eigenschaften mit Ausnahme der Dehngrenze eine positive Korrelation mit dem Mineralanteil des Knochens aufweisen. Der grosse Datensatz der experimentell bewerteten mikroskaligen Knocheneigenschaften ermöglichte, zusammen mit den verfügbaren klinischen Informationen der Patienten, die Anwendung von Algorithmen des maschinellen Lernens für die *in silico*-Frakturvorhersage. Die logistische Regressionsklassifikation legt nahe, dass die Eindruckhärte, relative Mineralisierung und die Fließspannung der Mikrosäule die wichtigsten Parameter für die Vorhersage des Knochenbruchrisikos sind.

Das Ergebnis dieser Arbeit ist die erste Datenbank mit experimentellen Messungen, die mikroskalige mechanische, chemische, morphologische und klinische Informationen über die Patienten integriert. Sie kann in Zukunft für den Vergleich bestehender Methoden zur Bewertung der Knochenqualität verwendet werden. Darüber hinaus können die vorgestellten Daten und Analyseansätze in Zukunft verwendet werden, um die Vorhersage des Frakturrisikos bei älteren Menschen zu verbessern.

Contents

Abstract	i
Zusammenfassung	iii
List of Figures	xv
List of Tables	xvi
List of Abbreviations	xvii
1 Introduction	1
1.1 Motivation	1
1.2 Hypothesis and aims of the thesis	2
1.3 Outline of the thesis	4
2 Theoretical Background	5
2.1 About bone	5
2.2 Why bone fails	7
2.2.1 Origins of bone toughness	9
2.2.2 Effect of aging and disease on bone fracture resistance	11
2.3 Methods to assess bone quantity and quality	13
2.3.1 Clinical methods	14
2.3.2 Laboratory-based methods	17
2.3.2.1 Structural characterization	17
2.3.2.2 Compositional characterization	23
2.3.2.3 Mechanical characterization	23
3 Development of methods to assess bone quality in animal models	27
3.1 Combining polarized Raman spectroscopy and micropillar compression to study microscale structure-property relationships in mineralized tissues (<i>Acta Biomaterialia</i> 119, 2021)	29
3.1.1 Introduction	31

3.1.2	Materials and methods	33
3.1.2.1	Samples	33
3.1.2.2	Raman spectroscopy and data processing	35
3.1.2.3	Independent verification of MCF orientation	37
3.1.2.4	Mechanical testing and analysis	38
3.1.2.5	Mechanical modeling	39
3.1.2.6	Statistical data analysis	40
3.1.3	Results	40
3.1.3.1	qPRS calibration on MTLT and validation study on bovine cortical bone lamella	40
3.1.3.2	Micropillar compression of bovine cortical bone lamella with known fibril orientation	42
3.1.3.3	Other parameters affecting microscale mechanical properties of bone	44
3.1.3.4	Post-yield behavior and failure modes	44
3.1.4	Discussion	46
3.1.4.1	Quantitative Polarized Raman spectroscopy (qPRS)	46
3.1.4.2	Mechanical testing	49
3.1.4.3	Post-yield behavior and failure modes	53
3.1.4.4	General limitations	55
3.1.5	Conclusion	56
3.2	Assessing minipig compact jawbone quality at the microscale (<i>Journal of the Mechanical Behavior of Biomedical Materials</i> 134, 2022)	57
3.2.1	Introduction	59
3.2.2	Materials and Methods	62
3.2.2.1	Sample preparation	62
3.2.2.2	Micromechanical characterization	62
3.2.2.3	Morphological and compositional analysis	64
3.2.2.4	Statistical analysis	65
3.2.3	Results	66
3.2.3.1	Whole sample level analysis	66
3.2.3.2	Site-matched micropillar compression and Raman spectroscopy	67
3.2.4	Discussion	72
3.2.4.1	Whole sample level analysis	72

3.2.4.2	Site-matched micropillar compression and Raman spectroscopy	73
3.2.4.3	Study limitations	74
3.2.5	Conclusion	75
4	High-throughput laboratory analysis of the bone quality in humans	77
4.1	Comparing microscale compact bone properties of patients who underwent hip arthroplasty: influence of age and gender (<i>in preparation</i>)	79
4.1.1	Introduction	81
4.1.2	Materials and methods	82
4.1.2.1	Sample preparation	82
4.1.2.2	Micromechanical characterization	83
4.1.2.3	Morphological and compositional analysis	85
4.1.2.4	Statistical analysis	86
4.1.3	Results	87
4.1.3.1	Sample cohort description	87
4.1.3.2	Bone properties in relation to patient gender, diagnosis and age	87
4.1.3.3	Compact bone structure-properties relationship	91
4.1.3.4	Overall correlation between measured bone properties	92
4.1.3.5	Perspective bone fracture biomarkers	93
4.1.4	Discussion	94
4.1.4.1	Microscale bone mechanical properties	94
4.1.4.2	Bone composition and morphology	95
4.1.4.3	Site-matched analysis of the bone structure-property relationship	97
4.1.4.4	Potential markers of bone quality	98
4.1.4.5	General Limitations	99
4.1.5	Conclusion	100
5	Overall Discussion and Outlook	103
5.1	Summary	103
5.2	Conclusion and Outlook	107
Appendix	Supporting information for the methods development and validation	111

A1	Combining polarized Raman spectroscopy and micropillar compression to study microscale structure-property relationships in mineralized tissues (<i>Acta Biomaterialia</i> 119, 2021)	113
A1.1	Details on sample preparation	114
A1.2	Polarized Raman spectroscopy	114
A1.3	Correlation between bone biochemistry parameters and mechanical properties	120
A1.4	SAXS measurements	123
A1.5	Osteonal angle calculation	124
A1.6	Mechanical data manipulation	124
A2	Assessing minipig compact jawbone quality at the microscale (<i>Journal of the Mechanical Behavior of Biomedical Materials</i> 134, 2022)	128
A2.1	Estimated heat accumulation during laser ablation	129
A2.2	FE simulations of micropillar taper effect on the output mechanical properties	130
A2.3	Raman spectra processing	131
A3	Comparing microscale compact bone properties of patients who underwent hip arthroplasty: influence of age and gender (<i>in preparation</i>)	133
A3.1	Micro-CT data processing	134
A3.2	Principal Component Analysis (PCA) and Logistic Regression (LR) classification on the final dataset	134
	References	177
	Acknowledgements	180
	Curriculum vitae and list of publications	181
	Declaration of Originality	189

List of Figures

1	This work is licensed under a Creative Commons Attribution 4.0 International License except where otherwise noted	3
1.1	(A) Estimated percentage of fragility fractures increase for the EU27+2 countries between 2019-2034; (B) Estimated (2010, 2019) and predicted (2025, 2034) number of fragility fractures for the EU27+2 countries with color-coded fracture sites; (C) The number of deaths associated with fragility fracture events in EU27+2 countries reported during 2019. Values are expressed per 100,000 of the population. The presented data is based on the recent report from Kanis et al. [3].	3
2.1	Structure of human cortical bone on a logarithmic scale.	6
2.2	Classification of bone fractures and their predisposing factors [47–49]. .	8
2.3	Typical stress-strain curve for bone compression loading until failure. .	9
2.4	Toughening mechanisms in bone. Adapted with permission [55]. Copyright 2010, Annual Reviews.	10
2.5	Femoral neck cortex from 89 y.o. female patient. Note the trabecularization at the endocortical region (bottom) as well as the overall porosity of the cortex.	12
2.6	Techniques for structural (red bars), compositional (blue bars), and mechanical (green bars) characterization of bone tissue. Note that some techniques for structural characterization are capable of assessing mineral content (marked with *) or elastic bone properties (marked with +), whereas some compositional methods can give information on the structural organization (marked with #). The schematic of bone structural units at corresponding length scales was created via BioRender.com. . .	18
2.7	(a) Arrangement of MCF with marked D-spacing, (b) schematic diffuse scattering and Bragg diffraction pattern in SAXS signal, (c) combined SAXS/WAXS signal [133].	19
2.8	Electron–matter interaction volume with emitted signals. Picture taken from: commons.wikimedia.org	20

2.9	Raman imaging principles.	24
2.10	(Left) typical load-displacement curve of an indentation experiment with marked stages: I- elasto-plastic loading, II - creep at a constant force, III - elastic unloading. (Right) equations for the unloading stiffness (S), reduced modulus (E_r) and hardness (H); where A_c is the contact area, β is a tip shape factor, E_{tip} and ν_{tip} are elastic modulus and Poisson's ratio of the tip, E_{ind} and ν_{ind} are the elastic modulus and Poisson's ratio of the tested material.	25
2.11	(Left) typical stress-strain curve of a micropillar compression experiment with marked yield (σ^{yield}) and ultimate stress (σ^{ult}) points, with a partial unloading segment in the elastic region. (Right) equations for the stress (σ), strain (ϵ), deformation length (Δl) and effective contact radius (a_c); where A , l_0 and r are the cross-section, initial height and radius of the pillar, F is the loading force, ν is the Poisson's ratio of the sample material, r_c is the radius of curvature at the base of the pillar and η is a constant term ($\eta = 1$ using Sneddon's method [190] and $\eta = 1.42$ using Zhang's method [191]).	26
2.12	Visual comparison between the FIB-milled and femtosecond (fs) laser ablated micropillar. Note the difference in the length scale.	26
3.1.1	MCF spatial orientation during Raman spectra acquisition with marked out-of-plane (θ) and in-plane (φ) angles. Set of Raman spectra collected at different incident laser polarization on MTLT. Highlighted characteristic collagen bands: amide III ($1215 - 1300cm^{-1}$, N-H bending and C-N stretching of the peptide backbone) and amide I ($1600 - 1700cm^{-1}$, C=O stretching). Polar plots: polarization dependence of $\int amide I / \int amide III$ with theoretical prediction and simplified fit to the experimental data (1) for two assumed orthogonal MCF orientations.	36
3.1.2	Schematic of micropillar compression test. (A) Indenter setup with controlled humidity sample chamber. (B) Sketch of the micropillar compression configuration. (C) HRSEM image of fabricated micropillars. (D) Stress-strain curve with marked output parameters: elastic modulus E , calculated as the slope of the stress-strain curve during the partial unloading segment; yield stress σ^y , defined as stress at 0.2% inelastic deformation; ultimate stress σ^{ult} - maximum stress value; plateau stress σ^{pl} - stress value at 0.08 strain.	39

3.1.3	(A) Anisotropy of MTLT collagen bands at different out-of-plane fibril orientation θ ; (B) Anisotropy of bovine cortical osteonal bone collagen bands at different osteon orientation, fitted with the calibration function from the MTLT study. The coefficients of determination R^2 are 0.98 and 0.82, respectively.	41
3.1.4	Stress-strain curves and HRSEM images after pillar compression of bovine cortical bone lamella with different mineralized collagen fibril orientation, scale bar 1 μm	43
3.1.5	Elastic modulus and yield stress dependence on the collagen fibril out-of-plane orientation. The coefficients of determination R^2 are 0.50 and 0.61, respectively.	43
3.1.6	Post-yield behavior and failure modes encountered in compression tests of micropillars with different out-of-plane MCF angles θ . Failure modes were analyzed visually based on HRSEM images, the representative HRSEM images of each failure mode with marked stress concentration regions are shown at the bottom (white arrows point to the vertical cracks, grey arrows point to the oblique cracks, and black arrows point to the horizontal cracks). Softening/hardening behavior was estimated from the relative change of stress after the yielding point R (equation 3.1.5) and fitted with hyperbolic tangent function (equation 3.1.6). The coefficient of determination $R^2 = 0.72$, scale bar 1 μm	45
3.2.1	Schematic of the laser ablation of bone in a unidirectional scanning mode with marked micropillar array positions (A) and the output micropillar geometry (B); optical overview image of the sample top surface with femtosecond laser ablated micropillar array (C); close-up SEM image of the micropillar array (D).	63
3.2.2	Optical images of the representative samples' top surfaces of each genotype with the marked plexiform zone (indigo) and the circumferential lamellae (green), as well as the osteonal (rose-colored) and interstitial (aquamarine) zones marked in the insets.	66
3.2.3	Tissue Mineral Density (TMD), Bone Volume fraction (BV/TV), and Degree of Anisotropy of Haversian porosity (DA) of the cortical region of the jawbone of three minipigs genotypes.	67

3.2.4	Mineral to matrix ratios as estimated at interstitial, osteonal, and plexiform zones of three minipigs genotypes. Statistical significance asterisks: * – $p \leq 0.05$, ** – $p \leq 0.01$, *** – $p \leq 0.001$, **** – $p \leq 0.0001$	68
3.2.5	Young modulus (E) and hardness (H) as estimated at interstitial, osteonal, and plexiform zones of three minipig genotypes: Yucatan, Göttingen, Sinclair. Statistical significance asterisks: * – $p \leq 0.05$, ** – $p \leq 0.01$, *** – $p \leq 0.001$, **** – $p \leq 0.0001$	69
3.2.6	Bone Young modulus (E) and hardness (H) versus bone mineral to matrix ratio.	70
3.2.7	Microscale bone properties of three minipigs genotypes. Statistical significance asterisks:* – $p \leq 0.05$, ** – $p \leq 0.01$, *** – $p \leq 0.001$, **** – $p \leq 0.0001$	71
3.2.8	Elastic modulus and yield properties versus the mineral to matrix ratio as assessed for three minipig genotypes.	71
3.2.9	Observed fracture modes of compressed micropillars. A – axial cracking, B – mushrooming, C – shear.	72
4.1.1	Bone sample extraction and orientation schematic.	83
4.1.2	Microscale analysis methods and their schematic location on the sample surface. The whole sample volume was scanned with micro-CT. Structural unit analysis on interstitial (Int) and osteonal (Ost) zones included nanoindentation maps and quantitative polarized Raman spectroscopy (qPRS) measurements on the mapping area. A typical indentation curve together with polarized Raman spectra are shown at the top right. A schematic of the bone micropillar compression is shown at the bottom. Compression tests were site-matched with qPRS measurements on each pillar. A typical stress-strain curve from the micropillar compression experiment is shown at the bottom right.	84
4.1.3	Histogram of patients' gender (A) and primary diagnosis (B) distributions across the age.	88
4.1.4	Compact bone properties in relation to the patient gender, primary diagnosis, age and analyzed cortical bone zone (interstitial, osteonal). Measured bone properties from top to bottom: elastic moduli (E), mineral to matrix ratio (mineral/matrix), $I_{\sim 1660}/I_{\sim 1683}$ (matrix maturity ratio), tissue mineral density (TMD) and bone volume fraction (BV/TV). . . .	89

4.1.5	Local mineral-mechanical relationships of compact bone in relation to the patient's age and primary diagnosis.	91
4.1.6	Pearson's correlation coefficients (r) from the multiple regression analysis of the measured bone properties.	92
5.2.1	Left: SHG overview image of the human cortex. Right: SHG images of the same osteonal region (marked on the overview image) acquired at different analyzer angles (0° , 45° , 90°) and the overlap image with all angles. Image credit: Dr. Justine Kusch-Wieser (Scope M, ETHZ). . . .	109
A1.1	(A) MTLT samples each containing a tendon section cut at 0° , 22.5° , 45° , 67.5° or 90° to the main tendon axis. (B) Bovine cortical bone rough cuts.	114
A1.2	Polarized Raman spectra processing steps for the raw data using Python software.	115
A1.3	Theoretically predicted anisotropy parameters A/B for different out-of-plane angles θ . The coefficient of determination $R^2 = 0.99$	117
A1.4	Polarized Raman line-maps collected from axial (A) and transverse (B) osteons. Top: optical microscope images with out-of-plane osteonal angles as determined from micro-CT, red line indicates where the scan was taken. Bottom: line-maps for the out-of-plane MCF angles determined using qPRS, blue line is the guide to the eye.	118
A1.5	Change of amide I and amide III integral areas over time. Blue and orange line are raw and averaged data, respectively, black dashed line indicates the 5% increase of the integral area.	119
A1.6	Out-of-plane MCF angles, calculated for MTLT using qPRS versus out-of-plane MCF angle θ , determined from SAXS measurements.	119
A1.7	Comparison of the amide I/ amide III and amide I/ ν_2PO_4 Raman band ratios that can be used for spectral anisotropy A/B calculation and consequent out-of-plane angle estimation. (A) Polarization dependence for the two Raman band ratios for both axial and transverse MTLT sample orientation. (B) Correlation between the two Raman band ratios as estimated for MTLT samples. (C) Anisotropy of amide I/ ν_2PO_4 Raman band ratios at different out-of-plane fibril orientation θ for MTLT samples. The coefficient of determination $R^2 = 0.99$	121

A1.8	Correlation between bone biochemistry parameters, as assessed by PRS, and mechanical properties, as measured using micropillar compression.(A-C) Correlation between the osteonal Mineral-to-matrix ratios (A), Crystallinity (B), Amide III/CH-bending ratios (C) and the output elastic modulus. (D-F) Correlation between the osteonal Mineral-to-matrix ratios (D), Crystallinity (E), Amide III/CH-bending ratios (F) and the output yield stress.(G-H) Correlation between the Amide I/CH-bending (G), Amide III/CH-bending ratios (H) and the out-of-plane MCFs angle. . .	122
A1.9	2D Nanography and 2D SAXS profiles with schematically marked q-range and output azimuthal profiles fitted with the Lorentzian function. . .	123
A1.10	Azimuthal broadening B_{obs} of the streak signal as a function of inverse scattering vector modulus q for MTLT samples presented together with the linear fit according to equation A1.11 and output misorientation width B_{phi}	124
A1.11	Osteonal orientation determination steps using using ImageJ and BoneJ. Left: micro-CT scan of the chosen sample was tilt corrected (Untilt Stack plugin) and correlated with the optical image to locate the osteons of interest; stacks with the chosen osteon were cropped and binarized. Right: snapshot of the 3D view on the binarized volume of interest (note: Haversian canal is shown in white); three orthogonal principal axes (grey lines on the snapshot) were automatically determined for each Haversian canal using the Moment of Inertia plugin, the rotation matrix in reference to the stacks main axis (z axis on the figure) was constructed. The out-of-plane orientation θ of each osteon was taken as the angle between the principal axis along the Haversian canal and the z axis of the stacks. . .	125
A1.12	Change of elastic modulus and yield stress within the measurement time. Values were normalized over the day of measurements.	127
A2.1	Distribution of von Mises stresses during compression simulations for micropillars with ideal (top) and tapered (bottom) geometries and corresponding stress-strain curves.	131
A2.2	Raman spectra processing steps for the raw data using Python software [221].	132
A3.1	Steps of the micro-CT image processing.	134

A3.2	Left: PCA analysis with first two Principal components score distributions for all 42 patients, colors of the points correspond to the patients primary diagnoses: coxarthrosis – grey, fracture – aquamarine. Right: top-10 bone parameters from the first Principal Component with their scores.	134
A3.3	Prediction of the bone fracture patients via Logistic regression algorithm. Left: confusion matrix for the classification. Right: dataset variables (features) sorted per importance.	135

List of Tables

2.1	Summary of clinical methods to assess skeletal health status.	14
2.2	Summary of laboratory-based methods for the structural, compositional and mechanical characterization of bone tissue at micro- to nanoscale. .	22
3.1.1	Output parameters from the apparent modulus 3.1.2 and yield stress 3.1.3 fit.	44
3.1.2	Reported mechanical anisotropy values and experimental details.	51
4.1.1	Bone compositional and structural parameters, assessed via Polarized Raman spectroscopy.	86
4.1.2	Summary of measured bone properties depending on the patients' gender, diagnosis or zone. P-values from the one-way ANOVA test with the nested mixed effect model of the bone characteristics compared within mentioned cohorts of patients. P-values for the group (gender, diagnosis or zone), age and their interaction are reported.	90
A2.1	Laser ablation and bone tissue parameters used for the heat accumulation calculations.	129

List of Abbreviations

LCN	Lacuno-canalicular network
MCF	Mineralized collagen fibril
HA	Hydroxyapatite
DXA	Dual-energy X-ray absorptiometry
QCT	Quantitative computer tomography
HR-QCT	High resolution QCT
Micro-CT	Micro-computed tomography
Nano-CT	Nano-computed tomography
SR-CT	Synchrotron CT
QUS	Quantitative ultrasound
MRI	Magnetic resonance imaging
FEA	Finite element analysis
EM	Electron microscopy
SEM	Scanning electron microscopy
TEM	Transmission electron microscopy
ET	Electron tomography
SAXS	Small-angle X-ray scattering
sSAXS	Scanning SAXS
WAXS	Wide-angle X-ray scattering
qBEI	quantitative backscattered electron imaging
EDX	Energy-dispersive X-ray
FTIR	Fourier-transform infrared spectroscopy
RS	Raman spectroscopy
PRS	Polarized Raman spectroscopy
qPRS	quantitative polarized Raman spectroscopy
PLM	Polarized light microscopy
CLSM	Confocal laser scanning microscopy
SHG	Second harmonic generation microscopy
SAM	Scanning acoustic microscopy
AFM	Atomic force microscopy
LC	Liquid chromatography
MS	Mass spectrometry

MTLT	Mineralized turkey leg tendon
FWHM	Full width at half maximum
NA	Numerical aperture
SNR	Signal to noise ratio
EFM	Extracelluar matrix
ECM	Extracellular matrix
NCP	Non-collagenous proteins
ROI	Region of interest
FIB	Focused ion beam
HR-SEM	High-resolution SEM
SEE	Standard error of the estimate
RH	Relative humidity
TMD	Tissue mineral density
BV/TV	Bone volume ratio, bone volume vs. the total volume
DA	Degree of anisotropy
fs	Femtosecond
IQR	Interquartile range
PCA	Principal component analysis

Medical and biological terms

Hematopoiesis — the formation of blood cellular components.

Hip
arthroplasty — hip replacement surgery.

Hypogonadism — diminished functional activity of the gonads (testes or ovaries) that may result in diminished production of sex hormones.

OI — Osteogenesis imperfecta, also known as brittle bone disease

Bovine bone — bone from the cattle species.

Ovine bone — bone from the sheep species.

Porcine bone — bone from the pig species.

Symbols

λ	[m]	Wavelength
$\lambda_{scatter}$	[m]	Wavelength of the scattered light
S	[N/m]	Stiffness
P	[N]	Force or load
P_{max}	[N]	Maximum force or load
P_{meas}	[N]	Measured force or load
E	[Pa]	Elastic modulus
E_a	[Pa]	Axial elastic modulus
E_{app}	[Pa]	Apparent elastic modulus
E_r	[Pa]	Reduced modulus
E_t	[Pa]	Transverse elastic modulus
A	[m^2]	Cross section area
ν	[$-$]	Poisson's ratio
ν_a, ν_t	[$-$]	Axial and transverse Poisson's ratio
ν_{ind}	[$-$]	Poisson's ratio of the indenter
β	[$-$]	Tip shape factor
H	[Pa]	Hardness
C	[m/N]	Compliance
σ	[Pa]	Stress
σ_{pl}	[Pa]	Plateau stress
σ_{ult}	[Pa]	Ultimate stress
σ_x	[Pa]	Stress applied along the loading axis
σ_{yield}	[Pa]	Yield stress
σ_a^y, σ_t^y	[Pa]	Axial and transverse yield stress
ε	[$-$]	Strain
$\dot{\varepsilon}$	[s^{-1}]	Strain rate
Δl	[m]	Length of deformation
l_0	[m]	Initial length
a_c	[m]	Effective radius of contact
η	[$-$]	Constant term determination of micropillar sink-in contribution
r	[m]	Pillar radius
r_c	[m]	Radius of the curvature at the base of the pillar
T	[K]	Temperature
τ	[Pa]	Shear stress
μ	[Pa]	Shear modulus

μ_a	[Pa]	Axial shear modulus
R	[—]	Relative change of stress after yielding
$wt.\%$	[—]	Weight percentage
α	[°]	Polarization angle
$\frac{A}{B}$	[—]	Spectral anisotropy parameter
ϕ	[°]	In-plane rotation angle
θ	[°]	Out-of-plane angle
θ^{err}	[°]	Angular uncertainty
X	[Pa]	Longitudinal strength of composite
Y	[Pa]	Transversal strength of composite
S	[Pa]	Shear strength of composite
R^2	[—]	Coefficient of determination
p	[—]	Level of significance

Chapter 1

Introduction

If you don't know where you are going,
any road will get you there.

Lewis Carroll

1.1 Motivation

With the increase in the average life expectancy in developed countries, a large part of the population is experiencing bone fragility fractures. These fractures can occur during everyday activities and are often linked to the weakening of bone, which can be a sign of underlying osteoporosis.

The term osteoporosis (from Greek *osteon* + *poros*) was introduced at the beginning of the 1820s by German-born French pathologist Jean G.C.F.M. Lobstein. To this day, there are scientific and clinical debates about the nature and appropriate diagnostic criteria for this bone disease [1,2]. Skeletal disorders like osteoporosis or, in its milder form, osteopenia are characterized by decreased bone mass and deterioration of bone microarchitecture, which leads to bone fragility and a subsequent increase in the risk of fractures.

Currently, more than 23 million men and women are at high risk of osteoporotic fractures in the European Union together with the UK and Switzerland (EU27+2) [3]. With the demographic growth of the elderly population (age 75 and above), the number of fragility fractures is projected to increase. The expected rate of fragility fractures growth varies within EU27+2 countries, starting from 8% for Latvia and going up to 58% for Ireland (Figure 1.1 A). Switzerland is expected to experience an estimated 38% increase in fragility fractures

over the next decade.

Fragility fractures are a growing challenge in the public health landscape, causing significant deterioration of the patient's quality of life and at worst leading to death [3]. According to the annual statistics about fragility fracture-related deaths for the EU27+2 countries, 107 deaths per 100,000 population were recorded in Switzerland in 2019, which is below the average for the investigated countries (Figure 1.1 C). Most commonly, fragility fractures occur in the spine, hip and forearm. The fracture incidents are projected to increase in all of the mentioned sites for the EU27+2 countries. Notably, hip fractures are expected to increase at the highest rate when compared to other fracture sites, with a 30% increase over the next decade (Figure 1.1 B).

Osteoporosis is the most common bone disease in humans, representing a major public health problem. It is more common in Caucasians, older people, and women. It is estimated that one in three women and at least one in six men will suffer an osteoporotic fracture in their lifetime. Osteoporosis is also called the "silent disease" because it often remains asymptomatic until fractures occur. Despite the significant medical and economic burden of osteoporosis, most individuals at high risk are never identified nor given appropriate treatment, leading to further fractures and poor health [4].

To date, clinicians frequently use bone mineral density (BMD) as an approximate measure of bone strength. Consequently, clinical methods to assess bone health status depend fully or to a great extent on BMD measurements. However, BMD can only act as a surrogate of bone strength, and methods to assess BMD are usually carried out only after the occurrence of the bone fracture [5,6]. More and more evidence is published by the scientific and medical community, demonstrating the urge for improvement of the clinical screening methods [6–11]. Of great scientific interest and major public impact is the study of bone parameters other than BMD, affecting the integrity of bone. This is the main focus of the presented thesis.

1.2 Hypothesis and aims of the thesis

The working hypothesis of this thesis is that the inclusion of additional bone parameters besides BMD, may improve fracture risk prediction. Such parameters include but are not limited to: bone extracellular matrix (ECM) composition, fibrillar structural organization and microscale mechanical properties.

The aims of this thesis were (i) to develop a multimodal framework of methods for bone quality and quantity assessment and (ii) to define bone ECM parameters, which can be used

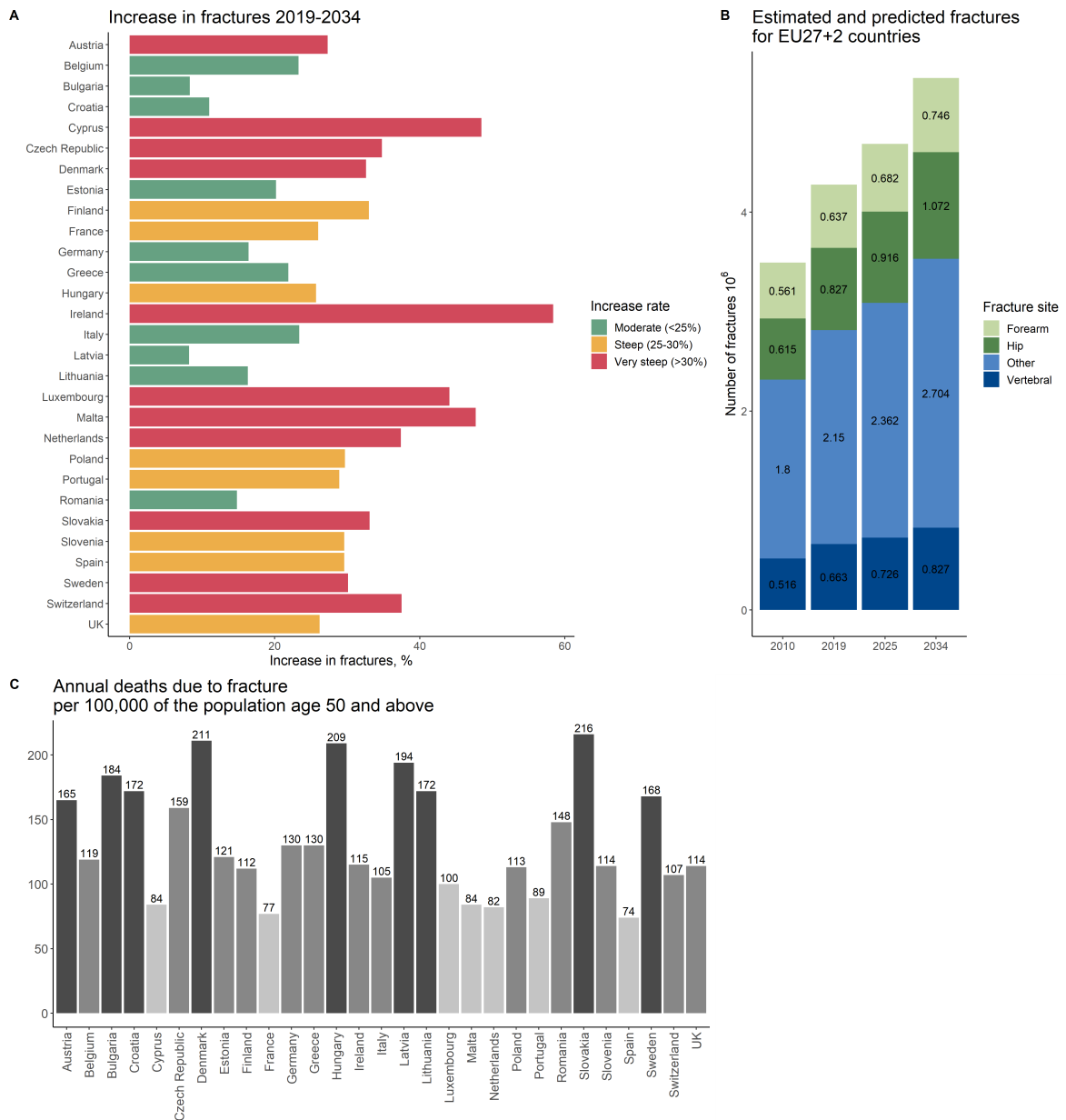


Figure 1.1 – (A) Estimated percentage of fragility fractures increase for the EU27+2 countries between 2019-2034; (B) Estimated (2010, 2019) and predicted (2025, 2034) number of fragility fractures for the EU27+2 countries with color-coded fracture sites; (C) The number of deaths associated with fragility fracture events in EU27+2 countries reported during 2019. Values are expressed per 100,000 of the population. The presented data is based on the recent report from Kanis et al. [3].

to improve fracture risk prediction.

To achieve these milestones, the first experimental part of this thesis was carried out on animal models. In contrast to human bone, animal bone often exhibits a simplified ultrastructure and less variability within the same genotype, thus reducing the complexity of the bone ECM measurements [12–14]. The established multimodal methodological framework was subsequently applied to human bones.

1.3 Outline of the thesis

This thesis consists of five chapters including the current introduction.

Chapter 1 provides the motivation for the current work as well as the hypothesis and aim of the thesis.

Chapter 2 contains a brief introduction to bone composition and its hierarchical organization at different length scales, which plays a key role in governing bone mechanical properties. Some details about bone toughening mechanisms and their alterations during aging and disease are mentioned. This chapter also describes current methods to estimate bone quality in clinics together with the recent developments for the bone quality assessment in laboratory-based methods.

Chapter 3 is based on the recent developments and application of methods to assess bone quality in animal models. This chapter is divided into 2 subsections.

- In the first section, microscale structure-property relationships in mineralized tissues were studied via a combination of two novel methods: quantitative polarized Raman spectroscopy (qPRS) and micropillar compression. The qPRS method was developed and validated on the mineralized turkey leg tendon, while the combination of qPRS and micropillar compression analysis was applied to the bovine cortical bone from the tibia.
- The second section describes the development of the multimodal analysis framework for the compact bone quality assessment in the minipig jawbone. A combination of Raman spectroscopy, microscale computed tomography, nanoindentation and high-throughput micropillar compression was carried out on the minipig cortical bone samples from three genotypes.

Chapter 4 describes the application of the recently developed high-throughput laboratory analysis methods of bone ECM properties in patients who underwent hip arthroplasty. Bone ECM properties were correlated within and between the patients with the ultimate goal to find the combination of bone parameters that influence hip fracture occurrence.

Chapter 5 provides an overall discussion and the outlook of the thesis.

Chapter 2

Theoretical Background

2.1 About bone

Bone is one of the oldest investigated matter and it has been of scientific interest for more than five centuries, starting from Leonardo's anatomical drawings of the human skeleton and its parts (circa 1510, [15]). Nowadays, bone is of major importance not only to clinicians, biologists and hematologists but also to materials scientists as well as biomechanists. The bone research is largely driven by the versatile roles bone plays in the body. Structurally, bones allow for overall support of the body, enable movement and simultaneously protects the inner organs. Additionally, bone acts as a storage site for minerals and allows hematopoiesis, i.e. the development and storage of blood cells.

Bone is a complex natural material exhibiting an exceptional combination of strength and toughness while being lightweight. These remarkable material properties are triggered by the evolutionary adaptation of bone to provide mechanical support and organ protection in the human body [16]. While bone is composed of ductile organic and brittle inorganic phases, the hierarchical arrangement of the constituents from macro- down to the nanoscale gives rise to the outstanding mechanical properties of bone. The schematic of bone's hierarchical structure is illustrated in figure 2.1.

At the macroscale, *trabecular* and *cortical* types of bones can be distinguished [17]. Trabecular bone is highly-porous bone tissue, also called spongy or cancellous bone, which can be found at the metaphysis of long bones, in the vertebral bodies, skull and pelvic bones. It consists of 5 – 40% of bone tissue with the remaining space being filled with marrow and fat. The cancellous bone transfers the load from joints to the compact bone of the cortex of long bones and acts as an important load-bearing component [18, 19].

Cortical bone plays a prominent role in defining the overall tissue's mechanical properties [20]. It forms the hard exterior (cortex) of bones, which is found on almost all bone surfaces, accounting for approximately 80% of the total skeletal mass of the human body. Cortical bone volume is permeated with cylindrical structures called *osteons*, typically 150-250 μm in diameter [21]. The thin outer layer of an osteon (1-5 μm) is known as the cement line. This thin layer is relatively highly mineralized (or collagen-deficient) or similarly mineralized in comparison to the surrounding bone matrix [22, 23]. Interstitial tissue surrounds osteons and is made of fragments of older osteons with higher mineralization [24] (figure 2.1).

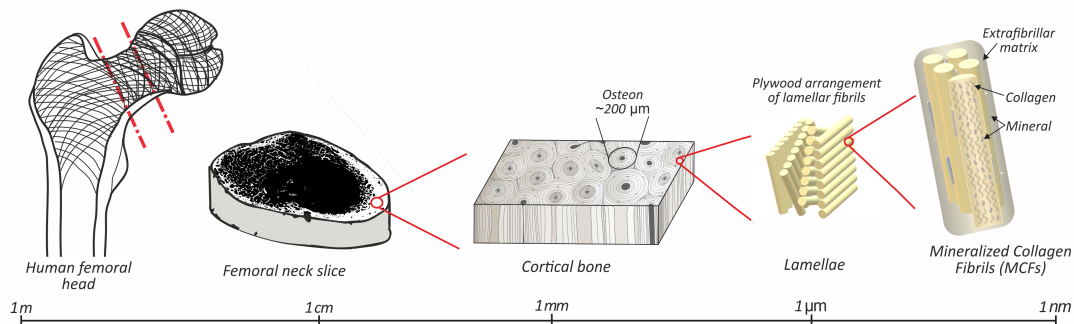


Figure 2.1 – Structure of human cortical bone on a logarithmic scale.

At the microscale level, each osteon is made of concentric coaxial layers about 3-7 μm thick, called *lamellae*, which can be found in both cortical and trabecular bone [25]. In the cortical bone, lamellae encompass the central canal within the osteon – the Haversian canal. Blood vessels and nerves pass through this canal to supply the osteocyte cells with nutrients. Osteocyte cells reside inside lacunae, distributed within the volume of bone matrix, they connect through canaliculi, forming an extensive *lacuno-canalicular network (LCN)* [26]. Bone lamellae consist of a stack of sub-lamellae sheets, approximately 1 μm thick, made of aligned collagen fibers (figure 2.1). In their turn, collagen fibers are made of *mineralized collagen fibril (MCF)* bundles, interconnected through collagen cross-linking [27]. MCFs are often referred to as the main mechanical building block of bone, reaching about 30-300 nm in diameter and up to hundreds of microns in length.

Currently, two mutually exclusive models have been proposed to describe the bone lamellae organization. The first model follows the work of Gebhardt [28] and it states that bone lamellae are made of densely packed and aligned MCFs layers. Based on the predominant MCFs orientation pattern within the lamellae, three types of morphology can be dis-

tinguished: longitudinal or transverse, where the principal MCFs orientation is parallel or orthogonal to the osteon main axis respectively, and alternating, where MCF orientation interchanges between transverse and longitudinal to the osteon axis [29–31]. According to the second model, the bone lamellae have an interwoven texture of the MCFs and the bone lamellation appears due to the alteration of collagen-rich (dense) and collagen-poor (loose) lamellae [32]. Despite the experimental evidence for both bone lamellation patterns, Gebhard's model is the most largely accepted one [33].

At the nanoscale, MCFs are formed from staggered arrays of collagen molecules (figure 2.1). Collagen fibril reaches around 500 nm in diameter. Crystal plates of *hydroxyapatite* (HA) assemble in the gap between the molecules, reaching tens of nanometers in length and 1-2 nm in thickness. This staggered arrangement creates an observable periodicity within the MCF known as the D-band with the repetition step of 67 nm (figure 2.7 from section 2.3.2.1). Bone HA nanocrystal contains structural water and many substitutions such as carbonate, magnesium and fluoride, which reduce the crystallinity of the apatite [34, 35]. A larger portion of the bone mineral is found between the MCFs and oriented parallel to the collagen fibrils [36]. Collagen molecules are composed of two $\alpha 1$ and one $\alpha 2$ helix of collagen type I (~ 200 nm in length and ~ 1.5 nm in diameter), stabilized by hydrogen bonds [37]. Within the MCF, collagen molecules are stabilized by post-translational modifications forming cross-links of the side chains near the end of the molecules [27, 38]. The extrafibrillar matrix is mainly composed of non-collagenous proteins (NCP) including osteopontin, osteocalcin, bone sialoproteins and proteoglycans [39–41].

Besides the organic and mineral phases of bone, water is another abundant component. It can be found in two states: unbound and bound to the bone matrix [42, 43]. Unbound water is located within the bone micropores including Haversian canals and LCN. Bound water is found attached to the collagen [44, 45] and mineral [46] surfaces of bone as well as being a part of their molecular and lattice structure.

Thereby, at the lowest scale, bone is made of calcium phosphate nanocrystals (HA, 50-60 wt.%) with impurities, proteins (mainly collagen type I and NCP, 30-40 wt.%), and water. Each of bone's constituents influences material strength and changes in different ways during aging and/or disease.

2.2 Why bone fails

Bone fractures are very common and can affect individuals at any age. Some fractures occur due to the excessive loading of bone (high impact fall) that exceeds the tissue threshold in

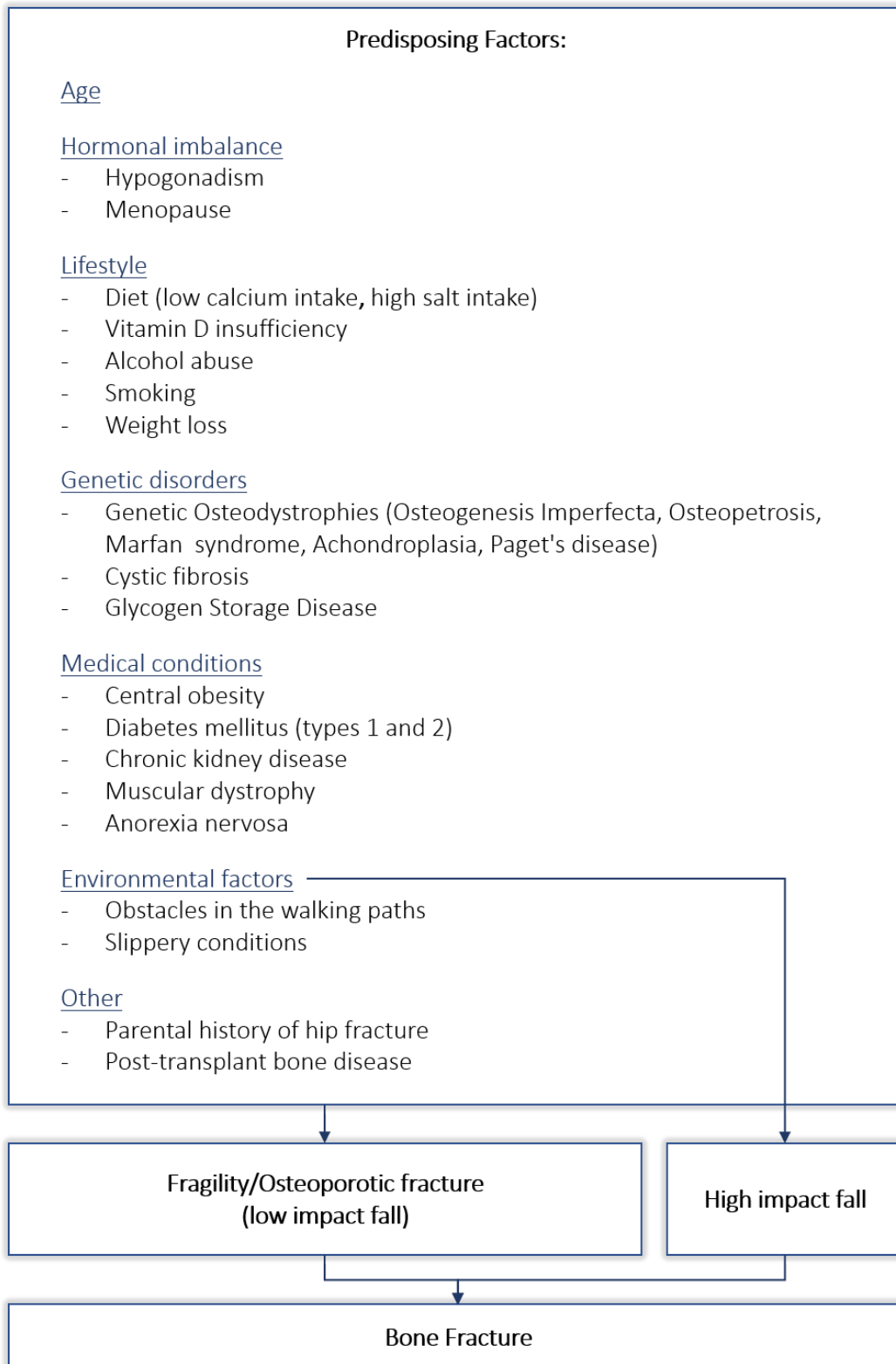


Figure 2.2 – Classification of bone fractures and their predisposing factors [47–49].

terms of damage and stress. Other bone fractures may occur at much lower loading forces (low impact fall) and are caused by the weakening of bone. Such bone fractures are known as fragility or osteoporotic fractures. Numerous factors may contribute to the occurrence of bone fracture, those factors are briefly summarized in figure 2.2. Primarily, whole-body aging, hormonal imbalance and genetic disorders are compromising bone performance. Moreover, different medications, changes in lifestyle, neurological and musculoskeletal factors, endocrine and hematological disorders may also cause the weakening of bone tissue.

2.2.1 Origins of bone toughness

The loading of bone tissue until failure can be separated into three main stages (figure 2.3). First comes a linear phase where material deforms reversibly until the yielding point, after which the second phase begins. In this phase, the material absorbs the energy by the means of microcrack propagation, causing permanent damage to the bone tissue. In the last phase, catastrophic failure occurs, accompanied by the moving of a crack or a fracture plane. Accordingly, the first phase represents the elastic deformation region, while the second and third are plastic deformation regions. The slope of the initial elastic region in the stress-strain curve corresponds to the Young's or elastic modulus, which is related to the stiffness of a material. Meanwhile, the toughness of a material is characterized by its ability to dissipate or absorb energy prior to failure.

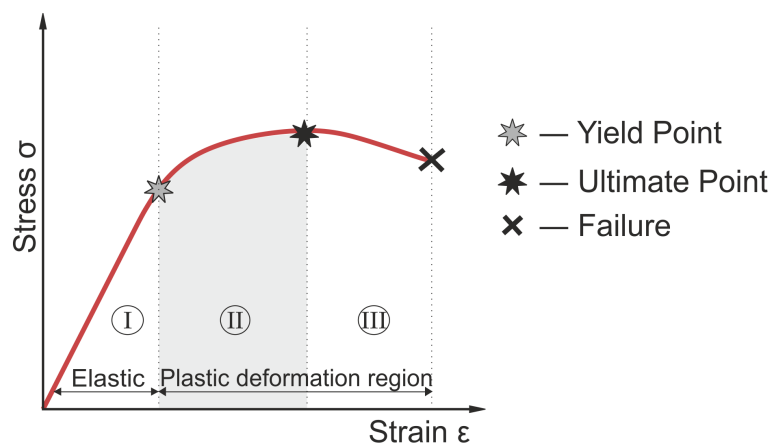


Figure 2.3 – Typical stress-strain curve for bone compression loading until failure.

Bone exhibits exceptional toughness thanks to the number of energy-dissipation mechanisms that work in synergy across several length scales, from the macroscopic to the molecular level (figure 2.4). The hierarchical arrangement of bone has a direct influence on the crack growth and failure process [50–54].

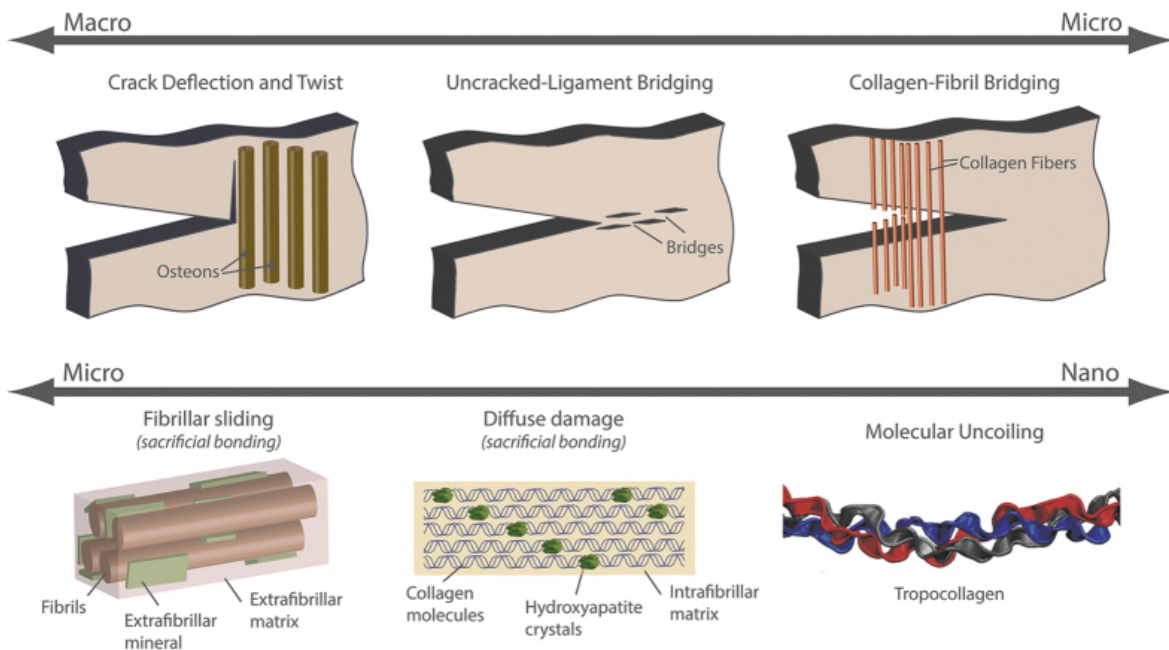


Figure 2.4 – Toughening mechanisms in bone. Adapted with permission [55]. Copyright 2010, Annual Reviews.

At the macro- to microscale, the osteonal structures with their outer cement lines and inner lamellae are naturally *deflecting and twisting the crack path* [56]. Moreover, *crack bridging* shields the crack from the full stress intensity by leaving the intact or uncracked material “bridges” behind the extending crack tip, which thereby carry partially the load and prevent the further propagation of the crack.

At the micro- to sub-microscale, *sacrificial bonds*, are expected to resist deformation through stretching within the molecular layer that is found between different interfaces. This amorphous “glue” layer is made of non-collagenous proteins and it links the fibrils, fibers and lamellae within the bone. Under stress, these weak but reformable bonds within the proteinous “glue” would break and the folded-up molecules would elongate, enabling a large increase in length with minimal increase in force [57,58].

Within the lamellae, the tissue plasticity is generated through *sliding mechanisms between and within the mineralized collagen fibrils* that are facilitated by sacrificial bonds. More specifically, when the interface between the fibers and the extracellular matrix reaches the yielding point, the fibers move past the matrix, forming and reforming the fiber/matrix bonds that break at a fraction of the force required to break the backbone of the macromolecules [59]. As for the fibrillar sliding between the MCF, molecular modeling and experimental X-ray analysis suggest that continuous glide between tropocollagen molecules and hydroxyapatite particles enables dissipative deformation, thus effectively increasing the

resistance to fracture [60].

Down to the nanoscale level, individual collagen molecules deform by *molecular uncoiling and unfolding* following intramolecular hydrogen bond breakage and reformation. These sliding motions provide the basis for large plastic strains without catastrophic brittle failure. The amount of collagen cross-links increases with age, which could lead to molecular fracture of the collagen fibrils and breaking of cross-links, consequently increasing the brittle material behavior [60].

The complex hierarchical structure of human cortical bone generates strength and toughness, through plasticity-based mechanisms at small length scales and crack-shielding mechanisms at larger length scales.

2.2.2 Effect of aging and disease on bone fracture resistance

Alterations in the bone structure caused by aging or disease can be directly linked to higher fracture risk. Below, some of the biological degradation processes, specifically aging, osteoporosis, osteogenesis imperfecta and Paget's disease are discussed based on works of Nyman et al. [51,61] and Zimmermann et al. [53,56].

With aging and/or osteoporosis, bone demonstrates a clear deterioration in its mechanical properties and structural integrity. An example of an optical microscope image of bone cortex extracted from an elderly patient (89 y.o.) is shown in figure 2.5. In addition to a loss in bone mass, the increase in fracture risk with aging can be related to a deterioration in the bone structure over multiple length-scales. The combined effects of a higher proportion of cross-links at the fibril level and a higher osteon density at the microstructural level reduce the mechanical integrity of aged bone. In theory, the cross-links constrain fibrillar plasticity and the higher osteon density reduces extrinsic toughness during crack extension [54,62].

Suppressed remodeling due to aging increases the homogeneity in tissue mineralization and decreases the local variability of collagen fiber orientation [63]. In its turn, the structural integrity of the collagen network correlates significantly with the toughness of bone, likely due to a relative increase of denatured collagen [64,65]. Furthermore, the remodeling reduction after the age of 50 facilitates the micro-cracks accumulation in cortical bone, which is leading to a steep decrease in meso- to microscale fracture resistance of bone tissue [66].

Osteoporosis is the most common metabolic bone disease. To date, osteoporosis can be classified into two main groups: primary and secondary. The latter includes different diseases, lifestyles and medications that can cause osteoporosis. Primary osteoporosis is di-

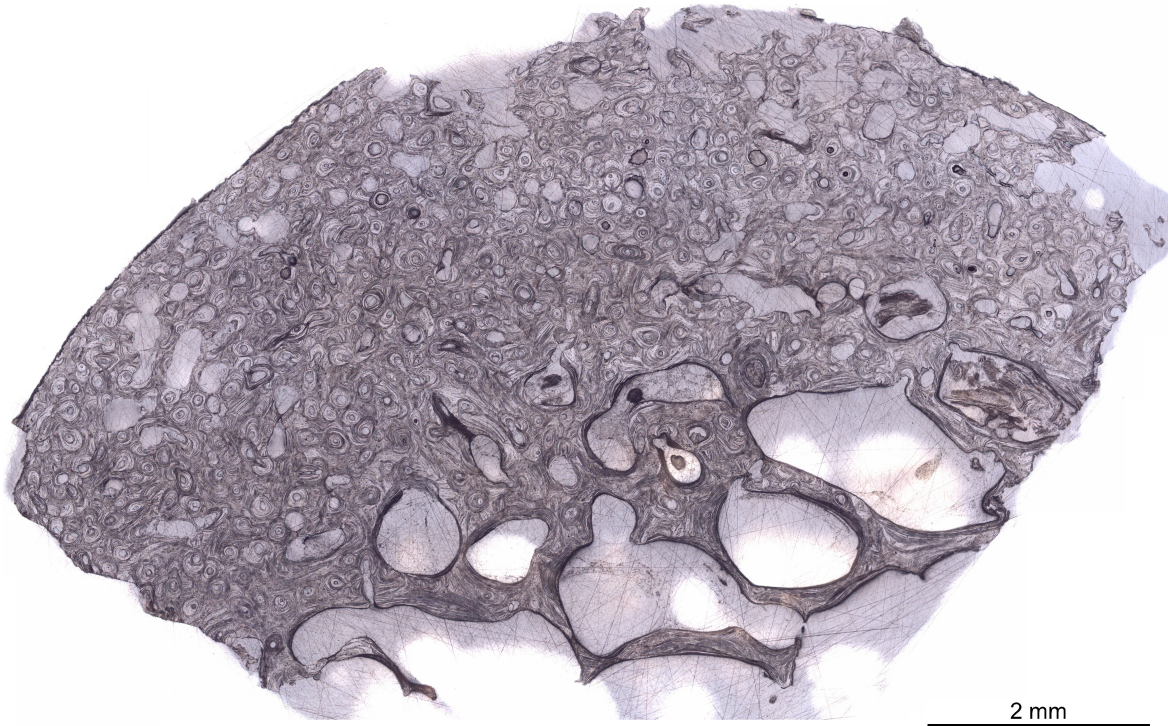


Figure 2.5 – Femoral neck cortex from 89 y.o. female patient. Note the trabecularization at the endocortical region (bottom) as well as the overall porosity of the cortex.

vided into two subgroups: type I, which is also called postmenopausal osteoporosis and is caused by the deficiency of estrogen, and type II, which is also called senile osteoporosis and is related to bone mass loss due to aging. Although osteoporosis can be detected at any age or ethnicity, it is predominantly common in Caucasians, older people, and women [67, 68].

While the term osteoporosis was introduced at the beginning of the XIX century, a definition of this disease was introduced by the World Health Organization (WHO) only in the early 1990s, following the consensus development conference statement [69]. Accordingly, osteoporosis was defined as "a disease characterized by low bone mass and microarchitectural deterioration of bone tissue, leading to enhanced bone fragility and a consequent increase in fracture risk". However, there is scientific evidence that osteoporosis may not only affect bone quantity and microarchitecture but also causes considerable changes in the ultrastructure and matrix itself, which can lead to a loss of bone quality [63, 70–72].

The loss in bone quantity due to osteoporosis and aging has been extensively studied and results from a remodeling imbalance where more bone is resorbed than deposited [63, 73–75]. Since bone remodeling occurs on osseous surfaces, the bone loss in early osteoporosis is mainly trabecular and becomes intracortical with increasing age [73].

Recent studies demonstrate that the organic bone matrix is as well affected by the dis-

ease [63, 76, 77]. In particular, the amount of non-collagenous proteins like osteopontin and osteocalcin was shown to decrease in osteoporotic patients [78]. Such a decrease may lead to the lower fracture toughness, which was nicely demonstrated in mice models [79]. Nevertheless, the specific changes in bone quality that differentiate osteoporosis from aging or other factors are not well-known and require further investigation.

Osteogenesis imperfecta (OI), also known as brittle bone disease, is a result of mutations in the type I collagen, which affect the quantity of bone and its structure [80]. A previous study on the OI mouse models (oim) demonstrates that oim bone has a significantly lower microscale toughness due to collagen defects affecting the formation of a normal fibrillar structure [81]. Additionally, the mesoscale toughness in oim bone is reduced due to a larger amount of woven bone, which lacks an oriented structure to deflect cracks and/or form crack bridges. It is moreover implied that the increased OI bone matrix mineralization will result in a lower plastic deformation capacity [82, 83]. However, recent studies demonstrate that the compressive strength of human iliac crest bone ECM is not reduced in OI [84], suggesting that further studies on the human bone matrix are required to analyze the disruptions in the toughening caused by this brittle bone disease.

In Paget's disease, pathological sites have an abnormally high bone turnover and an overall increase in bone volume [85, 86]. The changes to the bone structure result in symptoms of bone enlargement, bowing/deformity, cracking and pain. Paget's tissue has lower mineralization and a correspondingly lower hardness, which both indicate that the tissue has the capacity for higher levels of plasticity [87]. Tissues with low mineralization levels have previously been found to display significant plastic deformation [16]. Thus, while healthy bone has the macro- to mesoscale crack deflection toughening mechanisms, the Pagetic bone tissue may generate toughness primarily through micro- to nanoscale plasticity mechanisms that promote ductility.

2.3 Methods to assess bone quantity and quality

It becomes increasingly clear, that not only bone quantity but also bone quality plays an important role in osteoporosis progression and detection. Consequently, novel approaches to bone screening are expected to arise in the upcoming decades. In the meanwhile, this section summarises currently employed techniques in clinics and emerging methods used in scientific laboratories for bone quantity and quality assessment.

2.3.1 Clinical methods

According to the WHO guidelines from the year 1994, the survey of risk factors, as well as the bone mineral density measurements, were recommended for skeletal health screening [75]. Moreover, a quantification of the fracture risk was suggested by employing the T-score metrics. Following this method, the mean BMD values of the chosen patient are compared to that of a young adult of the same gender at a peak bone mineral density. T-score is defined as the number of standard deviations between the two. A normal T score is -1.0 and above, low bone density (osteopenia) is between -1.0 and -2.5, and osteoporosis is at -2.5 and lower.

Nowadays there are several methods to assess skeletal health status in a clinical setting, and the most common ones are summarized in the Table 2.1 [88, 89] and described in more detail below.

Table 2.1 – Summary of clinical methods to assess skeletal health status.

Methods	Bone parameters	Advantages	Disadvantages	Ref.
DXA	Areal Bone mineral density (aBMD), geometry	Easy to perform, low radiation exposure (1–6 μ Sv)	2D, Scans are affected by many artifacts, Low contrast	[6, 70, 90]
QCT, HR-QCT	Volumetric Bone mineral density (BMD), geometry, microarchitecture	3D results, low radiation dose: 5 μ Sv (HR-QCT)	High radiation dose: up to 1.2 mSv during hip QCT	[91]
FRAX	Bone fracture risk	Easy to use, open-source	Does not consider certain risk factors	[92, 93]
QCT-based FEA	Bone mechanical properties, fracture risk	Personalized bone strength predictions	Same as QCT, not standardized, high-resolution scans	[94, 95]
QUS	BMD, geometry, micro-architecture, elasticity	Non-invasive, portable, low-cost devices	Lack of standardization, scans are affected by many artifacts	[96]
MRI	Bone geometry, microarchitecture	Non-invasive	Indirect bone characterization, artifacts due to metal, complex data acquisition and analysis	[97]

Dual energy X-ray absorptiometry (DXA or DEXA) was introduced in 1987 [98] and was largely accepted in the clinical practice after demonstrating the evidence for BMD improvement during bone medications trials [99]. Today, almost 36 years later, it remains a gold standard for BMD measurements in medical facilities all over the world. The principles of this technique are following the single energy absorptiometry [100]. With the addition of the second X-ray beam with different energy levels, the absorption of the patient's bone as well as the soft tissue are measured [101]. After subtracting one from another, the bone areal

BMD (aBMD) can be determined.

Measurements with DXA are fast, easy to perform and expose patients to low radiation dose (1–6 μSv) [102]. Although DXA is superior to any other available methodology, it still has some drawbacks. In particular, due to the 2D measurement geometry, any high-density material in the path of the X-ray beam is assumed to be bone, which compromises the aBMD measurements. Moreover, any inherent variations in bone size will result in altered aBMD values because this measure is size-dependent [103]. Areal BMD results are also affected by body composition, thus measurements of obese or underweight patients are inaccurate. Lastly, there are still some discrepancies between the different machine manufacturers and the operation modes of measurements hardware [7].

Quantitative computed tomography (QCT) was introduced in the mid-1970s but was suppressed by the rapidly spreading DXA technology. Like DXA, QCT utilizes X-rays and provides an image based on the linear absorption coefficients. Following the calibration on the hydroxyapatite phantom, attenuation values are converted into bone mineral equivalents [104]. Unlike DXA, QCT collects 2D images from multiple angular projections, which are then reconstructed into the 3D model. Thus, QCT has obvious advantages over the DXA technique [91, 105]. First and foremost, QCT is capable to measure the spatially resolved bone properties, allowing separate measurements of cortical and trabecular bone geometrical parameters as well as the BMD. Moreover, it is capable to measure the volumetric density, which is not size-dependent. The major disadvantages of this technique are a relatively high radiation exposure (up to 2-3 mSv) and a need for a well-set IT infrastructure for the data pipelines [102]. Peripheral QCT reduces the radiation doses (down to 3 μSv) [106] by collecting single 2D scans on dedicated peripheral CT scanners [104, 106]. However, care should be taken for precise patient positioning and motion artifacts as it impacts the output BMD values [107].

Besides BMD, several clinical factors are associated with fracture risk. They primarily include the patient's age, gender, body mass index and previous fractures [108]. In order to include the influence of these factors, WHO released the Fracture Risk Assessment Tool (FRAX) in 2008 [109]. FRAX allows clinicians to estimate the ten-year probability of a major osteoporotic fracture based on the medical questionnaire about the fracture predisposing factors with or without the use of BMD [110]. FRAX embodies a significant advance in osteoporotic fracture risk prediction, therefore facilitating the treatment decisions by clinicians. Yet not all of the possible causes for osteoporosis are included in the questionnaire and care should be taken to tailor the results for personalized diagnosis. To cite Prof. John Kanis, who participated in the tool development and validation: *"The tool is, however, far from perfect, but*

better than BMD alone" [110].

Finite element analysis (FEA) was employed in estimating stresses in human bones in the early 1970s. But it was not widely used until the QCT started to gain momentum in the 1990s, where the generation of the anatomy-specific FE models of bones took place [111]. Further development of the software tools and computer hardware, endorsed the patient-specific FE modeling [112]. Currently, new approaches using 3D FE bone models derived from clinical QCT (QCT-based FEA) have the potential to provide enhanced bone strength predictions [113]. As a limiting points of this method for precise bone strength calculation, high-resolution images are required. Moreover, input material parameters are often generalized and not patient-specific.

Quantitative ultrasonography (QUS) was introduced in 1984 and it is still gaining popularity among scientists as well as medical practitioners [96, 114]. As can be deduced from the name of this technique, it uses ultrasound signals to estimate bone mineral status at the peripheral skeleton. The velocity and the amplitude of the ultrasounds waves are influenced by the bone tissue, reflecting its density, architecture, and elasticity. QUS is an inexpensive, transportable, and non-invasive method, which was shown to predict osteoporotic fractures in elderly women, as well as the DXA measurements [115, 116]. However, the results of this method are largely affected by the temperature and acoustic coupling (gel, water). Regarding the future standardization of QUS, large databases are needed for a correct interpretation of the results in clinical settings [117].

Magnetic Resonance Imaging (MRI) was first applied to the bone in the early 1990s [118]. MRI images are produced by radiofrequency signals that are generated from protons of hydrogen atoms. Accordingly, this technique is well suited for soft tissues with excessive water content. Since bone has less than 10% of water, most of the information is extracted from the contrast difference between the bone and neighboring soft tissue like cartilage and marrow fat [97]. Additionally, diffusion and perfusion MRI methods demonstrated differences in the corresponding MRI-extracted parameters (diffusion and perfusion indexes) for the osteoporotic and healthy patients [119, 120]. Yet, MRI methods can only provide an indirect estimation of the bone volume through the soft tissue signal within bone cavities.

Thus, although QUS and MRI have the valuable advantage of non-invasiveness and the absence of any ionizing radiation dose, they still need a better standardization to compete with the well-established DXA or QCT methods in a clinical setting. Data from high resolution peripheral quantitative computed tomography (HR-pQCT) gives a true volumetric bone mineral density as well as the information about bone microarchitecture, structure, and

mechanical strength. However, QCT methods are used to a lesser degree than DXA as the patients are exposed to a radiation dose from 5 μSv (HR-QCT) up to 1.2 mSv during hip QCT, while the annual dose limit for the general public is 1 mSv [102]. Although DXA has minimal radiation exposure (4 μSv) and correlates well with the fracture risk, the resulting data is affected by many artifacts, therefore such measurements are lacking in accuracy. In addition to existing clinical BMD measurements, fracture risk calculators, such as the FRAX tool, are used to predict an absolute fracture risk per person by combining the bone mineral density and the patient's medical information. Still, such calculators take over the drawbacks of BMD measurements. Another advanced analytical method is the FE modeling based on HR-QCT, which is useful for assessing bone strength and fracture risk. Yet, it requires tailored input for patient-specific results.

2.3.2 Laboratory-based methods

Bone quality is determined by a variety of compositional, morphological and mechanical properties of the bone matrix. Such properties are mainly investigated in laboratory settings. A summary of currently used laboratory-based methods for bone quality analysis is presented in the table 2.2. There, the methods that were used in the current thesis are highlighted in bold. The visual comparison of the length scales of described techniques is depicted in figure 2.6. General information about mentioned methods and some more details about the methods relevant to the current thesis are given below.

2.3.2.1 Structural characterization

Through the recent advances in biomedical imaging, various techniques have been used to assess bone's ultrastructure organization [121–124]. QCT modalities that are commonly used in laboratory settings for tissue imaging are micro- and nano-CT [125]. Micro-CT, also known as X-ray computerized microtomography, provides *ex vivo* characterization of trabecular and cortical bone microarchitecture at about 1-6 μm voxel size [126]. Generally, in micro- or nano-CT devices, the specimen stage is rotated for the projection collection, contrary to the clinical QCT, where X-ray source and detector are moving around the patient. Moreover, micro- or nano-CT devices can be used with the synchrotron source to maximize the resolution of microarchitectural features and local spatial gradients in tissue mineral content [127]. Such synchrotron CT (SR-CT) technique allows spatial investigations on the bone lacunae and the LCN [127]. Moreover, the new generation of nano-CT devices also uses a phase contrast detection approach (phase-contrast CT or X-ray phase nanotomography), rather than classical absorption imaging. In combination with the high brilliance of synchrotron radiation, this modality reaches sufficient resolution to access bone lamellae

ultrastructure down to the MCF bundles (i.e. up to tens of nanometers) [128–130]. This phase detection approach promotes a significant increase in spatial resolution even with the laboratory X-ray source [131]. Besides structural characterization, QCT-based methods also provide spatially-resolved information on the absolute bone mineral content.

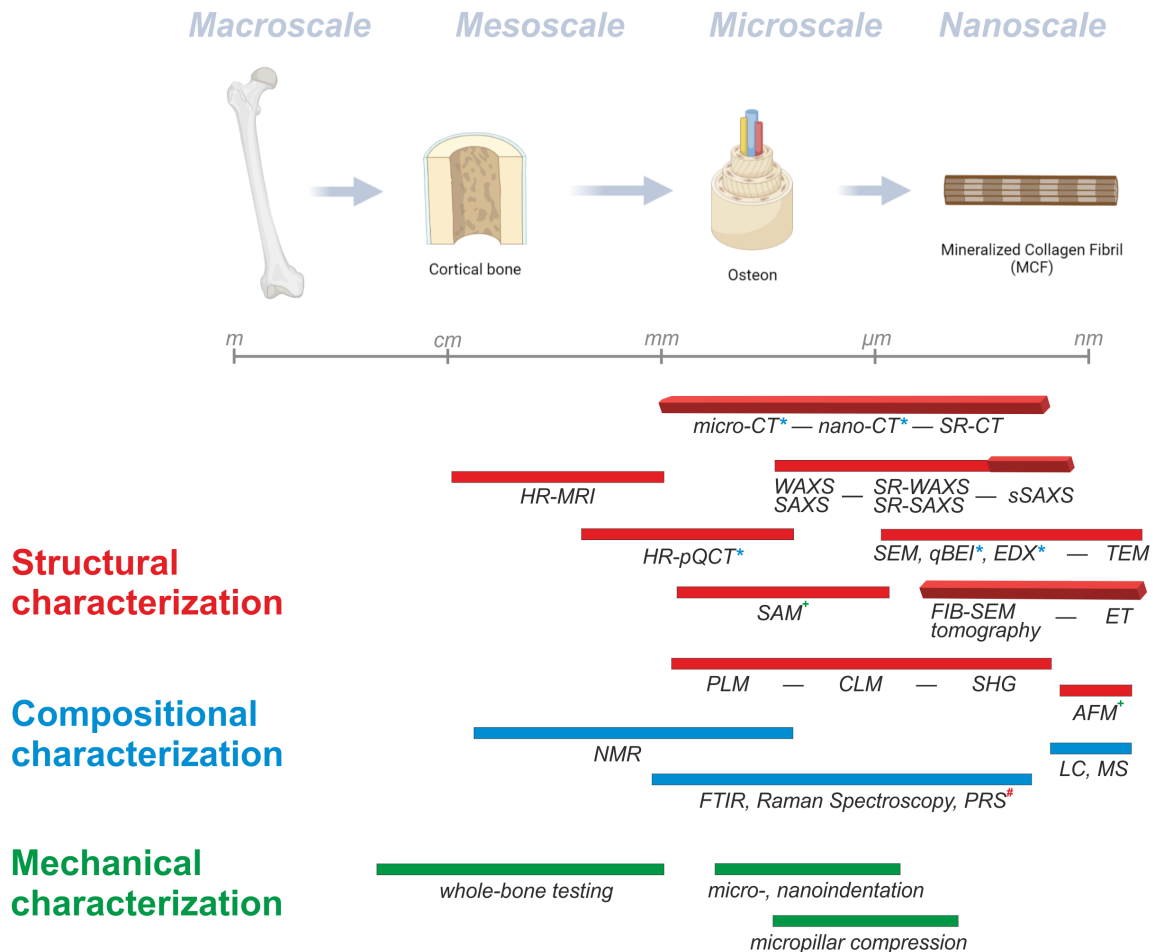


Figure 2.6 – Techniques for structural (red bars), compositional (blue bars), and mechanical (green bars) characterization of bone tissue. Note that some techniques for structural characterization are capable of assessing mineral content (marked with *) or elastic bone properties (marked with +), whereas some compositional methods can give information on the structural organization (marked with #). The schematic of bone structural units at corresponding length scales was created via BioRender.com.

Another family of methods based on X-ray beam interaction with material includes X-ray scattering modalities. These methods provide structural information about the bone tissue in the nano- to Angstrom-scale range, based on the scattering of the X-rays from the bone MCF (figure 2.7). Depending on the registered scattering angle range, Wide Angle X-ray Scattering (WAXS) and Small Angle X-ray Scattering (SAXS) are distinguished. WAXS provides information on crystal properties like crystal lattice parameters and crystal size, while SAXS

can be used to determine structural parameters arising from the regular pattern within the MCF [133]. Typically, the spatial resolution of these modalities is in the range of hundreds of micrometers. However, the resolution can be improved up to 200 nm when the high radiance of the synchrotron is used (SR-SAXS/WAXS, [134]). Recently a quantitative 3D scanning SAXS (sSAXS) method, also known as SAXS tensor tomography, was developed to spatially resolve the 3D arrangement and degree of orientation within the bone MCF [135, 136].

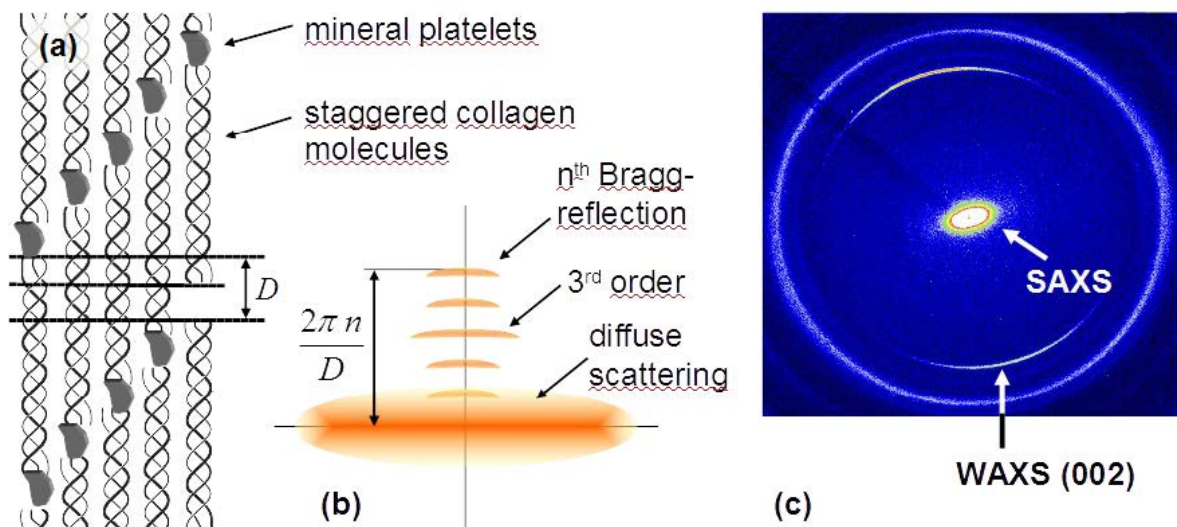


Figure 2.7 – (a) Arrangement of MCF with marked D-spacing, (b) schematic diffuse scattering and Bragg diffraction pattern in SAXS signal, (c) combined SAXS/WAXS signal [133].

Electron microscopy (EM) techniques are based on the interaction of the electron beam with the bone tissue, leading to *a priori* higher spatial resolution than the X-ray-based techniques. Scanning electron microscopy (SEM) is the most widely used EM modality. The signal gathered from the secondary electrons is used for SEM imaging (figure 2.8), enhancing sample surface and topography. To assess sample mineralization, the backscattered electrons are collected, and the corresponding imaging method is called quantitative Backscattered Electron Imaging (qBEI). In principle, the fraction of the backscattered electrons depends on the atomic number of the analyzed elements in the sample, therefore the greyscale level of the image can be correlated with the heaviest element (i.e Z-contrast can be reached). In the case of bone with its 'light' organic matrix, calcium will dominantly influence the qBEI analysis. On the other hand, energy-dispersive X-ray analysis (EDX) can be carried out on the emitted X-ray spectrum when a bone sample is bombarded with a high-energy beam. In bone, the most frequent application of EDX is the measurement of extracellular matrix for defining Ca and P content (and the Ca/P ratio) [137].

Focused Ion Beam (FIB) can be used in combination with SEM imaging, allowing high-resolution image acquisition of consequently milled sections of the sample. This technique is called FIB-SEM tomography [138], and it provides 3D information about the bone ultrastructure at a nanometer resolution. Besides being a tool for 3D SEM imaging, FIB milling is commonly used for microscale specimen manufacturing like micropillars for compression tests or thin bone sections for electron imaging in transmission mode [139].

Thin bone sections ($\sim 200\text{nm}$) can be analyzed via transmission electron microscopy (TEM), giving access to Angstrom-size features like morphology and organization of crystals within the mineralized collagenous matrix of bone [138]. Furthermore, electron tomography (ET) is a promising tool for the 3D bone ultrastructure characterization at the Angstrom level [138, 140]. At its core, it follows the basic tomography principles, where several projections are collected and the resulting 3D reconstruction is calculated from their superposition [141].

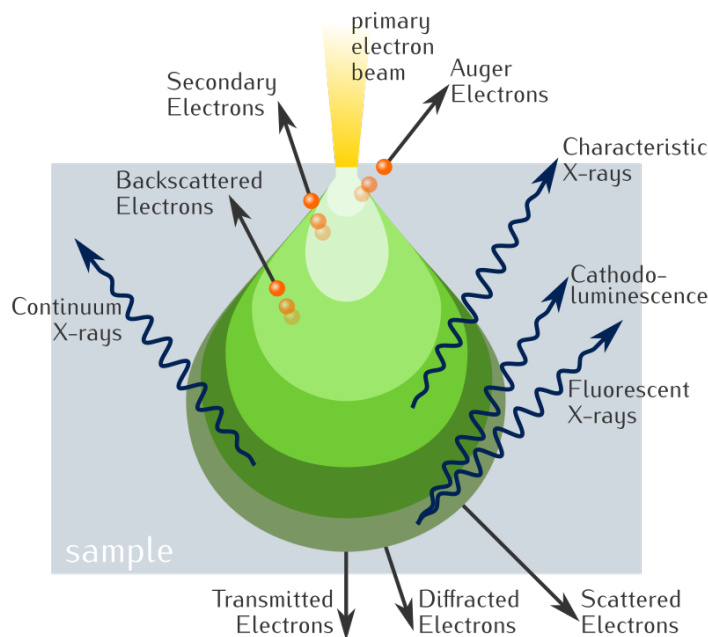


Figure 2.8 – Electron–matter interaction volume with emitted signals. Picture taken from: commons.wikimedia.org

Although both electron and X-ray-based methods can achieve remarkable spatial resolution, they both expose the material to ionizing radiation [142]. In this regard, light-based microscopy techniques are less invasive. One of them is polarized light microscopy (PLM) methods, which are using the different incoming light polarizations to visualize bone structural arrangement [143, 144]. The spatial resolution of this technique is limited by the diffraction limit of visible light, being approximately 250 nm. However, PLM imaging can only be done from the bone surface. This limitation can be partially overcome if the monochromatic light source is used in combination with a pinhole. The resultant confocal laser scanning micro-

scopy (CLSM) technique can achieve up to 150 nm resolution with the possibility to select the analysis plane up to a few hundred micrometers deep [145]. Second harmonic generation microscopy (SHG) utilizes a confocal laser system for bone structural imaging. This method is based on nonlinear optical effects in non-centrosymmetric structures [146] and is therefore optimal for collagen type I imaging in bone tissue. Moreover, the in-plane orientation of the fibrils can be visualized with the help of a polarizer–analyzer couple [147]. This method has a higher spatial resolution than CLSM (about 100 nm), but its penetration depth is lower (about 30nm).

Besides structural characterization, some of the imaging methods are capable to analyze the mechanical properties of bone tissue. One of them is the scanning acoustic microscopy (SAM) method. SAM uses an ultrasound beam to image the polished surface of bone based on the variation in sound velocity induced by the bone matrix [148]. Consequently, this method is also used for indirect assessment of bone elastic properties [149]. Another imaging method, where the probe mechanically interacts with the sample, is atomic force microscopy (AFM). This method provides a topographic map of a sample surface through force interactions between the probe and the surface features at a high spatial resolution (~ 0.1 nm) [150]. Moreover, this imaging technique can be successfully combined with the indentation measurements through the same probe tip [151], revealing elastic properties of a single collagen fibril [152, 153].

Table 2.2 – Summary of laboratory-based methods for the structural, compositional and mechanical characterization of bone tissue at micro- to nanoscale.

	Spatial resolution	Structural characterization	Compositional characterization	Mechanical characterization	Sample preparation requirements	Detailed description
Micro-CT/Nano-CT	1 – 6 μm	3D	BMD		Sample diameter < 15cm	[125–127]
SR-CT/ Phase-contrast CT	10 – 100nm	Volumetric bone properties at meso-down to sub-microscale			Free-standing sample (100 μm -1mm), substrate/ sample holders with certain density	
WAXS/SAXS	100 μm	2D			Free-standing sample (100 μm – 1mm)	[133, 135, 136]
SR-WAXS/SAXS	200nm	2D			substrate/ sample holders with certain density	
sSAXS	200nm	3D				
SEM	1 – 10nm	2D (surface)	Ca, P content		Sample surface preparation, heavy metal implantation or surface sputtering with conductive material	[139]
qBEI, EDX	1 – 10nm	2D (surface)				
FIB-SEM tomography	1 – 10nm	3D				
TEM	1 Å – 1nm	2D (section)				
ET	1 Å – 1nm	3D				
PLM	1 μm	2D (surface)			Sample surface preparation	[143, 145]
CLSM	150nm	2D+(surface / section)				[146, 154, 155]
SHG	30nm	2D				
AFM	1 Å	2D		Elastic modulus	Sample surface preparation	[150]
SAM	10 μm	2D		Sample elasticity		[24, 156]
FTIR	2 μm	2D	Relative organic and mineral content variations		Sample surface preparation	[157]
RS/ PRS	0.5 – 1 μm	2D				[158, 159]
qPRS	0.5 – 1 μm	3D (MCF)				[160, 161]
LC, MS	Molecular level	Bone porosity (indirect)	Organic composition		Destructive sample preparations	[162]
NMR	Atomic level					H, C, P, Ca
Nanoindentation	1 – 10 μm			Stiffness, hardness	Sample surface preparation	[166]
Micropillar compression	1 – 50 μm			Yield, post-yield and elastic properties		[167]

Methods used in the current thesis are written **in bold**.

2.3.2.2 **Compositional characterization**

Current techniques to characterize bone chemical composition include vibrational spectroscopy modalities, nuclear magnetic resonance (NMR) spectroscopy, liquid chromatography (LC) variations, mass spectroscopy (MS) and thermal gravimetric analyses. However, only vibrational spectroscopy methods are spatially resolved and therefore capable of capturing local variation in bone tissue properties [157]. Fourier transform infrared spectroscopy (FTIR) and Raman spectroscopy (RS) are the two types of vibrational spectroscopy that are commonly used to characterize the composition of bone tissue through changes in molecular vibrational energies upon excitation. The two methods are complementary, and although FTIR has a higher signal-to-noise ratio, RS provides a finer spatial resolution and is suitable for measurements on bulk bone samples in hydrated conditions. These advantages of the RS, are supporting its growing application in bone research.

Raman spectroscopy is based on collecting inelastic scattering photons from the specimen upon its excitation (figure 2.9). When a sample is irradiated with a monochromatic light source (typically a laser), two types of scattering may occur: elastic (Rayleigh) scattering, where the emitted photon energy is equal to the incident one, and inelastic (Raman) scattering, where the emitted photon has a different energy. This change in the emitted photon energies is due to the induced molecular vibrations [168]. These energy or frequency shifts (Raman shifts) give information about the vibrational modes in the system and are further assigned to certain chemical bonds [158, 159]. The typical Raman spectrum of bone with characteristic bands of mineral and organic components is shown in figure 2.9.

Besides providing the compositional information, RS may be used for the local orientation analysis of bone MCF. For this, the polarized excitation should be used with an optional analyzer. This RS modality is called Polarized Raman Spectroscopy (PRS) and is based on the anisotropic spectral response of mineralized collagen fibrils [160, 171–174] upon linearly-polarized excitation of varying orientation. Furthermore, by performing a careful calibration of this technique, a quantitative analysis of the MCF in- and out-of-plane orientation is possible (quantitative PRS, qPRS, [161]). More detail about this approach is given in Section 3.1.

2.3.2.3 **Mechanical characterization**

The field of micromechanical testing of bone is rapidly progressing: starting from the pioneering works on bone nanoindentation [175, 176] and going towards the state-of-the-art microscale tensile [177, 178], compression [167, 179–181] and bending [182] experiments on the lamellar or even the mineralized collagen fibril level [183, 184].

Nanoindentation is the most common experimental technique used to characterize the

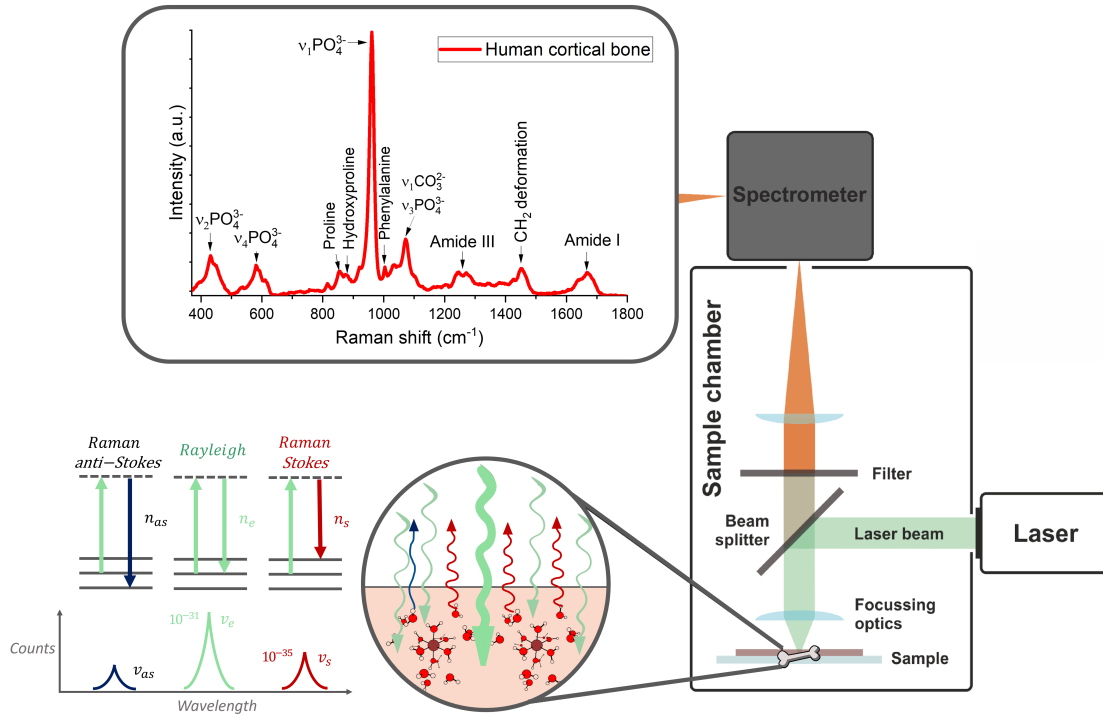


Figure 2.9 – Raman imaging principles.

mechanical properties of bone at the sub-micron length scale [176]. During indentation measurements, a hard and sharp tip (typically made of diamond) with a well-defined shape is driven into a flat surface of the sample while tip displacement and reaction forces are being measured. The typical load-displacement curve for the indentation experiment is shown in figure 2.10. Three main stages of the experiment can be distinguished: (i) elasto-plastic loading, (ii) creep at a constant force and (iii) elastic unloading. The hardness and elastic modulus of the material can be extracted following the method established by Oliver and Pharr [185, 186].

Nanoindentation allows the determination of local variations in elastic properties and hardness at the lamellar scale [187]. But it is less suitable for the assessment of yield properties and the analysis of dissipative mechanisms due to the complex stress state that develops below the tip [188]. A better understanding of bone post-yield behavior at the micrometer length scale can be achieved through uniaxial loading techniques such as micropillar compression.

Micropillar compression is a novel experimental method, introduced by Uchic et al. in the early 2000s [189]. The first micropillar compression of animal bone was done in the mid-2010s [167, 179]. More recently, this method was also applied to human bone biop-

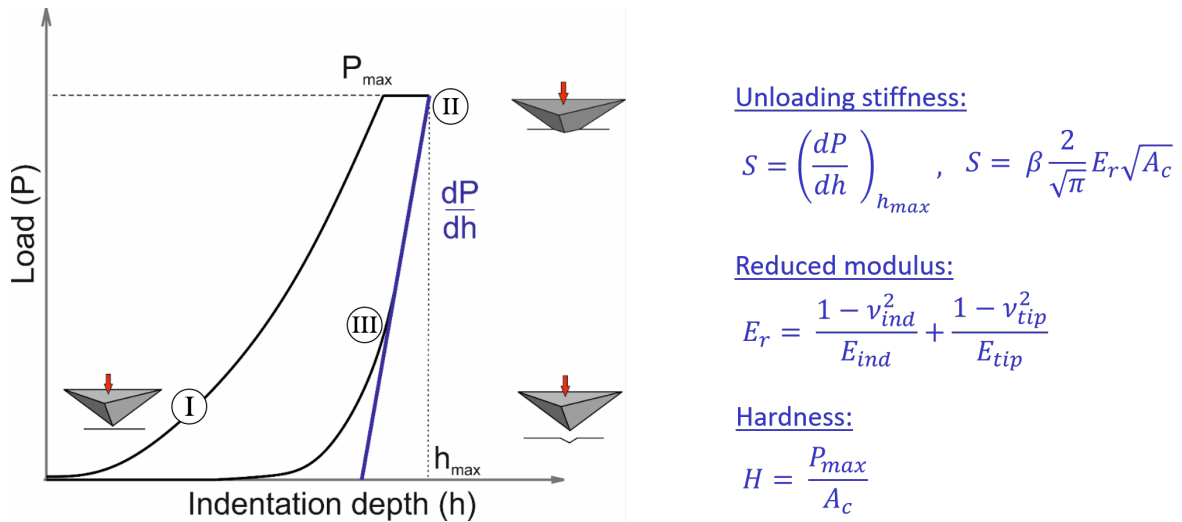
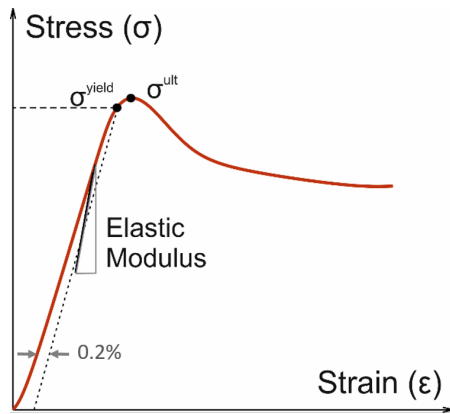


Figure 2.10 – (Left) typical load-displacement curve of an indentation experiment with marked stages: I- elasto-plastic loading, II - creep at a constant force, III - elastic unloading. (Right) equations for the unloading stiffness (S), reduced modulus (E_r) and hardness (H); where A_c is the contact area, β is a tip shape factor, E_{tip} and ν_{tip} are elastic modulus and Poisson's ratio of the tip, E_{ind} and ν_{ind} are the elastic modulus and Poisson's ratio of the tested material.

sies [84, 181]. The methodology is somewhat similar to the indentation approach, yet the specimens of a defined geometry are compressed instead of a flat sample surface. Commonly in this method, cylindrical or rectangular pillars with dimensions in the micrometer range are tested using an indenter setup equipped with a flat punch tip. This ensures a relatively uniaxial and uniform stress-strain field in the tested volume. A typical stress-strain curve from the micropillar compression experiment is shown in figure 2.11. By introducing a partial unloading segment in the elastic loading region, elastic modulus can be calculated in addition to the yield and ultimate stress values (figure 2.11). The yield point is usually defined as the stress needed for plastic deformation of a certain percentage, e.g. 0.2% (figure 2.11). During data analysis, care should be taken to account for the indenter frame compliance and the pillar sink-in effects due to the substrate deformation [190, 191]).

Although the data analysis is more straightforward for the micropillar compression tests, specimen fabrication is more challenging and requires time-consuming preparation. The bone micropillar fabrication is routinely done via FIB milling [167]. This high-precision method allows fabrication of the micropillar at the lamellar length scale, but it is time consuming and thus constrains the micropillar compression experiments to a small number of samples. Recent developments in the ultrashort pulsed laser ablation for bone micropillar fabrication allowed to drastically decrease the time costs for pillar micromachining [192, 193], which is then allowing high-throughput compression experiments, while approaching the measurement rate of the nanoindentation method. More details about the laser ablation protocol and output bone micropillar arrays can be found in Section 3.2. The visual



Stress and strain:

$$\sigma = \frac{F}{A}, \quad \epsilon = \frac{\Delta l}{l_0}$$

Deformation length:

$$\Delta l = \frac{-2l_0 a_c}{A(\nu^2 - 1) - 2l_0 a_c} l_{meas}$$

Effective contact radius:

$$a_c = \eta (r + r_c)$$

Figure 2.11 – (Left) typical stress-strain curve of a micropillar compression experiment with marked yield (σ^{yield}) and ultimate stress (σ^{ult}) points, with a partial unloading segment in the elastic region. (Right) equations for the stress (σ), strain (ϵ), deformation length (Δl) and effective contact radius (a_c); where A , l_0 and r are the cross-section, initial height and radius of the pillar, F is the loading force, ν is the Poisson's ratio of the sample material, r_c is the radius of curvature at the base of the pillar and η is a constant term ($\eta = 1$ using Sneddon's method [190] and $\eta = 1.42$ using Zhang's method [191]).

comparison between the FIB-milled micropillar and the one ablated with the femtosecond (fs) laser is shown in figure 2.12.

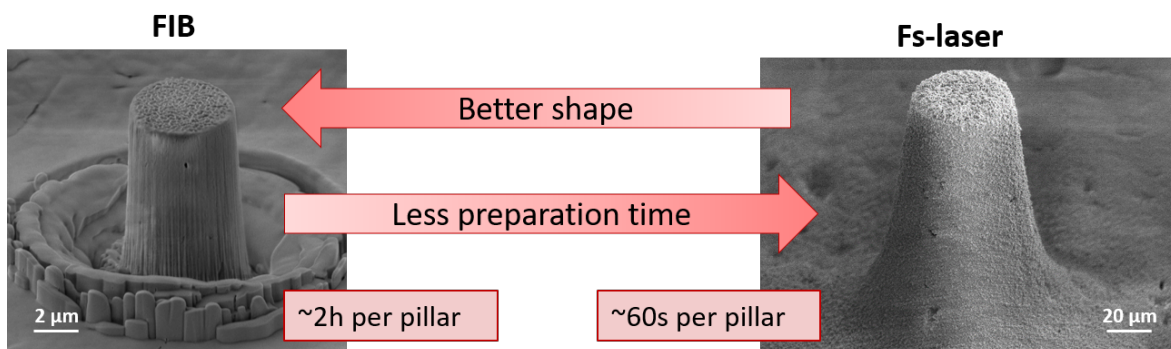


Figure 2.12 – Visual comparison between the FIB-milled and femtosecond (fs) laser ablated micropillar. Note the difference in the length scale.

Chapter 3

Development of methods to assess bone quality in animal models

In this chapter, novel methods for bone characterization were developed and validated on the animal bone models. This chapter consist of 2 subsections based on 2 manuscripts which are summarized below:

3.1 Tatiana Kochetkova, Cinzia Peruzzi, Oliver Braun, Jan Overbeck, Anjani K. Maurya, Antonia Neels, Michel Calame, Johann Michler, Philippe Zysset, Jakob Schwiedrzik; *"Combining polarized Raman spectroscopy and micropillar compression to study microscale structure-property relationships in mineralized tissues"* Acta Biomaterialia, 119, 390-404, 2021.

3.2 Tatiana Kochetkova, Alexander Groetsch, Michael Indermaur, Cinzia Peruzzi, Stefan Remund, Beat Neuenschwander, Benjamin Bellon, Johann Michler, Philippe Zysset, Jakob Schwiedrzik, (Journal of the Mechanical Behavior of Biomedical Materials 134, 2022); *"Assessing minipig compact jawbone quality at the microscale"* JMBBM 134, 2022.

3.1 Combining polarized Raman spectroscopy and micropillar compression to study microscale structure-property relationships in mineralized tissues[†] [§]

Tatiana Kochetkova^{1,*}, Cinzia Peruzzi^{1,*}, Oliver Braun^{2,4}, Jan Overbeck^{2,4,5}, Anjani K. Maurya^{3,6}, Antonia Neels³, Michel Calame^{2,4,5}, Johann Michler¹, Philippe Zysset⁷, Antonia Neels^{2,5}, Jakob Schwiedrzik^{*1}

¹*Empa, Swiss Federal Laboratories for Materials Science and Technology, Laboratory for Mechanics of Materials and Nanostructures, Thun, Switzerland*

²*Empa, Swiss Federal Laboratories for Materials Science and Technology, Transport at Nanoscale Interfaces Laboratory, Dübendorf, Switzerland*

³*Empa, Swiss Federal Laboratories for Materials Science and Technology, Center for X-Ray Analytics, Dübendorf, Switzerland*

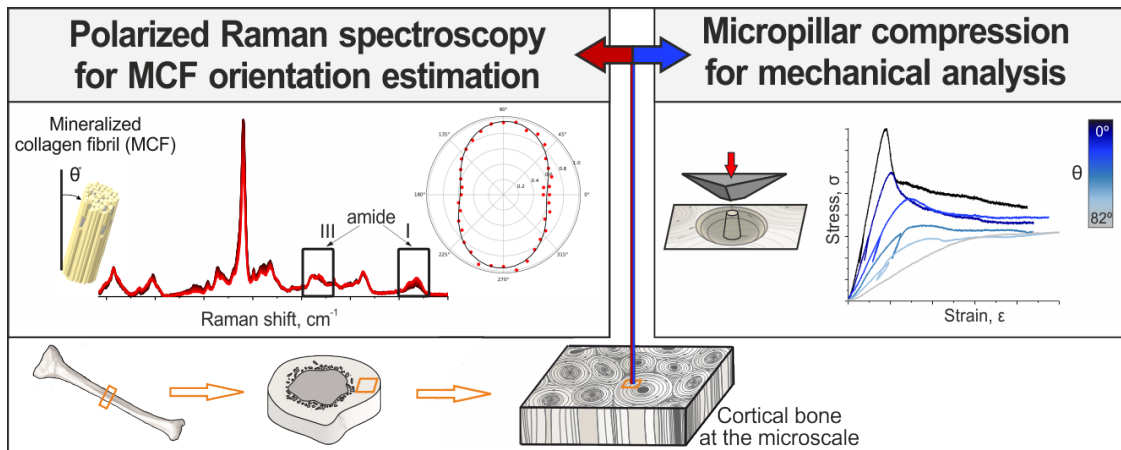
⁴*Department of Physics, University of Basel, Switzerland*

⁵*Swiss Nanoscience Institute, University of Basel, Switzerland*

⁶*Cellular and Biomedical Sciences, Faculty of Medicine, University of Bern, Switzerland*

⁷*ARTORG Center for Biomedical Engineering Research, University of Bern, Switzerland*

**These authors contributed equally to this work*



*Corresponding Authors: tatiana.kochetkova@empa.ch; jakob.schwiedrzik@empa.ch

[§]T. Kochetkova, C. Peruzzi, O. Braun, J. Overbeck, A. K. Maurya, A. Neels, M. Calame, J. Michler, P. Zysset, J. Schwiedrzik "Combining polarized Raman spectroscopy and micropillar compression to study microscale structure-property relationships in mineralized tissues" *Acta Biomaterialia*, 119, 390-404, 2021

Contribution: I performed the animal sample preparations, developed and calibrated quantitative polarized Raman spectroscopy method including measurements on two animal models of mineralized tissue, carried out the theoretical calculations of Raman polarized spectra responses, performed micropillar compression together with modeling of elastic and yield responses of the mineralized collagen fibril vs. the out-of-plane orientation angle, final data visualization and correlation, and wrote the manuscript with the feedback of all the co-authors.

Abstract

Bone is a natural composite possessing outstanding mechanical properties combined with a lightweight design. The key feature contributing to this unusual combination of properties is the bone hierarchical organization ranging from the nano- to the macro-scale. Bone anisotropic mechanical properties from two orthogonal planes (along and perpendicular to the main bone axis) have already been widely studied. In this work, we demonstrate the dependence of the microscale compressive mechanical properties on the angle between loading direction and the mineralized collagen fibril orientation in the range between 0° and 82° . For this, we calibrated polarized Raman spectroscopy for quantitative collagen fibril orientation determination and validated the method using widely used techniques (small angle X-ray scattering, micro-computed tomography). We then performed compression tests on bovine cortical bone micropillars with known mineralized collagen fibril angles. A strong dependence of the compressive micromechanical properties of bone on the fibril orientation was found with a high degree of anisotropy for both the elastic modulus ($E_a/E_t = 3.80$) and the yield stress ($\sigma_a^y/\sigma_t^y = 2.54$). Moreover, the post-yield behavior was found to depend on the MCF orientation with a transition between softening to hardening behavior at approximately 50° . The combination of methods described in this work allows to reliably determine structure-property relationships of bone at the microscale, which may be used as a measure of bone quality.

Keywords: Bone, collagen fibril orientation, quantitative polarized Raman spectroscopy, micropillar compression, failure mechanisms

3.1.1 Introduction

Bone possesses outstanding mechanical properties as a result of its well-organized hierarchical structure and composition. However, metabolic bone diseases, like osteoporosis, drastically affect the bone structure and mechanical properties, leading to an increase in bone fragility. As the life expectancy of the population increases, so will the incidence of osteoporosis and fragility fractures [4, 194]. Beyond quantity, bone fracture is predetermined by the bone quality, i.e. the combination of various parameters contributing to fracture resistance. At the moment, research groups all over the world are investigating various bone quality parameters that may lead to better bone fracture prediction [195, 196]. Recently, attempts were made to correlate both bone composition and mechanical properties at different length scales with patient age, gender and bone metabolism state [197]. As there are numerous interdependent factors contributing to the bone quality, a promising approach for quantifying bone quality lies in the identification of tissue-scale structure-property relationships.

Hierarchical structure of bone. Bone is a composite biomaterial, made of mineral crystals (hydroxyapatite, 50-60 wt.%), proteins (mainly collagen type I, 30-40 wt.%) and water (bound and unbound, 10-20 wt.%) [16, 25, 198]. Each of these components contribute to the overall bone mechanical properties. Aligned mineralized collagen fibrils (MCF, ~ 30 - 300 nm in diameter) with intra- and extra-fibrillar hydroxyapatite crystals form sub-lamellar sheets (~ 1 μm thickness), a stack of which is called a lamella (~ 3 - 7 μm thickness). Further up the scale, lamellae form trabecular packets in cancellous bone, whereas in cortical bone concentric cylindrical layers of lamellae arranged around a central blood vessel form osteons (~ 200 μm in diameter). Lamellae may be considered as the main building blocks of bone and their mechanical properties are critical in defining overall bone mechanics [182].

Quantitative analysis of bone fibril orientation. Thanks to the recent progress in biomedical imaging, various modalities have been used for visualizing the spatial arrangement of MCF [124]. Some of the most frequently used techniques are polarized light microscopy [199], second harmonic generation microscopy [200, 201], transmission electron microscopy [202] and small angle X-ray scattering (SAXS) [183, 201]. However, those methods require complex sample preparation and do not provide additional information on the local chemical composition. Polarized Raman spectroscopy (PRS) is a powerful non-destructive imaging technique that has been long applied in compositional analysis in bone research. Raman spectroscopy allows to detect the frequency shifts of inelastically scattered light coming from the specimen exposed to a monochromatic light source, usually a laser. The resulting Raman bands are assigned to vibrations of characteristic chemical bonds,

where for bone the bands of interest can be found in the range from $400 - 1800\text{cm}^{-1}$. Until now, polarized Raman spectroscopy has provided mostly qualitative information about spatial orientation of collagen fibrils in cortical bone [160, 172, 203, 204]. In this work, we demonstrate that quantitative information can also be obtained in 3D, which we independently verify by SAXS, and then correlate with mechanical properties.

Mechanical properties of bone are strongly affected by the bone composition and structural anisotropy [205]. As an example, changes in the collagen network may lead to significant variations in the bone bending strength, elastic modulus, and work to fracture [206–208]. Recent studies show how bone elastic and post-yield mechanical properties are furthermore affected by variations in water content [43, 61]. Bone mineral density (BMD) has been long employed in clinics for the indirect assessment of the mechanical behavior of bone and individual patient fracture risk estimations [72, 209], however, it does not take into account the spatial distribution of bone material, structural anisotropy, or tissue properties. The hierarchical structure of bone leads to anisotropy of its mechanical properties. Bone fracture is a multiscale process and needs to be studied at all relevant scales. The dependence of macroscale mechanical properties of cortical bone on the loading direction has been investigated for half a century and is mainly related to the osteonal orientation [210]. Later, the anisotropic mechanical properties of single osteons were identified [211, 212], demonstrating the importance of lamellar organization in governing the osteonal mechanical response. Over the past four decades, the directional dependence of mechanical properties has been studied more extensively at the length scale of a bone lamella [167, 179, 213, 214], which is significantly affected by the underlying MCF orientation. Although lamellae may be considered as the main building block of bone, to the best of our knowledge, no reports have been published describing the influence of mineralized collagen fibril orientation in a continuous range between $0^\circ - 90^\circ$ on their elastic, yield, and post-yield mechanical properties. Filling this knowledge gap would allow determining the structure-property relationships of bone at the lamellar length scale, which is a prerequisite for the development and validation of reliable multiscale models predicting bone failure.

Micromechanical testing on bone is an attractive technique to study bone mechanical properties, as it allows to limit the influence of local structural and compositional inhomogeneities on the overall mechanical response. The field of micromechanical testing of bone is rapidly progressing: starting from the pioneering works on bone nanoindentation [175, 176] and going towards the state-of-the-art microscale tensile [178, 213], compression [167, 179–182] and bending [182] experiments on the lamellar or even the mineralized collagen fibril level [183, 184]. One of the most common micromechanical testing techniques

for bone is indentation [166], however its interpretation in terms of post-yield behavior is complex [188]. Micropillar compression is a novel experimental method [189], where cylindrical samples with dimensions in the micrometer range are prepared by focused ion beam and subsequently compressed using a flat punch indenter. Unlike in classical indentation, the loading in the specimen is mostly uniaxial, which simplifies the interpretation of the output load-displacement curves in terms of stress-strain behavior. In this study, we performed micropillar compression experiments of cortical bone lamella under humid conditions, with a known collagen fibril orientation.

The aims of this study were to (i) establish a quantitative method for MCF spatial orientation estimation based on PRS and (ii) investigate the effect of MCF orientation on the yield stress and elastic modulus of cortical bone lamellae. For the first part, polarized Raman measurements were carried out on mineralized turkey leg tendon, a model material with known fibril spatial orientation [215], and then validated on bovine cortical bone osteonal lamellae. For the mechanical study, micropillar compression experiments were performed on isolated bovine cortical bone lamellae with MCF orientations ranging from 0° to 82° with respect to the loading direction.

3.1.2 Materials and methods

3.1.2.1 Samples

As a model material for polarized Raman calibration, **mineralized turkey leg tendon (MTLT)** was used. The main advantage of MTLT tissue is its simplified fiber arrangement compared to mammalian cortical bone structure. MTLT is composed of densely packed collagen fibrils, strongly aligned with the tendon axis [215–217], which means that global and local fibril orientation are highly correlated.

MTLT samples were prepared from a turkey leg, obtained from a local abattoir. Highly mineralized parts were dissected from the tendon bundles, mechanically cleaned and further cut with a diamond band saw under constant water irrigation (Exakt, Norderstedt, Reichert-Jung, Germany). The resulting tendon pieces of about 1.5mm in diameter and 4.0mm in length were dried under ambient conditions for 24h . For the PRS calibration, MTLT pieces were fixed on specially designed aluminum SEM stubs with a 2-component epoxy resin adhesive (Schnellfest, UHU, Germany) and cut at a specific angle to the main tendon axis using a high-precision diamond band saw (Leica EM TXP, Germany). Finally, the exposed specimen surfaces were polished with progressive grades of silicon carbide paper and finished manually on a soft cloth with a $1\ \mu\text{m}$ diamond suspension followed by $0.04\ \mu\text{mSiO}_2$ suspension resulting in a polished sample surface virtually parallel to the stub surface. A total of

five specimens were prepared, each containing a tendon section cut at 0° , 22.5° , 45° , 67.5° or 90° to the main tendon axis (figure A1.1, Appendix A1). The samples cut at 0° and 90° are referred to as axial and transverse samples, respectively. For precise MCF angle determination, small angle X-ray scattering measurements were performed on each sample (figure A1.9, Appendix A1).

Combined PRS and micropillar compression measurements were performed on **bovine cortical bone**, which represents an intermediate model material between the MTLT and human cortical bone. Bovine cortical bone, in comparison to human, exhibits higher mineralization, yielding a higher strength [218], however, zones with a similar microstructural organization with distinguishable osteonal and interstitial zones can be found in both tissues [219]. It should be noted that the lamellar arrangement in bovine cortical bone primary osteons has a more uniaxial orientation (as demonstrated in Appendix A1.2) in comparison to more complex MCF orientation patterns observed in human osteonal lamellae [30]. This makes bovine cortical bone an attractive animal model for basic research, prior to translation to human bones.

A bovine tibia was obtained from a local abattoir. Three medial slices of cortical bone from the diaphysis were cut radially into smaller sections. Posterior quadrant sections with higher osteonal bone content were used for further processing steps (figure A1.1, Appendix A1). The bone samples ($\sim 5\text{mm}$ cubes) were glued to specially designed SEM stubs and cut at five angles between 0° and 90° with respect to the longitudinal bone axis, following the same protocol as the MTLT specimens. In order to obtain plane surface for compression experiments, samples were additionally ultra-milled (Polycut E, Reichert-Jung, Germany) and consequently polished with 1000 grid silicon carbide and paper cloth with $0.3\ \mu\text{m}\ \text{Al}_2\text{O}_3$ lubricant. For micropillar fabrication after PRS measurements, the bovine cortical bone samples were additionally sputtered with 11 nm thick Au film (Leica EM ACE600, Germany) and a thin film of silver paste (Plano GmbH, Germany) was applied at the sample sides down to the aluminium holder to minimize the drift caused by electrostatic charging under the electron or ion beams. Considering the dimensions of the mechanically tested bone volumes ($5\ \mu\text{m}$ in diameter), the effect of the thin Au film (11 nm thickness) on the measured mechanical properties can be neglected. In total, 26 primary osteons with different orientations from 0° to 90° were chosen from five bovine cortical bone samples for the PRS measurements, 13 of which were then used for micropillar compression measurements.

3.1.2.2 Raman spectroscopy and data processing

In the present work, we used polarized Raman spectroscopy for quantitative orientation estimation of MCF in mineralized tissues. For this, the polarized Raman spectral response of MCF was theoretically and experimentally correlated with the fibril orientations.

Raman spectra were acquired using a WITec Alpha 300 R confocal Raman microscope in backscattering geometry. A diode-pumped linearly polarized continuous 785 nm laser was used in combination with a 50 \times objective (0.80 numerical aperture). The linear polarization of the exciting laser was adjusted with a motorized $\lambda/2$ plate. No analyzer plate was included in the light path after the sample. The Rayleigh scattered light was blocked by an edge filter. The backscattered light was coupled to a 400mm lens-based spectrometer with a grating of 300g/mm⁻¹ equipped with a cooled deep-depletion CCD. The laser power was set to 30mW, the estimated full width at half maximum (FWHM) of the focal spot was $\sim 0.4 \mu\text{m}$ in lateral and $\sim 1.7 \mu\text{m}$ in axial direction, as calculated from the confocal Rayleigh criteria [220]. At each region of interest (ROI), Raman spectra were collected at different excitation polarizations from 0 $^\circ$ to 180 $^\circ$ with a 10 $^\circ$ polarization angle step and 30s integration time. As a result, a set of 19 polarized Raman spectra was collected for a single ROI. For each MTLT sample, PRS measurements were carried on 5 to 8 ROI, whereas for bovine cortical bone sample a single ROI was measured per osteon. In total, 33 ROI were measured for the MTLT samples, corresponding to five different out-of-plane orientations, and 26 ROI for bovine samples, corresponding to 26 osteons with different out-of-plane orientation. Spectral analysis was done in a batch mode using Python v3.6 [221] and consisted of background removal, location of the peaks of interest (amide I, amide III, $\nu_1\text{PO}_4$, $\nu_2\text{PO}_4$, CH-bending) with consequent double or triple Lorentzian peak fit using a least square scheme (scipy.optimize.leastsq). The detailed PRS analysis procedure is described in Appendix A1.2, output spectra for different laser polarization angles are presented in figure 3.1.1.

The intensity of the Raman scattering depends on the molecular bond orientation relative to the laser polarization vector, as well as the excited vibration mode. As shown previously [160, 172, 203, 204], by collecting Raman spectra at different orientations of the incident polarized laser light, the anisotropic spectral response of the amide I band (mainly C=O stretching) can be used to derive information about the orientation of the collagen molecules [158, 171, 203, 222]. At the same time, the amide III band is considered as polarization-insensitive, as this vibration mode mainly involves N-H bending and C-N stretching that are equally distributed across the collagen amino acid sequence, this results in homogeneous Raman scattering [158, 174, 223, 224]. In this study, the MCF spatial orientation was estimated from the integrated area ratio of the amide I over the amide III band

collected at different laser polarizations.

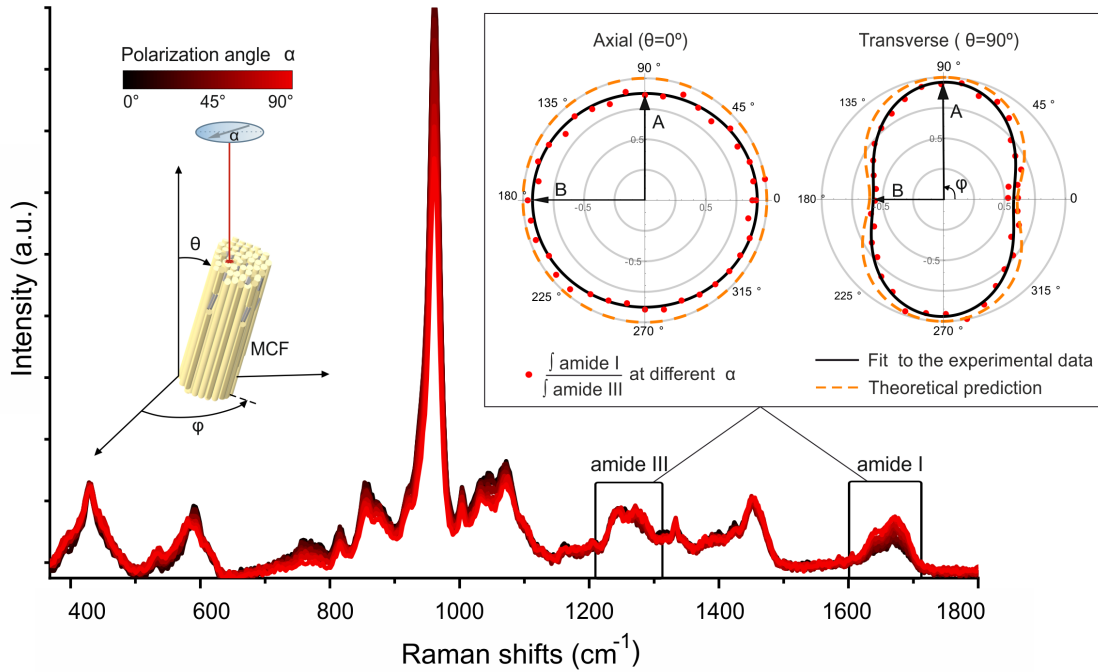


Figure 3.1.1 – MCF spatial orientation during Raman spectra acquisition with marked out-of-plane (θ) and in-plane (φ) angles. Set of Raman spectra collected at different incident laser polarization on MTLT. Highlighted characteristic collagen bands: amide III ($1215 - 1300\text{cm}^{-1}$, N-H bending and C-N stretching of the peptide backbone) and amide I ($1600 - 1700\text{cm}^{-1}$, C=O stretching). Polar plots: polarization dependence of $f_{\text{amide I}} / f_{\text{amide III}}$ with theoretical prediction and simplified fit to the experimental data (1) for two assumed orthogonal MCF orientations.

The theoretical calculations of amide I over amide III ratios at different laser polarization are in good agreement with the experimental data for 0° and 90° out of plane fibril angle as shown in figure 3.1.1 and Appendix A1.2. For the quantitative measurement of polarization anisotropy of a given set of polarized experiments in a single ROI, we used the simplified description proposed by [225]:

$$f(\alpha, \varphi) = A \cos^2(\alpha + \varphi) + B \sin^2(\alpha + \varphi). \quad (3.1.1)$$

Where α is the polarization angle of the laser, $\frac{A}{B}$ the introduced parameter of anisotropy ($\frac{A}{B} \rightarrow 1$ for isotropic sample), and φ the in-plane rotation angle for fibrils with respect to the laser polarization. The parameter of anisotropy $\frac{A}{B}$ depends on the out-of-plane fibril orientation, the exact relationship was determined by calibration on the MTLT samples. The Raman spectra with highlighted amide peaks and output polar plots with theoretical predictions and fit to the experimental data (1) for axial (parallel to the incident laser beam) and transverse (orthogonal to the incident laser beam) collagen fibrils orientation are shown in figure 3.1.1.

To assess the variation in bone mineralization, the ratio of the secondary phosphate (ν_2PO_4 , $370 - 500cm^{-1}$) over the amide III integrated intensity was analyzed. Following the study of Roschger et al. [226], the mineral to matrix ratios (ν_2PO_4 /amide III), can be correlated to the Ca content. For each ROI, the mineral to matrix ratio was averaged over 19 spectra. The mineral crystallinity [158,159,227,228] was assessed from $1/FWHM$ of the primary phosphate (ν_1PO_4 , $920 - 1000cm^{-1}$) and averaged over all laser polarizations for each ROI. To assess the variation of the non-collagenous proteins (NCP) content, the C-H bending at $1360 - 1500cm^{-1}$ was analyzed, to which both collagen and NCPs contribute [229]. Since amide III is polarization-independent and almost exclusively representative of the collagen phase, following the reasoning of Katsamenis et al. [230], the Raman integrated intensity ratio of amide III / CH-bending was used to quantify the relative concentrations of collagen versus NCPs.

3.1.2.3 Independent verification of MCF orientation

Small Angle X-ray Scattering (SAXS) experiments were performed on MTLT samples to validate fibril alignment after sample fabrication. SAXS experiments were performed with a Bruker Nanostar instrument (Bruker AXS GmbH, Karlsruhe, Germany). The instrument was equipped with a pinhole collimation system, a micro-focused X-ray Cu source (wavelength Cu $K\alpha = 1.5406\text{\AA}$) and a 2D MikroGap technology-based detector (VNTEC-2000 with 2048×2048 pixels and $68 \times 68 \mu m$ each pixel size) along with a custom built semi-transparent beam stop. The beam size at sample position was about $400\mu m$ in diameter. The instrument provided a resolvable scattering vector modulus q in a range between $0.06 - 2.1nm^{-1}$ for a $107cm$ sample to detector distance (SDD). The scattering frames were recorded for 1800s at room temperature in moderate vacuum condition of about $10^{-2}mbar$ to reduce air scattering. Prior to the experiments, the SDD was calibrated with standard silver behenate powder samples.

The misorientation width and true orientation of MCF with respect to the sample and holder surface in the MTLT samples was estimated from the streak-like diffuse scattering in 2D SAXS profiles. This streak is produced by extended scattering objects (i.e. collagen fibrils) along the fiber axis of the fibrous materials [231, 232]. The true orientation of collagen fibrils was determined by averaging the center values obtained from fitting the extracted azimuthal scans (q -range of $0.356 - 0.783nm^{-1}$ with step size of $0.036nm^{-1}$) with a Lorentzian function (see Appendix A1.4). The collagen fibrils misorientation width was calculated using the Ruland streak method [233, 234]. In this method, the azimuthal broadening of intensities along the streak axis is evaluated and linked to the fibril misorientation (Appendix A1.4).

Micro-computed tomography (micro-CT) scans of the bovine bone specimens (μ CT 100, SCANCO Medical AG, Switzerland) were collected on each of the bovine bone samples to access osteon orientation after sample preparation. Samples were scanned at a spatial resolution of $4.9 \mu\text{m}$ with 45kVp energy, $200 \mu\text{A}$ tube current and $2 \times 400\text{ms}$ integration time. The spatial orientation of the osteons was estimated using ImageJ 1.52v [235] and BoneJ 1.4.3 [236] as a screening step to choose osteons for later qPRS analysis. Firstly, the global sample tilt of each sample scan was corrected using the Untilt Stack plugin. Secondly, the osteons of interest were located and isolated by combining optical microscopy with micro-CT images. Output stacks were binarized using Otsu's threshold clustering algorithm. Prior to calculations, Haversian canals were checked for irregularities: only the top segments without branching or sudden changes in orientation were used. Using the Moment of Inertia plugin, three orthogonal principal axes were automatically determined for each Haversian canal and the rotation matrix in reference to the stacks main axis was constructed. The out-of-plane orientation of each osteon was taken as the angle between the principal axis along the Haversian canal and the z axis of stacks. The angle was extracted from the rotation matrix and correlated later with the polarized Raman measurements. For more details see Appendix A1.5.

3.1.2.4 Mechanical testing and analysis

Bone micropillars were fabricated using a focused ion beam workstation (Tescan Lyra, Czech Republic) with a well-established three step protocol described elsewhere [167, 179]. Within each bovine bone sample, 5 osteons were selected for compression tests. Depending on the osteonal morphology, 2 to 3 pillars were fabricated. Each pillar had a diameter of approximately $5 \mu\text{m}$ and an aspect ratio of 2, as determined from HRSEM imaging (Hitachi S-4800, Japan). Examples of fabricated micropillars are shown in figure 3.1.2 C.

A self-developed ex situ indenter setup was used in this study. The system is based on commercial hardware for actuation, sensing, and electronics (Alemnis AG, Switzerland). The experiments were conducted in displacement control to keep the strain rate constant even after the yield point. The system included an optical microscope to visualize the sample surface and to locate micropillars for compression tests and a custom environmental chamber. The relative humidity was controlled using a continuous gas stream from a humidity generator (WETSYS, Setaram, France) and feedback from a relative humidity sensor inside the chamber. The overview of the indenter setup and the schematic of the experiment are shown in figure 3.1.2 A.

Compression experiments were performed at ambient temperature and pressure, the rela-

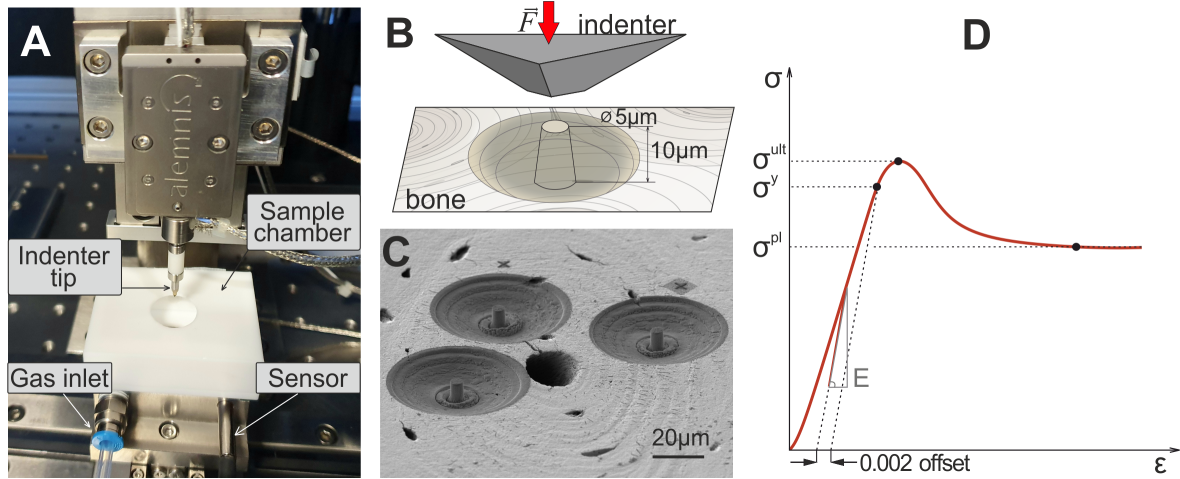


Figure 3.1.2 – Schematic of micropillar compression test. (A) Indenter setup with controlled humidity sample chamber. (B) Sketch of the micropillar compression configuration. (C) HRSEM image of fabricated micropillars. (D) Stress-strain curve with marked output parameters: elastic modulus E , calculated as the slope of the stress-strain curve during the partial unloading segment; yield stress σ^y , defined as stress at 0.2% inelastic deformation; ultimate stress σ^{ult} - maximum stress value; plateau stress σ^{pl} - stress value at 0.08 strain.

tive humidity was set to 93% for at least 4h prior to the compression experiments, ensuring hydration equilibrium of the sample. Pillars were compressed with a flat punch indenter tip with a diameter of 20 μm . The micropillar compression was performed in displacement control up to a maximum depth of 1 μm (10nm/s loading rate) corresponding to a strain rate of 10^{-3}s^{-1} with an intermittent unloading segment in the elastic region, which was used for the calculation of the elastic moduli (figure 3.1.2 D).

As micropillar compression features uniaxial loading, the stress-strain data was assessed from the load-displacement curves after frame compliance and pillar sink-in corrections [237]. The elastic modulus values were extracted from the loading/unloading cycle in the elastic region and the yield stress was computed as the stress that is needed for a plastic deformation of 0.2%. These properties were determined for every pillar using a custom Matlab code (R2018a, MathWorks Inc., Natick, MA, USA). After compression, the micropillars were imaged with a HRSEM.

3.1.2.5 Mechanical modeling

Apparent elastic modulus E_{app} was modeled as a function of collagen fibril orientation (Appendix A1.6):

$$E_{app} = \left(\frac{\cos^4(\theta)}{E_a} + \frac{\sin^4(\theta)}{E_t} + \left(\frac{1}{\mu_a} - 2\frac{\nu_a}{E_a} \right) \cos^2(\theta) \sin^2(\theta) \right)^{-1}. \quad (3.1.2)$$

Elastic moduli were extracted from micropillar compression tests and fibril orientation from PRS measurements, where E_a and E_t are the axial and transverse elastic modulus val-

ues accordingly, ν_a and ν_t the Poisson ratios and μ_a the shear modulus.

Yield stress was modeled as a function of collagen fibril orientation using the Tsai-Hill composite failure criterion (Appendix A1.6) [238]. For unidirectional fiber-reinforced composite materials subjected to in-plane stress, the failure criterion is given by:

$$\sigma_x = \left(\left(\frac{\cos^2(\theta)}{X} \right)^2 - \left(\frac{\sin(\theta)\cos(\theta)}{X} \right)^2 + \left(\frac{\sin^2(\theta)}{Y} \right)^2 + \left(\frac{\sin(\theta)\cos(\theta)}{S} \right)^2 \right)^{-\frac{1}{2}} \quad (3.1.3)$$

where σ_x is the stress applied along the loading axis; X , Y and S symbolize the longitudinal, transversal and shear strength of the composite. Here, bovine cortical bone yield strength was expressed as a function of MCF angle by fitting equation 3.1.3 with individual strengths obtained from micropillar compression tests and fibril orientation assessed from PRS.

3.1.2.6 Statistical data analysis

All data manipulations were performed using Python v3.6 [221] and MATLAB R2019b (MATLAB, 2018). Measurements are reported as mean \pm standard deviation. All non-linear curve fittings reported in this study were done using least squares regression (scipy.optimize, Python v3.6). The goodness of the non-linear fit was estimated from the coefficient of determination R^2 (sklearn.metrics) at $p < 0.05$, $R^2 = 1$ being the best possible score. Multiple linear regression analysis was performed using Python (sklearn.linear_model, statsmodels), the criterion for significance was $p < 0.05$.

3.1.3 Results

3.1.3.1 qPRS calibration on MTLT and validation study on bovine cortical bone lamella

Polarized Raman spectra were collected from the MTLT samples with known out-of-plane MCF angles θ measured by SAXS. For each MCF orientation 19 PRS measurements were taken on 5 to 8 ROI. The anisotropy parameter $\frac{A}{B}$, describing the maximum variation of the amide I/ amide III integral area as a function of incident laser polarization, was calculated for each of the samples by fitting equation 3.1.1. The anisotropy parameter $\frac{A}{B}$ was then correlated with the fibril out-of-plane angle θ , taken from the SAXS measurements (figure 3.1.3 A).

SAXS measurements were used for structural analysis of MCF in tendon samples cut at five angles between 0° and 90° . To correlate the average MCF orientation in the sample measured by SAXS with the local MCF orientation measured by PRS, the SAXS measure-

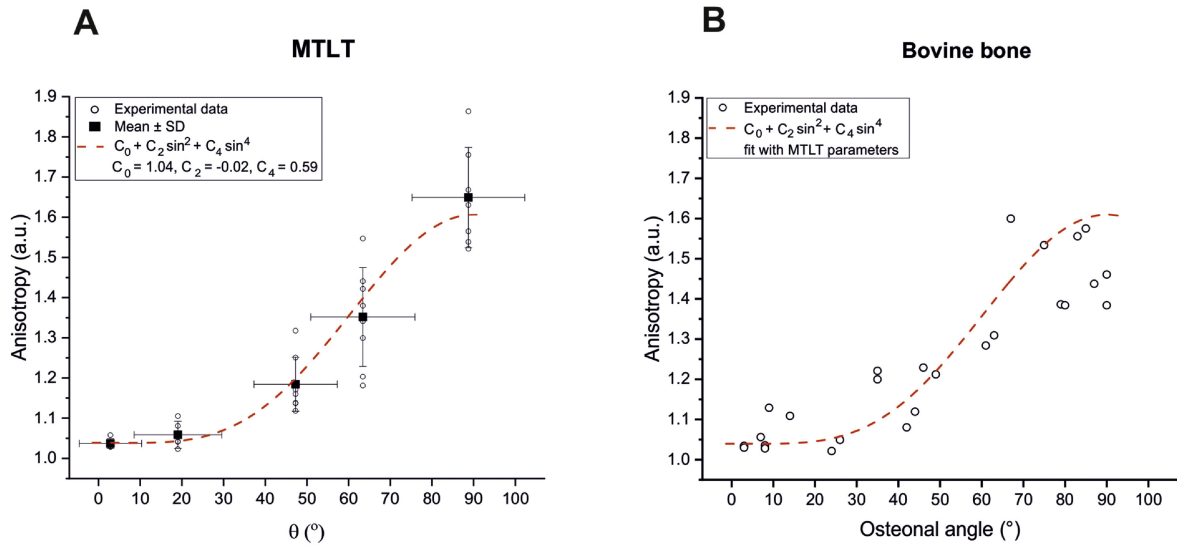


Figure 3.1.3 – (A) Anisotropy of MTLT collagen bands at different out-of-plane fibril orientation θ ; (B) Anisotropy of bovine cortical osteonal bone collagen bands at different osteon orientation, fitted with the calibration function from the MTLT study. The coefficients of determination R^2 are 0.98 and 0.82, respectively.

ments report the mean MCF out-of-plane angles θ together with the misorientation width of MCF determined by the Ruland method. From the azimuthal broadening of SAXS scattering intensities along the streak axis, the mean MCF out-of-plane angles θ were found to be close to the initial sample cutting angles: $2.88^\circ \pm 0.06^\circ$, $19.06^\circ \pm 0.05^\circ$, $47.28^\circ \pm 0.08^\circ$, $63.43^\circ \pm 0.06^\circ$ and $88.76^\circ \pm 0.04^\circ$. Following the Ruland streak method, the misorientation width of MCF was found to be higher for the higher out-of-plane angles θ , ranging from 15° to 27° (for more details see Appendix A1.4).

Theoretical calculations were used to determine the functional dependence of the anisotropy parameter $\frac{A}{B}$ on the MCF out-of-plane orientation, see Appendix A1.2 for further details. We found that a function of the form 3.1.4 is well suited to reproduce the theoretical prediction and retains the 180° periodicity ($R^2 = 0.99$, Appendix A1.2).

$$f(\theta) = C_0 + C_2 \sin^2(\theta) + C_4 \sin^4(\theta) \quad (3.1.4)$$

The average anisotropy parameter $\frac{A}{B}$ from the PRS measurements on each of the MTLT specimens was fitted with equation 3.1.4 versus the fibril out-of-plane angle (coefficient of determination $R^2 = 0.98$). The out-of-plane angular error in figure 3.1.3 A represents the fibril misorientation width, as determined from the SAXS measurements. From the MTLT fit, the following parameters of the calibration function 3.1.4 were found: $C_0 = 1.04$, $C_2 = -0.02$ and $C_4 = 0.59$. The qPRS out-of-plane angles were compared to the SAXS out-of-plane MCF angles and the standard error of the estimate (SEE) was taken as the angular uncertainty resulting in an error estimate of $\theta^{err} = 9.7^\circ$ (Appendix A1.2).

Next, polarized Raman spectra were collected on 26 bovine cortical bone osteons with different orientations from 0° to 90° , as measured by micro-CT. Figure 3.1.3 B shows a correlation between the anisotropy parameter $\frac{A}{B}$ for bovine cortical bone and the out-of-plane angles of the osteons. The data was compared to equation 3.1.4 with the parameters determined from the MTLT calibration and the osteon angles taken for θ (coefficient of determination $R^2 = 0.82$).

The out-of-plane MCF angles θ are extracted numerically from function 3.1.4. By extracting both the out-of-plane angle θ (equation 3.1.4) and the in-plane angle φ (equation 3.1.1) from the PRS spectra, a quantitative 3D orientation estimation of the MCF is possible. For further mechanical parameter analysis, we focused on the out-of-plane MCF angles θ .

3.1.3.2 Micropillar compression of bovine cortical bone lamella with known fibril orientation

Microscale compression tests were performed on FIB manufactured micropillars with known collagen fibril orientation measured by qPRS. A total of 44 micropillars were fabricated in 13 osteons on the bovine cortical bone samples, from which two had irregularities in geometry and were therefore excluded from the study, three were lost due to operator errors and three were excluded from the batch analysis due to excessive noise in the force-displacement data. The remaining micropillars ($N = 36$) were used for the actual testing and analysis. As a result, 2 to 3 micropillars were tested for each collagen fibril orientation ($N = 13$). Representative stress-strain curves as a function of the fibril angle, determined by qPRS, and the images of corresponding micropillars after compression are shown in figure 3.1.4.

The collected stress-strain curves for different MCF orientations (figure 3.1.4 A) demonstrate a clear dependency of the mechanical response on the fibril angle. This dependence is even more pronounced in figure 3.1.5, where elastic moduli and yield stress, extracted from the stress-strain curve, are plotted versus the out-of-plane MCF angles, known from previously performed qPRS measurements. The elastic modulus of lamellae with collagen fibrils parallel to the loading direction is more than 3.8 times higher than the modulus of lamellae with fibrils orthogonal to the loading direction. Similar behavior was observed for the yield stress, where axially aligned samples show a yield stress almost 2.5 higher than transverse samples. For further fitting, the mean values of the elastic moduli for each of the fibril orientation were used. The apparent elastic moduli were fitted as a function of MCF angles with the analytical expression for the apparent modulus in axial direction of a transversely isotropic compliance tensor rotated around one axis from the transverse plane (equation 3.1.2). For the analysis, the axial elastic modulus E_a was taken as the maximum

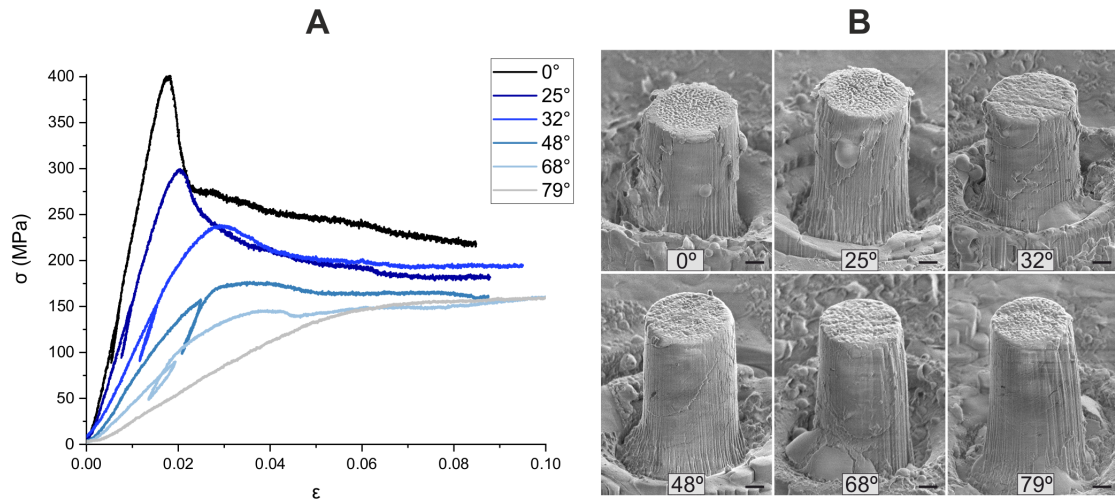


Figure 3.1.4 – Stress-strain curves and HRSEM images after pillar compression of bovine cortical bone lamella with different mineralized collagen fibril orientation, scale bar 1 μm .

value found from the micropillar compression tests and the transverse elastic modulus E_t was calculated as the average measured modulus of compression experiments of micropillars with a fibril angle $> 60^\circ$. The remaining free parameters ν_t , μ_a were determined using a least-squares fit of the fibril angle dependent data. The mean values of the yield stress for each of the fibril orientation were fitted with the Tsai-Hill composite failure model 3.1.3. The resulting optimal parameters determined from the fitting procedures are collected in table 3.1.1.

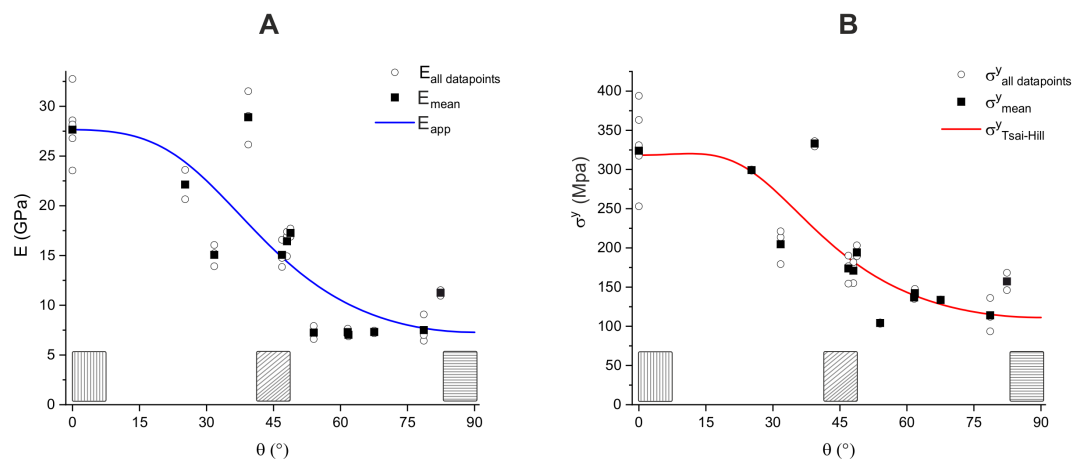


Figure 3.1.5 – Elastic modulus and yield stress dependence on the collagen fibril out-of-plane orientation. The coefficients of determination R^2 are 0.50 and 0.61, respectively.

Table 3.1.1 – Output parameters from the apparent modulus 3.1.2 and yield stress 3.1.3 fit.

Compliance tensor	Axial elastic modulus (E_a)	27.65 GPa
	Transverse elastic modulus (E_t)	7.28 GPa
	Out-of-plane Poisson ratio (ν_a)	0.7
	In-plane Poisson ratio (ν_t)	0.3*
	Shear modulus (μ_a)	8.22
Tsai-Hill	Strength along axial direction (X)	318 MPa
	Strength along transverse direction (Y)	111 MPa
	Shear strength (S)	206 MPa

* from [239]

3.1.3.3 Other parameters affecting microscale mechanical properties of bone

Besides MCF orientation, other factors like the degree of mineralization and overall variation in biochemistry may affect the mechanical properties of bone lamellae.

For all tested bovine osteons, a relative standard deviation of about 7% was observed for the mineral to matrix ratio, which was not sufficient to detect a significant correlation with the mechanical parameters ($p = 0.6$ for both elastic modulus and yield stress). The relative standard deviation of mineral crystallinity did not exceed 1% and no significant correlation with the elastic modulus ($p = 0.3$) nor with the yield stress ($p = 0.2$) was observed. Although the Raman intensity ratio of amide I/ CH bending has been reported to quantify the relative concentrations of collagen versus NCPs [230], it was found to be strongly dependent on the sample orientation ($R^2 = 0.68$, $p < 0.01$). We therefore used the Raman intensity ratio of amide III/ CH bending instead to quantify the relative concentrations of collagen versus NCPs, as it showed a trend but no significant dependence on the collagen orientation ($p = 0.1$). Around 4% of relative standard deviation of the collagen versus NCPs relative concentrations (amide III/ CH) was observed for the tested osteons. Moreover, a moderate dependence was found between the Raman intensity amide III/ CH ratio and the measured mechanical properties ($R^2 = 0.5$, $p = 0.01$ for both elastic modulus and yield stress). For further details, see Appendix A1.3.

3.1.3.4 Post-yield behavior and failure modes

The stress-strain curves from the micropillar compression show softening for small MCF angles and hardening with the MCF orientations close to the transverse direction. To quantitatively analyze the softening/hardening behavior, the relative change of stress after the yielding point R was evaluated with the following ratio:

$$R = \frac{(\sigma^{pl} - \sigma^y)}{\sigma^y} \quad (3.1.5)$$

where σ^{pl} signifies the stress value at the plateau region taken at 8% strain and σ^y is the yield stress (figure 3.1.1 D). Negative values of the ratio correspond to strain softening and positive to hardening behavior, respectively. The transition between softening and hardening post-yield behavior was found for the MCF orientations at $\theta = 48^\circ - 54^\circ$, as marked in figure 3.1.6. Relative change of stress after the yield point R (equation 3.1.5) was then fitted with a hyperbolic tangent function (equation 3.1.6), as it reflects well the behavior of the data.

$$R(\theta) = 0.21 \tanh(9.79(\theta - 49^\circ)) - 0.10 \quad (3.1.6)$$

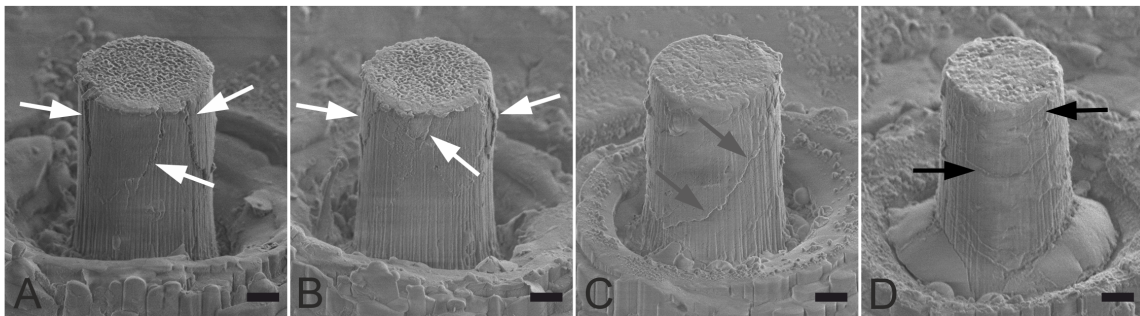
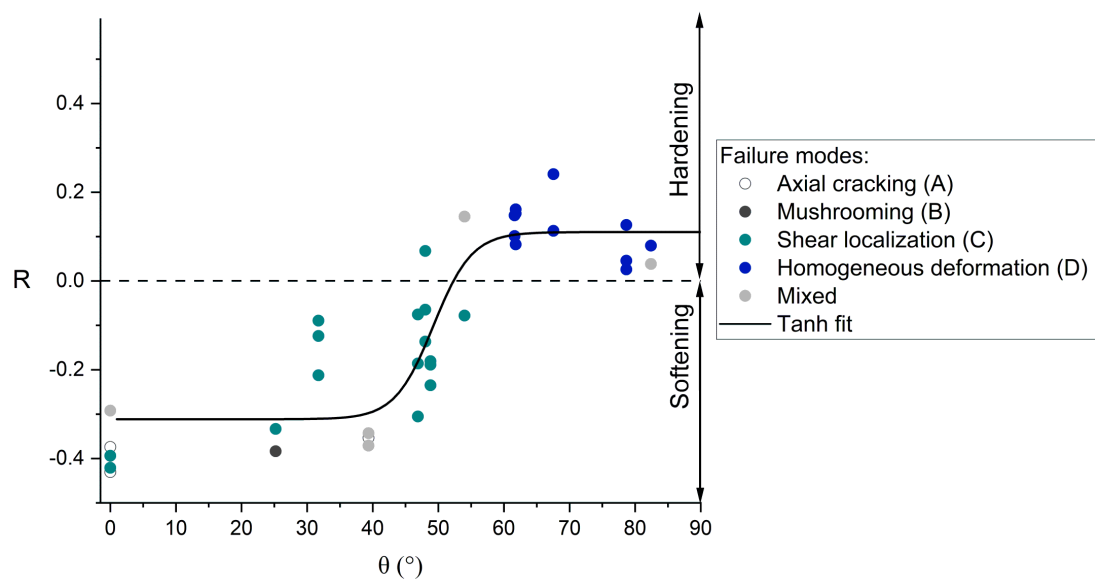


Figure 3.1.6 – Post-yield behavior and failure modes encountered in compression tests of micropillars with different out-of-plane MCF angles θ . Failure modes were analyzed visually based on HRSEM images, the representative HRSEM images of each failure mode with marked stress concentration regions are shown at the bottom (white arrows point to the vertical cracks, grey arrows point to the oblique cracks, and black arrows point to the horizontal cracks). Softening/hardening behavior was estimated from the relative change of stress after the yielding point R (equation 3.1.5) and fitted with hyperbolic tangent function (equation 3.1.6). The coefficient of determination $R^2 = 0.72$, scale bar $1 \mu m$.

From the HRSEM images, different failure modes were encountered during compression tests: axial cracking (figure 3.1.6 A), mushrooming (figure 3.1.6 B), shear localization (fig-

ure 3.1.6 C), homogeneous deformation (figure 3.1.6 D) and a combination of above. As demonstrated in figure 3.1.6, the majority of micropillars, which demonstrated softening behavior, failed in a localized shear crack, whereas those micropillars showing a hardening behavior deformed in a more homogeneous manner.

3.1.4 Discussion

The goal of this study was to assess the orientation dependent mechanical properties and deformation mechanisms of the basic building block of bone, the lamella. To this end, we developed and calibrated a procedure allowing to measure quantitatively the out-of-plane angle of MCF using qPRS with a high spatial resolution of $\sim 0.3\mu m^3$. We then performed a large number of uniaxial compression experiments in hydrated conditions ($N = 36$) on micropillars with known fibril orientation. Elastic modulus and yield stress were extracted and fitted using analytical models. Based on HRSEM images, the failure modes were identified as a function of fibril orientation. Finally, the post-yield behavior was extracted and related to the local fibril angle and observed failure mode. The different aspects of the study will be discussed in detail in the following paragraphs.

3.1.4.1 Quantitative Polarized Raman spectroscopy (qPRS)

qPRS is a non-invasive method for tissue composition and MCF orientation investigations with a high spatial resolution. In the past, it has been employed for quantitative analysis of MCF in-plane orientations [160]. Moreover, PRS was applied recently to resolve 3D orientation of MCF in rat tail tendons [203] and human cortical bone [204]. However, the reported studies on spatial MCF organization using PRS were mainly qualitative. To our knowledge, we are the first to report a method that allows applying PRS for quantitative estimation of bone MCF orientation in 3D. For this we performed PRS calibration on mineralized turkey leg tendon, a model material with highly aligned mineralized collagen fibrils, and validated it on bovine cortical bone.

Our calibration study followed the general methodology of Spiesz et al. [199], where a calibration function for quantifying MCF out-of-plane orientation was determined based on measurements performed on MTLT samples with a known uniaxial fiber orientation. Polarized light microscopy is a relatively fast and well-known technique, however it requires thin sample cuts at a fixed thickness over which the signal is integrated. This can pose significant problems if osteons are not oriented parallel to the light beam. In the present study, the application of PRS gives us significant advantage in the spatial resolution, since we use a confocal system and collect the signal from a $\sim 0.3\mu m^3$ volume. In case of bovine cortical

bone osteons with lamellar thickness of several microns, the Raman focal volume is small enough to collect information from locally aligned MCF. Even in the case of human cortical bone osteons, where each lamella (thickness $\sim 7 \mu\text{m}$) is composed of several sub-lamellae (thickness $\sim 1 \mu\text{m}$) [30], the resolution should be sufficient to supply information on the local MCF orientation, even though some averaging effects are likely to occur when the sample is misaligned with the laser beam [204].

In comparison with other available methods of MCF spatial orientation analysis, such as SAXS/WAXS and nano-CT, qPRS does not expose the sample to a high energy X-ray beam. With the qPRS parameters used throughout this work, no structural modifications of the sample were observed (Appendix A1.2). Moreover, qPRS does not require additional time-consuming sample preparation, as in the case of e.g. TEM imaging (Rubin et al., 2003). The spatial resolution of qPRS is defined by the Raman setup, for example the objective numerical aperture or the incident laser wavelength. In this study, the focal spot size was estimated to be $\sim 0.4 \mu\text{m}$ in diameter, which is suitable for the lamellar scale investigations.

PRS measurements on MTLT were in good agreement with the theoretical prediction (figure 3.1.1 and Appendix A1.2). The function from the theoretical prediction (equation S8, Appendix A1.2) was found to be not suitable for the MCF angle θ extraction due to the interdependency of the output parameters. We therefore used a simplified fitting function 3.1.1 following the methodology proposed by Bao et al. [225] to extract the output Raman parameters, including the parameter of anisotropy $\frac{A}{B}$. The simplified fit precision was comparable to the theoretical prediction (for both, $R^2 > 0.99$). The angular uncertainty of the qPRS method $\theta^{err} = 9.7^\circ$ (Appendix A1.2). While this error is not negligible, the application to bovine bone showed that the method is precise enough to extract meaningful data for studying microscale structure-property relationships.

Prior to the validation study on bovine cortical bone, polarized Raman line maps were collected on three bovine bone osteons to quantify the variation of fibril orientation within each osteon (Appendix A1.2). The out-of-plane MCF angle θ , averaged across the osteon, was different from the micro-CT measurements: $11 \pm 9^\circ$ for the 6° osteon and $8 \pm 7^\circ$ for the 4° osteon, resulting in an average disagreement of $4 - 5^\circ$ between the different methods. This is well below the angular uncertainty of both methods and therefore may be neglected. On average, a standard deviation of $\pm 7^\circ$ was found for the MCF alignment within each osteon. Again, as this standard deviation is below the experimental uncertainty of the proposed qPRS procedure for fibril out-of-plane angle estimation, it may be neglected. Therefore, we collected only one set of 19 polarized Raman spectra per osteon.

Micro-CT scans were used for osteonal orientation determination. With $\sim 5 \mu\text{m}$ resolution, this technique is suitable to locate the Haversian canals together with osteonal and interstitial zones of cortical bone, but does not have sufficient contrast and resolution to distinguish between individual bone lamellae. Osteonal angle, as determined from micro-CT, was used to screen the osteons on each sample to reach a homogeneous distribution of fibril orientations and to cross validate with qPRS.

Previously reported PRS studies on bone employed another experimental design using an additional analyzer plate in the path of the scattered light. There, the theoretical dependence of the Raman scattering on light polarization was calculated from four experimental configurations of polarizer/analyzer parallel and orthogonal alignments [160, 240]. In more recent works [172, 203, 204], the collection of the scattered light for a range of incoming laser polarization angles was proposed. In the present study, we established a method for quantitative estimation of MCF spatial orientation by determining a calibration function between polarization anisotropy and MCF out-of-plane angle on mineralized turkey leg tendon, a model material with a very similar composition and ultrastructure to bone featuring highly aligned collagen fibrils. The approach proposed in this study requires a higher number of measurements than the former, however, it increases the robustness and accuracy, as the collected scattered light has higher intensities due to the absence of an analyzer leading to an increased signal to noise ratio (SNR). Furthermore, the influence of data scatter due to natural variability and experimental artefacts is reduced due to the employed fitting procedure, which analyzes the best fit of many experiments rather than relying on the direct determination of the Raman tensor from a limited number of measurements, which is more sensitive to experimental artefacts.

In this work, the newly proposed qPRS method is used to evaluate the orientation of collagen fibers based on polarization dependence of amide Raman bands. However, alternative polarization dependent Raman bands may be used. We specifically acknowledge the possibility to use the amide I/ $\nu_2\text{PO}_4$ for MCF orientation estimation, following the same spectra acquisition and data processing protocols. Detailed analysis is presented in the Appendix A1.2. We demonstrate an excellent correlation between the two Raman band integrated intensity ratios for MTLT samples ($R^2 = 0.98$, $p = 0.01$). Moreover, we calibrated the anisotropy parameter $\frac{A}{B}$, extracted from amide I/ $\nu_2\text{PO}_4$ polarization dependence, with the fibril out-of-plane angle θ , taken from the SAXS measurements ($R^2 = 0.99$). Consequently, the parameters of the calibration function for amide I/ $\nu_2\text{PO}_4$ (equation 3.1.4) are: $C_0 = 1.09$, $C_2 = -0.05$ and $C_4 = 0.76$. These parameters can be used as an alternative for estimating the out-of-plane MCF angle based on local measurement of amide I/ $\nu_2\text{PO}_4$ Ra-

man band integrated intensity ratios. In the present work, all of the collected spectra had a high background fluorescence, overlapping with the ν_2PO_4 band intensity, as can be seen, for example, from the raw spectra presented in the Appendix A1.2. We therefore chose to use the amide I and amide III bands for the qPRS method, as they both were not affected by the sample fluorescence.

Besides MCF orientation, we also investigated the effects of mineral to matrix ratio, mineral crystallinity, and relative NCP content of the bovine cortical bone osteons. All of these parameters have a low relative standard deviation, which indicates the homogeneity of the tested tissue.

A clear limitation of the proposed method is related to the isotropy of the polarization response of both axially aligned and randomly oriented fibrils. As no polarization dependence exists for the integral area ratio of the collagen peaks of interest, special care needs to be taken to distinguish between these two types of fibril orientations. We have not encountered such a situation during this study, as we used model bone materials with a simplified, mostly uniaxially aligned microstructure. For future measurements, we propose, as a possible remedy, to collect additional spectra while tilting the sample by a known angle or to include amide I intensity into the analysis.

3.1.4.2 Mechanical testing

Here, we performed for the first time microscale compression experiments on the length scale of single bone lamellae in hydrated state for a broad spectrum of known local fibril orientations. The elastic modulus and strength nonlinearly decreased with the increasing MCF angle. The theory of linear elasticity for transversely isotropic materials and Tsai–Hill criterion were found to describe well the variation of these properties with the fiber orientation (figure 3.1.5). The found non-linear behavior as a function of MCF angle on the single lamella level of bone is comparable to what has been observed in other short fiber reinforced polymer composites [241]. In the majority of previously reported studies, the microscale mechanical properties of bone were investigated for two assumed MCF orientations: axial ($\theta = 0^\circ$) and transverse ($\theta = 90^\circ$). However, no means of quantification of the true fibril angles existed. Here, the mechanical compression experiments were performed on bone lamellae with 13 known MCF orientations in the range from 0° to 82° (figure 3.1.5). This provides a unique dataset for identifying the structure-property relationships of bone on the lamellar scale through a combination of micropillar compression and MCF orientation determination using non-invasive qPRS.

Fibril misalignment is a common phenomenon for natural materials, such as bone, and it significantly affects the accuracy of measured mechanical parameters. When it comes to

clinical investigations of bone strength as a function of age, gender, disease, or treatment, it becomes especially important to separate the respective contributions of macroscopic bone geometry and density, which are clinically assessed today [105], from the intrinsic tissue properties that depend on microstructural factors, like local degree of mineralization or fibril orientation distribution [94]. Multiscale structural organization and mechanical property analysis of bone biopsies may be used in the future for studying the changes in tissue organization and mechanical properties related to bone metabolic diseases like osteoporosis [124, 197, 242]. In preclinical osteoporosis and bone research, different large and small animal models are used as a model for human bone [13, 243]. For different species (e.g. human, canine, mice) the collagen fibrils in osteonal lamellae have been reported to feature an offset angle with respect to the bone's long axis in a range of $20 - 30^\circ$ [30, 160, 199, 244]. In this study, a variation of the MCF out-of-plane orientation of up to 16° was observed within the osteonal regions of the bovine cortical bone sample. This variation in fibril orientation is an intrinsic property of bone in different species that leads to considerable data scatter in mechanical experiments and warrants further investigation. Especially when analyzing micromechanical experiments, it is of high interest to employ methods for quantifying the local MCF orientation and degree of mineralization in the region of interest to reduce apparent data scatter and identify structure-property relationships with high fidelity.

As expected from the micropillar compression experiments, the highest value of elastic modulus was found for the axial MCF orientation ($E_a = 27.65\text{GPa}$, $\theta = 0^\circ$) and the lowest for transverse orientations ($E_t = 7.28\text{GPa}$, $\theta > 60^\circ$). This tendency is in good agreement with previously reported data on the mechanical experiments on bone, collected in table 3.1.2. The axial elastic modulus value is greater than the majority of values reported in literature for both micro- ($21 - 23\text{GPa}$, [245–247]) and macro-scale compression experiments ($\sim 20\text{GPa}$, [248, 249]). The first may be due to the natural variations in MCF orientation in cortical bone specimen that has been shown to be present in different species [30, 160, 199, 244]. As previous studies on microscale cortical bone mechanical properties did not verify the MCF orientation, the reported data is likely averaged over a MCF misorientation range of up to 30° , which can explain the reported lower average elastic modulus values. At the macroscale, the mechanical response is averaged over large regions with different degrees of mineralization and fibril orientation and includes the effect of Haversian porosity, therefore also from these experiments a lower apparent modulus can be expected [250].

Table 3.1.2 – Reported mechanical anisotropy values and experimental details.

Elastic anisotropy values	Plastic anisotropy values	Characteristic specimen size	Conditions	Method	Sample	Ref.
$\frac{27.7}{7.3} = 3.8$	$\frac{0.33}{0.13} = 2.54$	5 μm	Hydrated, > 93% RH	Compression	Bovine	Present work
$\frac{19.1(\pm 2.8)}{11.6(\pm 2.4)} = 1.6$	$\frac{0.18(\pm 0.02)}{0.11(\pm 0.02)} = 1.64$	5mm	Ambient	Compression	Bovine	[248]
$\frac{20.5(\pm 2.3)}{13.0(\pm 2.3)} = 1.6$	$\frac{0.18(\pm 0.02)}{0.16(\pm 0.01)} = 1.13$	5mm	Ambient	Compression	Bovine	[249]
$\frac{26.9}{22.6} = 1.2$ $\frac{26.9}{18.0} = 1.5$		350 nm	Ambient	Indentation	Bovine	[251]
$\frac{27.5(\pm 2.2)}{19.0(\pm 1.8)} = 1.5$	$\frac{1.01(\pm 0.13)}{0.68(\pm 0.08)} = 1.51$	7 μm	Ambient	Indentation	Ovine	[167]
$\frac{22.8(\pm 1.6)}{14.5(\pm 1.6)} = 1.6$	$\frac{0.60(\pm 0.11)}{0.51(\pm 0.08)} = 1.18$	7 μm	Hydrated, liquid immersion	Indentation	Ovine	[167]
$\frac{31.2(\pm 6.5)}{16.5(\pm 1.5)} = 1.9$	$\frac{0.50(\pm 0.10)}{0.30(\pm 0.02)} = 1.63$	5 μm	<i>in vacuo</i>	Compression	Ovine	[167]
	$\frac{0.17(\pm 0.02)}{0.13(\pm 0.03)} = 1.31$	5 μm	Hydrated, liquid immersion	Compression	Ovine	[179]
$\frac{13.7(\pm 0.8)}{6.5(\pm 1.0)} = 2.1$		17.5 μm	Ambient	Indentation	MTLT	[217]
$\frac{18.1(\pm 2.9)}{10.2(\pm 1.8)} = 1.8$		6.3 μm	Ambient	Indentation	MTLT	[217]
$\frac{12.9(\pm 1.6)}{2.9(\pm 0.8)} = 4.5$		17.5 μm	Hydrated	Indentation	MTLT	[217]
$\frac{30.2(\pm 4.1)}{17.6(\pm 1.9)} = 1.75$		1.8 μm	Ambient	Indentation	Human	[31]
$\frac{24.7(\pm 2.7)}{17.3(\pm 1.9)} = 1.4$		5.6 μm	Ambient	Indentation and orthotropic stiffness tensor model [253]	Human	[252]
$\frac{24.7(\pm 2.7)}{9.2(\pm 0.6)} = 2.7$						

Elastic anisotropy values: E_a/E_t ; plastic anisotropy values: H_a/H_t for indentation and σ_a^y/σ_t^y for compression tests; all reported mechanical values are in GPa; characteristic specimen size calculated as 7*(penetration depth) for indentation, pillar diameter for compression.

The measured transverse elastic modulus is lower than the previously reported values from both macro- and micro-scale mechanical tests on bovine bone [248, 249, 251, 254]. This leads to higher elastic anisotropy values (E_a/E_t), compared to previously reported data in the literature (table 3.1.2). This could be related to the fact that we are testing bundles of aligned collagen fibrils in the transverse direction, a situation not encountered during macroscopic experiments, where the tested volume contains a variety of fibril orientations. It should be noted, however, that our setup is likely prone to sample surface swelling artifacts in hydrated conditions. Similar behavior was already reported for hydrated ovine [167, 179], bovine [214] and MTLT [217] samples, where observed anisotropy ratios increased up to 2.5 times in comparison to dry experiments. Such anisotropic response to hydration might be a result of MCF structural changes. As was shown by Andriotis et al. [255], during single collagen fibril hydration, the stiffness will exhibit a fourfold higher reduction in transverse direction than in the axial direction, due to the different collagen packing density. In micropillars with fibrils aligned in axial orientation, the surrounding fibrils enforce a constraint on radial fibril swelling, therefore this effect is diminished. However, in transverse specimens, the radial swelling of fibrils at the top surface is not inhibited, which could lead to substantial artifacts in the mechanical measurements, as these surface fibrils are likely to be significantly more compliant and, from a mechanical perspective, arranged in series with the remaining micropillar.

In this work, the yield stress values measured in both axial and transverse directions ($\sigma_a^y = 329.97\text{MPa}$, $\sigma_t^y = 131.63\text{MPa}$) are higher than previously reported from macroscale compression tests [248, 249]. When compared to experiments performed on the same characteristic specimen size ($5\ \mu\text{m}$) on ovine cortical bone lamella, the values are also higher than those from hydrated tests in buffered solution [179] but lower than the data obtained *in vacuo* [167]. Overall, bone hydration is one of the important parameters affecting bone mechanical properties [256, 257]. In our study, the bone samples were measured in a humidified atmosphere, with relative humidity above 93% to mimic physiological conditions. Prior to the measurements, samples were kept in a hydrated atmosphere for at least 4h, to ensure the sample equilibration. We verified that the measured values of the elastic modulus and yield stress were constant within each day of experiments (see Appendix A1.6) therefore assuring that the specimens had reached an equilibrated hydration state prior to the measurements. We assume that the micropillar swelling affects the measured yield stress, as the micropillar geometry, used for stress and strain calculations, was assessed prior to mechanical testing. For future mechanical testing it is recommended to estimate the swelling effects on specimen geometry in humidified atmosphere. For this, high-resolution techniques, such as environmental SEM [258], atomic force microscopy [255] or SAXS [259] could be used.

Remarkably, the yield stress values observed for the MCF orientations from 0° and up to 25° are nearly constant. This was also reported for microscale tensile and compressive strength modelling of ovine cortical bone [213]. Such tolerance to the MCF small angle variations is in line with the natural variability in MCF orientation found in different species [30, 160, 199, 244], which could act as one of the bone's toughening mechanisms [260, 261].

Besides MCF orientation, osteonal bone lamellation and overall variation in biochemistry may affect microscale mechanical properties of bone. In present study, the degree of mineralization and the mineral crystallinity did not show significant correlations with the mechanical data due to their small respective variations. However, we found a weakly significant dependence of the observed mechanical properties with variations of collagen/ NCPs relative concentrations. Indeed, the spatial arrangement of NCPs within bone matrix may determine bone's mechanical properties including toughness [57, 262, 263]. It is therefore recommended to include alternative analysis methods for NCPs content and biochemistry screening for the future studies on bone microscale mechanical properties. Structural inhomogeneity in the volume of a single micropillar may be introduced due to the lamellar structure of osteonal bone. As was experimentally verified by Raman line scans taken in several osteons on the bovine bone specimen, MCF were highly aligned with the osteon axis with a standard deviation of 7° (Appendix A1.2) in contrast to the 30° average variation, that has been observed in human secondary osteons [30]. This suggests that the osteonal bone in our bovine specimen consisted mainly of primary osteons with highly aligned MCF uniaxially oriented in the osteon direction in each lamella.

3.1.4.3 Post-yield behavior and failure modes

As demonstrated in this study, post-yield behavior and failure modes of bone micropillars depend on MCF orientation. According to the stress-strain curves from the microcompression experiments (figure 3.1.4 A), a clear strain softening is observed for the MCF close to axial orientation and strain hardening for transverse MCF orientations. The same was observed in previously reported micropillar compression experiments on ovine cortical bone [167, 179]. Closer examination of the post-yield behavior (figure 3.1.6) revealed two plateau regions of the relative change in stress ratio (equation 3.1.5). The first one corresponds to the softening observed at lower MCF angles ($\theta < 30^\circ$). Interestingly, this plateau in softening ratio also coincides with the range of constant yield stress, demonstrating that the inelastic behavior of bone lamellae remains mostly unchanged for misalignment angles below 30° . The second plateau at higher MCF angles ($\theta > 50^\circ$) resembles post-yield hardening behavior. For the

intermediate MCF angles, a steep change from softening to hardening is observed, featuring a transition not only in the post-yield behavior, but also in the failure mode, which suggests a change in deformation mechanisms between axial and transverse specimens.

The structural complexity of bone leads to hierarchical and coupled deformation mechanisms (fibril - extrafibrillar matrix, mineral - collagen) down to the nanoscale [260]. A variety of failure modes occurred at $\theta \in (0^\circ, 50^\circ)$. At the angles close to axial ($0^\circ < \theta < 25^\circ$), MCF orientation is moderately aligned with the loading direction and most of the load is carried by the fibrils. In this case, axial cracking along the length of the pillars (figure 3.1.6 A) or localization at the top of the pillars (mushrooming, figure 3.1.6 B) is observed. The proposed deformation mechanism that could be directly tuned by the MCF misalignment with the loading direction is the fibril-extrafibrillar matrix (EFM) interfacial sliding [262]. Such deformation occurs due to interface failure between fibrils, e.g. axial cracking along the length of the pillars or mushrooming. Similar damage behavior for axially aligned MCF was observed in the work of S. Li et al. [248]. When the bone is compressed beyond the yield point, critical interfacial shear strength between the fibril and the matrix is exceeded. When this happens, matrix flows past the fibrils, resulting in frictional losses and de-bonding of the fibrils and extrafibrillar matrix [262]. The thin fibril-EFM interface then flows past the fibrils, resulting in frictional losses, similar to the shear lag model for tensile loadings [216, 264].

With the increase in MCF angle, localized shear cracks are observed. Interestingly, at the lower angles of MCF, the shear plane was steeper than at higher angles, which suggests the existence of a correlation between the MCF and shear plane orientations. This is in line with the notion of fibril-EFM interface failure for angles below 50° . For MCF orientations $\theta > 50^\circ$, the main failure mode occurring in this work is homogeneous deformation. We believe that when the MCF angles reach the softening threshold of $48^\circ - 54^\circ$, the shear load applied to the tilted fibril-matrix interface is not sufficient to cause deformation in localized shear zones, due to the high normal force and, therefore, an increased frictional component. The deformation is assumed to happen in the extrafibrillar matrix and homogeneously spread throughout the pillar volume, which is compacted so that frictional hardening occurs. Moreover, the nanogranular friction from mineral-mineral interparticle interactions may additionally influence the post-yield bone deformation mechanisms, especially in compression. As was shown in the work of Tai et al. [265], at the nanoscale, bone exhibits a pressure sensitive plasticity. Similar to other nanogranular materials, bone features a nanoscale porosity [266, 267], which leads to a plastic contraction under compressive loading. This, together with the fibril-extrafibrillar interfacial sliding, would lead to a cohesive frictional sliding with tunable softening/hardening behavior depending on the shear flow instabilities.

3.1.4.4 General limitations

The techniques used in this study analyze different volumes of interest. qPRS provides structural and compositional information from $\sim 0.3\mu\text{m}^3$ volume. For both MTLT and bovine cortical bone lamellae, such volume would include several MCFs. At the same time, SAXS beam size at sample position was about $400\mu\text{m}$ in diameter, which integrates over thousands of MCFs. However, we could combine these two techniques on the MTLT sample because of its extremely aligned ultrastructure, made up of densely packed MCF, therefore locally and globally the orientations are highly correlated [215–217].

In this study we combined qPRS and micropillar compression on bovine cortical bone samples. While qPRS gives structural information on the length scale of several MCF, the latter provides mechanical data on the lamellar scale (characteristic micropillar size $5\mu\text{m}$). However, we could show experimentally by Raman line scans taken in several osteons on the bovine bone specimen that MCFs in primary bovine osteons are highly aligned with the osteon axis (7° standard deviation) and that no plywood-like variation in MCFs was present (Appendix A1.2). It was furthermore verified that there is a clear correlation between osteonal and MCF angles (figure 3.1.3 B). This, together with the low scatter in the collected mechanical data for different MCF orientations, suggests a well aligned MCFs arrangement as determined by qPRS. We therefore assume that the tested micropillars were made up of homogeneously aligned MCFs, which is corroborated by our findings. In the future studies, when applying these techniques to a tissue with a more complicated microstructure such as human lamellar bone, care has to be taken to better match the tested volumes of the two methods, e.g. by scanning the focal spot through the micropillar and acquiring several qPRS measurements.

qPRS was not performed on each micropillar in this study because of the incompatible specimen fabrication steps. In order to fabricate micropillars on the bone surface the sample needs to be sputtered with conductive material (Au, 11 nm), which reflects the incoming laser beam and therefore significantly decreases the spectrum quality. Therefore, MCF orientation was measured before micropillar production in each osteon. As we found that MCFs are highly aligned and show little variation within an osteon, we could correlate the micromechanical properties to the average MCF orientation. However, for future studies combining these two methods on more complex tissues like human bone, another method should be used for micropillar preparation. A suitable approach would be employing femtosecond laser ablation [192], which does not require sputtering of a conductive film and therefore results in specimens suitable for local qPRS measurements.

3.1.5 Conclusion

The focus of this study was to investigate the effect of local microstructure, especially MCF orientation, on the microscale mechanical properties of isolated bone lamellae. In order to achieve this, a polarized Raman spectroscopy based method was developed that allows measuring local MCF angle with an angular uncertainty $< 10^\circ$. The combination of polarized Raman spectroscopy and micropillar compression made it possible to detect changes in mechanical properties with the MCF angle. This allowed us to measure a unique spectrum of microscale mechanical compression data for MCF orientations ranging from 0° to 82° . We could demonstrate a strong dependence of the microscale compressive mechanical properties of bone on the MCF orientations. On the other hand, the degree of mineralization and the mineral crystallinity did not show significant correlations with the mechanical data due to their small respective variations. A high degree of anisotropy was found for both the elastic modulus ($E_a/E_t = 3.80$) and the yield stress ($\sigma_a^y/\sigma_t^y = 2.54$). Moreover, the post-yield behavior was found to depend on the MCF orientation with a transition between softening to hardening at $\theta = 48^\circ - 54^\circ$. Measuring the local microstructural (such as MCF angle, mineralization) and mechanical properties in a site-matched fashion allowed us to reduce the apparent scatter in the collected mechanical data and to reliably determine structure-property relationships of bone at the lamellar level. This is a prerequisite for developing and validating multiscale models predicting bone failure in the future.

Declaration of competing interest

The authors declare no competing financial interests.

Acknowledgment

This work is funded by the Special Focus Area Personalized Health and Related Technologies (SFA PHRT) iDoc Project 2017-304 (TK), Swiss National Science Foundation (SNSF) Ambizione grant no. 174192 (CP and JS) and SNSF project no. 173012 (AKM and AN). The authors wish to thank B. Voumard for the help during the sample preparation, D. Casari for the FIB guidelines, M. Indermaur for the micro-CT guidelines and R. Muff for technical support during the automatization of the polarization dependent Raman measurements.

3.2 Assessing minipig compact jawbone quality at the microscale[†][§]

Tatiana Kochetkova¹, Alexander Groetsch¹, Michael Indermaur², Cinzia Peruzzi¹, Stefan Remund³, Beat Neuenschwander³, Benjamin Bellon^{4,5}, Johann Michler¹, Philippe Zysset², Jakob Schwiedrzik¹

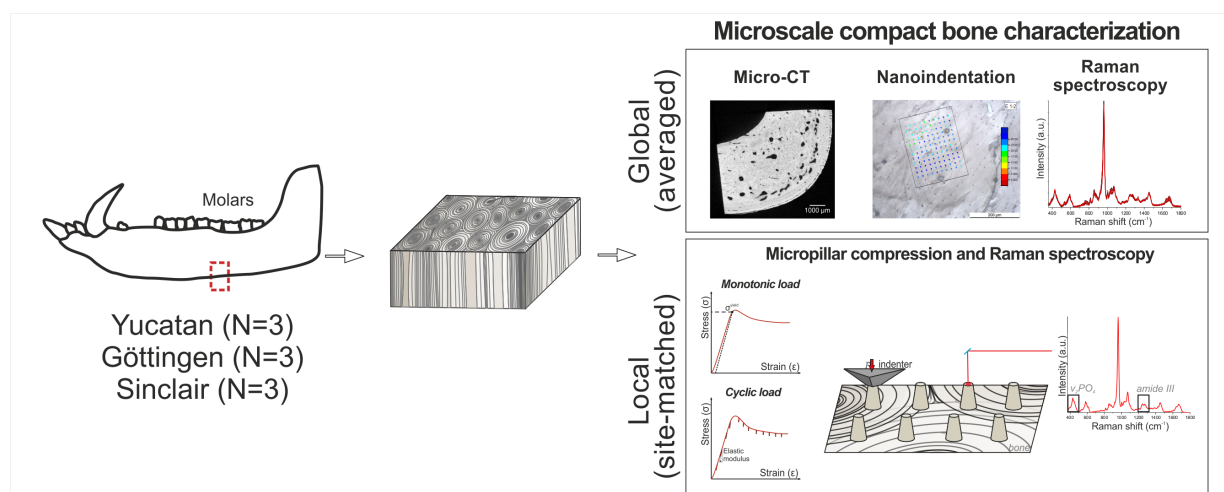
¹*Empa, Swiss Federal Laboratories for Materials Science and Technology, Laboratory for Mechanics of Materials and Nanostructures, Thun, Switzerland*

²*ARTORG Center for Biomedical Engineering Research, University of Bern, Switzerland*

³*Institute for Applied Laser, Photonics and Surface technologies (ALPS), Bern University of Applied Sciences, Burgdorf, Switzerland*

⁴*Institut Straumann AG, Basel, Switzerland*

⁵*Department of Periodontology, Faculty of Dentistry, University of Zürich, Zürich, Switzerland*



*Corresponding Authors: tatiana.kochetkova@empa.ch; jakob.schwiedrzik@empa.ch

[§]Tatiana Kochetkova, Alexander Groetsch, Michael Indermaur, Cinzia Peruzzi, Stefan Remund, Beat Neuenschwander, Benjamin Bellon, Johann Michler, Philippe Zysset, Jakob Schwiedrzik, "Assessing minipig compact jawbone quality at the microscale" (Journal of the Mechanical Behavior of Biomedical Materials 134, 2022)

Contribution: I performed sample preparations, Raman spectroscopy, nanoindentation, laser ablation protocol development and consequent micropillar fabrication, micro-CT scans, experimental data processing and final data analysis, and wrote the manuscript with the contribution of all the co-authors.

Abstract

Preclinical studies often require animal models for in vivo experiments. Particularly in dental research, pig species are extensively used due to their anatomical similarity to humans. However, there is a considerable knowledge gap on the multiscale morphological and mechanical properties of the miniature pigs' jawbones, which is crucial for implant studies and a direct comparison to human tissue. In the present work, we demonstrate a multimodal framework to assess the jawbone quantity and quality for a minipig animal model that could be further extended to humans.

Three minipig genotypes, commonly used in dental research, were examined: Yucatan, Göttingen, and Sinclair. Three animals per genotype were tested. Cortical bone samples were extracted from the premolar region of the mandible, opposite to the teeth growth. Global morphological, compositional, and mechanical properties were assessed using micro-computed tomography (micro-CT) together with Raman spectroscopy and nanoindentation measurements, averaged over the sample area. Local mineral-mechanical relationships were investigated with the site-matched Raman spectroscopy and micropillar compression tests. For this, a novel femtosecond laser ablation protocol was developed, allowing high-throughput micropillar fabrication and testing.

At the global averaged sample level, bone relative mineralization demonstrated a significant difference between the genotypes, which was not observed from the complementary micro-CT measurements. Moreover, bone hardness measured by nanoindentation showed a positive trend with the relative mineralization. For all genotypes, significant differences between the relative mineralization and elastic properties were more pronounced within the osteonal regions of cortical bone. Site-matched micropillar compression and Raman spectroscopy highlighted the differences between the genotypes' yield stress and mineral to matrix ratios.

The methods used at the global level (averaged over sample area) could be potentially correlated to the medical tools used to assess jawbone toughness and morphology in clinics. On the other hand, the local analysis methods can be applied to quantify compressive bone mechanical properties and their relationship to bone mineralization.

Keywords: Animal model, Miniature pig, Mandible, micro-CT, Raman spectroscopy, Nanoindentation, Femtosecond laser ablation, Micropillar compression, Structure-property relationships.

3.2.1 Introduction

Clinical assessment of the jawbone quality. Bone quality is often referred to as the determining parameter for dental implant studies. The term bone quality stands for the combination of various bone physiological, compositional, mechanical, and structural parameters [268, 269]. All of these bone properties are responsible, to a different extent, for bone fracture resistance and implant stability [270]. While the direct assessment of bone quality has not been established yet due to the complicated interrelationships between the bone parameters, indirect estimation of bone quantity in clinics relies to a greater extent on the bone mineral density measurements [271, 272].

Jawbone mineral density is often assessed during preoperative imaging techniques like intraoral or panoramic radiographs [273–275] and quantitative computed tomography [276, 277]. A variation of the latter, cone beam computed tomography is emerging as the most common imaging method employed in clinical practice [278–282]. Another method for the estimation of the bone mineral density is dual-energy X-ray absorptiometry (DXA). While it is widely used in bone density assessment at the spine, hip, and/or lower arm sites, it has been used solely in experimental settings for jawbone density evaluations [273, 283].

Despite the recent advances in imaging techniques, the most widely used approach for jawbone quality assessment in clinics still follows the grading system introduced by Lekholm and Zarb [284]. According to their classification, the bone quality is graded from 1 to 4 based on the tactile sensation of the surgeon during drilling. This subjective approach is often combined with imaging techniques and/or other methods related to primary and secondary implant stability, like the torque force measurements during the implant insertion [285–288]. There is a potential need to support this grading system with less invasive and quantitative methods [289].

Laboratory methods used in the current study to assess jawbone quality. Defining other possible bone biomarkers describing bone quality would improve the current clinical methods used for bone quality assessment. Laboratory-based techniques like nanoindentation, micropillar compression, microscale computed tomography, and Raman spectroscopy are attractive experimental techniques that allow the mechanical, morphological, and compositional analysis of microscale bone volumes.

Nanoindentation is an accepted method to probe local elastic properties, where a hard and sharp tip (typically made of diamond) with a well-defined shape is driven into a flat surface of the sample while tip displacement and reaction forces are being measured. The hardness and elastic modulus of the material can be extracted following the pioneering work of Oliver

and Pharr [185]. The nanoindentation technique was first applied in dental research on hard tissues like enamel and dentin in the early 1990s [290, 291]. Twenty years later, nanoindentation was used in jawbone characterization near implant sites, and recently in quality assessment in mice jawbone [292].

Micropillar compression is a relatively new experimental technique introduced by Uchic et al. in the early 2000s [189]. The methodology is similar to nanoindentation, but instead of a sharp tip, a flat punch compresses a small volume of material with a defined geometry. This produces a uniform stress field in the tested volume so that both elastic and yield properties of the material can be extracted, giving insights into the plastic deformation behavior of the material. The first micropillar compression of bone was done in the mid-2010s [167, 179] on ovine tibial bone. More recently, this method was also applied to the human bone biopsies [84, 181]. Using a portable micro-indenter setup further allows to combine it in a multimodal approach including synchrotron radiation providing information on multiple length scales [183].

Similar to computed tomography used in clinics, microscale computed tomography (micro-CT), developed in the early 1980s [293], is commonly used to visualize and analyze sample morphology and mineral density. However, clinical CT scanners can typically resolve about 1 mm, while micro-CT systems can reach resolutions of 1-5 μm [294, 295]. This allows for studying bone mineral density and morphology at a high spatial resolution. Recently phase-contrast nanometer computed tomography was employed to image single mineralized collagen fibers at a voxel size of $(20\text{nm})^3$. The high sensitivity of the technique for light elements as found in biological materials allowed it to distinguish features down to the fibril level [296].

Raman spectroscopy is a well-known technique in bone and dental research. In principle, Raman spectroscopy allows the detection of frequency shifts of inelastically scattered light coming from the specimen exposed to a monochromatic light source, commonly a laser. These Raman shifts are assigned to characteristic chemical bonds, giving information on the material composition. Since the first report of Raman spectra of a tooth in 1974 [297], this technique was used extensively in scientific studies of enamel and dentin [298–300].

Animal models. It is common nowadays to investigate biological phenomena on animal models, due to practical, ethical, and economical reasons [301]. Animal models promote the research in bone tissue engineering and modelling [302], as well as bone metastasis [303, 304] and repair processes [14]. Pig species exhibit many anatomical and physiological similarities with humans, making them an attractive choice for preclinical experimental

tion in various medical and biomedical fields [305–307]. In particular, miniature pig species (minipigs) were specifically developed for research purposes and are now extensively used for in vivo experiments prior to translation to humans [308–310]. While keeping the resemblance to humans, minipigs have convenient body dimensions and well-controlled genetics, which facilitates the handling and maintenance of these animals in the laboratory [306, 308]. Miniature pigs were first used in dental research several decades ago [311]. The facial and oral regions of minipigs exhibit similar physiology and development as that of humans [312]. Moreover, miniature pigs possess both permanent and deciduous sets of teeth and perform both chewing and biting jaw actions, like humans [311]. All of this, together with the low purchase and maintenance costs, makes minipigs an excellent animal model for various studies in dental research [312–314]. Miniature pig models are already reported in bone regeneration [313], osseointegration [315], and bone fracture healing during implantation [316]. Nevertheless, there is a considerable knowledge gap on the multiscale morphological and mechanical properties of the miniature pigs' jawbones, which is crucial for implant studies and a direct comparison to human tissue.

Study outline. Here, we report a multimodal approach to assess jawbone quantity and quality at the microscale. For this, we used an established animal model for dental research: the miniature pig. Three minipig genotypes were examined: Yucatan, Göttingen, and Sinclair. Through the combination of laboratory-based methods, we assessed bone mineralization, morphology, and mechanical properties on the local and global average levels. Microscale computed tomography, Raman spectroscopy, and nanoindentation were employed for sample characterization at the global level, averaged over the sample area. Nanoindentation gave access to the elastic properties of the cortical jawbone, while micro-CT and Raman spectroscopy to bone morphology and mineralization. To the best of our knowledge, this is the first study where Raman spectroscopy was applied to investigate the jawbone relative mineralization. At the local level, micropillar compression was used for the first time on the compact jawbone, to extract yield and elastic bone properties, which are critical in dental research. For the first time, micropillar compression tests were carried out on laser-fabricated bone micropillars, which enables high throughput mechanical characterization. Following our previous study [161], we combined Raman spectroscopy and micropillar compression measurements in a site-matched manner to estimate the mechanical properties of bone in correlation with the local bone mineralization level, giving access to structure-property relationships at the microscale.

3.2.2 Materials and Methods

3.2.2.1 Sample preparation

Jaw samples from skeletally mature minipigs of three genotypes (Yucatan, Göttingen, and Sinclair) of age between 23 and 27 months were obtained from Institut Straumann AG (Basel, Switzerland). The samples were obtained from dental studies after their completion and stored in formalin before further preparation. In total, three animals per genotype were used (N=9). The coronal cross-section of the mandibular premolar region was dissected from the rest of the jaw with a diamond band saw under constant water irrigation (Exakt, Norderstedt, Reichert-Jung). The cortical bone region, adjacent to the inferior border of the mandible, was further sectioned from the jawbone slice. The resulting bone pieces of about 3 mm in height and 4 x 4 mm in width x depth were mechanically cleaned and dried at ambient conditions for 24 h. The pieces were then glued onto an aluminium SEM stub with a 2-component epoxy resin adhesive (Schnellfest, UHU, Germany) so that the sample top surface followed the coronal plane from the mandibular cross-section. Finally, the exposed specimen surfaces were polished with progressive grades of silicon carbide paper and finished manually on a soft cloth with a 1 μm diamond suspension followed by a 0.04 μm SiO₂ suspension.

3.2.2.2 Micromechanical characterization

Nanoindentation

Nanoindentation maps were carried out using a Hysitron Ubi-1 nanomechanical testing system equipped with a Berkovich diamond tip. Measurements were performed at room temperature and ambient pressure and humidity. Nanoindentation maps consisted of 2x3 indents with a 20 μm step size, avoiding indentions in the vicinity of the deformation zone while being placed within the zones of interest, specifically osteons. Each indentation was performed under load-control mode with 10 mN maximum load and the following segment times: 20 s loading, 30 s holding at peak-load, and 20 s unloading segment. An additional 60 s waiting time was added between each indent to reduce instrument drift. Indentation maps were located either in the osteonal, interstitial, or plexiform regions. In total 10 maps for each region of interest were collected per animal sample resulting in 120-180 indents per sample. Indentation maps were distributed across the sample surface, consequently providing information on average elastic bone properties at the whole sample level.

Micropillar fabrication via femtosecond laser ablation

A novel laser ablation protocol was developed based on femtosecond (fs) laser ablation to prepare a micropillar array on each of the bone samples [192]. Fabrication of micropillars

on the sample surface was done using a femtosecond-pulsed laser (SATSUMA HPII, Amplitudes Systemes) at 515 nm wavelength with 320-350 fs pulse duration and 3 kHz repetition frequency, with an average laser power of 12 mW. The resulting laser pulse energy and peak fluence were $3.96 \mu\text{J}$ and 5.14 J/cm^2 accordingly. The ablation was done in a unidirectional scanning mode at 15 mm/s, enabling low heat accumulation (Appendix 1). An array of 5×5 micropillars was ablated on each sample surface for further mechanical testing (figure 3.2.1). The dimensions of the micropillars were estimated from high-resolution scanning electron microscopy (HRSEM) images taken at an acceleration voltage of 1.5kV (Hitachi S-4800, Japan). On average, the pillar diameter was $24 \pm 3 \mu\text{m}$ with an aspect ratio of 2.3 ± 0.3 and a taper angle of $15^\circ \pm 2^\circ$.

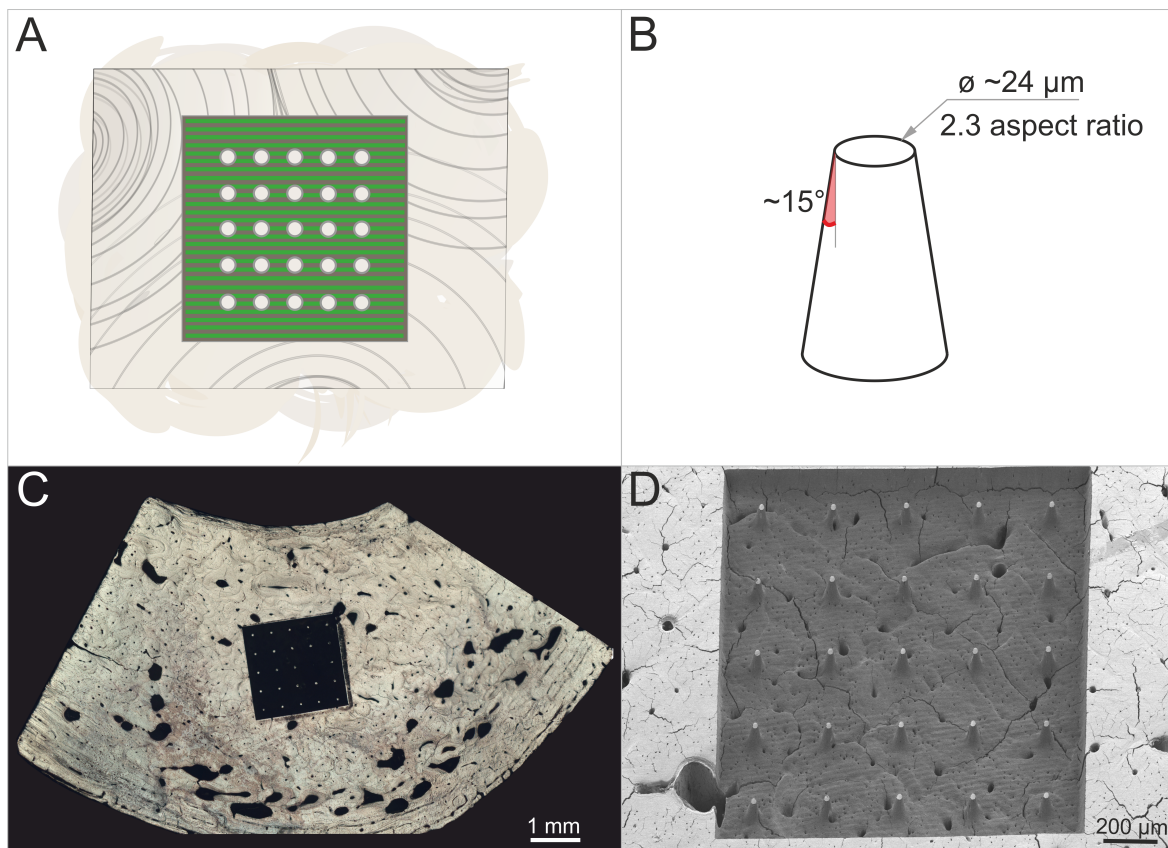


Figure 3.2.1 – Schematic of the laser ablation of bone in a unidirectional scanning mode with marked micropillar array positions (A) and the output micropillar geometry (B); optical overview image of the sample top surface with femtosecond laser ablated micropillar array (C); close-up SEM image of the micropillar array (D).

Micropillar compression

Micropillar compressions were performed using an ex-situ indenter setup developed in-house based on commercial hardware for actuation, sensing, and electronics (Alemnis AG, Switzerland) [161, 317]. Experiments were performed at ambient temperature and humidity

with a flat punch indenter tip (60 μm diameter). Samples were compressed uniaxially using a quasi-static displacement-controlled loading protocol at a strain rate of 10^{-3}s^{-1} and up to 15% of engineering strain. Two types of protocol were used: (i) monotonic and (ii) cyclic loading. The latter included repetitive segments of 750 nm loading and 250 nm partial unloading. The typical stress-strain curves for two testing protocols are presented in the graphical abstract. From both protocols, yield stress and strain were extracted, whereas from the cyclic loading protocol the elastic moduli were additionally extracted from the unloading segments, prior to the yield point. Yields stress in each stress-strain curve was computed as the stress that is needed for plastic deformation of 0.2%. On average, 20 micropillars were tested per animal sample, of which 5 were cyclically loaded.

Data analysis was done in Python v3.8 using an in-house script following the methodology of Schwiedrzik et al. [167] with the modified Sneddon approach of Zhang et al. [237] for substrate compliance corrections. The influence of the taper angle on the output mechanical properties was corrected using finite element simulations in Abaqus/CAE (Dassault Systemes Simulia Corp., Johnston, Rhode Island, USA) [318]. Compressions of two micropillar geometries were simulated: tapered, with the micropillar geometry matching the one used in the actual experiments, and ideal, where the diameter of the micropillar was constant over its length. A displacement of 10% of the micropillar height was applied from the top. A part of the substrate below the micropillar was also included in the model to account for substrate deformation. The von Mises plasticity model was used with input values based on the experimental results from a former study [161]: Young's modulus was set to $E = 27.65$ GPa, yield stress was set to $\sigma_y = 0.318$ GPa, and the Poisson's ratio to $\nu = 0.3$. The effect of the taper on the elastic modulus, yield stress, and strain was expressed with the help of taper correction coefficients, representing the ratio of the apparent yield stress estimated for the ideal geometry divided by the one of the tapered micropillar geometry. Further details on the finite element simulations can be found in Appendix 2.

3.2.2.3 Morphological and compositional analysis

Micro-CT

Microscale computed tomography (micro-CT) scans of the samples were collected using microCT 100 (SCANCO Medical AG, Switzerland). Scanning was done at 55 kVp energy, 200 μA tube current, 400×2 ms integration time, and a voxel size of 6.6 μm . Micro-CT scanner was calibrated using hydroxyapatite phantoms with known density (-15, 100, 210, 415 and 790 mg/cm^3). Following the reconstruction, image processing was done using an in-house Matlab script. The sample scans were segmented with a fixed threshold of 711.11 mg/cm^3 (averaged value of each specimen-specific threshold, automatically detected by

OTSU's method). For each sample average tissue mineral density (TMD) and bone volume ratio (BV/TV, bone volume vs. the total volume) were extracted. The main alignment of the sample pores was evaluated using an in-house Python script from an orthotropic fabric tensor with the mean surface length method as described by Hosseini et al. [319]. Consequently, the degree of anisotropy (DA) and the spatial orientation of the sample pores (out-of-plane angle) were calculated.

Raman spectroscopy

Raman spectra were acquired in ambient conditions using an upright Raman microscope (Nova Spectra, ND-MDT, Russia) equipped with a 633 nm laser. Spectra were collected through the 600 g/mm grid and 50× objective with a numerical aperture of 0.75. The resultant laser spot size was $\sim 0.5 \mu\text{m}$ in lateral and $1.6 \mu\text{m}$ in axial direction [220]. The laser power at the sample surface was $\sim 1 \text{ mW}$. For the whole-sample-level measurements, spectra were collected from interstitial (N=10) and osteonal (N=10) zones, as well as from plexiform zones (N=10) for the Göttingen samples. Raman spectra give local information on the composition, and by uniformly distributing the measurement locations over the sample surface, global information per sample could be extracted. For each cortical bone zone, 10 spectra, 60 s integration time each, were collected approximately $5 \mu\text{m}$ underneath the bulk surface, resulting in 20-30 spectra per sample. Additionally, Raman measurements were carried out on the bone micropillars. An average of three spectra, 30s integration time each, were collected approximately $5 \mu\text{m}$ underneath the pillar top, providing the local information on the mineral to matrix ratio. Spectra processing was done in Python, detailed analysis steps with corresponding figures are shown in Appendix 3. All spectra were background-subtracted and peaks of interest representing mineral and collagen content were further analyzed. The ratio of the secondary phosphate ($\nu_2\text{PO}_4$) over the amide III bands was used as an indirect estimation of the bone mineralization level [226]. Both peaks were fitted with a double Lorentzian function using a least-square scheme and the ratio of the integral areas provided the mineral to matrix ratio (Mineral/Matrix).

3.2.2.4 Statistical analysis

All statistical analysis was performed using R [320], rstatix package [321]. The Shapiro-Wilk test was used to test for the normality of variables. Significant differences between paired datasets were then tested using the Wilcoxon rank-sum test to account for the non-normally distributed data, and the significance threshold was chosen as $p < 0.05$. Results for the normally distributed datasets are reported as mean \pm SD, where SD stands for the standard deviation. Results for the non-normally distributed data are reported as median (IQR),

where IQR stands for the interquartile range, i.e. the difference between the first and third quartile. Correlation analysis was done through linear regression analysis (lmtest package).

3.2.3 Results

3.2.3.1 Whole sample level analysis

The visual analysis of the sample surfaces showed a discrepancy between observed zones of the cortical region. Similar to the human cortical bone morphology, osteonal and interstitial zones are observed on all three minipig genotypes (marked in the figure 3.2.1 insets). Moreover, circumferential lamellae are observed on the outer side of the Yucatan and Sinclair samples. A large area of the plexiform bone is observed for all Göttingen minipigs, as marked in figure 3.2.2.

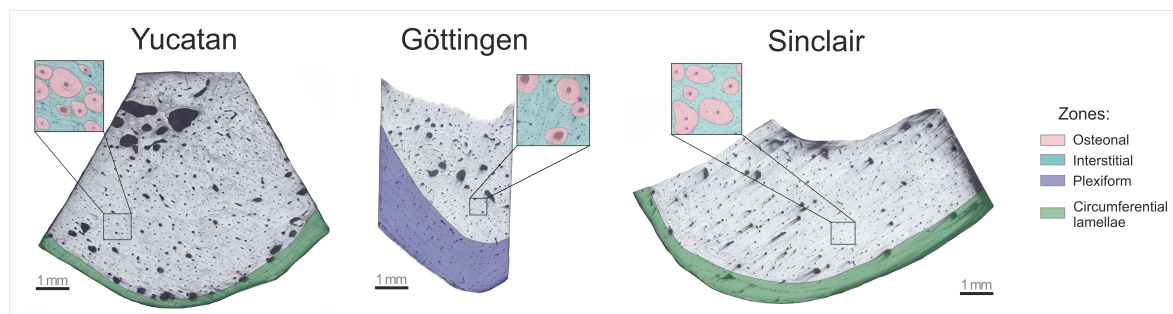


Figure 3.2.2 – Optical images of the representative samples' top surfaces of each genotype with the marked plexiform zone (indigo) and the circumferential lamellae (green), as well as the osteonal (rose-colored) and interstitial (aquamarine) zones marked in the insets.

Micro-CT data showed that Göttingen minipigs had the highest tissue mineral density of $1229 \pm 168 \text{ mg/cm}^3$ as well as the bone volume fraction of $98.1 \pm 0.5 \%$, while the Yucatan genotype demonstrated the lowest values: $1143 \pm 163 \text{ mg/cm}^3$ and $96.3 \pm 1.4\%$. Sinclair minipigs had a tissue mineral density of $1175 \pm 161 \text{ mg/cm}^3$ and a bone volume fraction of $97.8 \pm 0.7 \%$. However, no significant difference between the genotypes was found for bone morphology, mineral density, and degree of anisotropy (figure 3.2.3). Moreover, the averaged out-of-plane orientation of the pores within the sample, including the Haversian canals, was 55° with 2° variation between the samples.

A significant difference ($p \leq 0.01$) was observed in the mineral to matrix ratio between all cortical bone zones within each of the three genotypes, except the osteonal and plexiform zones of Göttingen minipig. For all three genotypes, values were higher for interstitial zones than osteonal with the highest values for the Göttingen minipigs: 0.81 (0.13) for interstitial and 0.66 (0.12) for osteonal zones, although not significantly different from the Sinclair minipigs (figure 3.2.4). Yucatan genotype showed the lowest mineral to matrix ratio (0.74

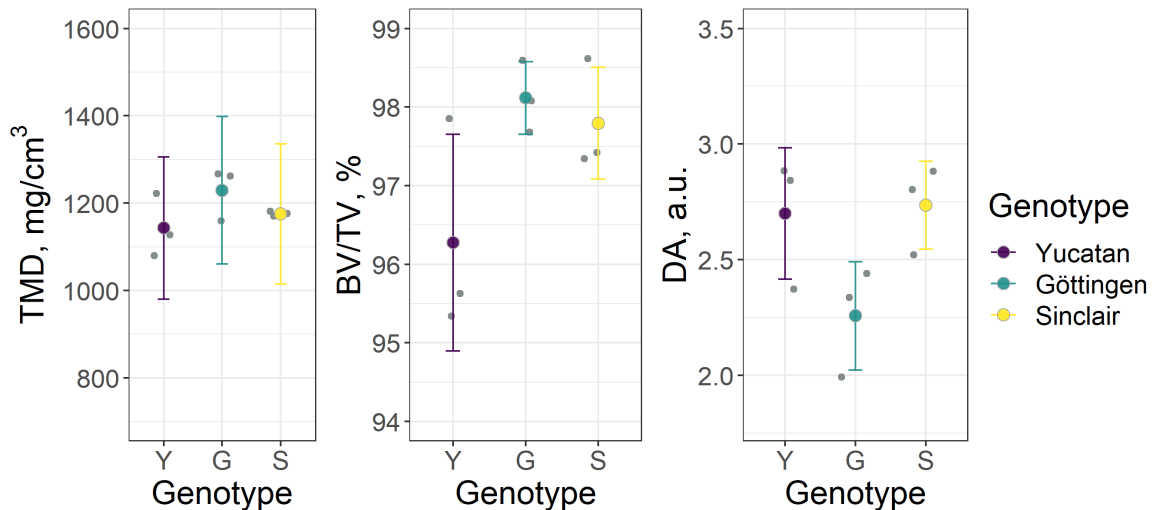


Figure 3.2.3 – Tissue Mineral Density (TMD), Bone Volume fraction (BV/TV), and Degree of Anisotropy of Haversian porosity (DA) of the cortical region of the jawbone of three minipigs genotypes.

(0.15) for interstitial and 0.57 (0.09) for osteonal zones), with a significant difference to the Göttingen minipigs for both zones. While this trend is similar to the mineral density data collected from micro-CT, a comparison between the two methods showed no significant correlation.

Indentation revealed higher elastic modulus and hardness for the interstitial zones of all genotypes compared to the osteonal and plexiform zones (figure 3.2.5). Göttingen and Sinclair samples showed a significant difference in elastic properties between the zones. Yucatan minipigs exhibited the highest variation of the mean values within the zones, however, the hardness was still significantly different between the interstitial and the osteonal zones.

Correlation analysis was performed to check the dependence between the average bone elastic properties measured via nanoindentation and average bone mineralization, as assessed through two techniques: micro-CT (TMD) and Raman spectroscopy (Mineral/Matrix ratio). No significant dependence was observed between the tissue mineral density and both elastic modulus and hardness. Moreover, no correlation was detected between the elastic modulus and the mineral to matrix ratio, while a significant positive trend was found between the hardness and the mineral to matrix ratio for pooled cortical bone zones (figure 3.2.6).

3.2.3.2 Site-matched micropillar compression and Raman spectroscopy

At the microscale level, significantly different mineralization was observed between the three genotypes, as assessed via the mineral to matrix Raman band ratio (figure 3.2.7). Göttingen and Yucatan genotypes exhibit the highest and the lowest mineral/matrix ratio accordingly. Observed alterations of bone mineralization at the microscale match the mineral/matrix ratio

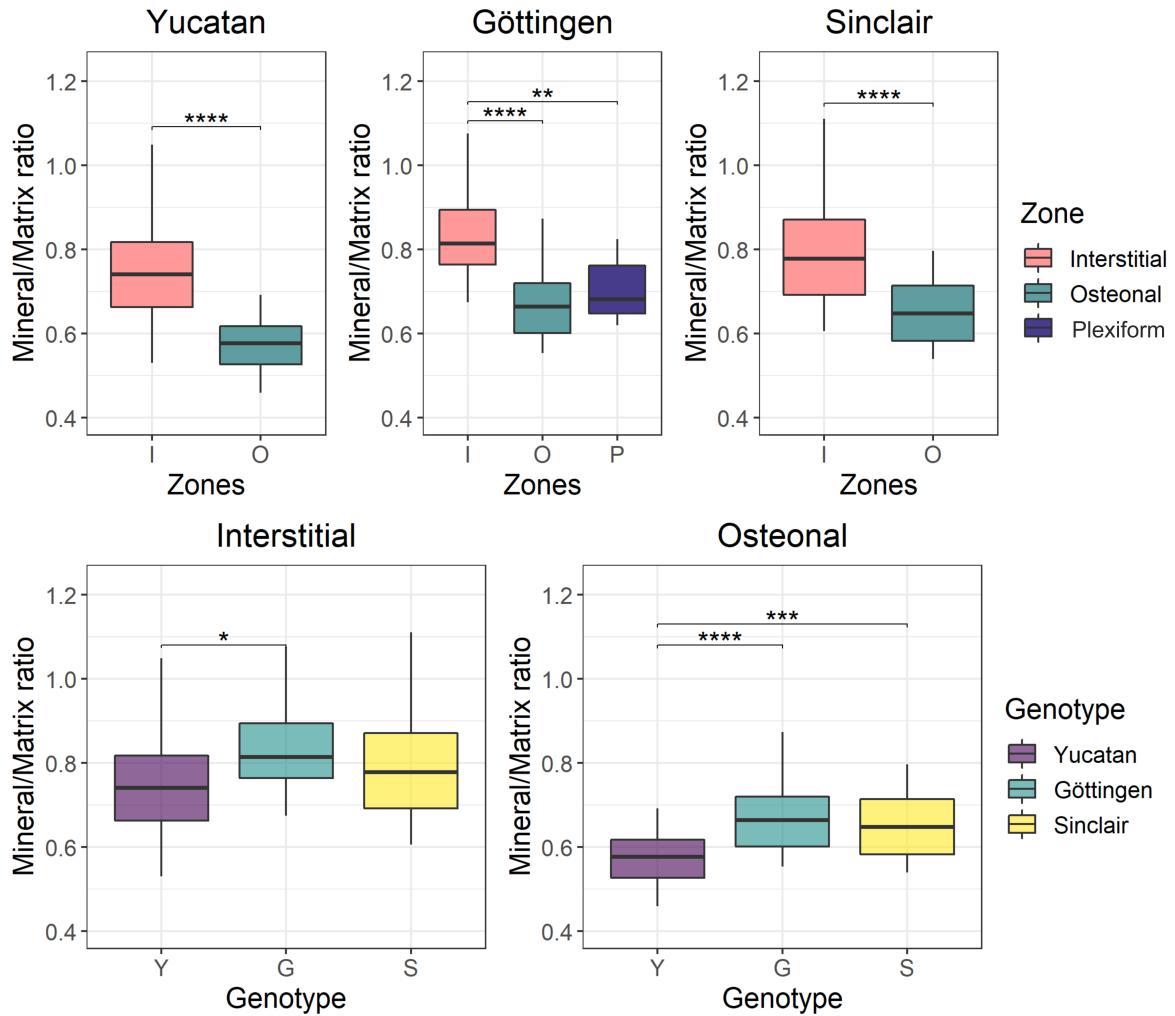


Figure 3.2.4 – Mineral to matrix ratios as estimated at interstitial, osteonal, and plexiform zones of three minipigs genotypes. Statistical significance asterisks: * – $p \leq 0.05$, ** – $p \leq 0.01$, *** – $p \leq 0.001$, **** – $p \leq 0.0001$.

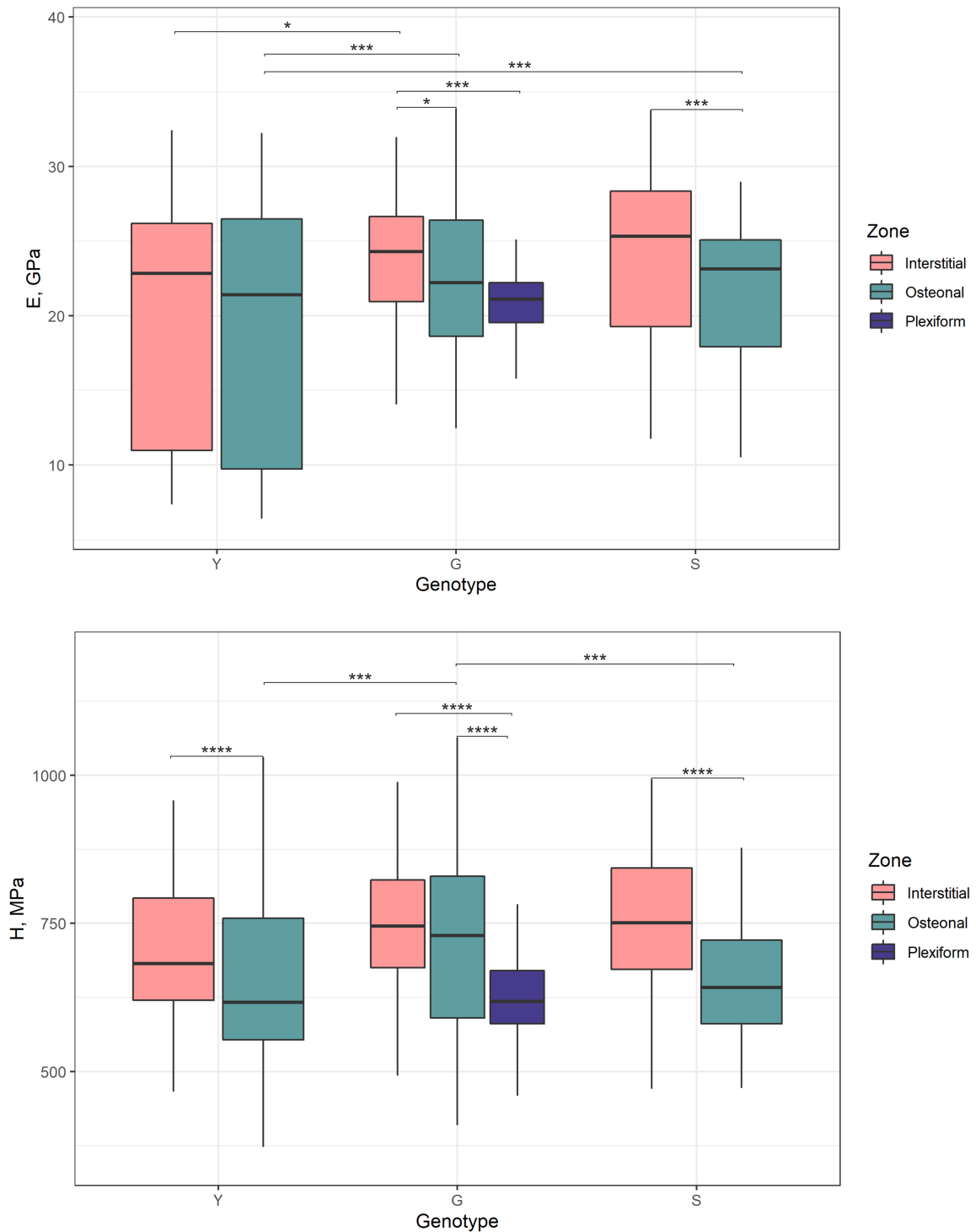


Figure 3.2.5 – Young modulus (E) and hardness (H) as estimated at interstitial, osteonal, and plexiform zones of three minipig genotypes: Yucatan, Göttingen, Sinclair. Statistical significance asterisks: * – $p \leq 0.05$, ** – $p \leq 0.01$, *** – $p \leq 0.001$, **** – $p \leq 0.0001$.

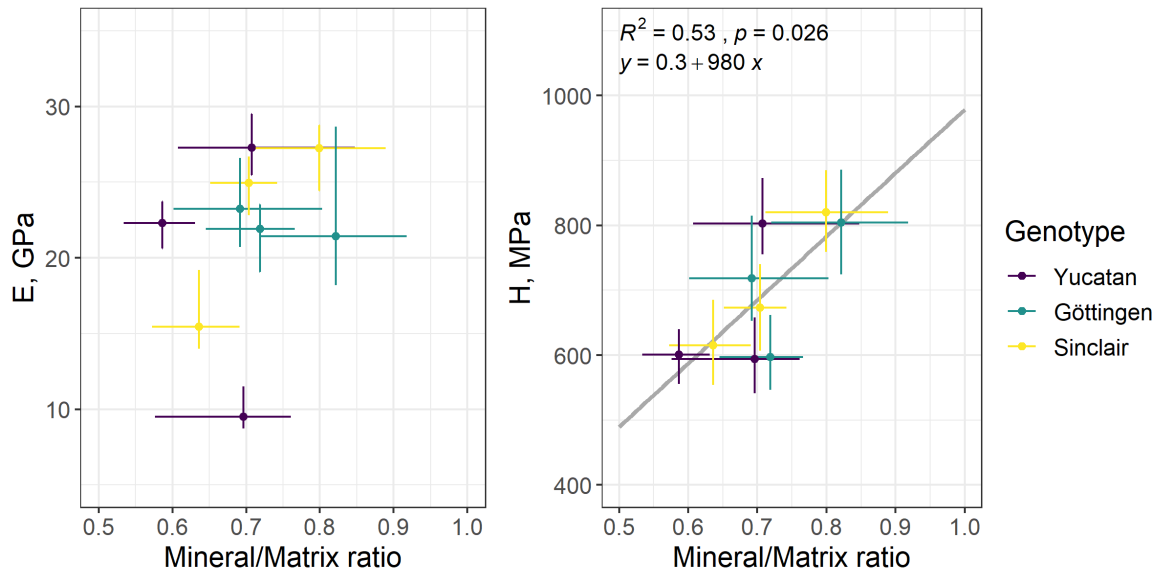


Figure 3.2.6 – Bone Young modulus (E) and hardness (H) versus bone mineral to matrix ratio.

variations at the whole sample level (figure 3.2.4).

Micropillar compression revealed the highest mean value of the Young's modulus for the Sinclair minipigs, although only the difference with the Yucatan minipigs was significant due to the scatter of the Young's modulus data of the Sinclair minipigs. No significant difference was observed between the Young's modulus mean values of the Yucatan and Göttingen genotypes. The mean yield stress values follow the genotype mineralization, with the Göttingen and Yucatan minipigs demonstrating the highest and the lowest values, respectively. However, the yield strain mean values were not significantly different between the Göttingen and Sinclair genotypes, but both were significantly lower than the ones of the Yucatan ($p \leq 0.0001$).

Site-matched micropillar compression and Raman spectra collection allowed us to assess the relationship between the genotype relative mineralization and the local mechanical properties. The correlative analysis showed no significant dependence between the local elastic and the yield properties versus the mineral to matrix ratio (figure 3.2.8).

Three distinct micropillar failure modes were observed after compression. Axial cracking, where the fracture followed the main micropillar axis (figure 3.2.9 A), was the most common mode followed by shear (figure 3.2.9 C) and mushrooming (figure 3.2.9 B), where the major deformation occurred at the micropillar top. The correlative analysis showed no dependence between the failure modes and the mechanical properties or relative mineralization.

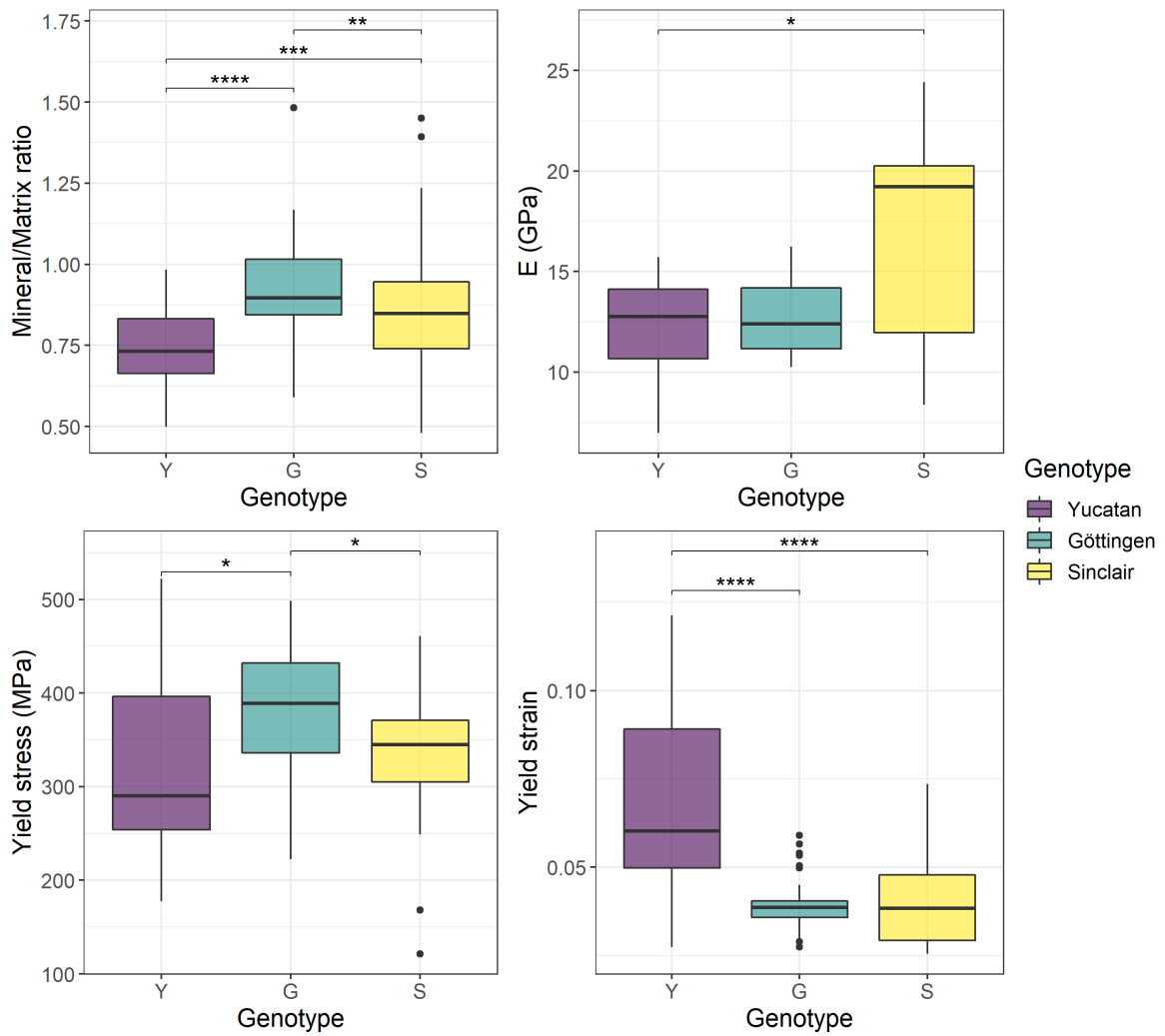


Figure 3.2.7 – Microscale bone properties of three minipigs genotypes. Statistical significance asterisks: * – $p \leq 0.05$, ** – $p \leq 0.01$, *** – $p \leq 0.001$, **** – $p \leq 0.0001$.

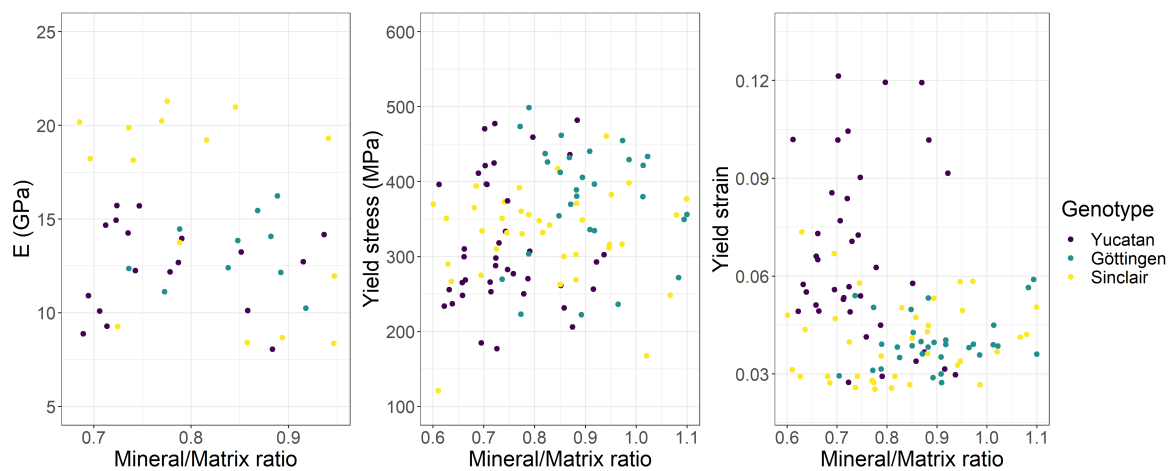


Figure 3.2.8 – Elastic modulus and yield properties versus the mineral to matrix ratio as assessed for three minipig genotypes.

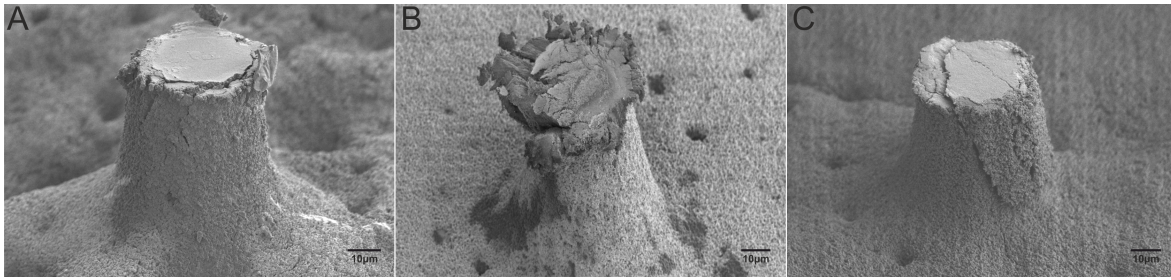


Figure 3.2.9 – Observed fracture modes of compressed micropillars. A – axial cracking, B – mushrooming, C – shear.

3.2.4 Discussion

This study presented the framework for the multimodal characterization of the jawbone in an animal model that could be further extended to humans. It is the first report on the jawbone properties at the microscale level for the three minipig genotypes: Yucatan, Göttingen, and Sinclair, all commonly used in dental research due to their anatomical similarity to humans.

3.2.4.1 Whole sample level analysis

At the whole sample level measurements, the micro-CT technique was used to shed light on potential differences between the genotypes both in mineralization and bone volume fraction. No statistically significant differences were observed between the genotypes, most likely due to the very low pore volume fraction and variation in zonal properties within the samples. Testing a larger number of regions of interest per mandibular bone would improve the comparison between the genotype. It is of high interest to investigate several sections within each mandibular in the future, to account for the inherent variations of compositional and, consequently, mechanical properties within the whole bone volume. Surprisingly, tissue mineral density, extracted from the micro-CT, did not correlate with the Raman mineral to matrix ratio as reported in the study of Indermaur et al. [84], which might be rationalized by the relatively low number of samples (N=3 per genotype) together with the small range of mineral to matrix ratio.

Since the jawbone has irregular morphology with highly-porous alveolar and dense compact bone regions, the available data on the jawbone mineralization could not be compared to the measurements on the compact mandibular bone from the current study. However, investigated bone regions exhibited clear zonal morphology with low porosity, similar to that of other types of human cortical bone. Indeed, the Raman mineral to matrix ratio of examined minipig jaws was within the range of the reported values for the human femoral midshafts: 0.57-0.81 for the minipig jaws examined in the current study and 0.3-1.5 for the human femur [226]. Moreover, the TMD values of investigated minipig jaws were at the lower border of the reported TMD range for the human femoral cortex, measured at a similar voxel size:

1128-1260 mg/cm³ for the minipigs and 1200-1600 mg/cm³ for the human femur [76]. Since only the cortical part from the inferior jawbone border was examined, the bone volume fraction was high for all tested minipigs jaws samples, with only 2-4% porosity. These values are close to those of the other animal species (5-6%) [322, 323].

A clear difference between the interstitial and osteonal zones was visible for both Raman and nanoindentation measurements. This is similar to what is usually observed in the cortical parts of other skeletal bones, with the interstitial zone exhibiting higher mineralization and hardness [176, 324]. Interestingly, a significant difference between the genotypes was more pronounced between the osteonal regions of cortical bone. This might be a result of constant jawbone turnover, during which the interstitial zones rapidly reach the saturated mineralization levels [325], which are comparable between the three genotypes.

An increase in mineral to matrix ratio accounted for the jawbone hardness increase but no dependence was observed for the elastic moduli. Since elastic modulus is more sensitive to the alterations in the underlying sample morphology, other factors like structural anisotropy and microporosity may have a comparable influence on the elastic properties thereby concealing a possible correlation with mineral to matrix ratio. Moreover, the large variations of the elastic modulus values within the Yucatan genotype might have faded the possible correlation between the elastic modulus and the relative mineralization.

3.2.4.2 Site-matched micropillar compression and Raman spectroscopy

To date, microscale compression experiments on bone were solely performed on focused ion beam (FIB) milled micropillars [84, 161, 167, 179, 183, 317]. In the current study, bone micropillars were fabricated using ultrashort pulsed laser ablation, drastically decreasing the time costs for micromachining and simultaneously enabling high throughput analysis. However, we had to compromise the output micropillar geometry: the micropillars were approximately 5 times bigger in comparison to previous studies on micropillar compression. Moreover, laser-fabricated micropillars had a taper, which affected the stress distribution and hence also the measured apparent yield point of the compression experiments. A possible remedy for the pillar taper would be additional FIB milling atop a fabricated pillar, similarly to the study of Groetsch et al. [183], however, this approach would be still time-consuming (~1h per pillar). We, therefore, kept the laser-ablated micropillars with geometrical flaws and accounted for the deviation from the ideal cylindrical shape by finite-element simulations. This way we were able to keep the high throughput of microscale compression experiments, meanwhile correcting the output mechanical properties for the micropillar taper. Since laser ablation was done at the normal atmospheric pressure and relative humidity, we

reduced the crack formation at the sample surface, which is commonly observed after high vacuum exposure during FIB milling. Another advantage of the laser-ablated micropillars is the possibility to carry the site-matched Raman spectra collection. This was not possible earlier with the FIB milled micropillars due to inevitable sample sputtering with a conductive metal, which hinders the Raman signal.

From the micropillar measurements, we were able to detect significant differences between the genotypes' mineralization and yield properties. While local measurements of relative mineralization followed those at the global level, the differences between genotypes were more pronounced at the local level. Surprisingly, neither elastic nor yield mechanical properties of jawbone micropillars showed a correlation with the bone relative mineralization. Such correlation was previously observed by Indermaur et al. [84] in human transilliac osteonal bone. However, the micropillars dimensions used in the current study were five times bigger and thus contained a higher number of lacunae inclusions and lamellar interfaces. As was shown by Casari et al. [213], the increase in the size of the microscale specimen leads to lower strength rationalized by the higher probability of finding flaws in a critical orientation. The dominant failure mode of micropillars in our study was axial cracking. As was demonstrated in other studies on micropillar compression of the ovine and bovine bone [161,317], such failure mode is most likely driven by the axial alignment of the mineralized collagen fibrils.

Overall, we observe large variations of mechanical properties within the minipig genotypes, both for the nanoindentation and micropillar compression measurements. This is likely caused by the inherent structural variations at different locations in the jaw as well as between the animals of the same genotype. Besides, the mineralized collagen fibrils orientation within the tested local volumes was assumed to match the overall orientation of Haversian canals within the sample volume. For future experiments, the quantitative polarized Raman method can be applied for the simultaneous mineralized collagen fibrils orientation estimation and compositional characterization [161].

3.2.4.3 Study limitations

The current study was carried out on the premolar region of the mandible, opposite to the teeth growth. It is, however, of high interest to investigate the alveolar bone, due to its relevant location for implant placement and other dental manipulations. The samples used in the current work were collected after the completion of other dental studies, for which the alveolar bone was already extracted. Yet, we hypothesize that the mandibular part of the jaw opposite to the teeth growth may be of interest for future studies using CT imaging because

it is not affected by the intensity of artifacts coming from metallic implants, crowns, or fillings [326, 327]. Nevertheless, the proposed framework for the bone quality assessment can be applied to the alveolar region of bone in the future.

All samples were stored in formalin before any preparation steps. It is accepted that fresh bones represent the *in vivo* conditions better than formalin-fixed ones. Nevertheless, formalin-fixed specimens are frequently used in biomechanical testing due to the lack of fresh bones. Chemical fixation with formalin affects the organic fraction of the bone, in particular, the collagen cross-links [328, 329]. In the current study, we abstain from any direct analysis of the organic bone components, but future analysis of the fresh bone samples following the proposed framework can be done through Raman spectroscopy. As was shown in the study of K. J. Burkhart et al., formalin-fixed human diaphyseal bone exhibit higher stiffness (about 14% after 6 weeks of conservation) but no differences in bone mineral density values [330]. Similarly, S.J. Edmondston and colleagues stated that formalin fixation may result in a slight increase in compressive strength but this does not appear to be associated with a systematic change in mineral density [331]. Considering that earlier reported mechanical experiments were performed at the macroscale, we expect a higher effect of formalin fixation at the microscale mechanical properties of mandibular bone. However, the sample storage and preparation steps were consistent between the samples of all genotypes, allowing us to detect the differences between the inherent genotypes' properties.

3.2.5 Conclusion

We report the jawbone's mechanical and morphological properties together with relative mineralization at the microscale. Three minipig genotypes were examined: Yucatan, Göttingen, and Sinclair, all commonly used in preclinical dental research. Raman spectroscopy proved to be a perspective method for relative mineralization estimation, highlighting the differences between the mineral to matrix ratios of the minipig genotypes. A novel laser-ablation protocol for micropillar fabrication allowed a high throughput analysis of the microscale compressive properties of the jawbone. Site-matched micropillar compression and Raman spectroscopy then gave access to the bone structure-property relationships. Observed variations in the output mechanical parameters, both at the local and averaged global levels, may be attributed to the structural and compositional heterogeneity of the samples. Measuring local compositional and mechanical properties in a site-matched fashion can shed light on structure-property relationships of bone at the microscale. However, to extend the analysis, mineralized collagen fibril orientation and structural defects like hidden osteocytes and microvascular channels need to be taken into account explicitly in the future. Overall,

the methods used at the whole sample level could be potentially correlated to the medical tools used to assess jawbone toughness and morphology in clinics. At the same time, the site-matched characterization methods can be applied to specify the local mechanical and mineralization properties of the jawbone.

Conflict of interest statement

The authors declare no competing financial interests.

Acknowledgment

This work is funded by the Special Focus Area Personalized Health and Related Technologies (SFA PHRT) iDoc Project 2017-304 (TK) and Swiss National Science Foundation (SNSF) Ambizione grant no. 174192 (CP and JS) and SNSF grant no. 165510 (MI). The authors would like to thank J. Hofstetter, B. Pippenger, and R. Wagner for the helpful discussions, and P. Bühlmann for statistical advice.

Author contribution

The initial study conceptualization was done by TK, JS, and BB. The samples were provided by Institut Straumann AG. Sample preparation, nanoindentation, and Raman spectroscopy measurements with the consequent data curation were done by TK. Laser ablation of bone micropillars was done by TK, SR, and BN. Micro-CT measurements and analysis were done by TK and MI. Micropillar compression tests and data curation were done by TK and AG. FEM for the micropillar taper correction was done by CP. The final data analysis and interpretation were performed by TK in cooperation with JS, AG, and PZ. The original draft was written by TK, with support from AG and JS. The final manuscript version was revised by all authors.

Chapter 4

High-throughput laboratory analysis of the bone quality in humans

In this chapter, previously developed multimodal bone characterization methods are applied to human bone biopsy specimens. This study is based on the following manuscript:

Tatiana Kochetkova, Markus S. Hanke, Michael Indermaur, Alexander Groetsch, Stefan Remund, Beat Neuenschwander, Johann Michler, Klaus A. Siebenrock, Philippe Zysset, Jakob Schwiedrzik; *"Comparing microscale compact bone properties of patients who underwent hip arthroplasty: influence of age and gender"* (In preparation) [§]

[§]As of 25 September 2023, the revised version of this manuscript was accepted in the Bone journal: T. Kochetkova, M.S. Hanke, M. Indermaur, A. Groetsch, S. Remund, B. Neuenschwander, J. Michler, K.A. Siebenrock, P. Zysset, J. Schwiedrzik "Composition and micromechanical properties of the femoral neck compact bone in relation to patient age, sex and hip fracture occurrence" Bone, 177, 116920, 2023

4.1 Comparing microscale compact bone properties of patients who underwent hip arthroplasty: influence of age and gender† §

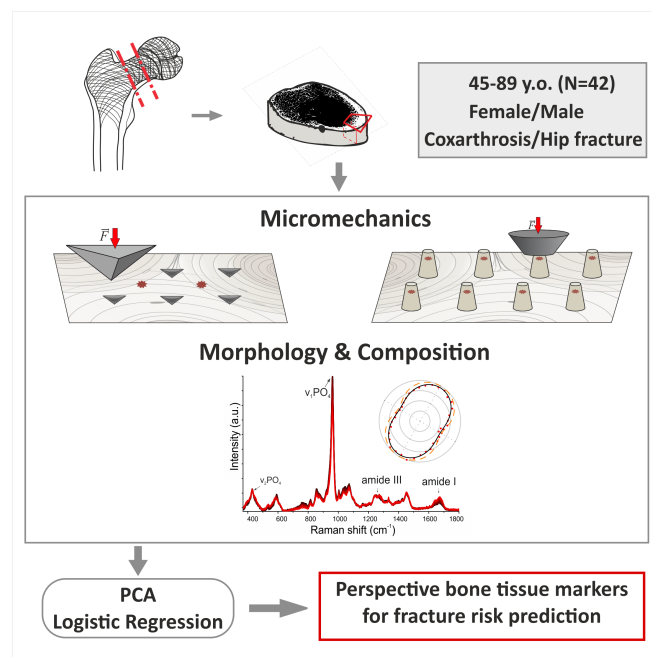
Tatiana Kochetkova¹, Markus S. Hanke², Michael Indermaur³, Alexander Groetsch¹, Stefan Remund⁴, Beat Neuenschwander³, Johann Michler¹, Klaus A. Siebenrock², Philippe Zysset³, Jakob Schwiedrzik¹

¹*Empa, Swiss Federal Laboratories for Materials Science and Technology, Laboratory for Mechanics of Materials and Nanostructures, Thun, Switzerland*

²*Department of Orthopedic Surgery, Inselspital, University of Bern, Switzerland*

³*ARTORG Center for Biomedical Engineering Research, University of Bern, Switzerland*

⁴*Institute for Applied Laser, Photonics and Surface technologies (ALPS), Bern University of Applied Sciences, Burgdorf, Switzerland*



*Corresponding Authors: tatiana.kochetkova@empa.ch; jakob.schwiedrzik@empa.ch

§T. Kochetkova, M.S. Hanke, M. Indermaur, A. Groetsch, S. Remund, B. Neuenschwander, J. Michler, K.A. Siebenrock, P. Zysset, J. Schwiedrzik "Comparing microscale compact bone properties of patients who underwent hip arthroplasty: influence of age and gender" (In preparation)

Contribution: I performed the human bone sample preparations, experimental measurements: micro-CT, nanoindentation, qPRS, micropillar compression. Carried out the statistical data analysis involving basic machine learning algorithms, final data visualization, and wrote the manuscript with the feedback of all the co-authors.

Abstract

Metabolic bone diseases like osteoporosis lead to increased bone fragility and consequent implications for the patient lifestyle and health expenses. In the present aging society, fragility fractures pose significant health and economic burden. Current clinical methods to assess bone health status fully or to a great extent depend on bone mineral density (BMD) measurements. However, these methods bear considerable errors in predicting bone strength and are often only carried out after the occurrence of the fracture. This study aims at assessing bone parameters other than BMD, which can potentially improve the current fracture risk prediction approaches.

Femoral neck samples from 42 patients who underwent hip arthroplasty were collected together with anonymous clinical information about age, gender, and primary diagnosis (coxarthrosis or hip fracture). The femoral neck cortex from the inferomedial region was analyzed *ex vivo* in a site-matched manner using the combination of the micromechanical testing techniques (nanoindentation, micropillar compression) together with micro-CT and the recently developed quantitative polarized Raman spectroscopy method for both morphological and compositional characterization.

All of the investigated bone properties were found to be independent of the patient's gender and diagnosis. Mechanical properties as well as the sample-level mineral density were nearly constant over age. Only compositional properties demonstrate dependence on the patient age: the mineral to matrix ratio was found to decline with age ($p=0.02$, $R^2 = 0.13$, 2.6% per decade), while the amide I sub-peak ratio $I_{\sim 1660} / I_{\sim 1683}$ increases ($p=0.04$, $R^2 = 0.11$, 1.5% per decade). A clear zonal dependence between interstitial and osteonal cortical zones was observed for compositional and elastic bone properties ($p<0.0001$). Site-matched microscale analysis confirmed that all investigated mechanical properties except yield strain demonstrate a positive correlation with the mineral fraction of bone.

Logistic regression classification was further applied to the final dataset of measured bone properties with the patient's clinical information. The analysis showed that indentation hardness, mineral to matrix ratio and micropillar yield stress are the most relevant parameters for bone fracture risk prediction. The presented data and analysis approaches may be used in the future to improve the prediction of fracture risk in the elderly. What is more, this knowledge may help to form a better understanding of the mechanisms through which bone tissue is affected by aging.

Keywords: Hip fracture, coxarthrosis, aging, nanoindentation, quantitative Polarized Raman spectroscopy, femtosecond laser ablation, micropillar compression, logistic regression.

4.1.1 Introduction

Bone fragility poses a significant socioeconomic burden on modern societies worldwide. With increased longevity, bone fractures are bound to increase in number. According to the International Osteoporosis Foundation, fragility fractures in Europe are projected to increase by 23%: from 2.7 million in 2017 to 3.3 million in 2030 [4]. Accordingly, the resulting annual fracture-related costs are expected to increase by 27%. Accounting for much of the health care expenditures and mortality, hip and vertebral fractures are the two most serious types [4, 332].

Fragility fractures result from low-energy trauma, arising from the reduced load-bearing capacity of bone. Such fractures are considered the main consequence of osteoporosis [333, 334] – a skeletal disorder characterized by low bone density and structural deterioration of the bone tissue [2, 4, 194, 335, 336]. Osteoporosis is referred to as a "silent disease" since it is often left undertreated and undetected until it manifests in the form of fracture [337, 338].

Bone strength depends on both bone quantity and quality. The first is also known as the bone mass or bone mineral density (BMD) and it is the most common predictor for clinical fracture risk assessment [339]. Current clinical methods to assess bone health status fully or to a great extent depend on BMD measurements. However, BMD can only act as a surrogate of bone strength, and methods to assess BMD are usually carried out only after the occurrence of the bone fracture [340]. On the other hand, evidence is emerging suggesting a significant influence of tissue quality on whole bone strength [70–72]. Bone quality is a cumulative term that includes various parameters like metabolism, composition and microarchitecture excluding BMD, that contribute to the overall fracture resistance [268, 341–343]. Most of the recent research on bone quality was carried out using laboratory-based methods, which allow precise analysis of the hierarchical structure and its constituents.

Bone is a fascinating biological material, able to achieve superior strength and fracture resistance characteristics beyond its individual constituents. At the lowest level, bone is made of organic and mineral phases (mainly of collagen type I and hydroxyapatite crystals) with water inclusions. Both mineral and organic bone constituents contribute to the mechanical properties of bone tissue [239, 344]. The mineral part of bone largely determines its stiffness [22], while the collagen part together with bound water and non-collagenous proteins are primarily responsible for bone toughness, i.e. the ability of bone to dissipate energy during failure [61, 345]. Besides the influence of the individual bone components, bone possesses a unique hierarchical arrangement, which contributes drastically to its outstanding mechanical and morphological properties [124, 346, 347].

Although more and more parameters linked to bone quality are investigated, to date there is no universally accepted bone quality characteristic that can be used to predict the risk of fragility fracture. Accordingly, the aim of the current study was (i) to assess both bone quantity and quality at the femoral neck sites of the patients who underwent a hip arthroplasty and (ii) to test which of the investigated bone properties may be the most relevant for fracture prediction.

4.1.2 Materials and methods

4.1.2.1 Sample preparation

Human femoral neck slices were collected during total hip arthroplasty at the University Hospital of Bern and Tiefenau Hospital. A double osteotomy was done to extract a femoral neck slice of about 10 mm thickness. After extraction, samples were rinsed with Ringer's solution, dab dried, and stored in the freezer at -20°C . The collection of samples together with the corresponding patient information was done following the Ethical approval 2018-01815 of the Kantonale Ethikkommission Bern. Patient information in pseudonymized form was securely stored in the SharePoint server of the University Hospital of Bern. In total, 59 femoral necks were collected, of which 42 had intact inferomedial regions and therefore were suitable for the current study.

A schematic of the sample preparation is shown in figure 4.1.1. Pieces of bone cortex from the inferomedial part of the femoral necks were cut manually with a hand saw. The extracted bone pieces of about 3-10 mm in height and 5x5 mm width x depth were mechanically cleaned with a scalpel and ultrasonic cleaner. Samples were then embedded in 10% phosphate-buffered formalin solution at room temperature for at least 2 days, dehydrated with increasing ethanol concentrations (70-100%), followed up by xylol and methylmethacrylate+dibutylphtalate (80%+20%) solutions in the course of 7-10 days. Finally, samples were embedded in MMA (80% methylmethacrylate + 20% dibutylphtalate + 1% perkadox) and left for polymerization at room temperature for at least 2 days.

The upper part of the embedded bone piece, closer to the femoral shaft, was further sectioned with a diamond-coated saw. The resulting bone pieces of about 2 mm in height and $5 \times 5 \text{ mm}^2$ area were then fixed onto an aluminum SEM stub with a 2-component epoxy resin adhesive (Schnellfest, UHU, Germany). Finally, the exposed specimen surfaces were ultra-milled (Polycut E, Reichert-Jung, Germany) and consequently polished with 1000 grid silicon carbide and paper cloth with $0.3 \mu\text{m Al}_2\text{O}_3$ lubricant.

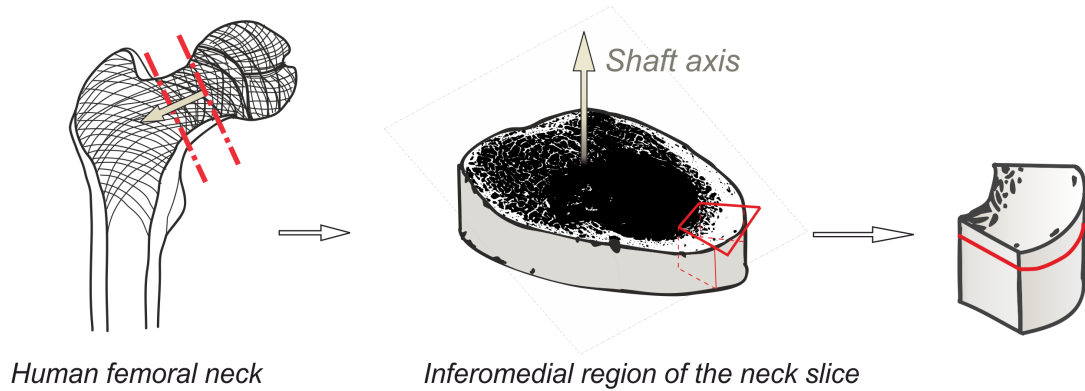


Figure 4.1.1 – Bone sample extraction and orientation schematic.

4.1.2.2 Micromechanical characterization

Nanoindentation

Indentation maps were performed using a Zwick Roell nanoindenter system (ZHN Nanoindenter, ZwickRoell GmbH & Co. KG, Ulm, Germany), equipped with a Berkovich diamond tip. In total, 20 bone structural units (BSU) per patient, distributed across the sample surface were measured (figure 4.1.2), of which 10 were within osteonal and 10 in the neighboring interstitial regions. In each BSU, a 2x3 indentation map was carried out. For each indent, a trapezoidal load control protocol was used [167] consisting of a loading segment at a rate of 1.5 mN/s, reaching up to 15 mN maximum force with about 1-1.2 μm penetration depth, holding for 5 s, and unloading at 3.75 mN/s. As output, hardness and elastic modulus were calculated following the Oliver-Pharr method [185] with an assumed Poisson ratio of 0.3. Measurements were performed at room temperature and ambient pressure and humidity. Indentation maps were distributed across the sample surface, consequently providing information on average elastic modulus and hardness at the whole sample level.

Micropillar compression

Regular arrays of bone micropillars were prepared on the sample surfaces following a previously developed femtosecond (fs) laser ablation protocol [193]. Micropillar fabrication was done using a 515 nm laser (SATSUMA HPII, Amplitudes Systemes) with 320-350 fs pulse duration, 3 kHz repetition frequency and 12 mW average laser power. Since each sample presented a unique cortex morphology, different combinations of micropillar arrays were fabricated across the sample surface: 5x9, 5x5, 4x5, 3x5, 3x10, 5x6 and 3x3. As a result, each sample contained 45 to 65 bone micropillars, of which less than 8% were a priori defective (fabricated fully or partially on Haversian canals or other pores). Micropillar geometry was assessed from each array on each sample via an optical profilometer (S Neox, Sensofar Metrology, Spain). On average, micropillars were $62 \pm 2 \mu\text{m}$ high with a $26 \pm 1 \mu\text{m}$ top diameter and $14 \pm 2^\circ$ taper (N=1441).

Micropillar compression experiments were performed using an ex-situ indenter setup developed in-house based on commercial hardware for actuation, sensing, and electronics (Alemnis AG, Switzerland) [161,317]. Experiments were performed at ambient temperature and humidity with a flat punch indenter tip ($60\ \mu\text{m}$ diameter). Samples were compressed uniaxially using a quasi-static displacement-controlled loading protocol at a strain rate of 10^{-3}s^{-1} and up to 13% of engineering strain. As output, yield stress and strain values were extracted at 0.2% plastic deformation. Per each sample, 30 to 50 micropillars were tested (figure 4.1.2).

Data analysis was done in Python v3.8 [221] using an in-house script following the methodology of Schwiedrzik et al. [167] with the modified Sneddon approach of Zhang et al. [237] for substrate compliance corrections. The influence of the taper angle on the output mechanical properties was corrected using finite element simulations in Abaqus/CAE (Dassault Systemes Simulia Corp., Johnston, Rhode Island, USA) [318] following our previous work [193].

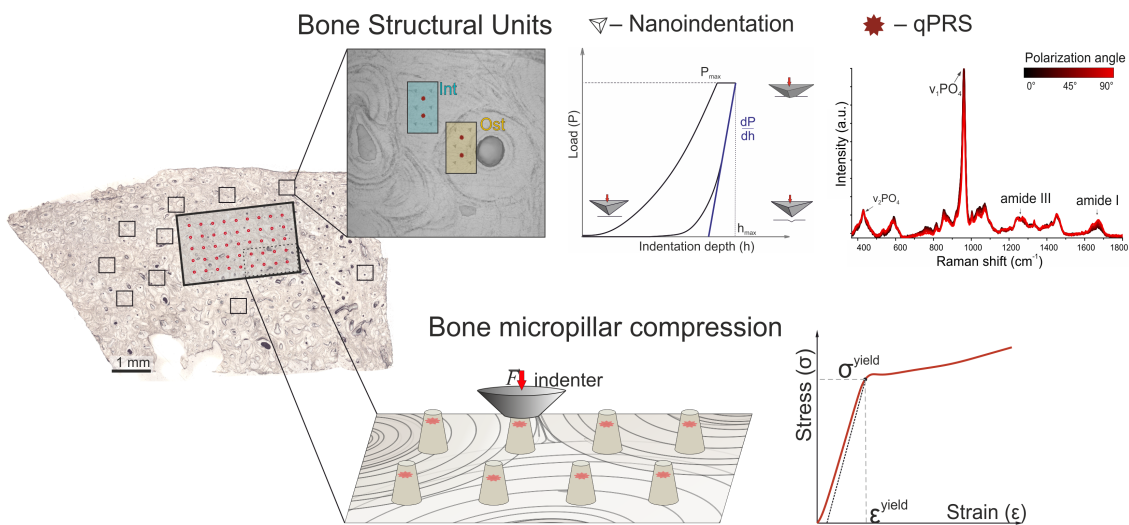


Figure 4.1.2 – Microscale analysis methods and their schematic location on the sample surface. The whole sample volume was scanned with micro-CT. Structural unit analysis on interstitial (Int) and osteonal (Ost) zones included nanoindentation maps and quantitative polarized Raman spectroscopy (qPRS) measurements on the mapping area. A typical indentation curve together with polarized Raman spectra are shown at the top right. A schematic of the bone micropillar compression is shown at the bottom. Compression tests were site-matched with qPRS measurements on each pillar. A typical stress-strain curve from the micropillar compression experiment is shown at the bottom right.

4.1.2.3 Morphological and compositional analysis

Micro-CT

Hydroxyapatite-calibrated micro-computed tomography (micro-CT) scans of the samples were collected (microCT 100, SCANCO Medical AG, Switzerland). Scanning was done at 55 kVp energy, 200 μ A tube current, 300 ms integration time, with a resulting voxel size of 17.2 μ m. Following the reconstruction, image processing was done using in-house Matlab code (Matlab R2019a). A schematic of the image processing steps is shown in figure A3.1. For each sample, cortical bone mineral density (BMD), tissue mineral density (TMD) and bone volume ratio (BV/TV, bone volume vs. the total volume) were extracted.

Quantitative polarized Raman spectroscopy (qPRS)

Raman spectra were acquired in ambient conditions via an upright Raman microscope (Nova Spectra, ND-MDT, Russia) with a 633 nm laser. The linear polarization of the exciting laser was adjusted with a motorized $\lambda/2$ plate. No analyzer plate was included in the light path after the sample. Spectra were collected using a 600 g/mm grating and 50 \times objective with a numerical aperture of 0.55. The resultant laser spot size was ~ 0.7 μ m in the lateral and 4.2 μ m in the axial direction [220]. The laser power at the sample surface was ~ 7 mW.

Two sets of measurements were collected for each sample. First, two sets of polarized spectra were acquired after the nanoindentation measurements from bone structural units within interstitial and osteonal regions, matching the location of the indentation maps (Figure 2). The second set of measurements was done on the bone micropillars before compression tests, approximately 5 μ m underneath the pillar top surface. Each set of polarized Raman measurements consisted of 10 spectra, collected at increasing angles of polarizer from 0 to 180° with a 20° angular step. Following the recently validated qPRS method [161], the local orientation of the mineralized collagen fibrils (MCF) was estimated. Local in- and out-of-plane MCF angles were calculated and used for the subsequent correlation analysis. Moreover, traditional information on the bone microscale composition was quantified through the peak band ratios.

The peaks of interest were chosen based on the principal component analysis [348]. For this, all spectra were background subtracted and averaged spectra from all samples were analyzed. The peaks with the highest intensities variation were detected as elements from the first eigenvector after the dimensionality reduction. The peaks with the highest variation included primary and secondary phosphate ($\nu_1 PO_4$, $\nu_2 PO_4$), proteoglycans, and collagen bands (amide I and amide III). Accordingly, the compositional parameters presented in Table 4.1.1 were extracted from the Raman spectra. The corresponding peaks were background subtracted and fit with a linear combination of Lorentzian functions, as described

Table 4.1.1 – Bone compositional and structural parameters, assessed via Polarized Raman spectroscopy.

	Parameters	Quantification of the parameters	Interpretation
1	Mineral to matrix ratio	Integrated area of ν_1PO_4 (410-460 cm^{-1}) over amide III (1215-1300 cm^{-1})	Relative mineralization level. Correlates with Ca content [226]
2	Mineral crystallinity index	Inverse value of ν_1PO_4 full width at half maximum	Mineral crystallite chemistry, size and shape [159, 349]
3	Amide I sub-peak ratio $I_{\sim 1670}/I_{\sim 1640}$, collagen disorder/order ratio	Intensity ratio of amide I subbands: $I_{\sim 1670}/I_{\sim 1640}$	Collagen helical structure disorderliness [350, 351]
4	Amide I sub-peak ratio $I_{\sim 1660}/I_{\sim 1683}$, matrix maturity ratio	Integrated area ratio of amide I subbands: $I_{\sim 1660}/I_{\sim 1683}$	Nonquantitative measure of cross-link maturity [351–353]
5	MCF in- and out-of-plane orientation	Integrated area ratio of amide I (1215-1300 cm^{-1}) over amide III (1600-1700 cm^{-1})	MCF spatial orientation [161]

elsewhere [161, 193]. To exclude the polarization dependence from the analyzed parameters (1-4, Table 4.1.1), the results from each measured ROI were averaged over the laser polarizations.

4.1.2.4 Statistical analysis

Descriptive statistics and correlation analysis were performed in R v.4.2 [320] with the `rstatix` [321], `lme4` [354], `lmerTest` and `lmttest` packages. The Shapiro-Wilk test and QQ plots were used to verify the normality of variables. To account for the repeated tests per sample and within the bone structural units (BSU) of each sample, a mixed-effect model was used. For this, groups (gender, diagnoses, zones) and patient's age were treated as fixed effects, while samples and bone structural units (within interstitial or osteonal zones) within the samples were taken as random effects (equation 4.1.1). The influence of the group, age and their interaction on the measured variables was accounted for in the model:

$$variable \sim Group * Age + (1 | Sample) + (1 | BSU : Sample). \quad (4.1.1)$$

The likelihood ratio test confirmed that the random effects have a significant influence on the model for all of the measured variables. Differences in the mean between the groups were tested using the one-way ANOVA test with the mixed model (4.1.2), F-statistic was computed with Satterthwaite's method, the significance threshold was chosen as $p < 0.05$. Measurements are reported as mean \pm SD, where SD stands for the standard deviation. Linear correlation of the measured variables from the patient's age was combined with the mixed effect model, similar to the group analysis:

$$variable \sim Age + (1 | Sample). \quad (4.1.2)$$

A multiple regression analysis was used to check any possible correlation between measured bone properties (Python's NumPy module [355]). For this, Pearson correlation coeffi-

cients were analyzed in a form of a correlation matrix.

Principal component analysis (PCA) was carried out on the final normalized dataset combining the mean of the measured bone parameters per each sample, combined with the clinical information for each patient. PCA was done in Python v.3.9 [221] via the Scikit-learn machine learning library [356]. Logistic regression analysis (Scikit-learn) was applied for the prediction of fractured and non-fractured patients [357]. For this, the final dataset was transformed to avoid categorical inputs and split into training and test sets with a 0.75 to 0.25 ratio respectively. The model accuracy was calculated as the ability of the classifier to find all the positive samples, being the ratio of True Positive/ (True positive + False positive).

4.1.3 Results

4.1.3.1 Sample cohort description

In total, 42 patients participated in this study, with the age varying from 45 to 89 y.o. (figure 4.1.3). A fair distribution of patients' age and genders was observed, with a close number of female and male patients: 19 and 23, respectively (figure 4.1.3 A). Following the clinical information about the patient's primary diagnosis, samples were assigned to one of the two groups: coxarthrosis (N=31), where patients suffered from hip osteoarthritis but had no clinical record of the metabolic bone disease, and fracture patients (N=11), who had to be operated due to hip fractures (figure 4.1.3 B). Such fractures in the context of a low-energy trauma are considered the most serious complication of osteoporosis. While the fracture patients were not formally diagnosed with osteoporosis, we consider them as patients at high risk of osteoporosis. Hip fractures were only observed in patients aged 60 years and above.

4.1.3.2 Bone properties in relation to patient gender, diagnosis and age

A summary of measured bone properties depending on the patients' cohorts is collected in Table 4.1.2. All of the investigated bone properties were found to be independent of the patient's gender and diagnosis (fracture or coxarthrosis).

Zonal dependence between investigated bone structural units was observed for mechanical and some compositional characteristics (figure 4.1.4). Specifically, the mineral to matrix ratio was on average 5% higher in the interstitial zone than in the osteonal ($p < 0.0001$). Meanwhile, the amide I sub-peak ratio $I_{\sim 1670} / I_{\sim 1640}$ (collagen disorder/order ratio) was 1.2% higher in the osteonal bone region ($p < 0.0001$). As for the micromechanical properties, both elastic moduli and hardness of interstitial zones were on average 1.4% and 2.6% higher than those of osteonal zones ($p < 0.0001$).

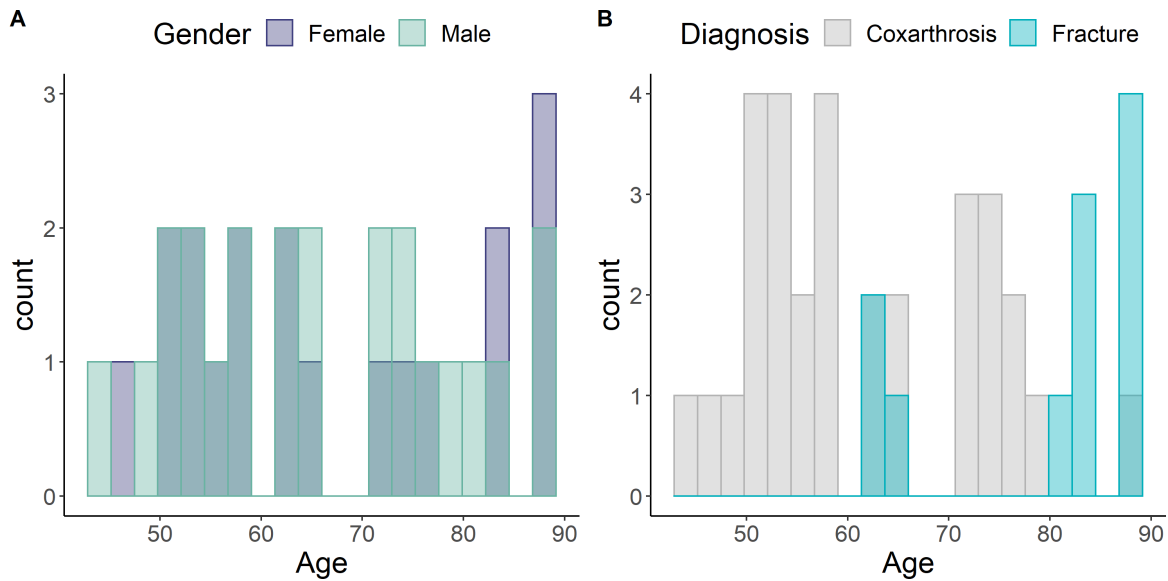


Figure 4.1.3 – Histogram of patients' gender (A) and primary diagnosis (B) distributions across the age.

Neither elastic nor yield properties of bone tissue demonstrate any dependence on the patients' age (figure 4.1.4). The same is true for the bone mineral densities and the volumetric ratio. Only local bone composition demonstrates a marginal correlation with the patient's age. Particularly, the mineral to matrix ratio declines with age ($p=0.02$, $R^2=0.13$, 2.6% per decade), while the amide I sub-peak ratio $I_{\sim 1660}/I_{\sim 1683}$, also referred to as matrix maturity ratio, increases ($p=0.04$, $R^2=0.11$, 1.5% per decade).

4.1. Comparing microscale compact bone properties of patients who underwent hip arthroplasty: influence of age and gender (in preparation)

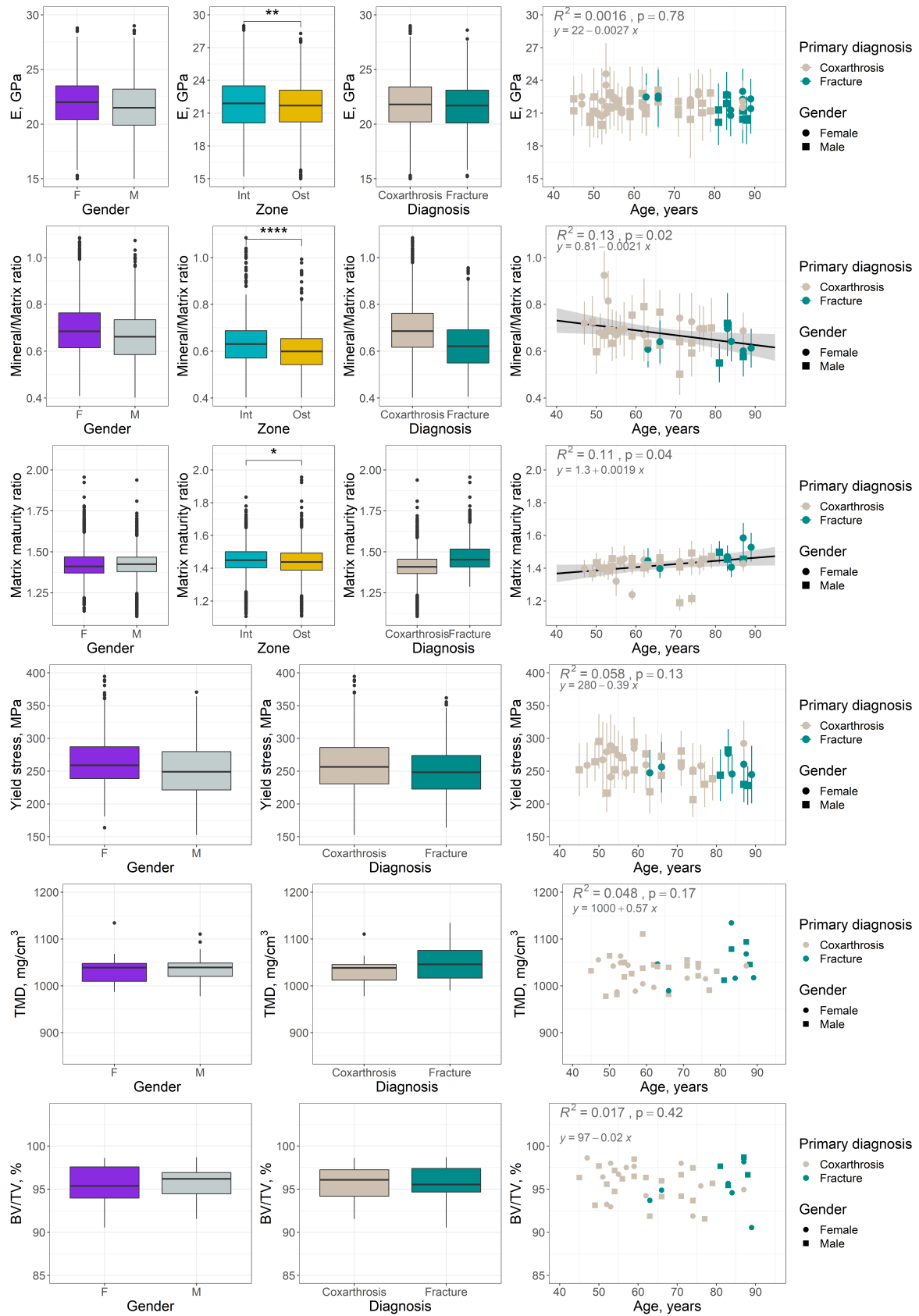


Figure 4.1.4 – Compact bone properties in relation to the patient gender, primary diagnosis, age and analyzed cortical bone zone (interstitial, osteonal). Measured bone properties from top to bottom: elastic moduli (E), mineral to matrix ratio (mineral/matrix), $I_{\sim 1660} / I_{\sim 1683}$ (matrix maturity ratio), tissue mineral density (TMD) and bone volume fraction (BV/TV).

Table 4.1.2 – Summary of measured bone properties depending on the patients’ gender, diagnosis or zone. P-values from the one-way ANOVA test with the nested mixed effect model of the bone characteristics compared within mentioned cohorts of patients. P-values for the group (gender, diagnosis or zone), age and their interaction are reported.

Method	Bone character	Gender			Diagnosis			Zone		
		Female	Male	p-values	Coxarthrosis	Fracture	p-values	Interstitial	Osteonal	p-values
Nanoindentation	E GPa	22.0±2.3	21.5±2.3	0.95 (group) 0.74 (Age) 0.65 (interaction)	21.77±2.3	21.6±2.3	0.35 (group) 0.54 (Age) 0.31 (interaction)	21.9±2.4	21.6±2.3	<0.0001 (group) 0.79 (Age) 0.001 (interaction)
	H MPa	716.7±88.5	706.2±90.4	0.99 (group) 0.38 (Age) 0.81 (interaction)	710.7±89.7	711.3±90.0	0.33 (group) 0.87 (Age) 0.28 (interaction)	721.3±88.3	702.3±90.2	0.001 (group) 0.36 (Age) 0.11 (interaction)
Micropillar compression	Yield stress MPa	263.6±38.5	252.2±41.9	0.41 (group) 0.11 (Age) 0.27 (interaction)	259.3±41.8	251.1±36.8	0.86 (group) 0.46 (Age) 0.89 (interaction)	-	-	-
	Yield strain -	0.030±0.001	0.030±0.001	0.11 (group) 0.67 (Age) 0.10 (interaction)	0.030±0.001	0.030±0.001	0.74 (group) 0.73 (Age) 0.70 (interaction)	-	-	-
Micro-CT	BMD mg/cm ³	1000.7±40.4	1007.0±41.0	0.62 (group) 0.42 (Age) 0.58 (interaction)	999.4±36.1	1019.4±51.0	0.17 (group) 0.96 (Age) 0.16 (interaction)	-	-	-
	TMD mg/cm ³	1032.4±35.7	1035.9±33.7	0.75 (group) 0.17 (Age) 0.89 (interaction)	1029.3±29.6	1050.2±44.1	0.09 (group) 0.65 (Age) 0.24 (interaction)	-	-	-
	BV/TV %	95±2	96±2	0.64 (group) 0.42 (Age) 0.25 (interaction)	96±2	96±2	0.99 (group) 0.29 (Age) 0.20 (interaction)	-	-	-
Raman Spectroscopy	Mineral/Matrix ratio	0.69±0.12	0.66±0.12	0.54 (group) 0.026 (Age) 0.74 (interaction)	0.69±0.12	0.63±0.11	0.51 (group) 0.58 (Age) 0.62 (interaction)	0.63±0.10	0.60±0.10	<0.0001 (group) 0.006 (Age) <0.0001 (interaction)
	Mineral crystallinity index	0.130±0.001	0.130±0.001	0.57 (group) 0.75 (Age) 0.41 (interaction)	0.130±0.001	0.130±0.001	0.34 (group) 0.34 (Age) 0.43 (interaction)	0.130±0.001	0.130±0.001	0.0001 (group) 0.92 (Age) 0.009 (interaction)
	$I_{\sim 1670}/I_{\sim 1640}$ collagen disorder/order ratio	1.70±0.09	1.69±0.07	0.66 (group) 0.38 (Age) 0.61 (interaction)	1.70±0.08	1.68±0.08	0.60 (group) 0.12 (Age) 0.78 (interaction)	1.67±0.08	1.69±0.08	<0.0001 (group) 0.29 (Age) 0.014 (interaction)
	$I_{\sim 1660}/I_{\sim 1683}$ matrix maturity ratio	1.42±0.10	1.42	0.22 (group) 0.06 (Age) 0.20 (interaction)	1.40±0.09	1.47±0.09	0.42 (group) 0.20 (Age) 0.30 (interaction)	1.45±0.11	1.43±0.11	0.10 (group) 0.03 (Age) 0.019 (interaction)

4.1.3.3 Compact bone structure-properties relationship

Investigated mechanical properties of compact bone exhibited an apparent correlation with the tissue mineralization levels, as depicted in figure 4.1.5. Average sample hardness and yield stress showed a positive correlation with bone tissue mineral density ($p < 0.02$). No dependence was observed for the averaged elastic moduli ($p > 0.6$).

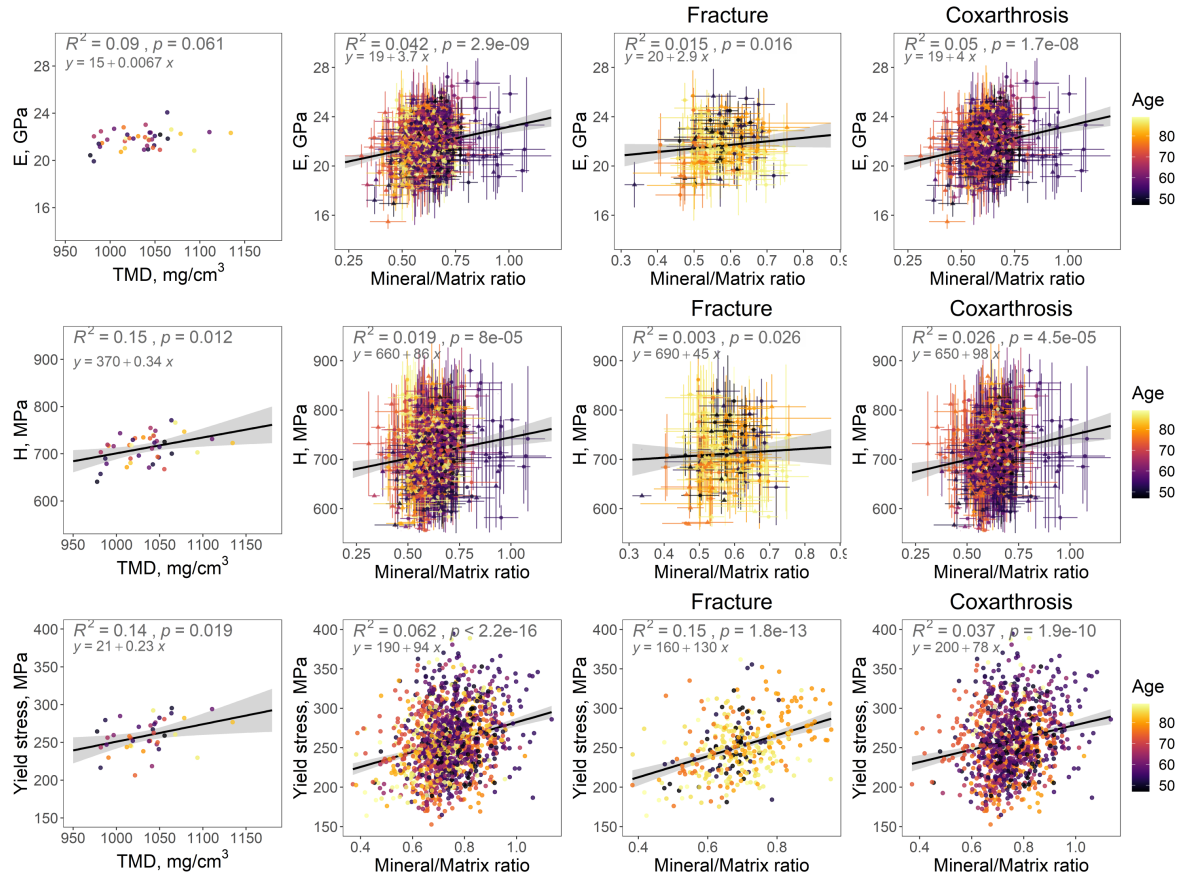


Figure 4.1.5 – Local mineral-mechanical relationships of compact bone in relation to the patient's age and primary diagnosis.

The site-matched analysis of microscale mechanical, compositional and morphological properties sheds light on the local structure-properties relationships of compact bone. Both elastic moduli and hardness demonstrated a positive correlation with the mineral to matrix ratio ($p = 2.9 \times 10^{-9}$, $R^2=0.042$ and $p = 8 \times 10^{-5}$, $R^2=0.019$ respectively). The correlation coefficient reduces for the patients with hip fractures: $p=0.16$ for E and $p=0.026$ for H versus $p < 0.0001$ for both E and H of coxarthrosis patients. Most likely, this is due to the smaller sample size: 11 patients with hip fractures versus 31 coxarthrosis patients. The same relation with the mineral to matrix ratio was observed for the local yield stress ($p < 2.2 \times 10^{-16}$, $R^2=0.062$). This positive correlation remains for both coxarthrosis ($p = 1.9 \times 10^{-10}$, $R^2=0.037$) and fracture patients ($p = 1.8 \times 10^{-13}$, $R^2=0.15$) (figure 4.1.5). Besides local mineralization levels, also out-of-plane MCF orientation was measured following

the qPRS method. Neither elastic nor yield micromechanical properties exhibited a significant correlation with the MCF out-of-plane angle ($p=0.45$, $p=0.82$ respectively).

4.1.3.4 Overall correlation between measured bone properties

To assess the overall correlation between measured bone properties, a multiple regression analysis was carried out. Pearson correlation matrix, shown in figure 4.1.6, summarizes the output correlation coefficients r , where $r \rightarrow 0$ for a dismal correlation and $r \rightarrow 1 / -1$ suggests a distinct positive/negative correlation between the parameters.

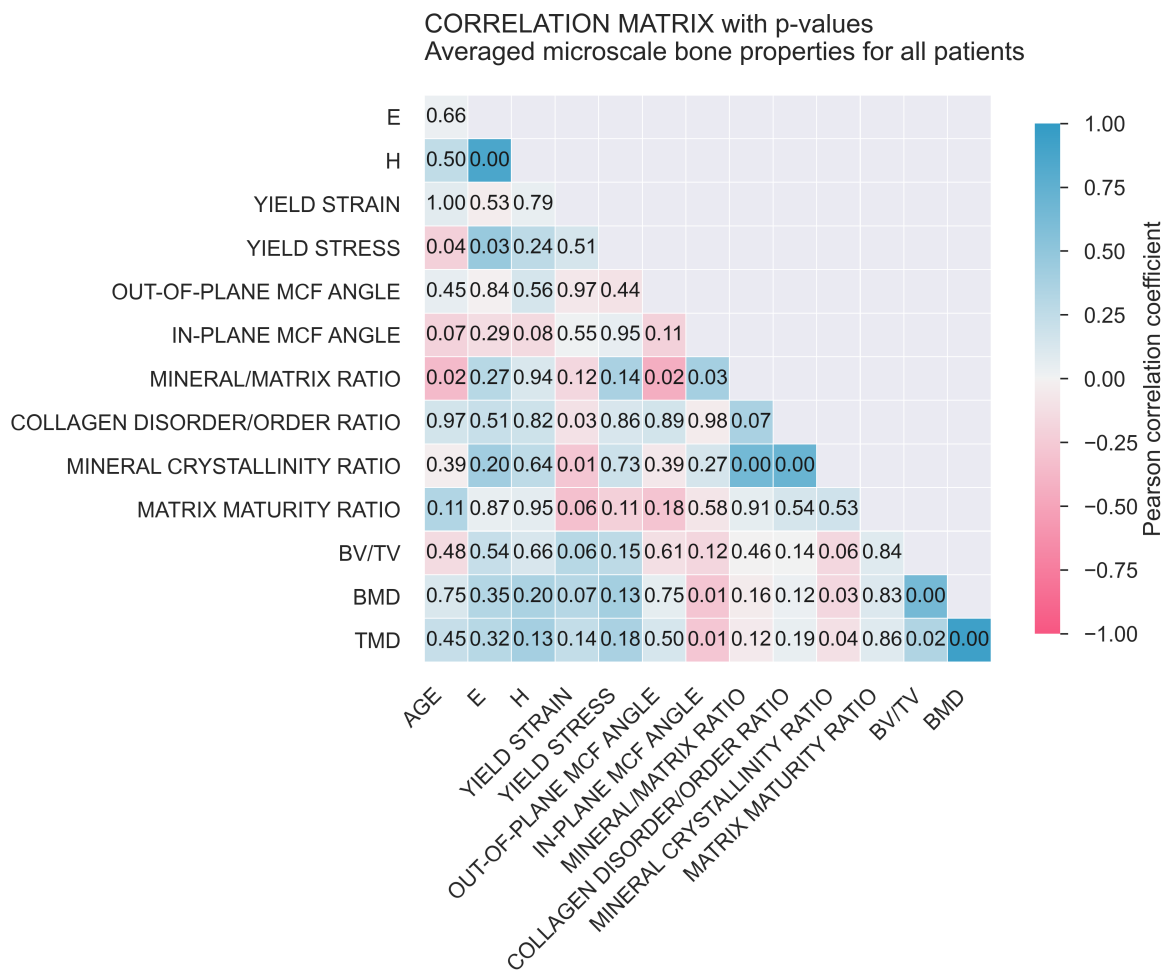


Figure 4.1.6 – Pearson’s correlation coefficients (r) from the multiple regression analysis of the measured bone properties.

As shown in figure 4.1.6, local crystallinity demonstrates a strong positive correlation with elastic moduli ($r=0.42$) and a moderate correlation with hardness ($r=0.26$). Moreover, it increases with the mineral to matrix ratio ($r=0.66$) but does not correlate with the sample-level TMD ($r=-0.12$). Similarly, the mineral to matrix ratio does not correlate with TMD ($r=-0.05$). However, both local crystallinity and the mineral to matrix ratio correlate positively

with the amide I sub-peak ratio $I_{\sim 1670}/I_{\sim 1640}$ ($r=0.77$ and $r=0.37$ respectively), suggesting a hidden interplay of mineral and organic bone fractions. Mineralized collagen fibrils' out-of-plane orientation demonstrates correlation with the mineral to matrix ratio ($r=-0.54$) as well as the in-plane MCF orientation ($r=0.34$), however, this is likely due to the Raman ratios quantification similarities since all of these Raman parameters depend on the amide III integral area.

Overall, bone elastic properties demonstrate a strong correlation with the mineral fraction of bone: TMD ($r=0.30$), mineral crystallinity ($r=0.42$), mineral to matrix ratio ($r=0.30$). However, no dependence on the amide I sub-peak ratio $I_{\sim 1660}/I_{\sim 1683}$ was observed ($r=0.04$), with a marginal correlation to the collagen disorder/order ratio ($r=0.22$). What is more, elastic moduli correlate strongly with hardness ($r=0.86$), as expected from the methodology [166].

As for the yielding bone properties, yield stresses correlate positively with the mineral characteristics of the bone fraction ($r=0.37$ for the TMD and $r=0.37$ for the mineral to matrix ratio), yet it demonstrates a marginally negative correlation with the amide I sub-peak ratio $I_{\sim 1660}/I_{\sim 1683}$ ($r=-0.22$). Yield strain shows a negative correlation with the mineral crystallinity ($r=-0.28$) and the $I_{\sim 1660}/I_{\sim 1683}$ ratio ($r=-0.32$). Interestingly, yield stresses correlate strongly with the elastic moduli ($r=0.47$).

4.1.3.5 Perspective bone fracture biomarkers

Principal component analysis (PCA) was employed to define a combination of bone parameters measured in this study, which would explain the observed variations in bone properties. It allowed us to reduce the dimensionality of the collected data by defining linear combinations of bone properties, acting as new eigenvectors (principal components) for our multidimensional dataset. In total, 8 variables were included in the PCA: patients' age, bone hardness, yield stress and strain, mineral to matrix ratio, amide I sub-peak ratios, TMD. According to the PCA (figure A3.2), the first two principal components were able to explain $\sim 45\%$ of observed variations between the patients.

Four classification algorithms were tested on the PCA-processed final data with reduced collinearity: logistic regression, support vector machines, naive Bayes and K nearest neighbor (KKN) models. As a result, with the training-to-test dataset ratio of 0.75:0.25 the first three models showed matching accuracy scores of 0.7, while KKN was only able to reach a 0.5 score. The logistic regression algorithm was chosen for the final data classification as it is often considered the standard method for clinical classification problems [357]. Accordingly, the variables that contributed the most to the fracture predictions were the indentation

hardness, mineral to matrix ratio and micropillar yield stress. Exact scores can be found in Appendix A3, figure A3.3. Consequently, these bone parameters can be considered potential bone markers for the future analysis of bone quality in preclinical studies.

4.1.4 Discussion

In this study, microscale elastic and yield mechanical properties, as well as bone composition and morphology, were assessed in 42 aging patients. All measurements were done *ex vivo* using laboratory-based methods for precise morphological, compositional, and micromechanical compact bone properties assessment. The collected experimental data included compact bone tissue mineral density and volumetric fraction, measured via micro-CT. Compositional properties related to mineral and organic content were assessed via polarized Raman spectroscopy, and microscale mechanical properties, both elastic and yield, were measured through nanoindentation and micropillar compression techniques. The output collection of bone properties was combined with the clinical information about the patient's age, gender and primary diagnosis, including the incidence of the hip fracture. Statistical analyses within the collected data frame as well as between the site-matched bone properties were performed with the aim of better understanding the structure-mechanical property relationships in compact bone at the microscale and identify bone parameters related to bone fracture.

4.1.4.1 Microscale bone mechanical properties

The elastic moduli of the cortical bone regions of the femoral necks investigated in this study varied from 15 to 28 GPa between the patients. Similarly, hardness values from 530 to 880 MPa were observed. This is in line with the currently available nanoindentation data on the human femur with approximately 16 to 28 GPa reported elastic moduli values [166, 176, 187, 252, 358] and about 300 to 760 MPa hardness values accordingly [176, 359, 360].

Microscale bone hardness and elastic moduli did not depend on patients' age, gender or diagnosis. A similar absence of correlation between the elastic properties and the fracture status of the femoral necks was shown by Fratzi-Zelman et al. for the femoral neck samples from elderly female patients [358]. In another study by Mirzaali and Schwiedrzik et al. [197], indentation measurements were done on proximal femurs from donors of age 46-99, and microindentation properties were shown to be constant over age and not gender-dependent. In a more recent study by Bonicelli et al., lamellar bone hardness of the femoral head was found to be lower for donors with hip fractures [361].

While nanoindentation is a commonly used laboratory-based method of bone mechanical properties analysis [166], micropillar compression studies are scarce. Indeed, the micropillar compression technique requires time-consuming preparation of the bone micropillars [84, 161, 167, 179, 181, 183, 317], in contrast to the plain polished surface that is required for the nanoindentation measurements. On the other hand, micropillar compression can provide information not only on bone elastic properties but also on yielding and post-yielding behavior. In the current study, we employed a recently developed laser ablation protocol for fast and repeatable micropillar fabrication [193]. This allowed us to carry out a high-throughput micropillar compression study, approaching the measurement rate of the nanoindentation method.

This is the first study, where high-throughput micropillar compression experiments (N=1441) were carried out on a large number (N=42) of human cortices. Consequently, we cannot directly compare measured microscale yielding bone properties at the femoral neck site with other studies. Observed yield stress values varied from 200 to 300 MPa between the patients. These values are somewhat lower than available data on femoral condyle trabecular bone (313-327 MPa, 3 μm pillar diameter [60]) or iliac crest cortex (\sim 350 MPa, 5 μm pillar diameter [63]). However, as was nicely demonstrated by Tertuliano and Greer, micropillar size affects drastically the output properties, since different levels of hierarchy are being tested [181]. As a tradeoff for the high-throughput measurements, laser-ablated micropillars had a bigger size (almost 5 times larger diameter than in previously reported studies [84, 161, 167, 179, 181, 317]) and a taper, which influence was accounted for through the use of FE simulations [193]. Consequently, a larger number of material defects like lacunae or lamellae interfaces are present within the micropillar. Even more drastic decrease in strength values with the specimen size was observed by Casari et al. during microscale tensile testing [213].

Microscale yield stress values were consistent between female and male patients across investigated ages (45-89 y.o.). The occurrence of the hip fracture also seems to not affect the compressive yield stress and strain at this scale, although the tensile strain is reported to be lower for the fractured donors at the femoral head trabeculae [361].

4.1.4.2 Bone composition and morphology

Tissue mineral density values assessed in the current work were in line with available studies (868-1020 mgHA/cm^3 [362, 363]). Bone volume fraction levels are similar to reported measurements, reaching up to 99% of BV/TV (1% porosity, [363]). However, we are likely not able to segment the smaller pores like lacunae with the available resolution (17.2 μm

voxel size). Bone density (BMD, TMD) as well as the bone volume fraction were consistent between the patients' cohorts (both genders, both diagnoses) and were seemingly constant across the investigated patient ages. On contrary, Voumard et al. observed decreased aBMD as well as the bone volume fraction with the donor's age [362]. Most probably, we do not observe any correlation with age because we only measured the inferomedial region of the femoral neck, in contrast to the whole neck slice [362].

Bone compositional parameters, as assessed via quantitative Polarized Raman spectroscopy, were in line with previously reported values on human femurs: 0.4-1.6 mineral to matrix ratio [226], 1.35-1.60 amide I sub-peak ratio $I_{\sim 1670}/I_{\sim 1640}$ [350, 351]. Available data on the Raman $I_{\sim 1660}/I_{\sim 1683}$ ratio is only reported for the young mice models: 1.9-2.5 [352]. We observed increased mineral crystallinity values (0.13 in comparison to 0.05-0.06 in other works [197, 324, 364]), which may indicate changes in the strain environment of the lattice possibly caused by the sample fixation and embedding procedure [228]. As anticipated, clear zonal dependence is present for investigated compositional parameters. More specifically, interstitial bone regions exhibit 5% higher mineral to matrix ratios, similar to other studies [324, 345]. Averaged mineral to matrix ratios did not correlate with sample level TMD, most likely due to the small range of both parameters.

In the current work, only bone compositional characteristics were found to correlate with the patient's age. In particular, the bone mineral to matrix ratio was found to decrease with age. This might be an unexpected finding because it is well-accepted that mineralization generally increases with age [227], or stays constant after reaching skeletal maturity [197]. It is likely that the observed decrease in the mineral to matrix ratio is due to an age-related increase in bone turnover. Moreover, since both mineral and organic bone fraction contribute to the mineral to matrix ratio, we hypothesize that it is actually an increase in bone collagen with age that leads to decreasing mineral to matrix ratio. Indeed, we observe an increasing with age amide I sub-peak ratio $I_{\sim 1660}/I_{\sim 1683}$. As was shown in FTIR studies, the ratio of these amide I sub-peaks provides the ratio of non-reducible (mature trivalent) over reducible (immature divalent) enzymatic crosslinks [365]. However, it is debatable whether this sub-peak ratio can be representative of mature to immature crosslink ratio in Raman spectroscopy measurements [352, 353].

We argue that this interplay of the mineral-organic fractions may smoothen the observed variations in the mechanical properties versus the patients' age. As a potential pathway, extensive collagen cross-linking may increase the stiffness of the organic part thus compensating for the reduced tissue mineralization and keeping the averaged microscale mechanical properties constant for patients at ages 45 to 89. Similar conclusions were drawn in the work

of Fratzl-Zelman et al. [358].

4.1.4.3 Site-matched analysis of the bone structure-property relationship

Besides assessing averaged microscale properties of the compact bone, site-matched qPRS with nanoindentation, as well as micropillar compression, allowed assessing local structure-property relationship analysis. All investigated mechanical properties except yield strain demonstrate a positive correlation with the mineral fraction of bone, which is in line with previous studies [366, 367]. On the averaged bone level, the correlation between the yield stress, elastic moduli and hardness versus TMD (Pearson's coefficients 0.37, 0.3 and 0.39 accordingly) was comparable to the one at the local site-matched analyses. Interestingly, the highest correlations for the site-matched local analysis were observed between the yield stress vs. the mineral to matrix ratio and the elastic modulus vs. the mineral crystallinity (Pearson's coefficients 0.37 and 0.42, respectively). This suggests that the yield properties of bone lamellae depend on both mineral and organic bone portions, while elastic properties are more strongly influenced by changes in the mineral bone phase. However, as discussed in section 4.2, it is actually the interplay of organic and mineral phases that affects the mechanical properties.

To our surprise, local micromechanical properties were independent of the out-of-plane MCF angle. The inclusion of the angle in a multilinear model for the local mechanical properties versus the mineral to matrix ratio did not improve the correlation. This is striking since a strong dependence on the out-of-plane MCF angle is expected for this anisotropic nanocomposite and was demonstrated in earlier studies [161]. A likely explanation for this discrepancy is the diverging volume of interests of the different measurements. For the nanoindentation maps, qPRS measurements were carried inside the map yet not within exact indentation spots but rather in between. Since the distance between the indents was 20 μm , different lamellae could have been measured. While the polarized Raman spectra from the bone micropillar were collected within the pillar dimensions, the analyzed volumes from qPRS ($\sim 8.6 \mu\text{m}^3$) and compressions ($\sim 90 \mu\text{m}^3$) were around an order of magnitude different. Thus, the MCF orientation within the larger portion of the micropillar volume was not analyzed. In future studies, care should be taken to strictly site-match measurements and to choose volumes of interest for the microstructural measurements as close as possible to those of the mechanical measurements. Yet the microscale mechanical properties demonstrate a prominent correlation with the mineral to matrix ratio, suggesting that the local composition is more continuous at measured volumes.

4.1.4.4 Potential markers of bone quality

This study provides a framework of laboratory-based methods for the bone composition, morphology, elastic and yield mechanical properties analysis. Consequently, wide spectra of bone parameters were measured and correlated with the patient's gender, primary diagnosis and age. Another motivation for this study was to find the most perspective bone characteristics, which could be used for fracture risk prediction in the future. For this, we run the Logistic Regression classification algorithm on the final matrix of collected bone properties per patient. Logistic regression is a standard method for building prediction models for a binary outcome and has been extended for disease classification [357, 368–370] including osteoporosis [371–373]. Here, we apply this algorithm to multimodal characteristics of bone measured in this study for fracture prediction. As a result, 0.7 prediction accuracy was achieved, highlighting the perspective variables for bone fracture prediction: the indentation hardness, mineral to matrix ratio and micropillar yield stress. All of these are often overlooked and are not included in general patient screening due to the lack of high-precision low-cost instruments for their measurements.

Nowadays more and more studies emphasize the influence of micromechanical bone properties on macroscale bone strength and toughness [197]. We can only anticipate the future bone characterization techniques and their potential impact. Moreover, bone compositional properties, as assessed via Raman spectroscopy, were also shown to correlate with bone fracture toughness [350, 351]. This is in line with the proposed classification model, where mineral to matrix ratio demonstrates a high influence on fracture prediction. Surprisingly, patient age did not dominate the fracture prediction model. However, the influence of age might be indirectly included in the model through compositional variations (e.g. mineral to matrix ratio, matrix maturity ratio). From the patient cohort analysis, it is evident that older patients have an increased risk of bone fractures, in line with the clinical fracture risk questionnaire.

It is important to highlight that the sample size in this analysis is too low to claim a universal classification model. With the small to moderate sample size, the logistic regression algorithm was shown to overestimate the odds ratios [374]. However, the proposed analysis strategy can be applied in further research on combining different bone quantity and quality parameters for fracture risk predictions. Although difficult to achieve in a clinical setting, a larger number of patients ($N > 200$) is required.

4.1.4.5 General Limitations

Collected clinical information from the patients involved in this study was fairly limited and did not include clinical information about DXA scans for osteoporosis and/ or osteopenia screening. However, previous bone fractures for the population >50 y.o. is considered one of the major risk factors for osteoporosis [375]. Therefore, in this study, we consider the cohort of patients with fractures as patients at a high risk of osteoporosis. What is more, no clinical record of long-term medication was available. Bisphosphonate drugs have a drastic influence on bone remodeling and mineralization levels [376] and would certainly have affected the observed variations in the measured bone properties. Another limitation of the study was the comparison between coxarthrosis and fracture patients. It is unknown if matrix-related changes during the development of osteoarthritis are linked to the development of bone fragility.

As anticipated, femoral neck height and morphologies were not always consistent between the patients. Nevertheless, the surgeon followed the double osteotomy protocol, aiming to extract approximately 10 mm femoral neck slices from all patients. Originally 59 femoral necks were extracted during the surgeries and further screened using the laboratory-based micro-CT. In the end, only 42 femoral necks had intact inferomedial regions and were used in this study. Inconsistent morphology between the samples restricted comparative morphological analysis. For future study planning, it is crucial to take into account the morphological variations between the human bone samples, leading to decreased number of suitable biopsies.

As discussed above, all reported measurements in this study were carried out on the inferomedial part of the femoral neck slice. This region carries most of the compressive loading in the femoral neck site [377, 378] and consequently has an abundant amount of cortical bone. However, it is of high interest to study also the posterior region of the femoral neck, since most of the hip fractures nucleate from that region. However, several limitations have to be overcome first. For example (1) scaling down the analysis to match the lower amount of cortex, and (2) increasing the number of patients since this neck region is often fragmented and poorly suitable for the analysis proposed in this study.

We would like to highlight that all the samples used in the study were fixed and embedded due to the biosafety regulations in the testing facilities. This procedure in principle affects the organic fraction of the bone matrix and slightly modifies the mechanical properties of the bone: an increase in stiffness and compressive strength is reported [330, 331]. However, all specimens were fixed the same way and, therefore, relative comparison between samples was possible. For future studies involving compositional analysis, the use of fresh bone sam-

ples is endorsed.

Finally, yet importantly, there is always room for more study participants and additional clinical information. Specifically, the number of patients with hip fractures that we analyzed in this work was almost three times lower than the number of patients with coxarthrosis. However, the involved number of fracture patients (N=11) was still sufficient following the a priori statistical power analysis [379]. For statistically significant differences between two patient cohorts with the available cohort size (N=42), with an α error probability of 0.08, an allocation ratio of 3, and the effect of size $d=0.85$, differences in the mean of 10% are detected with a power of 0.8. Moreover, having patients screened for osteoporosis or osteopenia would have as well improved the final analysis of the potential bone quality markers. Although we consider the hip fracture patient as being at high risk of osteoporosis, additional clinical screening is mandatory before assigning them to osteoporotic cases.

4.1.5 Conclusion

In this study, bone quality and quantity were assessed at the femoral neck sites of the patients who underwent hip arthroplasty. A combination of high-throughput micromechanical testing techniques (nanoindentation, micropillar compression) together with micro-CT and the recently developed quantitative polarized Raman spectroscopy method, allowed us to create a unique data frame of the bone properties for each patient. Microscale mechanical and compact bone level properties were independent of patient gender or fracture occurrence. Only local bone composition (specifically mineral to matrix ratio and $I_{\sim 1660}/I_{\sim 1683}$ ratio), as assessed via qPRS, varied with age. With the logistic regression algorithms, a classification model was built for hip fracture prediction at a 0.7 accuracy. Accordingly, the indentation hardness, mineral to matrix ratio and micropillar yield stress are the most perspective parameters for fracture risk prediction. The presented data and analysis approaches can be used in the future for the prediction of fracture risk in the elderly. What is more, this knowledge may help to form a better understanding of the mechanisms through which bone tissue is affected by aging.

Declaration of competing interest

The authors declare no competing financial interests.

Acknowledgment

This work is funded by the Special Focus Area Personalized Health and Related Technologies (SFA PHRT) iDoc Project 2017-304. The authors would like to thank B. Voumard, E. Jäggi and K. Leeb for the sample and patient information collection; K. Lang, S. Owusu and

D. Bosshardt for their support during bone sample fixation. F. Klimashin for the assistance with the nanoindentation setup, C. Peruzzi and D. Casari for the FE simulations. F. Kurdze-sau, P. Bühlmann for their statistical advice and G. Goyal for her great help with the PCA and classification algorithms.

Author contribution

Tatiana Kochetkova: Writing – original draft, review & editing, Visualization, Project administration, Methodology, Investigation, Formal analysis, Data curation, Conceptualization. Markus S. Hanke: Writing – review & editing, Methodology, Investigation, Resources, Conceptualization. Michael Indermaur: Writing – review & editing, Investigation, Formal analysis, Data curation. Alexander Groetsch: Writing – review & editing, Methodology, Investigation. Stefan Remund: Writing – review & editing, Methodology. Beat Neuen-schwander: Writing – review & editing, Methodology, Resources. Johann Michler: Writing – review & editing, Funding acquisition, Resources. Klaus A. Siebenrock: Writing – review & editing, Funding acquisition, Resources. Philippe Zysset: Writing – review & editing, Supervision, Resources, Conceptualization. Jakob Schwiedrzik: Writing – review & editing, Supervision, Resources, Funding acquisition, Conceptualization.

Chapter 5

Overall Discussion and Outlook

5.1 Summary

Aging and disease cause a clear deterioration in the mechanical properties and structural integrity of bone, leading to an increased risk of fracture. With the increased longevity of modern countries, bone fractures are bound to increase in number [3]. The loss of bone mass or quantity is a widely accepted indicator of declining skeletal health status [209]. Consequently, all clinical methods of bone screening depend to a large extent on bone mineral density measurements [4]. Yet, emerging scientific evidence suggests that not only bone quantity but also bone quality plays an important role in bone weakening progression and detection [242, 351, 380]. Bone quality includes various parameters of metabolism, composition and microarchitecture excluding BMD, that contribute to the overall fracture resistance [268]. To date, no universally accepted bone quality characteristic can be used to predict the risk of fragility fracture. This thesis was focused on developing a laboratory-based analysis framework to simultaneously assess various bone quality parameters such as compositional, structural, and mechanical properties of the bone matrix. The ultimate aim of the presented research was to define perspective bone quality characteristics that can be useful for bone fracture prediction, besides the well-accepted BMD values. This objective as well as additional research questions were addressed using novel experimental approaches in three separate studies. This section summarizes their main outcomes.

Combining polarized Raman spectroscopy and micropillar compression to study microscale structure-property relationships in mineralized tissues

Key outcomes: Investigation of the effect of local MCF orientation on the microscale mechanical properties of isolated bone lamellae. For this, a method based on polarized Raman spectroscopy, namely quantitative Polarized Raman Spectroscopy, was calibrated and validated.

In chapter 3.1, the correlation between the compressive mechanical properties and the local MCF orientation in the isolated bone lamellae was analyzed. This was done using a combination of novel laboratory-based methods for bone compositional, structural and mechanical characterization at the microscale level: micropillar compression and quantitative Polarized Raman spectroscopy. By combining these two techniques, a unique spectrum of microscale mechanical compression data for MCF orientations ranging from 0° to 82° was collected. The quantitative analysis of the MCF out-of-plane orientation became possible following the careful calibration and validation of the PRS method using “gold-standard” techniques (small angle X-ray scattering and micro-computed tomography). With the calibrated qPRS method we were able to retrieve quantitative rather than just qualitative information about the out-of-plane angle of the mineralized collagen fibrils with an angular certainty of $< 10^\circ$. A strong dependence of the compressive micromechanical properties of bone on the fibril orientation was found with a high degree of anisotropy for both the elastic modulus and the yield stress. Moreover, the post-yield behavior was found to depend on the MCF orientation with a transition between softening to hardening behavior at approximately 50° .

All measurements were carried out on the animal bone samples: qPRS validation on mineralized turkey leg tendon and micropillar compression at known MCF angle on bovine cortical bone samples. Bovine osteonal bone from this study exhibited a relatively low variation of MCF out-of-plane orientations within osteonal lamellae ($< 10^\circ$, Section A1, Figure A1.4). This might not be the case for human cortical bone with experimentally observed oscillating MCF orientations [30, 31, 381]. For the forthcoming analysis of microscale mechanical properties of human bone, determining the mineralized collagen fibril orientation before the mechanical testing and incorporating this information into the data analysis may reduce the apparent scatter in the collected data.

In this study, FIB-milled micropillars were used for the compression tests. This allowed to pre-select regions of interest for the mechanical tests precisely at the osteonal lamellae. However, for this pillar fabrication method, a conductive thin film is applied on the sam-

ple surface for the imaging and milling inside the electron microscope, thus prohibiting the Raman spectroscopy measurements. Here, the qPRS analysis was done prior to micropillar fabrication and it bared adequate results since the inherent MCF orientation variation within bovine osteons was below the angular detection limit of the qPRS technique. Yet, for human lamellar bone such approach might be challenging. What is more, micropillar fabrication via FIB is extremely time-consuming (minimum of 2 h per single micropillar). Although other studies have attempted to make cohort comparisons of human bone biopsies (N=12) using FIB-milled micropillar compression, it is very demanding to upscale this fabrication method for a larger number of samples. To address this major limitation, a new method for bone micropillar fabrication via laser ablation was developed and applied to another animal bone model in the follow-up study.

Assessing minipig compact jawbone quality at the microscale

Key outcomes: A multimodal framework for bone characterization was developed in an animal model that could be further extended to humans. This framework included morphological bone analysis via micro-CT, relative mineralization assessment via Raman Spectroscopy and mechanical characterization via high-throughput micropillar compression and nanoindentation. Consequently, jawbone mineralization, morphology, and mechanical properties were assessed in three minipigs genotypes.

In chapter 3.2, a multimodal approach to assess jawbone quantity and quality at the microscale was presented. A common animal model for dental research was examined: the miniature pig. Three minipig genotypes were examined, and samples were extracted from three animals per genotype. Through the combination of laboratory-based methods, bone mineralization, morphology, and mechanical properties were analyzed at the local and global average levels. Microscale computed tomography, Raman spectroscopy, and nanoindentation were employed for sample characterization at the global level, averaged over the sample area. Nanoindentation assessed the elastic properties of the cortical jawbone, while micro-CT and Raman spectroscopy the bone morphology and mineralization. At the local level, micropillar compression was used, to extract yield and elastic bone properties, which are critical in dental research. For the first time, micropillar compression tests were carried out on laser-fabricated bone micropillars, which enables high throughput mechanical characterization. Raman spectroscopy and micropillar compression measurements were combined in a pillar-matched manner to estimate the mechanical properties of bone in correlation with the local bone mineralization level, giving access to structure-property relationships at the microscale.

Using Raman spectroscopy, the differences in relative mineralization levels (mineral/matrix ratios) were detected within the investigated cortical regions, which was not possible using micro-CT. Moreover, relative mineralization levels from three genotypes correlated positively with averaged bone hardness. Site-matched micropillar compression and Raman spectroscopy further highlighted the differences between the genotypes' yield stress and mineral to matrix ratios. This experimental study highlights the advantages of assessing the microscale bone properties for the comparison of species with different genotypes. However, to extend the analysis, mineralized collagen fibril orientation needs to be taken into account explicitly in the future. The proposed framework is further applied to human bone samples in the next study.

Comparing microscale compact bone properties of patients who underwent hip arthroplasty: influence of age and gender

Key outcomes: Microscale compact bone properties were analyzed for 42 patients who underwent hip arthroplasty. Gender as well as the occurrence of fracture did not affect microscale mechanical, compositional, or mesoscale morphological properties of the inferomedial compact bone of the femoral neck. Only local compositional properties were influenced by the patient's age. Logistic regression classification showed that indentation hardness, mineral to matrix ratio and micropillar yield stress are the most relevant parameters for bone fracture risk prediction among the investigated bone properties and available clinical information about the patients.

This study was carried out on the femoral neck samples from 42 patients who underwent hip arthroplasty. The cortex from the inferomedial region was analyzed *ex vivo* in a site-matched manner using a combination of micromechanical testing (nanoindentation, micropillar compression) together with micro-CT and quantitative polarized Raman spectroscopy for both morphological and compositional characterization. The output bone properties were correlated with the clinical information about age, gender, and primary diagnosis (coxarthrosis or hip fracture) of the participating patients.

Patient gender and diagnosis did not influence any of the investigated bone properties. Moreover, all mechanical properties as well as the sample-level mineral density were nearly constant over all ages (45-89 y.o.). Only local tissue composition was found to change significantly with age: decline in mineral to matrix ratio and increase in matrix maturity ratio. Site-matched microscale analysis confirmed that all investigated mechanical properties except yield strain demonstrate a positive correlation with the mineral fraction of bone.

The large dataset of experimentally assessed microscale bone properties together with the

available patient clinical information allowed the application of machine learning algorithms for fracture prediction *in silico*. Logistic regression classification showed that with a 0.7 accuracy micropillar indentation hardness, mineral to matrix ratio and micropillar yield stress are the most relevant parameters for bone fracture risk prediction. The presented data and analysis approaches may be used in the future to improve the prediction of fracture risk in the elderly.

5.2 Conclusion and Outlook

In the course of this thesis, a unique framework for multimodal assessment of bone quality was developed and validated on animal models (Chapters 3.1, 3.2) and then applied to humans (Chapter 4.1). These laboratory-based methods allow for concurrent assessment of bone structural, compositional and mechanical properties in the micrometer range.

The unprecedented highlight of this thesis is the application of high-throughput micropillar compression on a large number of human samples (N=42). This has only become possible thanks to the ultra-short-pulsed laser ablation approach for bone micropillar fabrication. The previous micropillar compression tests on bone were done on the FIB-milled micropillars under a vacuum. In contrast, laser ablation allows pillar fabrication at normal atmospheric pressure and relative humidity, thus reducing the strong dehydration effects of exposing the sample to a vacuum. The heat accumulation during pillar fabrication was estimated to be below the denaturation point of native hydrated collagen, as well as dehydrated mineralized collagen (Appendix A2). And last but not the least, pillar fabrication via laser ablation drastically decreases the time costs for pillar micromachining and therefore enables high throughput micropillar compression tests. The drawback of this method is the geometrical imperfection of laser-fabricated micropillars versus the FIB-milled one. The resultant micropillar taper angle compromises the stress distributions within the micropillar volume during compression and thus distorts the output mechanical properties. The effects of the micropillars' taper on the elastic modulus, yield stress, and strain were estimated through FE simulations (Appendix A2) and corrected accordingly. Unfortunately, it was not possible to analyze the true post-yield behavior due to the prominent hardening induced by the tapered geometry.

Although the laser ablation protocol developed in this thesis gives arrays of micropillars with reasonable geometry, there is still some room for improvement. For example, the most promising direction for the pillar taper reduction would be modifying the laser beam profile from Gaussian to the top-hat one [382, 383]. This would reduce the heating at the sample

surface while maintaining a “straight” ablation profile.

Furthermore, a method for quantitative collagen fibril orientation estimation based on polarized Raman spectroscopy (qPRS) was developed, calibrated, and validated. The calibrated PRS method gives quantitative values of the out-of-plane MCF orientation together with the local compositional information in a non-invasive manner. As was demonstrated in this thesis, this method can be combined with mechanical testing like nanoindentation or micropillar compression to assess the structure-properties relationship of bone at the microscale. qPRS can probe volumes down to the sub-micron quantities ($\sim 0.5\mu\text{m}^3$). While it allows precise analysis of small volumes, the scanning of a larger surface area becomes time-consuming. Future studies on high-throughput structure-properties analysis would benefit from a scaled-up method for MCF spatial orientation. Such a method could emerge from the Second Harmonic Generation (SHG) spectroscopy (Chapter 2, Section 2.3.2.1).

In contrast to qPRS imaging, SHG microscopy provides high-resolution images of the collagen fibrils in bone in a record time. This method cannot provide information about compositional variation, but with the inclusion of the polarizer-analyzer couple, it can visualize the in-plane orientation of the MCF (Figure 5.2.1). Theoretically, similarly to the qPRS method, it is possible to calibrate polarized SHG microscopy. Although not yet done on bone, there are studies on SHG application for quantitative orientation and concentration analysis of other materials [384–386]. Potentially, a method like quantitative polarized SHG could analyze a large sample area (mm-range) at a high-speed ($\sim \text{mm}^2/\text{min}$) and a resolution of up to 30 nm. Such areal mapping of MCF spatial orientation could facilitate high-throughput mechanical testing on a micro- to the nanometer range.

Another experimental highlight in this thesis was the site-matched nature of the performed measurements. Matching the locations of the nanoindentation and micropillar compression tests with the qPRS gave assess of the underlying relationship between bone tissue composition and output mechanical properties. While there is a number of reported studies where nanoindentation measurements were spatially matched with the Raman spectroscopy [387–389] or even PRS [390], the site-matched compression tests with qPRS analysis were done for the first time in the course of this thesis. Microscale yield stress properties were found to correlate with the relative mineral content (mineral to matrix ratio) for all investigated species (cow, minipig, human). The correlation between yield stress and the MCF out-of-plane orientation was confirmed in the study on the bovine bone (Chapter 3.1), yet it was not significant for the human bone tissue (Chapter 3.2). This emphasizes that not only site-matched but also volume-matched measurements are required for the future analysis of the structure-properties relationship in human bone tissue.

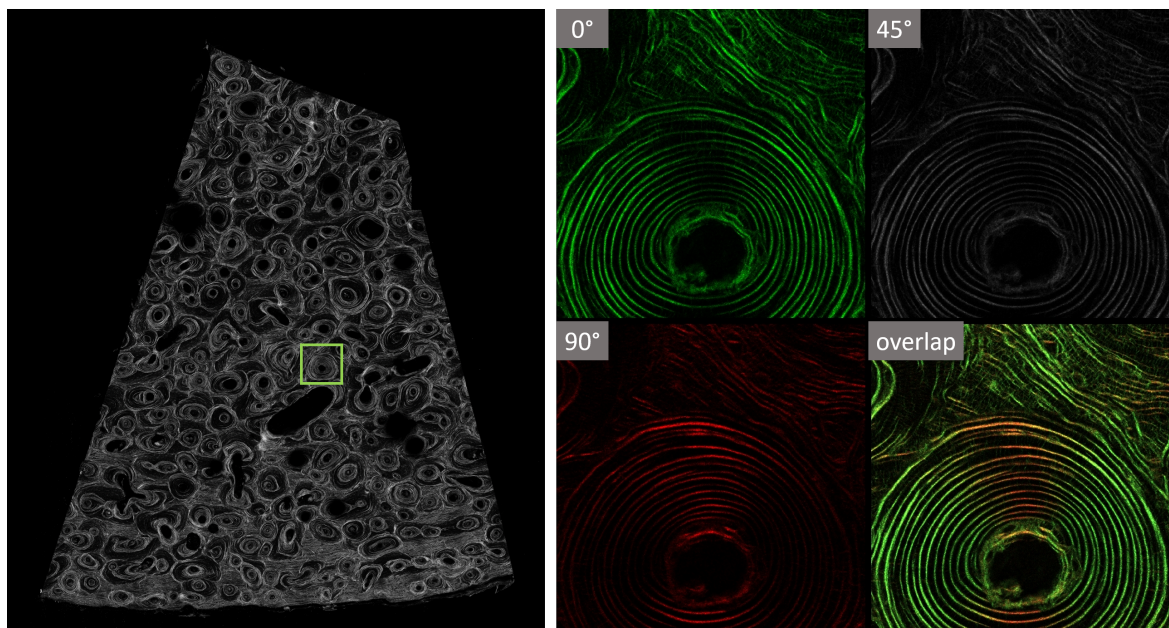


Figure 5.2.1 – Left: SHG overview image of the human cortex. Right: SHG images of the same osteonal region (marked on the overview image) acquired at different analyzer angles (0° , 45° , 90°) and the overlap image with all angles. Image credit: Dr. Justine Kusch-Wieser (Scope M, ETHZ).

As a major part of this thesis, a multimodal high-throughput bone quality assessment in patients was carried out. Although most of the investigated bone characteristics were independent of patient age or gender, the tissue composition did vary with age. More specifically, the collagen cross-link or maturity ratio increased with age, most likely causing the decrease in the relative mineral to matrix content. Different types of the collagen cross-links were already reported to correlate with age [38, 61, 62]. However, a more in-depth analysis of the collagen post-translational modification as well as the variations in non-collagenous proteome for patients would be of high interest for future studies. For this purpose, Raman spectroscopy might not be the most suitable method. But the recent developments in tandem liquid chromatography-mass spectrometry allow to achieve the resolution and robustness to detect hundreds of proteins within the sub-millimeter volumes of bone matrix [162,391,392].

As a result of the multimodal analysis of human bone tissue, a large dataset of experimentally assessed microscale bone properties was collected. The measured yield properties in combination with the local compositional variations expand the currently available data set of bone properties at the microscale. Moreover, bone tissue properties measured in this study were able to predict fracture occurrence with a 0.67 accuracy. This suggests that the inclusion of tissue properties like yield stress, hardness and the patient's age together with the BMD values would improve the current clinical predictions of the bone strength and therefore the fracture risk predictions. Therefore, further studies combining tissue bone properties

with clinically measured BMD values and the patient's medical history are essential for the development of improved fracture risk assessment.

In conclusion, this thesis highlights the complex interplay of tissue-level bone parameters. The applied multimodal framework for bone tissue characterization sheds light on the microscale mechanical, compositional and structural properties and their evolution with age. Assessing bone ECM parameters together with BMD is a perspective approach for fracture risk prediction in the elderly. The developed multimodal framework for the laboratory-based analysis of bone tissue properties could be employed in future studies to analyze the effect of disease and/or treatment on bone performance and skeletal health status.

Appendix

Supporting information for the methods development and validation

A1 Combining polarized Raman spectroscopy and micropillar compression to study microscale structure-property relationships in mineralized tissues

Tatiana Kochetkova^{1,*}, Cinzia Peruzzi^{1,*}, Oliver Braun^{2,4}, Jan Overbeck^{2,4,5}, Anjani K. Maurya^{3,6}, Antonia Neels³, Michel Calame^{2,4,5}, Johann Michler¹, Philippe Zysset⁷, Antonia Neels^{2,5}, Jakob Schwiedrzik^{*1}

¹*Empa, Swiss Federal Laboratories for Materials Science and Technology, Laboratory for Mechanics of Materials and Nanostructures, Thun, Switzerland*

²*Empa, Swiss Federal Laboratories for Materials Science and Technology, Transport at Nanoscale Interfaces Laboratory, Dübendorf, Switzerland*

³*Empa, Swiss Federal Laboratories for Materials Science and Technology, Center for X-Ray Analytics, Dübendorf, Switzerland*

⁴*Department of Physics, University of Basel, Switzerland*

⁵*Swiss Nanoscience Institute, University of Basel, Switzerland*

⁶*Cellular and Biomedical Sciences, Faculty of Medicine, University of Bern, Switzerland*

⁷*ARTORG Center for Biomedical Engineering Research, University of Bern, Switzerland*

**These authors contributed equally to this work*

A1.1 Details on sample preparation

MTLT samples were fixed in specially designed SEM stubs produced in the lab's mechanical workshop, shown in Figure A1.1 A. The stubs featured an angular accuracy $< 0.1^\circ$, so that after polishing using a special holder, the polished sample surface was effectively parallel to the lower stub surface. PRS and SAXS measurements were performed separately on the same MTLT samples with fixed out-of-plane orientations.

Bovine cortical bone samples were cut from the medial part of a cow tibia. Three medial slices were cut radially into smaller sections as shown in Figure A1.1 B. Posterior quadrant sections with higher osteonal bone content were used for the further processing steps described in the main text.

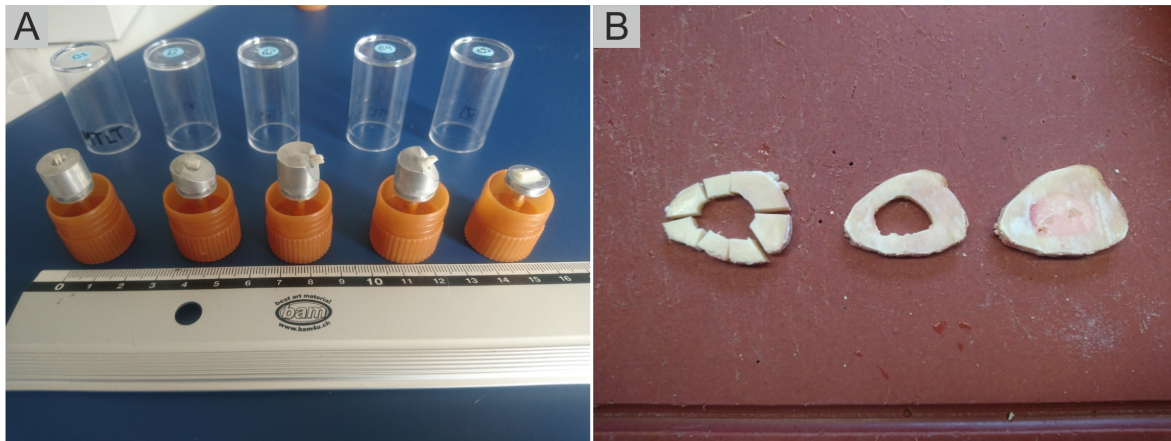


Figure A1.1 – (A) MTLT samples each containing a tendon section cut at 0° , 22.5° , 45° , 67.5° or 90° to the main tendon axis. (B) Bovine cortical bone rough cuts.

A1.2 Polarized Raman spectroscopy

Spectra analysis

- Figure A1.2 (A) Background (BG) subtraction and cosmic ray removal (CRR) for the whole spectra (first order polynomial fit for local minima, `numpy.polyfit`).
- Figure A1.2 (B,C) amide I and amide III peak analysis:
 1. additional linear BG subtraction (`numpy.polyfit`);
 2. double-Lorentzian fit (red) of both amide I and amide III, extracting peak parameters.
- Figure A1.2 (D) Polar plots of integral area of amide I / amide III vs polarization angle θ (red datapoints) fitted with equation 1 from the main text (black solid line) together with theoretical prediction (orange dashed line) as determined using equation S8 described in the section below.

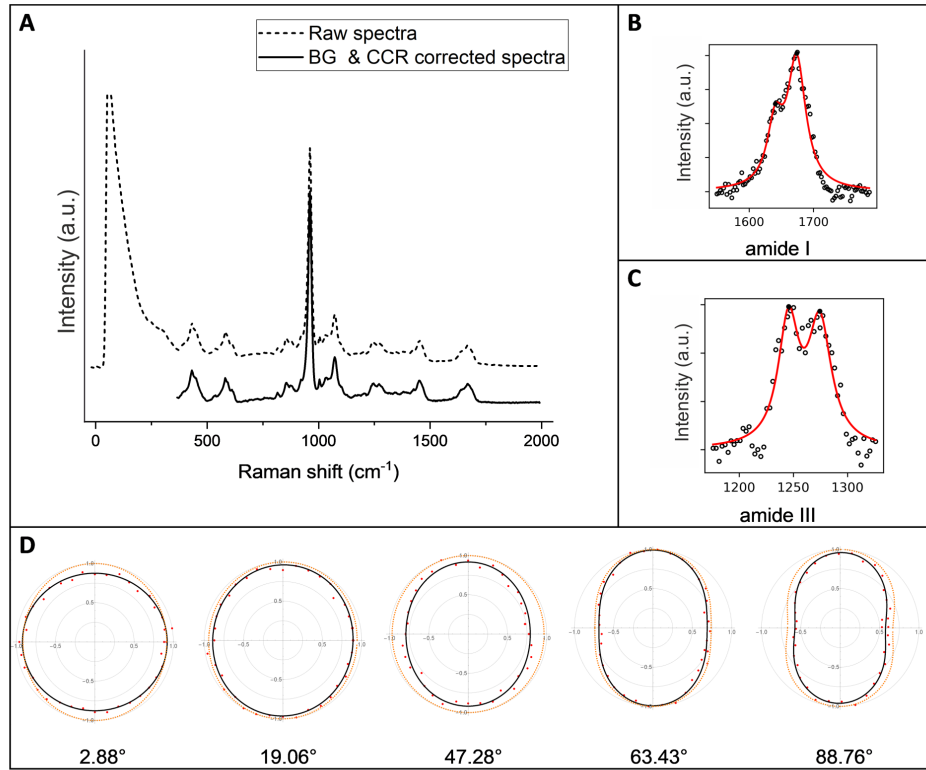


Figure A1.2 – Polarized Raman spectra processing steps for the raw data using Python software.

Theoretical calculations of polarization-dependent Raman scattering intensity

In classic representation of polarized Raman experiments [393] [394], the scattering intensity I_s is proportional to a matrix product between the polarization vectors of the incoming ϵ_i and scattered light ϵ_s and the Raman tensor \mathbf{R} :

$$I_s \propto |\epsilon_i \mathbf{R} \epsilon_s|^2. \quad (\text{A1.1})$$

In our experiments there is no polarizer in the path of scattered light, so the scattering intensity is a norm of a multiplication vector between the Raman tensor and polarization vector of the incoming light [395]:

$$I_s \propto \|\mathbf{R} \epsilon_i\|^2 \quad (\text{A1.2})$$

$$\epsilon_i = (\cos \alpha, \sin \alpha, 0), \quad (\text{A1.3})$$

where α is the polarization angle and the Raman tensors \mathbf{R} for amide I and amide III vibrations in the α -helix polypeptide are isotropic in the orthogonal plane with the respective factors: $a = 0.537$ and $b = 0.707$ [396] [397].

$$\mathbf{R}_{amideI} = \begin{pmatrix} \alpha & 0 & 0 \\ 0 & \alpha & 0 \\ 0 & 0 & \alpha \end{pmatrix} \quad (\text{A1.4})$$

$$\mathbf{R}_{amideIII} = \begin{pmatrix} b & 0 & 0 \\ 0 & b & 0 \\ 0 & 0 & 1 \end{pmatrix} \quad (\text{A1.5})$$

The Raman tensors were rotated around the X axis (out-of-plane, θ) and Z axis (in-plane, φ) to align with the assumed MCF direction. The output theoretical predictions for amide I and amide III scattering intensities for different orientations of the collagen molecule were calculated using equation A1.2 and are shown below.

$$\begin{aligned} I_{amideI} &= 4 \left[(a-1) \cos[\alpha] \cos[\varphi] \sin[\theta]^2 \sin[\varphi] - \sin[\alpha] \left(\cos[\varphi]^2 (a \cos[\theta]^2 \right. \right. \\ &\quad \left. \left. + \sin[\theta]^2) + a \sin[\varphi]^2 \right) \right]^2 \\ &\quad + 4 \left[(a-1) \cos[\varphi] \sin[\alpha] \sin[\theta]^2 \sin[\varphi] - \cos[\alpha] \left(a \cos[\varphi]^2 \right. \right. \\ &\quad \left. \left. + (a \cos[\theta]^2 + \sin[\theta]^2) \sin[\varphi]^2 \right) \right]^2 + [(a-1) \sin[2\theta] \sin[\alpha + \varphi]]^2 \quad (\text{A1.6}) \end{aligned}$$

$$\begin{aligned} I_{amideIII} &= 4 \left[(b-1) \cos[\alpha] \cos[\varphi] \sin[\theta]^2 \sin[\varphi] - \sin[\alpha] \left(\cos[\varphi]^2 (b \cos[\theta]^2 \right. \right. \\ &\quad \left. \left. + \sin[\theta]^2) + b \sin[\varphi]^2 \right) \right]^2 \\ &\quad + 4 \left[(b-1) \cos[\varphi] \sin[\alpha] \sin[\theta]^2 \sin[\varphi] - \cos[\alpha] \left(b \cos[\varphi]^2 \right. \right. \\ &\quad \left. \left. + (b \cos[\theta]^2 + \sin[\theta]^2) \sin[\varphi]^2 \right) \right]^2 + [(b-1) \sin[2\theta] \sin[\alpha + \varphi]]^2 \quad (\text{A1.7}) \end{aligned}$$

The output theoretical prediction I_s for the present study:

$$I_s = I_{amideI} / I_{amideIII} \quad (\text{A1.8})$$

We found that the theoretical prediction function I_s (Equation A1.8) was not suitable for the analytical out-of-plane angle θ extraction due to the interdependency of the output parameters and the numerical problems during data fitting that follow. Instead of using the theoretical function to fit the experimental polarization-dependent intensities, we therefore proceeded to utilize the simplified function proposed by Bao et al. [225]:

$$f(\alpha, \varphi) = A \cos^2(\alpha + \varphi) + B \sin^2(\alpha + \varphi). \quad (\text{A1.9})$$

We measured the Raman scattering intensity of amide I / amide III versus the out-of-plane angle of the MCFs for the model material (MTLT), yielding the theta-dependent ratio A/B . In order to make an educated guess for the theta dependence of A/B we matched the theoreti-

cal prediction function (Equation A1.8) to the simplified one (Equation A1.9 (Equation 3.1.1 from chapter 3.1)). This was accomplished by fixing $\varphi = 0$ and comparing the two resulting intensities for a given set of out-of-plane angles θ and polarization angles α . This allowed us to correlate the ratio A/B to the out of plane angle theta. However, due to the complicated mathematical form of the theoretical prediction I_s (Equation A1.8), we were not able to obtain a closed and compact expression for A/B as a function of theta. The anisotropy parameter A/B as a function of out-of-plane angle θ , showed good agreement with equation A1.10(3.1.4) ($R^2 > 0.99$, Figure A1.3). We decided to continue working with equation A1.10(3.1.4) from the chapter 3.1 as it resembles the theoretical prediction but has a simplified form. This function was used to fit experimentally collected anisotropy parameters A/B for the different out-of-plane angles (Chapter 3.1, Figure 3.1.3).

$$f(\theta) = C_0 + C_2 \sin^2(\theta) + C_4 \sin^4(\theta) \quad (\text{A1.10})$$

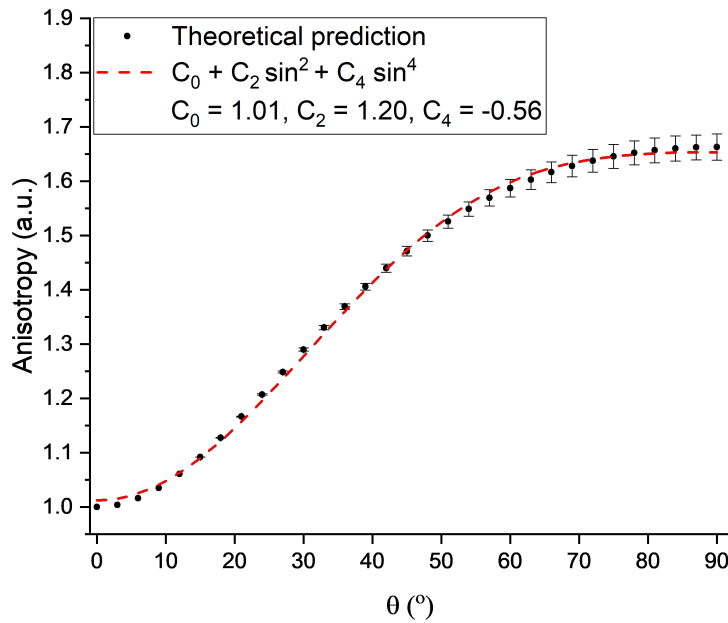


Figure A1.3 – Theoretically predicted anisotropy parameters A/B for different out-of-plane angles θ . The coefficient of determination $R^2 = 0.99$.

Line-mapping of bovine cortical bone osteon

Polarized Raman line-maps were collected on three bovine bone osteons to check for fibril orientation variations within each osteon. For each map a set of polarized Raman spectra were collected along the line with $2\mu\text{m}$ steps going from Haversian canal towards the outer end of the osteon, as marked in Figure A1.4. The data processing for each step was as described in Supplementary information A1.2. The values of out-of-plane angles for axial and in-plane angles for transverse osteons were taken for analysis of fibril alignment along

the Haversian canal.

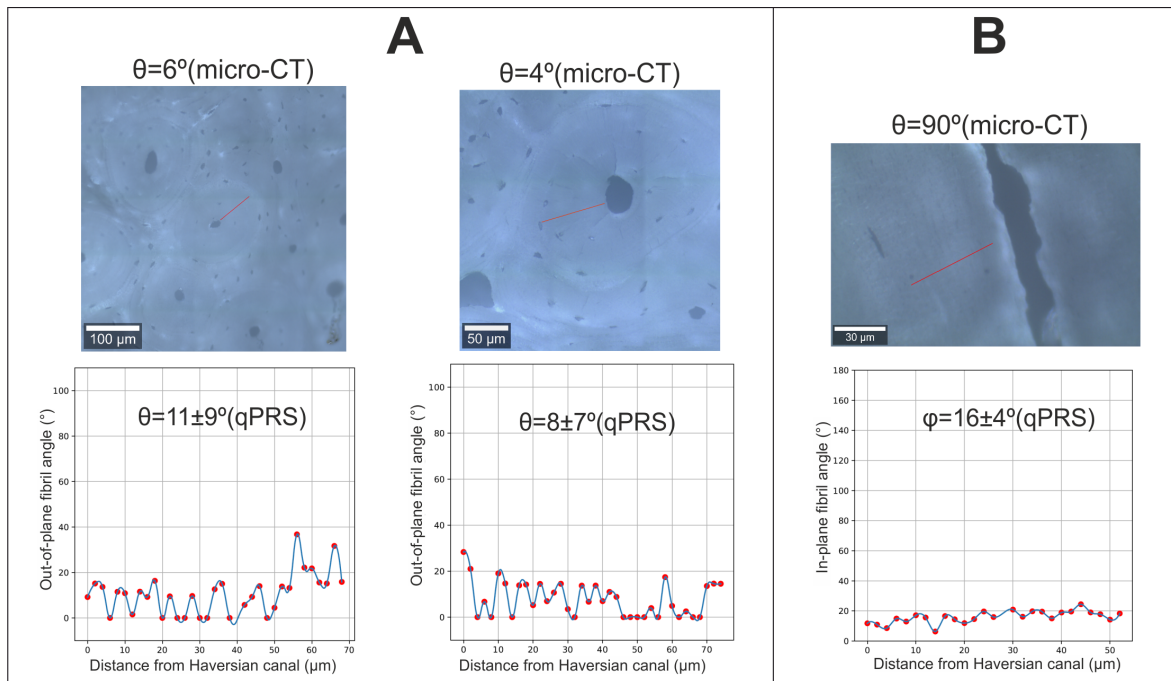


Figure A1.4 – Polarized Raman line-maps collected from axial (A) and transverse (B) osteons. Top: optical microscope images with out-of-plane osteonal angles as determined from micro-CT, red line indicates where the scan was taken. Bottom: line-maps for the out-of-plane MCF angles determined using qPRS, blue line is the guide to the eye.

Sample integrity during Raman measurements

To determine that the imaging parameters (power, integration time) do not cause structural modifications of the mineralized tissue, we performed time dependent measurements of 50 minutes (five times the time of a usual experiment) and monitored the integral area of the amide I and amide III peak. For this, a set of polarized Raman spectra was collected from the same spot of the cortical bone osteon with the fixed laser polarization. Each of 100 spectra was collected for 30s with the setup parameters as used in this work: 785nm laser at 30mW power with 50x objective, $NA = 0.80$. As can be seen in Figure A1.5, there is a clear increase of peak integral area for both amide I and III. However, the change of the integral area is below 5% for the first 20 spectra for both amide I and amide III vibrations, which corresponds to the time needed to collect a set of polarized Raman spectra in the present work. We therefore conclude that the sample integrity is preserved during the complete qPRS measurements.

qPRS angular uncertainty

To estimate the error of the qPRS method, we correlated the real out-of-plane angles of MCF, determined from the SAXS measurements, with the re-calculated angles, determined from

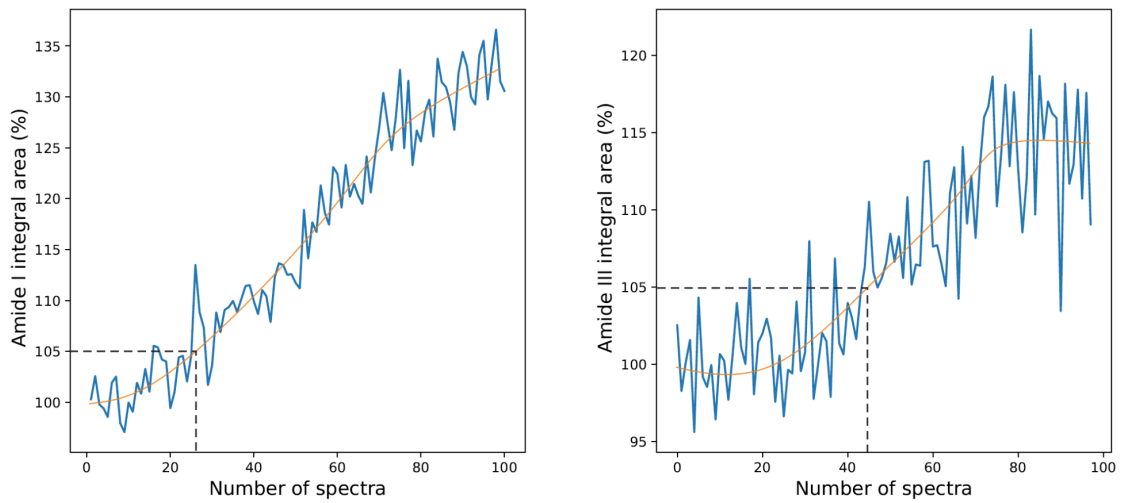


Figure A1.5 – Change of amide I and amide III integral areas over time. Blue and orange line are raw and averaged data, respectively, black dashed line indicates the 5% increase of the integral area.

the Raman measurements. The standard error of the estimate (SEE) from the linear fit was taken as the angular uncertainty resulting in $\theta^{err} = 9.7^\circ$.

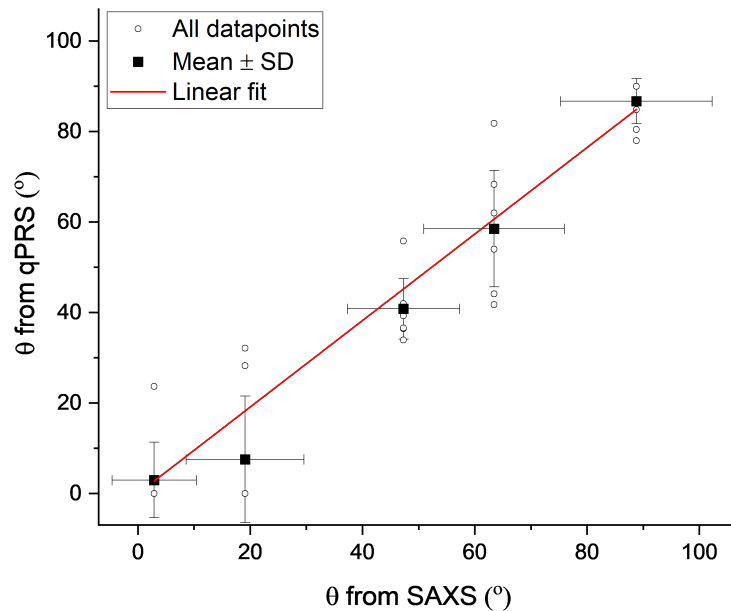


Figure A1.6 – Out-of-plane MCF angles, calculated for MTLT using qPRS versus out-of-plane MCF angle θ , determined from SAXS measurements.

qPRS method using amide I/ ν_2PO_4

The ratio of amide I over ν_2PO_4 is a possible alternative indicator of MCFs orientation. The SNR ratio of the amide I/ ν_2PO_4 is comparable to the one of amide I/ amide III and follows as well the polarization dependence of the amide I band. A possible pitfall would come up from the variation in the mineral content: while the ratio of amide I/ amide III corresponds solely to the organic constituents, the ratio of amide I over ν_2PO_4 is dependent on the level of mineralization. Nevertheless, since our data analysis procedure includes normalizing the output polar plot of the peak ratios vs laser polarization (Figure A1.7 A), the extracted anisotropy parameter A/B will not be dependent on the tissue mineralization. We demonstrate an excellent correlation between the two Raman band ratios for MTLT samples (Figure A1.7 B, $R^2 = 0.98$, $p = 0.01$). Moreover, we calibrated the anisotropy parameter A/B, extracted from amide I/ ν_2PO_4 polarization dependence, with the fibril out-of-plane angle θ , taken from the SAXS measurements (Figure A1.7 C, $R^2 = 0.99$). The new parameters of the calibration function (Equation 3.1.4 from chapter 3.1 are shown in the Figure A1.7 and can be used in the future for correlating the out-of-plane MCF angle with the anisotropy parameters extracted from amide I/ ν_2PO_4 Raman band ratios.

A1.3 Correlation between bone biochemistry parameters and mechanical properties

All of the bovine cortical bone samples used in this study were cut from the same tibia and underwent identical sample preparation steps. Following the study of Roschger et al. [226], the mineral to matrix ratios (ν_2PO_4 /amide III), determined in this study, can be correlated to the Ca content. For all of the tested bovine osteons, a relative standard deviation of mineral to matrix ratios of $\sim 7\%$ was observed, which was not sufficient to detect a significant correlation with the mechanical parameters ($p = 0.6$ for both elastic modulus and yield stress, Figure A1.8 A,D). To assess the mineral biochemistry of the specimens, we additionally analyzed the mineral crystallinity [227] [158] [159] [228] using the collected polarized Raman spectra. As a measure of mineral crystallinity, we used the inverse of the primary phosphate peak width, averaged over different laser polarizations. The relative standard deviation of crystallinity between the tested bovine cortical bone osteons did not exceed 1% and no significant correlation with the elastic modulus ($p = 0.3$, Figure A1.8 B) nor the yield stress ($p = 0.2$, Figure S9 E) was observed.

For the qPRS method we employed the polarization dependence of amide I and amide III Raman bands, which mainly correspond to the collagenous matrix [174]. However, the variations of non-collagenous proteins (NCPs) content may as well affect the output mechanical properties. To assess the variation of NCP content, we additionally analyzed the C-H bending Raman band at 1458cm^{-1} , which corresponds to both collagen and NCPs [229]. Although

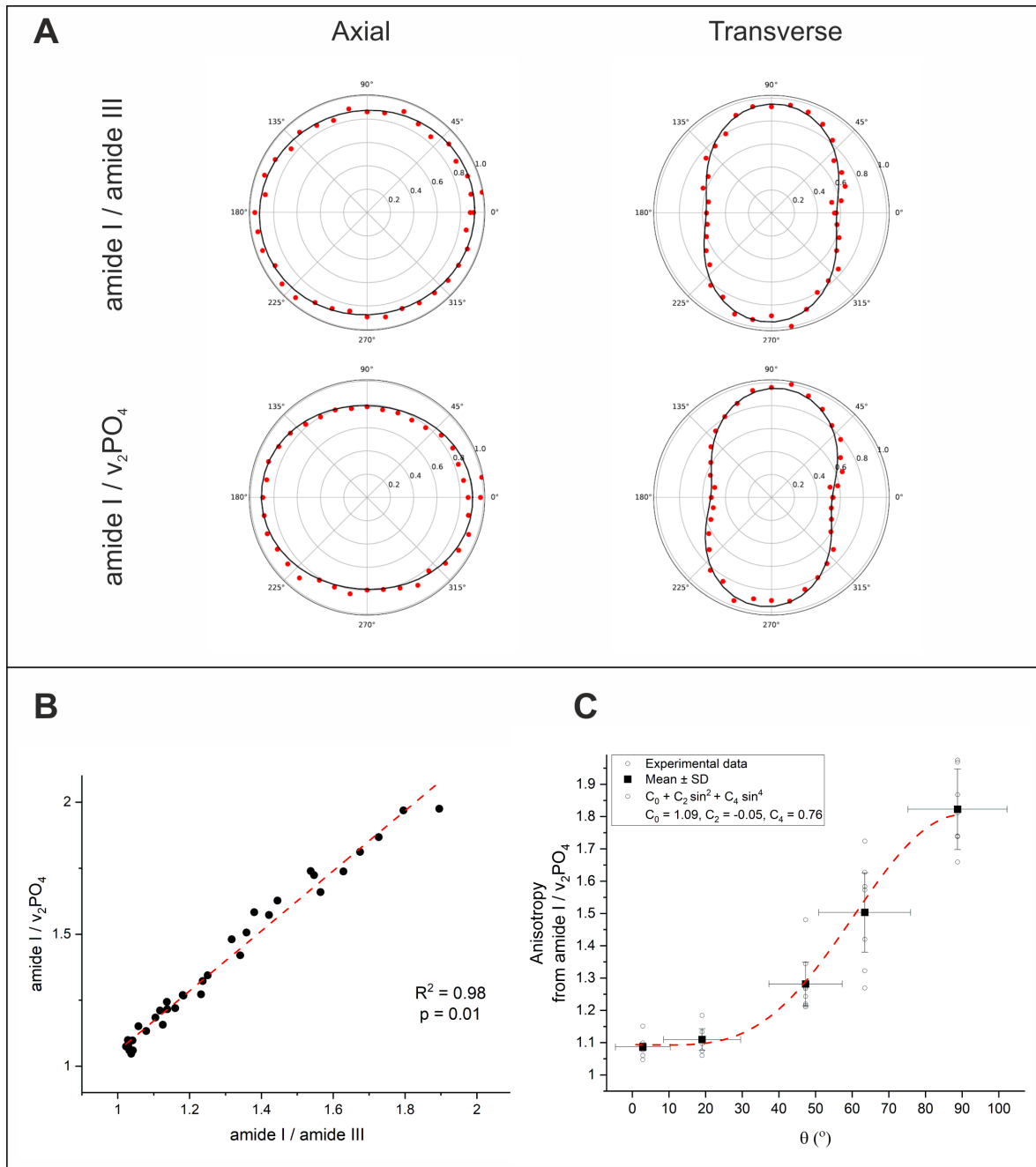


Figure A1.7 – Comparison of the amide I/ amide III and amide I/ ν_2PO_4 Raman band ratios that can be used for spectral anisotropy A/B calculation and consequent out-of-plane angle estimation. (A) Polarization dependence for the two Raman band ratios for both axial and transverse MTLT sample orientation. (B) Correlation between the two Raman band ratios as estimated for MTLT samples. (C) Anisotropy of amide I/ ν_2PO_4 Raman band ratios at different out-of-plane fibril orientation θ for MTLT samples. The coefficient of determination $R^2 = 0.99$.

the ratio of amide I/ CH bending has been reported to quantify the relative concentrations of collagen versus NCPs [230], we found it to be strongly dependent on the MCF orientation ($R^2 = 0.68$, $p < 0.01$, Figure A1.8 G). We therefore used the ratio of amide III/ CH bending to quantify the relative concentrations of collagen versus NCPs, as it has no significant orientation dependence ($p = 0.1$, Figure A1.8 H). Around 4% of relative standard deviation of Amide III/ CH ratios was observed for the tested osteons. Moreover, we found a moderate dependence between the Amide III/ CH ratio and the measured mechanical properties ($R^2 = 0.5$, $p = 0.01$ for both elastic modulus and yield stress, Figure A1.8 C,F). We acknowledge that observed variations of collagen/NCPs relative concentrations partially contribute to the observed variations of the mechanical properties.

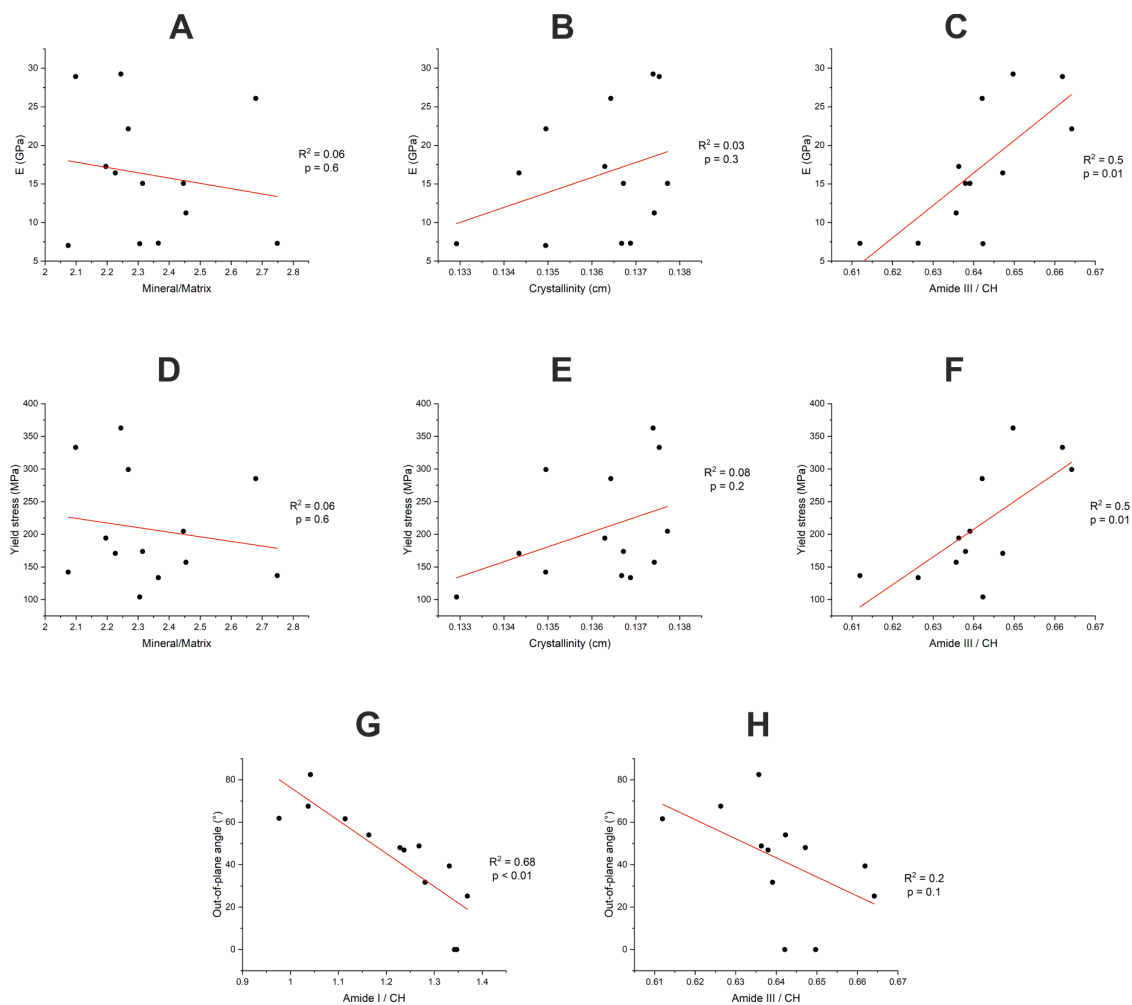


Figure A1.8 – Correlation between bone biochemistry parameters, as assessed by PRS, and mechanical properties, as measured using micropillar compression.(A-C) Correlation between the osteonal Mineral-to-matrix ratios (A), Crystallinity (B), Amide III/CH-bending ratios (C) and the output elastic modulus. (D-F) Correlation between the osteonal Mineral-to-matrix ratios (D), Crystallinity (E), Amide III/CH-bending ratios (F) and the output yield stress.(G-H) Correlation between the Amide I/CH-bending (G), Amide III/CH-bending ratios (H) and the out-of-plane MCFs angle.

A1.4 SAXS measurements

Orientation analysis of MCF in MTLT

The orientation of MCF were estimated from the azimuthal broadening of intensities along the streak axis. For this, the azimuthal profiles were extracted in the q range of $0.356 - 0.783 \text{ nm}^{-1}$ and fitted with the Lorentzian function. The angular position of the maximum intensity was extracted for each fitted profile with respect to the surface normal vector orientation, obtained from 2D Nanography (Figure A1.9). 2D Nanography was obtained by representing the total intensity counts from 0.5 seconds frame on the detector for each 0.01 mm steps sample movement in corresponding x and y direction. The mean out-of-plane MCF angle θ was taken as the averaged position of the profiles maximum intensity. Azimuthal scans and all the fittings were obtained using Matlab R2019b.

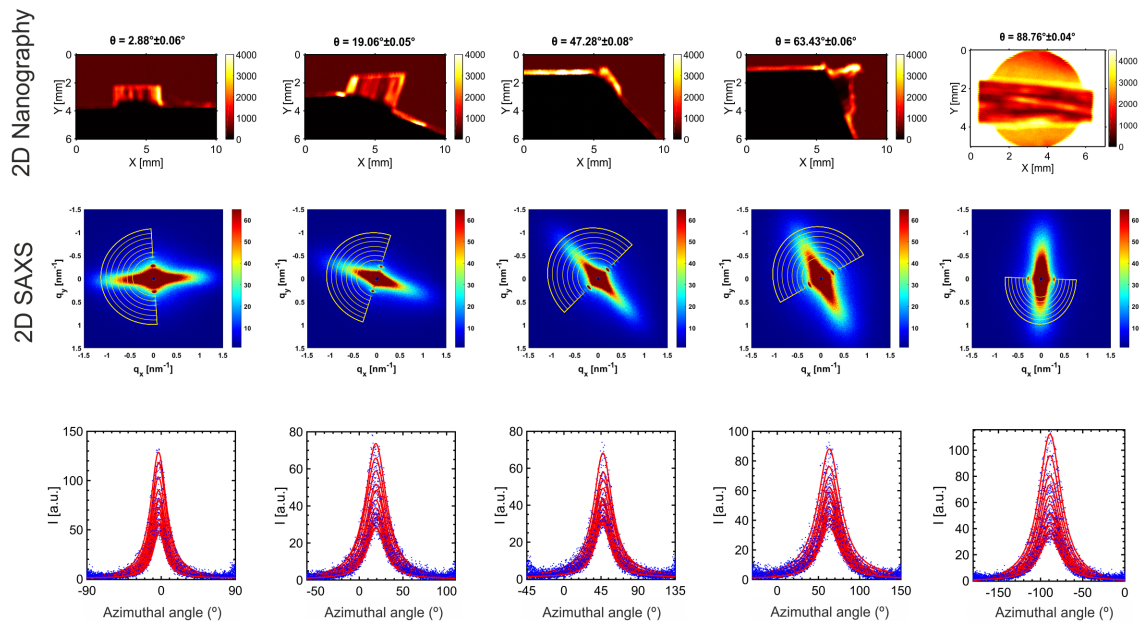


Figure A1.9 – 2D Nanography and 2D SAXS profiles with schematically marked q -range and output azimuthal profiles fitted with the Lorentzian function.

Ruland streak method for MCF misorientation estimation

We applied the Ruland analysis on the streak signal to quantify the alignment of MCF. In this method, the azimuthal broadening of intensities along the streak axis, which relates to the anisotropic scattering in the aligned fibrous samples, is evaluated [234] [398]. From the azimuthal broadening B_{obs} , the fibril length l_f and misorientation width B_{phi} were obtained from the following equation:

$$B_{obs} = \frac{2\pi}{l_f q} + B_{phi} \quad (\text{A1.11})$$

where the azimuthal broadening B_{obs} is defined as the full width at half maximum (FWHM) of the azimuthal profile fitted using the Lorentzian peak function at particular q (bottom of

Figure A1.9). In this study, azimuthal profiles were extracted in the q -range of $0.356 - 0.783\text{nm}^{-1}$ with step size of 0.036nm^{-1} . The misorientation width was obtained from the intercept of the B_{obs} vs. the inverse scattering vector modulus q^{-1} , as presented in Figure A1.10.

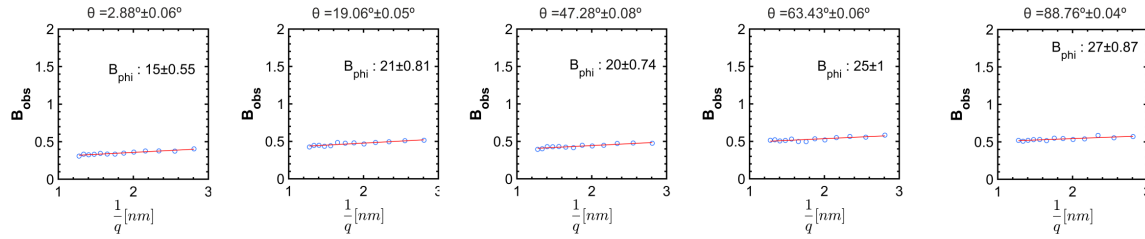


Figure A1.10 – Azimuthal broadening B_{obs} of the streak signal as a function of inverse scattering vector modulus q for MTLT samples presented together with the linear fit according to equation A1.11 and output misorientation width B_{phi} .

A1.5 Osteonal angle calculation

The spatial orientation of osteons was estimated using ImageJ 1.52v [235] and BoneJ 1.4.3 [236]. The main analysis steps are demonstrated in the Figure A1.11. All sample scans were tilt corrected (Untilt Stack plugin) and correlated with the optical image to locate the osteons of interest. Chosen osteons were cropped and binarized using Otsu's threshold clustering algorithm. At the same time Haversian canal of the osteon was checked for irregularities: only the top segment without branching or sudden changes in orientation was used. Using the Moment of Inertia plugin, three orthogonal principal axes were automatically determined for each Haversian canal and the rotation matrix in reference to the stacks main axis was constructed. The out-of-plane orientation θ of each osteon was taken as the angle between the principal axis along the Haversian canal and the z axis of stacks (Figure A1.11, right). The angle was extracted from the rotation matrix and correlated later with the polarized Raman measurements.

A1.6 Mechanical data manipulation

Mechanical modeling

Apparent elastic modulus E_{app} was modeled as a function of collagen fibril orientation. For this, a transversely isotropic compliance tensor (Equation A1.12) was rotated around one axis from the transverse plane. By fitting the output equation (Equation A1.13), the apparent elastic modulus was expressed as a function of the fibrils angle.

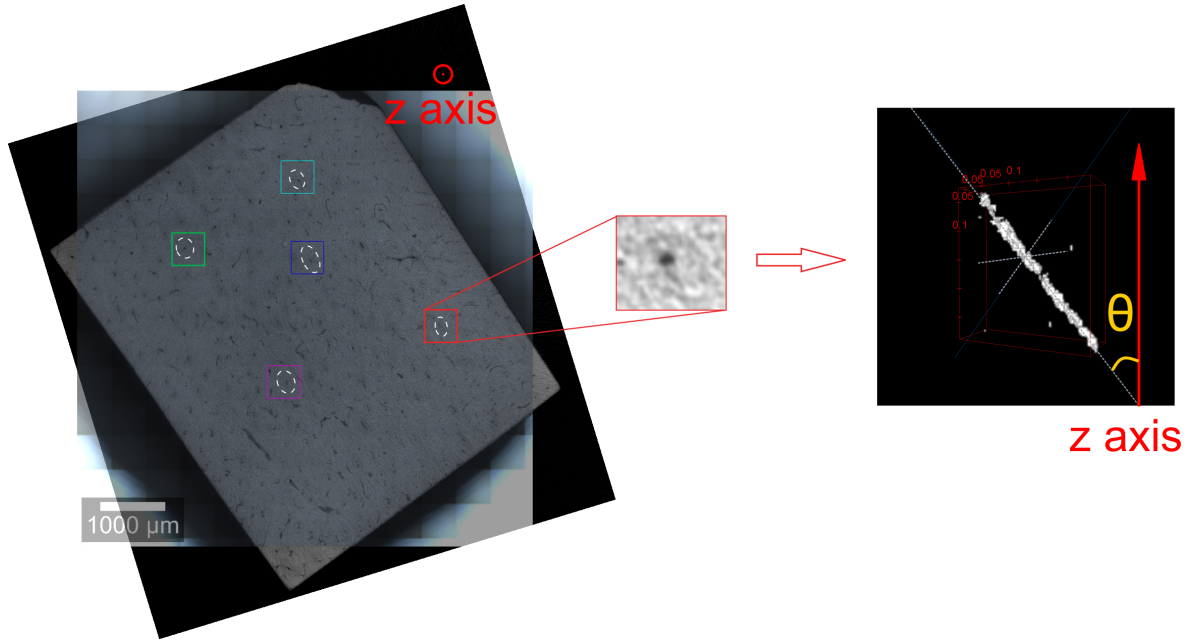


Figure A1.11 – Osteonal orientation determination steps using using ImageJ and BoneJ. Left: micro-CT scan of the chosen sample was tilt corrected (Untilt Stack plugin) and correlated with the optical image to locate the osteons of interest; stacks with the chosen osteon were cropped and binarized. Right: snapshot of the 3D view on the binarized volume of interest (note: Haversian canal is shown in white); three orthogonal principal axes (grey lines on the snapshot) were automatically determined for each Haversian canal using the Moment of Inertia plugin, the rotation matrix in reference to the stacks main axis (z axis on the figure) was constructed. The out-of-plane orientation θ of each osteon was taken as the angle between the principal axis along the Haversian canal and the z axis of the stacks.

$$[[C]] = \begin{pmatrix} \frac{1}{E_t} & -\frac{\nu_t}{E_t} & -\frac{\nu_a}{E_a} & 0 & 0 & 0 \\ -\frac{\nu_t}{E_t} & \frac{1}{E_t} & -\frac{\nu_a}{E_a} & 0 & 0 & 0 \\ -\frac{\nu_a}{E_a} & -\frac{\nu_a}{E_a} & \frac{1}{E_a} & 0 & 0 & 0 \\ 0 & 0 & 0 & \frac{1}{2\mu_a} & 0 & 0 \\ 0 & 0 & 0 & 0 & \frac{1}{2\mu_a} & 0 \\ 0 & 0 & 0 & 0 & 0 & \frac{1+\nu_t}{E_t} \end{pmatrix} \quad (A1.12)$$

$$E_{app} = \left(\frac{\cos^4(\theta)}{E_a} + \frac{\sin^4(\theta)}{E_t} + \left(\frac{1}{\mu_a} - 2\frac{\nu_a}{E_a} \right) \cos^2(\theta) \sin^2(\theta) \right)^{-1} \quad (A1.13)$$

Elastic moduli were extracted from micropillar compression tests and fibril orientation from PRS measurements, where E_a and E_t - axial and transverse elastic modulus values accordingly, ν_a and ν_t – Poisson ratios and μ_a - shear modulus.

Compliance tensor (Equation A1.12) was estimated based on the output elastic moduli from

the micropillar compression tests and is reported here for the sake of completeness.

$$[[C]] = \begin{pmatrix} 0.13 & -0.041 & -0.025 & 0 & 0 & 0 \\ -0.041 & 0.13 & -0.025 & 0 & 0 & 0 \\ -0.025 & -0.025 & 0.036 & 0 & 0 & 0 \\ 0 & 0 & 0 & 0.061 & 0 & 0 \\ 0 & 0 & 0 & 0 & 0.061 & 0 \\ 0 & 0 & 0 & 0 & 0 & 0.17 \end{pmatrix}$$

Yield stress was modeled as a function of collagen fibril orientation using the Tsai-Hill composite failure criterion [238]. For unidirectional fiber-reinforced composite materials subjected to in-plane stress, the failure criterion is given by:

$$\left(\frac{\sigma_a}{X}\right)^2 + \left(\frac{\sigma_a \sigma_t}{X^2}\right) \left(\frac{\sigma_t}{Y}\right)^2 + \left(\frac{\tau}{S}\right)^2 = 1 \quad (\text{A1.14})$$

where σ_a and σ_t are the normal stresses along the axial and transverse directions of the composite, respectively, whereas τ is the in-plane shear stress. X , Y and S symbolize the longitudinal, transversal and shear strength of the composite [238].

Under uniaxial loading, the normal and shear stresses can be defined as a function of the fiber angle θ , as:

$$\begin{aligned} \sigma_a &= \sigma_x \cos^2(\theta) \\ \sigma_t &= \sigma_x \sin^2(\theta) \\ \tau &= \sigma_x \cos(\theta) \sin(\theta) \end{aligned} \quad (\text{A1.15})$$

where σ_x is the stress applied along the loading axis [238]. For a composite having its fibers oriented along $\theta = 0^\circ$, it is possible to express its strength with respect to the uniaxial loading direction by inserting equations (A1.15) into equation (A1.14) [238]:

$$\sigma_x = \left(\left(\frac{\cos^2(\theta)}{X} \right)^2 - \left(\frac{\sin(\theta) \cos(\theta)}{X} \right)^2 + \left(\frac{\sin^2(\theta)}{Y} \right)^2 + \left(\frac{\sin(\theta) \cos(\theta)}{S} \right)^2 \right)^{-1/2} \quad (\text{A1.16})$$

Mechanical data over measurement time

To assess whether or not an equilibrium state had been reached in terms of hydration of the micropillars, it was checked whether the measured mechanical properties, i.e. elastic modulus and yield stress, changed over time throughout the experimental campaign. No

significant trend was found for elastic modulus or yield stress ($p > 0.05$) as a function of time.

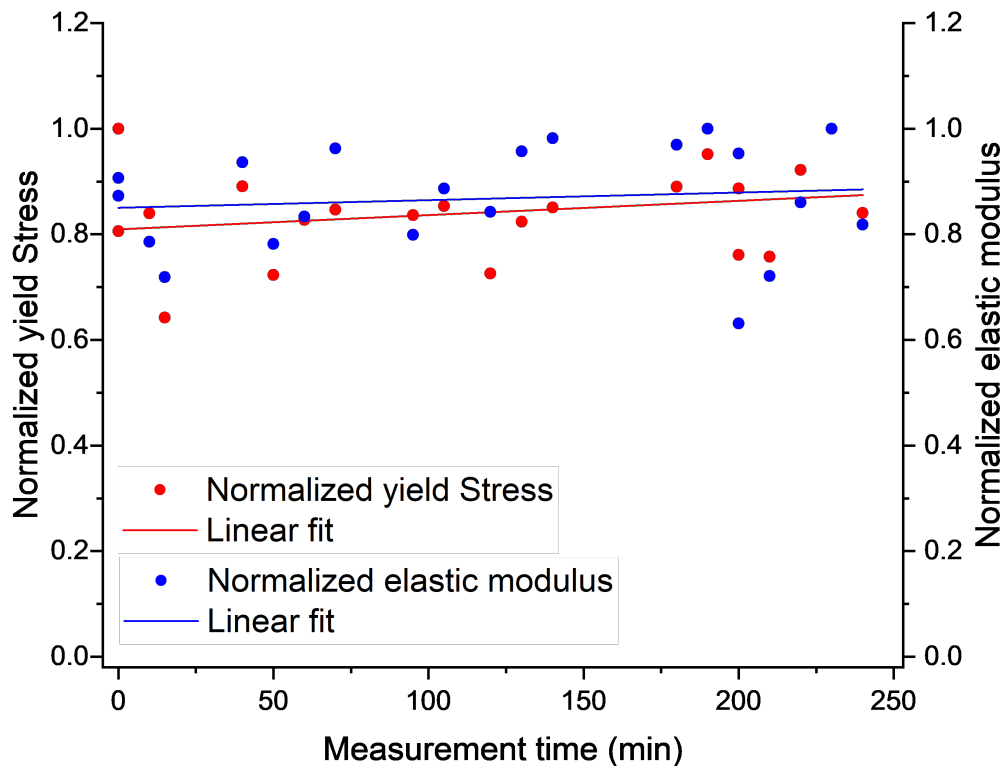


Figure A1.12 – Change of elastic modulus and yield stress within the measurement time. Values were normalized over the day of measurements.

A2 Assessing minipig compact jawbone quality at the microscale

Tatiana Kochetkova¹, Alexander Groetsch¹, Michael Indermaur², Cinzia Peruzzi¹, Stefan Remund³, Beat Neuenschwander³, Benjamin Bellon^{4,5}, Johann Michler¹, Philippe Zysset², Jakob Schwiedrzik¹

¹*Empa, Swiss Federal Laboratories for Materials Science and Technology, Laboratory for Mechanics of Materials and Nanostructures, Thun, Switzerland*

²*ARTORG Center for Biomedical Engineering Research, University of Bern, Switzerland*

³*Institute for Applied Laser, Photonics and Surface technologies (ALPS), Bern University of Applied Sciences, Burgdorf, Switzerland*

⁴*Institut Straumann AG, Basel, Switzerland*

⁵*Department of Periodontology, Faculty of Dentistry, University of Zürich, Zürich, Switzerland*

***Corresponding Authors:** tatiana.kochetkova@empa.ch; jakob.schwiedrzik@empa.ch

A2.1 Estimated heat accumulation during laser ablation

Accumulated heat during laser ablation was estimated following the work of R. Weber et al. [399,400]. For the unidirectional scanning mode, the finite number of subsequent pulses on the same spot causes heat accumulation. The temperature fields of each pulse can be summed up in time and space when the material parameters are taken as constant. Solving the heat conduction equation for the 3D heat flow leads to the temperature field shown in eq. A2.17, where the heat residual Q_{3D} define the heat which is released in an infinitely short time at $t = 0$.

$$\Delta T = \frac{Q_{3D}}{\rho c_p \sqrt{\left(\frac{4\pi\kappa}{f_r}\right)^3}} b_{3D} \quad (\text{A2.17})$$

Where

$$b_{3D} = -\frac{2}{\sqrt{\Delta f_r}} + 2.61. \quad (\text{A2.18})$$

The input values used for the calculations are summed up in Table A1. The bone tissue parameters were taken from S. McPhee and A. Groetsch et al. [401].

Table A2.1 – Laser ablation and bone tissue parameters used for the heat accumulation calculations.

$P_{av} =$	0.012	W	Average lase power
$f_{rep} =$	3	kHz	Repetition rate
$E_p =$	4	μJ	Pulse energy
$w_0 =$	7	μm	Spot radius
$R =$	0.4		Surface Reflectivity
$\eta =$	0.5		Absorbed part converted to heat
$v_{mark} =$	15	mm/s	Laser scanning speed
$p_x =$	5	μm	Distance between 2 pulses
$n_p =$	3		Number of pulses at the same position*
$t =$	0.001	s	Time for n_p Pulses
$\rho =$	2033	kg/m ³	Density
$c_p =$	1440	J/kg/K	Specific heat
$k =$	0.54	W/m/K	Thermal conductivity
$\kappa =$	1.8E-07	m ² /s	Thermal diffusivity

* The number of pulses is calculated by dividing the beam diameter by the distance between 2 pulses.

As a result, residual heat is estimated to be $Q_{3D}=2.4 \mu\text{J}$ and the maximum temperature increase $\Delta T = 55.6^\circ\text{C}$. This temperature is about 10°C below the denaturation point of na-

tive hydrated collagen, and 100°C below the denaturation point of dehydrated mineralized collagen [402]. Since the period between two consecutive laser ablations at the same spot exceeds 2 min, there is no additional heat accumulation between the consecutive ablation layers. Moreover, these calculations were carried out with several assumptions: (i) energy input is taken as the point source with instantaneous stationary energy, (ii) surface instead of volume absorption, and (iii) the surface is assumed to be fully isolated. These simplifications lead to overestimated heat accumulation. We assume that the real heat accumulations during ablation are below the calculated ones.

It is important to mention that we used simplified estimations of the pulse to pulse heat accumulations, as the heating from the pulse itself on a short timescale was not discussed. This aspect would require additional, more time expensive simulations following the two temperature model as proposed by S. McPhee and A. Groetsch et al. [401].

A2.2 FE simulations of micropillar taper effect on the output mechanical properties

We determined the effects of the micropillars' taper on the elastic modulus, yield stress, and strain by means of finite element (FE) simulations. The average dimensions of the nine samples (25 micropillars per sample) were determined by HRSEM (Hitachi S4800, Japan). These average dimensions were used to model the micropillars with and without taper in Abaqus/CAE (Dassault Systemes Simulia Corp., Johnston, Rhode Island, USA). For the micropillars without taper, the bottom diameter was set equal to the top diameter. The substrate below the micropillar was also included in the model to account for substrate compliance. A displacement of 10% of the micropillar height was applied, which is equal to 10% strain. Young's modulus was set to $E = 27.65$ GPa and Poisson's ratio to $\nu = 0.3$. The standard von Mises plasticity model was used and the yield stress was set to $\sigma_y = 0.318$ GPa. The Young's modulus and the yield stress are based on experimental results from a former study [161]. Hexahedral elements (C3D8) were used to mesh the model and a mesh sensitivity analysis was conducted. The mesh convergence was achieved when reducing the size of the elements by half resulted in a change in yield stress of less than 0.1%. The effect of the taper on the elastic modulus, the yield stress and strain are represented as

$$k_E = \frac{E_{ideal}}{E_{tapered}}, k_\sigma = \frac{\sigma_{ideal}}{\sigma_{tapered}}, k_\xi = \frac{\xi_{ideal}}{\xi_{tapered}}. \quad (A2.19)$$

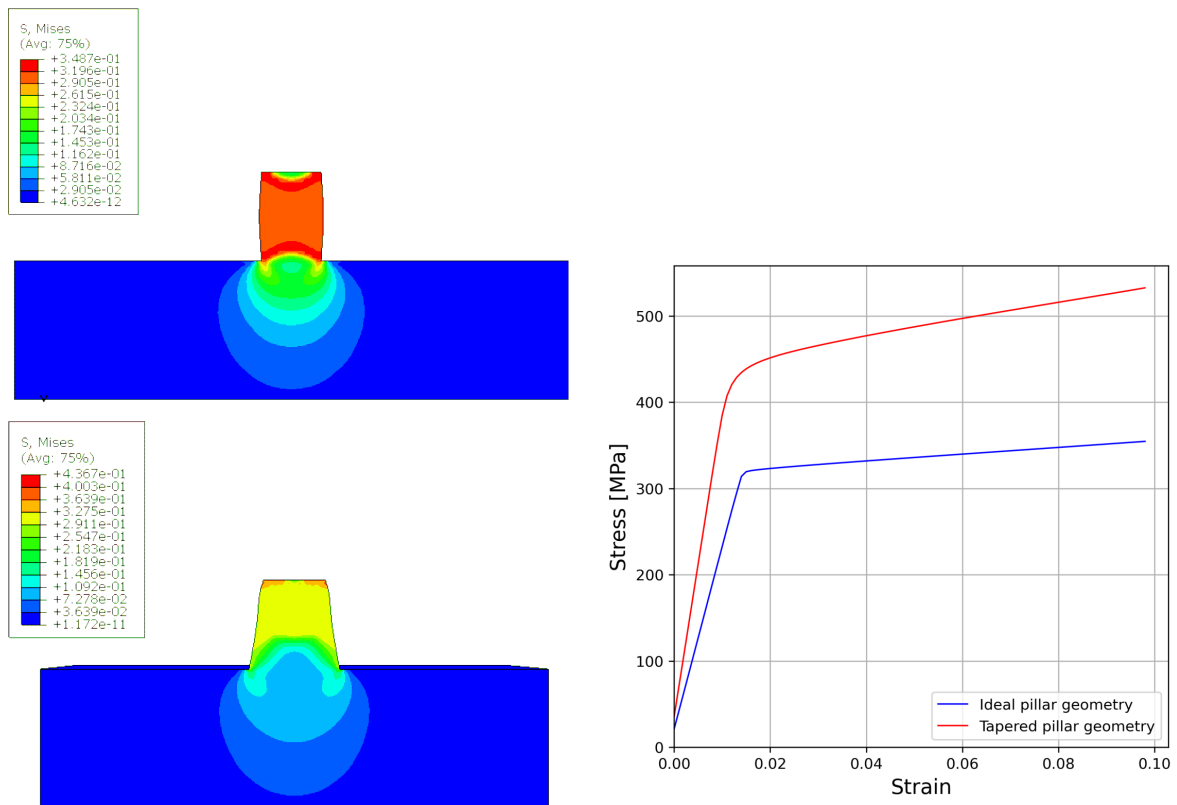


Figure A2.1 – Distribution of von Mises stresses during compression simulations for micropillars with ideal (top) and tapered (bottom) geometries and corresponding stress-strain curves.

A2.3 Raman spectra processing

(A) Background (BG) subtraction for the whole spectra (second-order polynomial fit for local minima, `numpy.polyfit`). (B) ν_2PO_4 and amide III band analysis:

- additional linear BG subtraction (first order polynomial fit for local minima on both sides of the band, `numpy.polyfit`);
- double-Lorentzian fit of ν_2PO_4 (blue) and amide III (red); extracting peak integral areas: $410\text{-}460\text{ cm}^{-1}$ for ν_2PO_4 and $1215\text{-}1300\text{ cm}^{-1}$ for amide III [226].

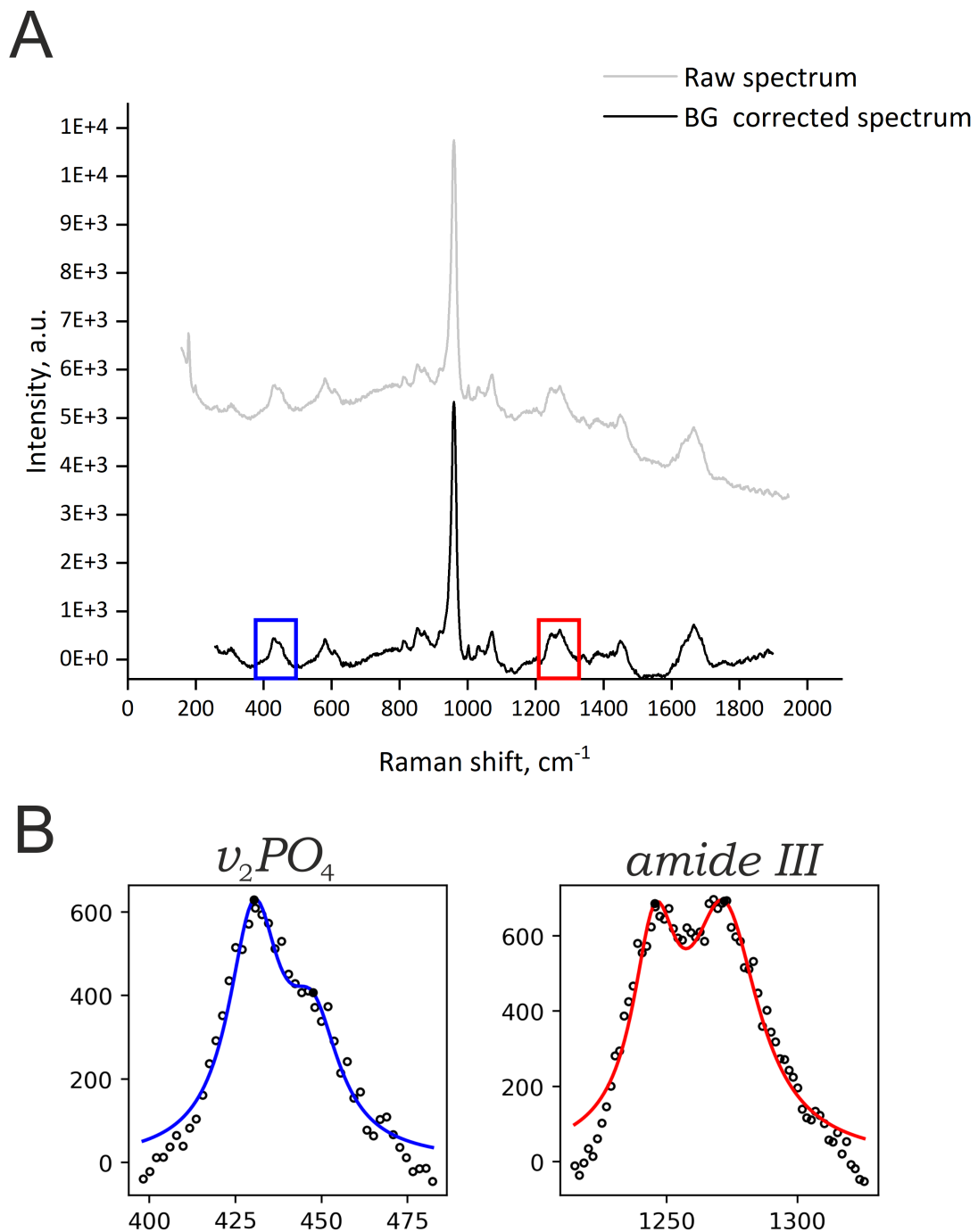


Figure A2.2 – Raman spectra processing steps for the raw data using Python software [221].

A3 Comparing microscale compact bone properties of patients who underwent hip arthroplasty: influence of age and gender

Tatiana Kochetkova¹, Markus S. Hanke⁴, Michael Indermaur², Alexander Groetsch¹, Stefan Remund³, Beat Neuenschwander³, Johann Michler¹, Klaus A. Siebenrock⁴, Philippe Zysset², Jakob Schwiedrzik¹

¹*Empa, Swiss Federal Laboratories for Materials Science and Technology, Laboratory for Mechanics of Materials and Nanostructures, Thun, Switzerland*

²*ARTORG Center for Biomedical Engineering Research, University of Bern, Switzerland*

³*Institute for Applied Laser, Photonics and Surface technologies (ALPS), Bern University of Applied Sciences, Burgdorf, Switzerland*

⁴*Department of Orthopedic Surgery, Inselspital, University of Bern, Switzerland*

A3.1 Micro-CT data processing

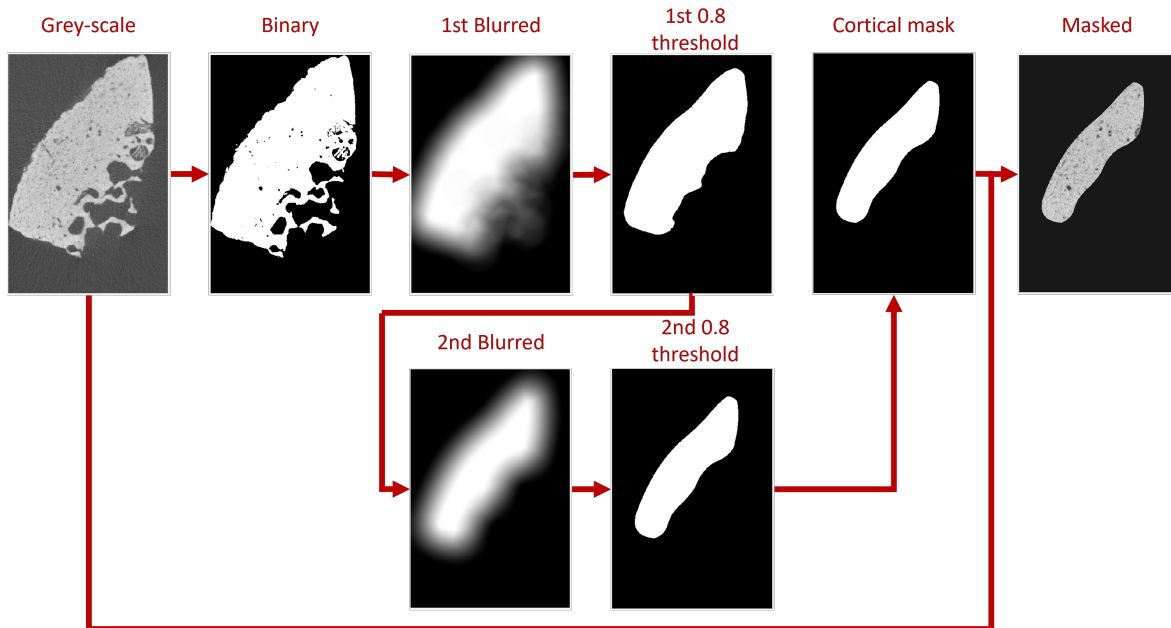


Figure A3.1 – Steps of the micro-CT image processing.

A3.2 Principal Component Analysis (PCA) and Logistic Regression (LR) classification on the final dataset

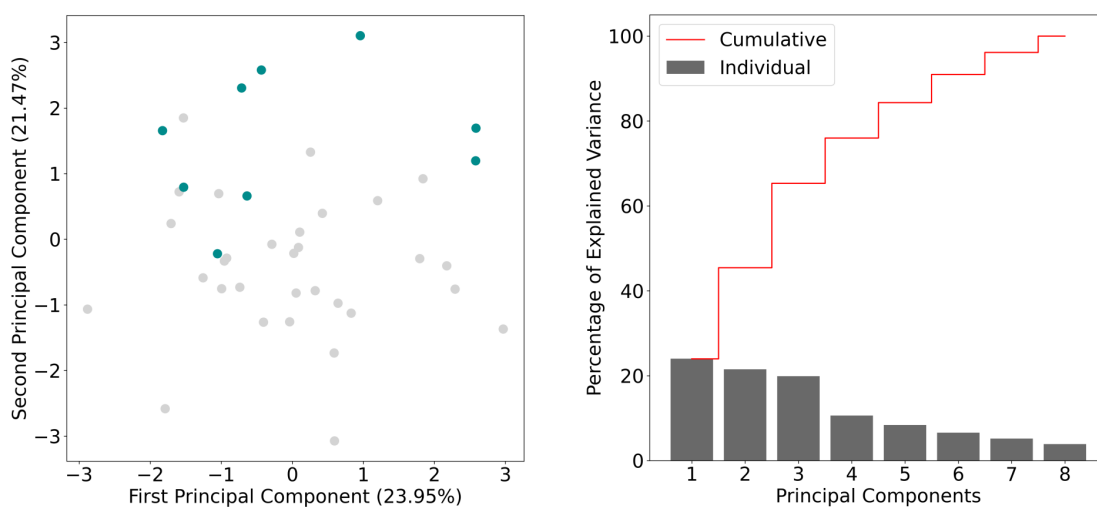
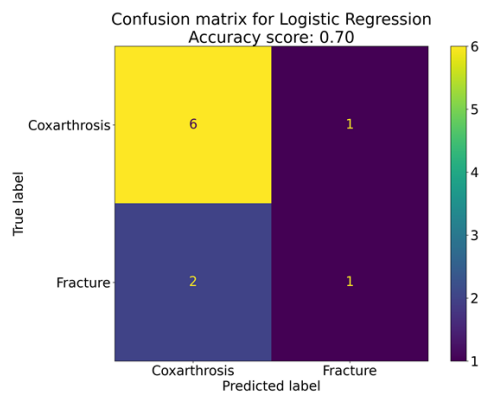


Figure A3.2 – Left: PCA analysis with first two Principal components score distributions for all 42 patients, colors of the points correspond to the patients primary diagnoses: coxarthrosis – grey, fracture – aquamarine. Right: top-10 bone parameters from the first Principal Component with their scores.

A3. Comparing microscale compact bone properties of patients who underwent hip arthroplasty: influence of age and gender (in preparation)



Feature	Abs contribution to the model
H	3.20775
Mineral/Matrix ratio	1.50493
Yield stress	1.29860
Yield strain	1.00579
Age	0.77508
Amide I sub-peak ratio $I_{\sim 1670} / I_{\sim 1640}$	0.50215
Amide I sub-peak ratio $I_{\sim 1660} / I_{\sim 1683}$	0.41052
TMD	0.04873

Figure A3.3 – Prediction of the bone fracture patients via Logistic regression algorithm. Left: confusion matrix for the classification. Right: dataset variables (features) sorted per importance.

References

- [1] D. Schapira and C. Schapira. Osteoporosis: The evolution of a scientific term. *Osteoporosis International*, 2(4):164–167, 1992.
- [2] Gerald N. Grob. *Aging Bones: A Short History of Osteoporosis*. Johns Hopkins University Press, Baltimore, 2014.
- [3] John A. Kanis, Nicholas Norton, Nicholas C. Harvey, Trolle Jacobson, Helena Johansson, Mattias Lorentzon, Eugene V. McCloskey, Carl Willers, and Fredrik Borgström. SCOPE 2021: a new scorecard for osteoporosis in Europe. *Archives of Osteoporosis*, 16(1), 2021.
- [4] Fredrik Borgström, Linda Karlsson, Gustav Ortsäter, Nicolas Norton, Philippe Halbout, Cyrus Cooper, Mattias Lorentzon, Eugene V. McCloskey, Nicholas C. Harvey, Muhamamd K. Javaid, John A. Kanis, Jean Yves Reginster, and Serge Ferrari. Fragility fractures in Europe: burden, management and opportunities. *Archives of Osteoporosis*, 15(1), 2020.
- [5] N. E. Morden, W. L. Schpero, R. Zaha, T. D. Sequist, and C. H. Colla. Overuse of short-interval bone densitometry: assessing rates of low-value care. *Osteoporosis International*, 25(9):2307–2311, May 2014.
- [6] Palak Choksi, Karl J. Jepsen, and Gregory A. Clines. The challenges of diagnosing osteoporosis and the limitations of currently available tools. *Clinical Diabetes and Endocrinology*, 4(1):1–13, dec 2018.
- [7] Institute of Medicine (US) Committee on Military Nutrition Research, Sydne J. Carlson-Newberry, and Rebecca B. Costello. National Academies Press, Sep 1997.
- [8] D. Krueger, E. Shives, E. Siglinsky, J. Libber, B. Buehring, K.E. Hansen, and N. Binkley. Dxa errors are common and reduced by use of a reporting template. *Journal of Clinical Densitometry*, 22(1):115–124, Jan 2019.

-
- [9] Nelson B. Watts. Fundamentals and pitfalls of bone densitometry using dual-energy x-ray absorptiometry (dxa). *Osteoporosis International*, 15(11):847–854, Aug 2004.
- [10] Susan Williams, Leila Khan, and Angelo A. Licata. Dxa and clinical challenges of fracture risk assessment in primary care. *Cleveland Clinic Journal of Medicine*, 88(11):615–622, Nov 2021.
- [11] Ae-Ja Park, Jun-Il Yoo, Jee-Hye Choi, Kyun Shik Chae, Chang Geun Kim, and Dal Sik Kim. Measurement uncertainty in spine bone mineral density by dual energy x-ray absorptiometry. *Journal of Bone Metabolism*, 24(2):105, 2017.
- [12] W.K. Sietsema. Animal models of cortical porosity. *Bone*, 17(4):S297–S305, oct 1995.
- [13] A. I. Pearce, R. G. Richards, S. Milz, E. Schneider, and S. G. Pearce. Animal models for implant biomaterial research in bone: A review. *European Cells and Materials*, 13(0):1–10, 2007.
- [14] Yuehuei H An and Richard J Friedman, editors. *Animal Models in Orthopaedic Research*. CRC Press, apr 2020.
- [15] Martin Clayton and Ron Philo. Number 5. Royal Collection Trust, London, U.K., Oct 2012.
- [16] John D. Currey. Princeton University Press, 2013.
- [17] Susan M. Ott. Cortical or trabecular bone: What’s the difference? *American Journal of Nephrology*, 47(6):373–375, 2018.
- [18] Tony M Keaveny, Elise F Morgan, Glen L Niebur, and Oscar C Yeh. Iomechanics of. 2001.
- [19] Ramin Oftadeh, Miguel Perez-Viloria, Juan C. Villa-Camacho, Ashkan Vaziri, and Ara Nazarian. Biomechanics and Mechanobiology of Trabecular Bone: A Review, jan 2015.
- [20] Peter Augat and Sandra Schorlemmer. The role of cortical bone and its microstructure in bone strength. *Age and Ageing*, 35(S.2):27–31, 2006.
- [21] J. Jowsey. Studies of haversian systems in man and some animals. *Journal of anatomy*, 100(Pt 4):857–64, 1966.

- [22] John G Skedros, Jennifer L Holmes, Eric G Vajda, and Roy D Bloebaum. Cement lines of secondary osteons in human bone are not mineral-deficient: New data in a historical perspective. *Anatomical Record - Part A Discoveries in Molecular, Cellular, and Evolutionary Biology*, 286(1):781–803, 2005.
- [23] David B. Burr, Mitchell B. Schaffler, and Richard G. Frederickson. Composition of the cement line and its possible mechanical role as a local interface in human compact bone. *Journal of Biomechanics*, 21(11):939–945, jan 1988.
- [24] K. Raum, I. Leguerney, F. Chandelier, M. Talmant, A. Saïed, F. Peyrin, and P. Laugier. Site-matched assessment of structural and tissue properties of cortical bone using scanning acoustic microscopy and synchrotron radiation ct. *Physics in Medicine and Biology*, 51(3):733–746, Jan 2006.
- [25] Jae Young Rho, Liisa Kuhn-Spearing, and Peter Zioupos. Mechanical properties and the hierarchical structure of bone. *Medical Engineering and Physics*, 20(2):92–102, 1998.
- [26] Philipp Schneider, Matias Meier, Roger Wepf, and Ralph Müller. Towards quantitative 3D imaging of the osteocyte lacuno-canalicular network. *Bone*, 47(5):848–858, 2010.
- [27] Mitsuo Yamauchi. Collagen: The Major Matrix Molecule in Mineralized Tissues. In John Anderson and Sanford Garner, editors, *Calcium and Phosphorus in Health and Disease (Modern Nutrition)*, chapter 9, pages 127–147. CRC Press, 1st edition, oct 1995.
- [28] Walter Gebhardt. *Über funktionell wichtige Anordnungsweisen der feineren und größeren Bauelemente des Wirbeltierknochens*. 1905.
- [29] Steve Weiner, Wolfie Traub, and H. Daniel Wagner. Lamellar Bone: Structure–Function Relations. *Journal of Structural Biology*, 126(3):241–255, jun 1999.
- [30] W. Wagermaier, H. S. Gupta, A. Gourrier, M. Burghammer, P. Roschger, and P. Fratzl. Spiral twisting of fiber orientation inside bone lamellae. *Biointerphases*, 1(1):1–5, 2006.
- [31] Andreas G. Reisinger, Dieter H. Pahr, and Philippe K. Zysset. Elastic anisotropy of bone lamellae as a function of fibril orientation pattern. *Biomechanics and Modeling in Mechanobiology*, 10(1):67–77, 2011.
- [32] Gastone Marotti. A New Theory of Bone Lamellation. Technical Report 1, 1993.

- [33] Jessica Mitchell and Anneke H. van Heteren. A literature review of the spatial organization of lamellar bone. *Comptes Rendus Palevol*, 15(1-2):23–31, Jan 2016.
- [34] H. Ou-Yang, E. P. Paschalis, W. E. Mayo, A. L. Boskey, and R. Mendelsohn. Infrared microscopic imaging of bone: Spatial distribution of co32. *Journal of Bone and Mineral Research*, 16(5):893–900, May 2001.
- [35] Bin Wang, Zuoqi Zhang, and Haobo Pan. Bone apatite nanocrystal: Crystalline structure, chemical composition, and architecture. *Biomimetics*, 8(1):90, Feb 2023.
- [36] Elizabeth A. McNally, Henry P. Schwarcz, Gianluigi A. Botton, and A. Larry Arsenault. A model for the ultrastructure of bone based on electron microscopy of ion-milled sections. *PLoS ONE*, 7(1):1–12, jan 2012.
- [37] Patrick Garnero. The Role of Collagen Organization on the Properties of Bone. *Calcified Tissue International*, 97(3):229–240, sep 2015.
- [38] M. Saito and K. Marumo. Collagen cross-links as a determinant of bone quality: A possible explanation for bone fragility in aging, osteoporosis, and diabetes mellitus. *Osteoporosis International*, 21(2):195–214, 2010.
- [39] Xiao Lin, Suryaji Patil, Yong Guang Gao, and Airong Qian. The Bone Extracellular Matrix in Bone Formation and Regeneration. *Frontiers in Pharmacology*, 11(May):1–15, 2020.
- [40] Erica R. Wise, Sergey Maltsev, M. Elisabeth Davies, Melinda J. Duer, Christian Jaeger, Nigel Loveridge, Rachel C. Murray, and David G. Reid. The organic-mineral interface in bone is predominantly polysaccharide, oct 2007.
- [41] Grazyna E. Sroga and Deepak Vashishth. Effects of bone matrix proteins on fracture and fragility in osteoporosis. *Current Osteoporosis Reports*, 10(2):141–150, jun 2012.
- [42] Mustafa Unal, Shan Yang, and Ozan Akkus. Molecular spectroscopic identification of the water compartments in bone. *Bone*, 67:228–236, 2014.
- [43] Mustafa Unal and Ozan Akkus. Raman spectral classification of mineral- and collagen-bound water’s associations to elastic and post-yield mechanical properties of cortical bone. *Bone*, 81:315–326, 2015.
- [44] Yuri A. Lazarev, Boris A. Grishkovsky, Tatyana B. Khromova, Alisa A. Lazareva, and Vera S. Grechishko. Bound water in the collagen-like triple-helical structure. *Biopolymers*, 32(2):189–195, Feb 1992.

- [45] R. Adam Horch, Jeffry S. Nyman, Daniel F. Gochberg, Richard D. Dortch, and Mark D. Does. Characterization of ^1H NMR signal in human cortical bone for magnetic resonance imaging. *Magnetic Resonance in Medicine*, 64(3):680–687, sep 2010.
- [46] Erin E Wilson, Ayorinde Awonusi, Michael D Morris, David H Kohn, Mary MJ Tecklenburg, and Larry W Beck. Highly Ordered Interstitial Water Observed in Bone by Nuclear Magnetic Resonance. *Journal of Bone and Mineral Research*, 20(4):625–634, dec 2004.
- [47] Nelson B. Watts, John P. Bilezikian, Pauline M. Camacho, Susan L. Greenspan, Steven T. Harris, Stephen F. Hodgson, Michael Kleerekoper, Marjorie M. Luckey, Michael R. McClung, Rachel Pessah Pollack, Steven M. Petak, Donald A. Bergman, Neil Binkley, and Paul D. Miller. American Association of Clinical Endocrinologists Medical Guidelines for Clinical Practice for the Diagnosis and Treatment of Postmenopausal Osteoporosis. *Endocrine Practice*, 16:1–37, Nov 2010.
- [48] Tumay Sozen, Lale Ozisik, and Nursel Calik Basaran. An overview and management of osteoporosis. *European Journal of Rheumatology*, 4(1):46–56, 2017.
- [49] Sirisha Vammi, Jaya Lakshmi Bukyya, Anulekha Avinash CK, M. L. Avinash Tejasvi, Archana Pokala, Chanchala HP, Priyanka Talwade, Praveen Kumar Neela, T. K. Shyamilee, Mary Oshin, and Veenila Pantala. Genetic disorders of bone or osteodys-trophies of jaws — a review. *Global Medical Genetics*, 08(02):041–050, jun 2021.
- [50] Uwe Wolfram and Jakob Schwiedrzik. Post-yield and failure properties of cortical bone. *BoneKEy Reports*, 5(March):1–10, 2016.
- [51] Jeffry S. Nyman, Michael Reyes, and Xiaodu Wang. Effect of ultrastructural changes on the toughness of bone. *Micron*, 36(7-8):566–582, Oct 2005.
- [52] H. S. Gupta and P. Zioupos. Fracture of bone tissue: The ‘hows’ and the ‘whys’. *Medical Engineering and Physics*, 30(10):1209–1226, dec 2008.
- [53] Elizabeth A Zimmermann, Björn Busse, and Robert O Ritchie. The fracture mechanics of human bone: influence of disease and treatment. *BoneKEy Reports*, 4(June):1–13, sep 2015.
- [54] Elizabeth A Zimmermann, Eric Schaible, Hrishikesh Bale, Holly D Barth, Simon Y Tang, Peter Reichert, Bjoern Busse, Tamara Alliston, J. W. Ager, and Robert O Ritchie. Age-related changes in the plasticity and toughness of human cortical

- bone at multiple length scales. *Proceedings of the National Academy of Sciences*, 108(35):14416–14421, aug 2011.
- [55] Maximilien E. Launey, Markus J. Buehler, and Robert O. Ritchie. On the Mechanistic Origins of Toughness in Bone. *Annual Review of Materials Research*, 40(1):25–53, 2010.
- [56] Elizabeth A. Zimmermann and Robert O. Ritchie. Bone as a Structural Material. *Advanced Healthcare Materials*, 4(9):1287–1304, jun 2015.
- [57] Paul K. Hansma, G. E. Fantner, J. H. Kindt, P. J. Thurner, G. Schitter, P. J. Turner, S. F. Udwin, and M. M. Finch. Sacrificial bonds in the interfibrillar matrix of bone. *Journal of Musculoskeletal Neuronal Interactions*, 5(4):313–315, 2005.
- [58] Georg E. Fantner, Emin Oroudjev, Georg Schitter, Laura S. Golde, Philipp Thurner, Marquesa M. Finch, Patricia Turner, Thomas Gutschmann, Daniel E. Morse, Helen Hansma, and Paul K. Hansma. Sacrificial bonds and hidden length: Unraveling molecular mesostructures in tough materials. *Biophysical Journal*, 90(4):1411–1418, 2006.
- [59] Georg E. Fantner, Tue Hassenkam, Johannes H. Kindt, James C. Weaver, Henrik Birkedal, Leonid Pechenik, Jacqueline A. Cutroni, Geraldo A.G. G Cidade, Galen D. Stucky, Daniel E. Morse, and Paul K. Hansma. Sacrificial bonds and hidden length dissipate energy as mineralized fibrils separate during bone fracture. *Nature Materials*, 4(8):612–616, 2005.
- [60] Markus J Buehler. Molecular nanomechanics of nascent bone: Fibrillar toughening by mineralization. *Nanotechnology*, 18(29), 2007.
- [61] Jeffrey S. Nyman, Anuradha Roy, Rae L. Acuna, Heather J. Gayle, Michael J. Reyes, Jerrod H. Tyler, David D. Dean, and Xiaodu Wang. Age-related effect on the concentration of collagen crosslinks in human osteonal and interstitial bone tissue. *Bone*, 39(6):1210–1217, 2006.
- [62] David B. Burr. Changes in bone matrix properties with aging. *Bone*, 120:85–93, Mar 2019.
- [63] Georg Osterhoff, Elise F. Morgan, Sandra J. Shefelbine, Lamya Karim, Laoise M. McNamara, and Peter Augat. Bone mechanical properties and changes with osteoporosis. *Injury*, 47:S11–S20, Jun 2016.

- [64] P. Zioupos, J.D. Currey, and A.J. Hamer. The role of collagen in the declining mechanical properties of aging human cortical bone. *Journal of biomedical materials research*, 45(2), 2013.
- [65] Xiaodu Wang, Ruud A. Bank, Johan M. Tekoppele, and C. Mauli Agrawal. The role of collagen in determining bone mechanical properties. *Journal of Orthopaedic Research*, 19(6):1021–1026, Nov 2001.
- [66] M.B. Schaffler, K. Choi, and C. Milgrom. Aging and matrix microdamage accumulation in human compact bone. *Bone*, 17(6):521–525, Dec 1995.
- [67] S.F. Lei, Y. Chen, D. H. Xiong, L. M. Li, and H. W. Deng. Ethnic difference in osteoporosis-related phenotypes and its potential underlying genetic determination. *Journal of musculoskeletal & neuronal interactions*, 6(1), 2006.
- [68] L. Joseph Melton. The prevalence of osteoporosis: Gender and racial comparison. *Calcified Tissue International*, 69(4):179–181, Sep 2001.
- [69] Consensus development conference: prophylaxis and treatment of osteoporosis. *The American Journal of Medicine*, 90(1):107–110, Jan 1991.
- [70] Andréa Marques, Ricardo J.O. O Ferreira, Eduardo Santos, Estíbaliz Loza, Loreto Carmona, and José António Pereira Da Silva. The accuracy of osteoporotic fracture risk prediction tools: A systematic review and meta-analysis. *Annals of the Rheumatic Diseases*, 74(11):1958–1967, nov 2015.
- [71] C. Greenwood, J. Clement, A. Dicken, J. P.O. O Evans, I. Lyburn, R. M. Martin, K. Rogers, N. Stone, and P. Zioupos. Towards new material biomarkers for fracture risk. *Bone*, 93:55–63, 2016.
- [72] P. Ammann, Ae R Rizzoli, and R. Rizzoli. Bone strength and its determinants. *Osteoporosis international : a journal established as result of cooperation between the European Foundation for Osteoporosis and the National Osteoporosis Foundation of the USA*, 14 Suppl 3:13–18, 2003.
- [73] Ego Seeman. Reduced bone formation and increased bone resorption: rational targets for the treatment of osteoporosis. *Osteoporosis International*, 14(S3):2–8, Mar 2003.
- [74] Fatme Al Anouti, Zainab Taha, Sadia Shamim, Kinda Khalaf, Leena Al Kaabi, and Habiba Alsafar. An insight into the paradigms of osteoporosis: From genetics to biomechanics. *Bone Reports*, 11:100216, Dec 2019.

- [75] World Health Organization. Assessment of fracture risk and its application to screening for postmenopausal osteoporosis : report of a who study group [meeting held in rome from 22 to 25 june 1992]. *WHO technical report series*, 1992.
- [76] Marian F. Young. Bone matrix proteins: their function, regulation, and relationship to osteoporosis. *Osteoporosis International*, 14(S3):35–42, Mar 2003.
- [77] Philipp J. Thurner and Orestis L. Katsamenis. The role of nanoscale toughening mechanisms in osteoporosis. *Current Osteoporosis Reports*, 12(3):351–356, Jun 2014.
- [78] M.D. Grynblas, J.H. Tupy, and J. Sodek. The distribution of soluble, mineral-bound, and matrix-bound proteins in osteoporotic and normal bones. *Bone*, 15(5):505–513, Sep 1994.
- [79] Philipp J. Thurner, Carol G. Chen, Sophi Ionova-Martin, Luling Sun, Adam Harman, Alexandra Porter, Joel W. Ager, Robert O. Ritchie, and Tamara Alliston. Osteopontin deficiency increases bone fragility but preserves bone mass. *Bone*, 46(6):1564–1573, Jun 2010.
- [80] J.R. Shapiro, J. Kassim, and P. Sponseller. *Osteogenesis Imperfecta: A Translational Approach to Brittle Bone Disease*. Elsevier Science, 2013.
- [81] Alessandra Carriero, Elizabeth A. Zimmermann, Adriana Paluszny, Simon Y. Tang, Hrishikesh Bale, Bjorn Busse, Tamara Alliston, Galateia Kazakia, Robert O. Ritchie, and Sandra J. Shefelbine. How tough is brittle bone? Investigating osteogenesis imperfecta in mouse bone. *Journal of Bone and Mineral Research*, 29(6):1392–1401, 2014.
- [82] W. H. Nijhuis, D. M. Eastwood, J. Allgrove, I. Hvid, H. H. Weinans, R. A. Bank, and R. J. Sakkars. Current concepts in osteogenesis imperfecta: Bone structure, biomechanics and medical management. *Journal of Children’s Orthopaedics*, 13(1):1–11, Feb 2019.
- [83] S. J. Jones, F. H. Glorieux, R. Travers, and A. Boyde. The microscopic structure of bone in normal children and patients with osteogenesis imperfecta: A survey using backscattered electron imaging. *Calcified Tissue International*, 64(1):8–17, Jan 1999.
- [84] Michael Indermaur, Daniele Casari, Tatiana Kochetkova, Cinzia Peruzzi, Elizabeth Zimmermann, Frank Rauch, Bettina Willie, Johann Michler, Jakob Schwiedrzik, and Philippe Zysset. Compressive Strength of Iliac Bone ECM Is Not Reduced in Osteogenesis Imperfecta and Increases With Mineralization. *Journal of Bone and Mineral Research*, 7(36):1364–1375, 2021.

- [85] G. David Roodman and Jolene J. Windle. Paget disease of bone. *Journal of Clinical Investigation*, 115(2):200–208, Feb 2005.
- [86] Frederick R. Singer. Bone quality in paget’s disease of bone. *Current Osteoporosis Reports*, 14(2):39–42, Mar 2016.
- [87] Elizabeth A Zimmermann, Till Köhne, Hrishikesh A Bale, Brian Panganiban, Bernd Gludovatz, Jozsef Zustin, Michael Hahn, Michael Amling, Robert O Ritchie, and Björn Busse. Modifications to nano- and microstructural quality and the effects on mechanical integrity in paget’s disease of bone. *Journal of Bone and Mineral Research*, 30(2):264–273, Jan 2015.
- [88] Judith E. Adams. Advances in bone imaging for osteoporosis. *Nature Reviews Endocrinology*, 9(1):28–42, Dec 2012.
- [89] H. K. Genant. Advanced imaging assessment of bone quality. *Annals of the New York Academy of Sciences*, 1068(1):410–428, Apr 2006.
- [90] Roland Krug, Andrew J. Burghardt, Sharmila Majumdar, and Thomas M. Link. High-Resolution Imaging Techniques for the Assessment of Osteoporosis. *Radiologic Clinics of North America*, 48(3):601–621, may 2010.
- [91] Marc Kachelrieß. *Micro-CT*. In Wolfhard Semmler and Markus Schwaiger, editors, *Molecular Imaging I*, page 23–52. Springer Berlin Heidelberg, Berlin, Heidelberg, 2008.
- [92] John A. Kanis, Anders Oden, Helena Johansson, Fredrik Borgström, Oskar Ström, and Eugene McCloskey. FRAX® and its applications to clinical practice. *Bone*, 44(5):734–743, may 2009.
- [93] Teresa A Hillier, Jane A Cauley, Joanne H Rizzo, Kathryn L Pedula, Kristine E Ensrud, Douglas C Bauer, Li-Yung Lui, Kimberly K Vesco, Dennis M Black, Meghan G Donaldson, Erin S LeBlanc, and Steven R Cummings. Who absolute fracture risk models (frax): Do clinical risk factors improve fracture prediction in older women without osteoporosis? *Journal of Bone and Mineral Research*, 26(8):1774–1782, Jul 2011.
- [94] Fjola Johannesdottir, Brett Allaire, and Mary L. Bouxsein. Fracture Prediction by Computed Tomography and Finite Element Analysis : Current and Future Perspectives. *Current Osteoporosis Reports*, 16(4):411–422, aug 2018.

- [95] Philippe K Zysset, Enrico Dall’Ara, Peter Varga, and Dieter H Pahr. Finite element analysis for prediction of bone strength. *BoneKEy Reports*, 2(June):1–9, 2013.
- [96] Kay Raum, Quentin Grimal, Peter Varga, Reinhard Barkmann, Claus C. Glüer, and Pascal Laugier. Ultrasound to assess bone quality. *Current Osteoporosis Reports*, 12(2):154–162, Mar 2014.
- [97] Danielle Ayumi Nishimura, Isabela Goulart Gil Choi, Emiko Saita Arita, and Arthur Rodriguez Gonzalez Cortes. Estimating bone mineral density using mri in medicine and dentistry: a literature review. *Oral Radiology*, 37(3):366–375, Sep 2020.
- [98] I. D. Cullum, P. J. Ell, and J. P. Ryder. X-ray dual-photon absorptiometry: a new method for the measurement of bone density. *The British Journal of Radiology*, 62(739):587–592, Jul 1989.
- [99] Tommy Storm, Gorm Thamsborg, Torben Steiniche, Harry K. Genant, and Ole Helmer Sorensen. Effect of intermittent cyclical etidronate therapy on bone mass and fracture rate in women with postmenopausal osteoporosis. *New England Journal of Medicine*, 322(18):1265–1271, May 1990.
- [100] John R. Cameron and James Sorenson. Measurement of bone mineral in vivo: An improved method. *Science*, 142(3589):230–232, Oct 1963.
- [101] R.M. Lorente Ramos, J. Azpeitia Armán, N. Arévalo Galeano, A. Muñoz Hernández, J.M. García Gómez, and J. Gredilla Molinero. Absorciometría con rayos x de doble energía. fundamentos, metodología y aplicaciones clínicas. *Radiología*, 54(5):410–423, Sep 2012.
- [102] John Damilakis, Judith E. Adams, Giuseppe Guglielmi, and Thomas M. Link. Radiation exposure in x-ray-based imaging techniques used in osteoporosis. *European Radiology*, 20(11):2707–2714, Jun 2010.
- [103] R.R. van Rijn and C. Van Kuijk. Of small bones and big mistakes; bone densitometry in children revisited. *European Journal of Radiology*, 71(3):432–439, Sep 2009.
- [104] Judith E. Adams. Quantitative computed tomography. *European Journal of Radiology*, 71(3):415–424, Sep 2009.
- [105] E. Dall’Ara, D. Pahr, P. Varga, F. Kainberger, and P. Zysset. QCT-based finite element models predict human vertebral strength in vitro significantly better than simulated DEXA. *Osteoporosis International*, 23(2):563–572, 2012.

- [106] Klaus Engelke, Judith E. Adams, Gabriele Armbrecht, Peter Augat, Cesar E. Bogado, Mary L. Bouxsein, Dieter Felsenberg, Masako Ito, Sven Prevrhal, Didier B. Hans, and E. Michael Lewiecki. Clinical use of quantitative computed tomography and peripheral quantitative computed tomography in the management of osteoporosis in adults: The 2007 iscd official positions. *Journal of Clinical Densitometry*, 11(1):123–162, Jan 2008.
- [107] E. J. Marjanovic, K. A. Ward, and J. E. Adams. The impact of accurate positioning on measurements made by peripheral qct in the distal radius. *Osteoporosis International*, 20(7):1207–1214, Nov 2008.
- [108] Aasis Unnanuntana, Brian P Gladnick, Eve Donnelly, and Joseph M Lane. The assessment of fracture risk. *The Journal of Bone and Joint Surgery-American Volume*, 92(3):743–753, Mar 2010.
- [109] John A. Kanis, Helena Johansson, Nicholas C. Harvey, and Eugene V. McCloskey. A brief history of frax. *Archives of Osteoporosis*, 13(1), Oct 2018.
- [110] John A. Kanis, Anders Oden, Helena Johansson, Fredrik Borgström, Oskar Ström, and Eugene McCloskey. Frax® and its applications to clinical practice. *Bone*, 44(5):734–743, May 2009.
- [111] P.J. Prendergast. Finite element models in tissue mechanics and orthopaedic implant design. *Clinical Biomechanics*, 12(6):343–366, Sep 1997.
- [112] Philippe K Zysset, Enrico Dall’Ara, Peter Varga, and Dieter H Pahr. Finite element analysis for prediction of bone strength. *BoneKEy Reports*, 2, Aug 2013.
- [113] Pall Asgeir Bjornsson, Alexander Baker, Ingmar Fleps, Yves Pauchard, Halldor Pals-son, Stephen J. Ferguson, Sigurdur Sigurdsson, Vilmundur Gudnason, Benedikt Helgason, and Lotta Maria Ellingsen. Fast and robust femur segmentation from computed tomography images for patient-specific hip fracture risk screening. *Computer Methods in Biomechanics and Biomedical Engineering: Imaging & Visualization*, 0(0):1–13, 2022.
- [114] C. M. Langton, S. B. Palmer, and R. W. Porter. The measurement of broadband ultrasonic attenuation in cancellous bone. *Engineering in Medicine*, 13(2):89–91, Apr 1984.
- [115] Fernando Marín, Jesús González-Macías, Adolfo Díez-Pérez, Silvia Palma, and Miguel Delgado-Rodríguez. Relationship between bone quantitative ultrasound and

- fractures: A meta-analysis. *Journal of Bone and Mineral Research*, 21(7):1126–1135, May 2006.
- [116] Marc-Antoine Krieg, Reinhart Barkmann, Stefano Gonnelli, Alison Stewart, Douglas C. Bauer, Luis Del Rio Barquero, Jonathan J. Kaufman, Roman Lorenc, Paul D. Miller, Wojciech P. Olszynski, Catalina Poiana, Anne-Marie Schott, E. Michael Lewiecki, and Didier Hans. Quantitative ultrasound in the management of osteoporosis: The 2007 iscd official positions. *Journal of Clinical Densitometry*, 11(1):163–187, Jan 2008.
- [117] Giampiero I Baroncelli. Quantitative ultrasound methods to assess bone mineral status in children: Technical characteristics, performance, and clinical application. *Pediatric Research*, 63(3):220–228, Mar 2008.
- [118] Masako Ito, Kuniaki Hayashi, Masataka Uetani, Yasuhiro Kawahara, Masafumi Ohki, Miho Yamada, Hideki Kitamori, Masaru Noguchi, and Masahiro Ito. Bone mineral and other bone components in vertebrae evaluated by qct and mri. *Skeletal Radiology*, 22(2), Feb 1993.
- [119] David K. W. Yeung, Samuel Y.S. Wong, James F. Griffith, and Edith M.C. Lau. Bone marrow diffusion in osteoporosis: Evaluation with quantitative mr diffusion imaging. *Journal of Magnetic Resonance Imaging*, 19(2):222–228, 2004.
- [120] James F. Griffith, David K. W. Yeung, Gregory E. Antonio, Samuel Y. S. Wong, Timothy C. Y. Kwok, Jean Woo, and Ping C. Leung. Vertebral marrow fat content and diffusion and perfusion indexes in women with varying bone density: Mr evaluation. *Radiology*, 241(3):831–838, Dec 2006.
- [121] Ralph Müller. Hierarchical microimaging of bone structure and function. *Nature Reviews Rheumatology*, 5(7):373–381, Jul 2009.
- [122] D. Chappard, M.F. Baslé, E. Legrand, and M. Audran. New laboratory tools in the assessment of bone quality. *Osteoporosis International*, 22(8):2225–2240, Feb 2011.
- [123] Nina K. Wittig and Henrik Birkedal. Bone hierarchical structure: spatial variation across length scales. *Acta Crystallographica Section B Structural Science, Crystal Engineering and Materials*, 78(3):305–311, Mar 2022.
- [124] Marios Georgiadis, Ralph Müller, and Philipp Schneider. Techniques to assess bone ultrastructure organization: Orientation and arrangement of mineralized collagen fibrils. *Journal of the Royal Society Interface*, 13(119), 2016.

- [125] Françoise Peyrin, Pei Dong, Alexandra Pacureanu, and Max Langer. Micro- and nano-ct for the study of bone ultrastructure. *Current Osteoporosis Reports*, 12(4):465–474, Oct 2014.
- [126] Mary L. Bouxsein, Stephen K. Boyd, Blaine A. Christiansen, Robert E. Guldberg, Karl J. Jepsen, and Ralph Müller. Guidelines for assessment of bone microstructure in rodents using micro-computed tomography. *Journal of Bone and Mineral Research*, 25(7):1468–1486, 2010.
- [127] F. Peyrin. Investigation of bone with synchrotron radiation imaging: from micro to nano. *Osteoporosis International*, 20(6):1057–1063, Apr 2009.
- [128] Peter Varga, Alexandra Pacureanu, Max Langer, Heikki Suhonen, Bernhard Hesse, Quentin Grimal, Peter Cloetens, Kay Raum, and Françoise Peyrin. Investigation of the three-dimensional orientation of mineralized collagen fibrils in human lamellar bone using synchrotron X-ray phase nano-tomography. *Acta Biomaterialia*, 9(9):8118–8127, 2013.
- [129] Bernhard Hesse, Peter Varga, Max Langer, Alexandra Pacureanu, Susanne Schrof, Nils Männicke, Heikki Suhonen, Peter Maurer, Peter Cloetens, Françoise Peyrin, and Kay Raum. Canalicular network morphology is the major determinant of the spatial distribution of mass density in human bone tissue: Evidence by means of synchrotron radiation phase-contrast nano-ct. *Journal of Bone and Mineral Research*, 30(2):346–356, Jan 2015.
- [130] Susanne Schrof, Peter Varga, Bernhard Hesse, Martin Schöne, Roman Schütz, Admir Masic, and Kay Raum. Multimodal correlative investigation of the interplaying micro-architecture, chemical composition and mechanical properties of human cortical bone tissue reveals predominant role of fibrillar organization in determining microelastic tissue properties. *Acta Biomaterialia*, 44:51–64, Oct 2016.
- [131] Tatiana Kormilina, Silvan Englisch, Tatiana Kochetkova, Dominik Drobek, Janis Wirth, Benjamin Apeleo Zubiri, Jakob Schwiedrzik, and Erdmann Spiecker. Multimodal characterization of collagen fibril orientation in human cortical bone by a combination of quantitative polarized raman spectroscopy, nanoscale x-ray computed tomography and 360° electron tomography. *Microscopy and Microanalysis*, 27(S1):96–101, Jul 2021.
- [132] Eve Donnelly. Methods for assessing bone quality: A review. *Clinical Orthopaedics & Related Research*, 469(8):2128–2138, Aug 2011.

- [133] Wolfgang Wagermaier, Aurelien Gourrier, and Barbara Aichmayer. *Materials Design Inspired by Nature. Chapter 3: Understanding Hierarchy and Functions of Bone Using Scanning X-ray Scattering Methods*. Royal Society of Chemistry, 2013.
- [134] Robin Seidel, Aurélien Gourrier, Manfred Burghammer, Christian Riekkel, George Jeronimidis, and Oskar Paris. Mapping fibre orientation in complex-shaped biological systems with micrometre resolution by scanning x-ray microdiffraction. *Micron*, 39(2):198–205, Feb 2008.
- [135] Marios Georgiadis, Manuel Guizar-Sicairos, Alexander Zwahlen, Andreas J. Trüssel, Oliver Bunk, Ralph Müller, and Philipp Schneider. 3d scanning saxs: A novel method for the assessment of bone ultrastructure orientation. *Bone*, 71:42–52, Feb 2015.
- [136] Marianne Liebi, Marios Georgiadis, Joachim Kohlbrecher, Mirko Holler, Jörg Raabe, Ivan Usov, Andreas Menzel, Philipp Schneider, Oliver Bunk, and Manuel Guizar-Sicairos. Small-angle x-ray scattering tensor tomography: model of the three-dimensional reciprocal-space map, reconstruction algorithm and angular sampling requirements. *Acta Crystallographica Section A Foundations and Advances*, 74(1):12–24, Jan 2018.
- [137] K. Åkesson, M. D. Grynpsas, R. G. V. Hancock, R. Odselius, and K. J. Obrant. Energy-dispersive x-ray microanalysis of the bone mineral content in human trabecular bone: A comparison with icpes and neutron activation analysis. *Calcified Tissue International*, 55(3):236–239, Sep 1994.
- [138] Natalie Reznikov, Matthew Bilton, Leonardo Lari, Molly M. Stevens, and Roland Kröger. Fractal-like hierarchical organization of bone begins at the nanoscale. *Science*, 360(6388), May 2018.
- [139] Furqan A. Shah, Krisztina Ruscsák, and Anders Palmquist. 50 years of scanning electron microscopy of bone—a comprehensive overview of the important discoveries made and insights gained into bone material properties in health, disease, and taphonomy. *Bone Research*, 7(1), May 2019.
- [140] T. Kormilina, T. Kochetkova, S. Englisch, D. Drobek, J. Schwiedrzik, and E. Spiecker. Electron tomography in a correlative approach to multimodal characterization of human bone. Apr 2022. 12th ASEM Workshop : Austrian Society for Electron Microscopy.
- [141] Matthew Weyland and Paul A. Midgley. Electron tomography. *Materials Today*, 7(12):32–40, Dec 2004.

- [142] Ming Du and Chris Jacobsen. Relative merits and limiting factors for x-ray and electron microscopy of thick, hydrated organic materials. *Ultramicroscopy*, 184:293–309, Jan 2018.
- [143] Ewa M. Spiesz, Werner Kaminsky, and Philippe K. Zysset. A quantitative collagen fibers orientation assessment using birefringence measurements: Calibration and application to human osteons. *Journal of Structural Biology*, 176(3):302–306, Dec 2011.
- [144] Marie-Madeleine Giraud-Guille, Laurence Besseau, and Raquel Martin. Liquid crystalline assemblies of collagen in bone and in vitro systems. *Journal of Biomechanics*, 36(10):1571–1579, Oct 2003.
- [145] Stéphane Blouin, Andreas Roschger, Franz Varga, Barbara Misof, Silvia Spitzer, Paul Roschger, and Klaus Klaushofer. Confocal laser scanning microscopy—a powerful tool in bone research. *Wiener Medizinische Wochenschrift*, 168(11-12):314–321, May 2018.
- [146] Xiyi Chen, Oleg Nadiarynk, Sergey Plotnikov, and Paul J Campagnola. Second harmonic generation microscopy for quantitative analysis of collagen fibrillar structure. *Nature Protocols*, 7(4):654–669, Mar 2012.
- [147] Theodossis A. Theodossiou, Christopher Thrasivoulou, Chidi Ekwobi, and David L. Becker. Second harmonic generation confocal microscopy of collagen type i from rat tendon cryosections. *Biophysical Journal*, 91(12):4665–4677, Dec 2006.
- [148] Markus Regauer, Philipp Jürgens, Ursula Budenhofer, Martina Hartstock, Wolfgang Böcker, Dominik Bürklein, Wolf Mutschler, Robert Sader, and Matthias Schieker. Quantitative scanning acoustic microscopy compared to microradiography for assessment of new bone formation. *Bone*, 38(4):564–570, Apr 2006.
- [149] S. Puchegger, D. Fix, C. Pilz-Allen, P. Roschger, P. Fratzl, and R. Weinkamer. The role of angular reflection in assessing elastic properties of bone by scanning acoustic microscopy. *Journal of the Mechanical Behavior of Biomedical Materials*, 29:438–450, Jan 2014.
- [150] Joseph M. Wallace. Applications of atomic force microscopy for the assessment of nanoscale morphological and mechanical properties of bone. *Bone*, 50(1):420–427, Jan 2012.

- [151] S Hengsbeger, A Kulik, and Ph Zysset. A combined atomic force microscopy and nanoindentation technique to investigate the elastic properties of bone structural units. *European Cells and Materials*, 1:12–17, Jan 2001.
- [152] Marco P.E. Wenger, Laurent Bozec, Michael A. Horton, and Patrick Mesquida. Mechanical properties of collagen fibrils. *Biophysical Journal*, 93(4):1255–1263, Aug 2007.
- [153] Orestis G. Andriotis, Wiparat Manuyakorn, Jurgita Zekonyte, Orestis L. Katsamenis, Sebastien Fabri, Peter H. Howarth, Donna E. Davies, and Philipp J. Thurner. Nanomechanical assessment of human and murine collagen fibrils via atomic force microscopy cantilever-based nanoindentation. *Journal of the Mechanical Behavior of Biomedical Materials*, 39:9–26, Nov 2014.
- [154] Anupama Nair, Shu-Chun Chuang, Yi-Shan Lin, Chung-Hwan Chen, Ting-Chen Fang, Hsiao-Chi Chiu, Chi-Hsiang Lien, and Shean-Jen Chen. Characterization of collagen response to bone fracture healing using polarization-shg. *Scientific Reports*, 12(1), Nov 2022.
- [155] Emily Pendleton, Kayvan Tehrani, Ruth Barrow, and Luke Mortensen. Second harmonic generation characterization of collagen in whole bone. *Biomedical Optics Express*, 11(8):4379–4396, 2020.
- [156] Sauwanan Bumrerraj and J. Lawrence Katz. Scanning acoustic microscopy study of human cortical and trabecular bone. *Annals of Biomedical Engineering*, 29(12):1034–1042, Dec 2001.
- [157] Erik A. Taylor and Eve Donnelly. Raman and fourier transform infrared imaging for characterization of bone material properties. *Bone*, 139:115490, Oct 2020.
- [158] Gurjit S Mandair and Michael D Morris. Contributions of Raman spectroscopy to the understanding of bone strength. *BoneKEY Reports*, 4(August 2014):1–8, 2015.
- [159] Michael D. Morris and Gurjit S. Mandair. Raman Assessment of Bone Quality. *Clinical Orthopaedics and Related Research*®, 469(8):2160–2169, aug 2011.
- [160] Mekhala Raghavan, Nadder D. Sahar, Robert H. Wilson, Mary-Ann Mycek, Nancy Pleshko, David H. Kohn, and Michael D. Morris. Quantitative polarized Raman spectroscopy in highly turbid bone tissue. *Journal of Biomedical Optics*, 15(3):037001, 2010.

- [161] Tatiana Kochetkova, Cinzia Peruzzi, Oliver Braun, Jan Overbeck, Anjani K. Maurya, Antonia Neels, Michel Calame, Johann Michler, Philippe Zysset, and Jakob Schwiedrzik. Combining polarized raman spectroscopy and micropillar compression to study microscale structure-property relationships in mineralized tissues. *Acta Biomaterialia*, 119:390–404, 1 2021.
- [162] Ji-Hyun Lee and Je-Yoel Cho. Proteomics approaches for the studies of bone metabolism. *BMB Reports*, 47(3):141–148, Mar 2014.
- [163] Marco Barbieri, Paola Fantazzini, Claudia Testa, Villiam Bortolotti, Fabio Baruffaldi, Feliks Kogan, and Leonardo Brizi. Characterization of structural bone properties through portable single-sided nmr devices: State of the art and future perspectives. *International Journal of Molecular Sciences*, 22(14):7318, Jul 2021.
- [164] R. Adam Horch, Jeffry S. Nyman, Daniel F. Gochberg, Richard D. Dortch, and Mark D. Does. Characterization of 1 h nmr signal in human cortical bone for magnetic resonance imaging. *Magnetic Resonance in Medicine*, 64(3):680–687, May 2010.
- [165] Hua-Dong Xue, Yu Yin, Tian He, Haixin Song, Jianhua Li, and Xueqian Kong. Solid-state nmr studies on the organic matrix of bone. *Nano Research*, Oct 2022.
- [166] Philippe K. Zysset. Indentation of bone tissue: A short review. *Osteoporosis International*, 20(6):1049–1055, 2009.
- [167] Jakob Schwiedrzik, Rejin Raghavan, Alexander Bürki, Victor Lenader, Uwe Wolfram, Johann Michler, and Philippe Zysset. In situ micropillar compression reveals superior strength and ductility but an absence of damage in lamellar bone. *Nature Materials*, 13(7):740–747, 2014.
- [168] Howell G M Edwards. Modern raman spectroscopy — a practical approach. *Journal of Raman Spectroscopy*, 36(8):835, 2005.
- [169] Lee Weller, Maxim Kuvshinov, and Simone Hochgreb. Gas-phase raman spectroscopy of non-reacting flows: comparison between free-space and cavity-based spontaneous raman emission. *Applied Optics*, 58(10):C92, Mar 2019.
- [170] Thomas Schmid and Petra Dariz. Raman microspectroscopic imaging of binder remnants in historical mortars reveals processing conditions. *Heritage*, 2(2):1662–1683, Jun 2019.
- [171] Admir Masic, Luca Bertinetti, Roman Schuetz, Leonardo Galvis, Nadya Timofeeva, John W.C. C Dunlop, Jong Seto, Markus A. Hartmann, and Peter Fratzl. Observations

- of multiscale, stress-induced changes of collagen orientation in tendon by polarized Raman spectroscopy. *Biomacromolecules*, 12(11):3989–3996, 2011.
- [172] Sonja Gamsjaeger, A. Masic, P. Roschger, M. Kazanci, J. W.C. C Dunlop, K. Klaushofer, E. P. Paschalis, and P. Fratzl. Cortical bone composition and orientation as a function of animal and tissue age in mice by Raman spectroscopy. *Bone*, 47(2):392–399, 2010.
- [173] Guillaume Falgayrac, Sébastien Facq, Gérard Leroy, Bernard Cortet, and Guillaume Penel. New method for raman investigation of the orientation of collagen fibrils and crystallites in the haversian system of bone. *Applied Spectroscopy*, 64(7):775–780, 2010.
- [174] M. Kazanci, P. Roschger, E. P. Paschalis, K. Klaushofer, and P. Fratzl. Bone osteonal tissues by Raman spectral mapping : Orientation – composition. *Journal of Structural Biology*, 156(3):489–496, 2006.
- [175] Jae Young Rho, Ting Y. Tsui, and George M. Pharr. Elastic properties of human cortical and trabecular lamellar bone measured by nanoindentation. *Biomaterials*, 18(20):1325–1330, 1997.
- [176] Philippe K. Zysset, X. Edward Guo, C. Edward Hoffler, Kristin E. Moore, and Steven A. Goldstein. Elastic modulus and hardness of cortical and trabecular bone lamellae measured by nanoindentation in the human femur. *Journal of Biomechanics*, 32(10):1005–1012, 1999.
- [177] Daniele Casari, Johann Michler, Philippe Zysset, and Jakob Schwiedrzik. Microtensile properties and failure mechanisms of cortical bone at the lamellar level. *Acta Biomaterialia*, 120:135–145, 2020.
- [178] Spencer P. Lake, Kristin S. Miller, Dawn M. Elliott, and Louis J. Soslowsky. Effect of fiber distribution and realignment on the nonlinear and inhomogeneous mechanical properties of human supraspinatus tendon under longitudinal tensile loading. *Journal of Orthopaedic Research*, 27(12):1596–1602, 2009.
- [179] Jakob Schwiedrzik, Aidan Taylor, Daniele Casari, Uwe Wolfram, Philippe Zysset, and Johann Michler. Nanoscale deformation mechanisms and yield properties of hydrated bone extracellular matrix. *Acta Biomaterialia*, 60:302–314, 2017.
- [180] Krzysztof W. Luczynski, Andreas Steiger-Thirsfeld, Johannes Bernardi, Josef Eberhardsteiner, and Christian Hellmich. Extracellular bone matrix exhibits hardening

- elastoplasticity and more than double cortical strength: Evidence from homogeneous compression of non-tapered single micron-sized pillars welded to a rigid substrate. *Journal of the Mechanical Behavior of Biomedical Materials*, 52:51–62, 2015.
- [181] Ottman A. Tertuliano and Julia R. Greer. The nanocomposite nature of bone drives its strength and damage resistance. *Nature Materials*, 15(11):1195–1202, 2016.
- [182] Ines Jimenez-Palomar, Anna Shipov, Ron Shahar, and Asa H. Barber. Structural orientation dependent sub-lamellar bone mechanics. *Journal of the Mechanical Behavior of Biomedical Materials*, 52:63–71, 2015.
- [183] Alexander Groetsch, Aurélien Gourrier, Jakob Schwiedrzik, Michael Sztucki, Rainer J. Beck, Jonathan D. Shephard, Johann Michler, Philippe K. Zysset, and Uwe Wolfram. Compressive behaviour of uniaxially aligned individual mineralised collagen fibres at the micro- and nanoscale. *Acta Biomaterialia*, 89:313–329, 2019.
- [184] Fei Hang and Asa H. Barber. Nano-mechanical properties of individual mineralized collagen fibrils from bone tissue. *Journal of the Royal Society Interface*, 8(57):500–505, 2011.
- [185] W.C. C Oliver and G.M. M Pharr. An improved technique for determining hardness and elastic modulus using load and displacement sensing indentation experiments. *Journal of Materials Research*, 7(6):1564–1583, jun 1992.
- [186] W.C. Oliver and G.M. Pharr. Measurement of hardness and elastic modulus by instrumented indentation: Advances in understanding and refinements to methodology. *Journal of Materials Research*, 19(1):1–20, 2004.
- [187] Andreas G. Reisinger, Dieter H. Pahr, and Philippe K. Zysset. Principal stiffness orientation and degree of anisotropy of human osteons based on nanoindentation in three distinct planes. *Journal of the Mechanical Behavior of Biomedical Materials*, 4(8):2113–2127, 2011.
- [188] Xi Chen, Nagahisa Ogasawara, Manhong Zhao, and Norimasa Chiba. On the uniqueness of measuring elastoplastic properties from indentation: The indistinguishable mystical materials. *Journal of the Mechanics and Physics of Solids*, 55(8):1618–1660, 2007.
- [189] Michael D. Uchic and Dennis M. Dimiduk. A methodology to investigate size scale effects in crystalline plasticity using uniaxial compression testing. *Materials Science and Engineering A*, 400-401(1-2 SUPPL.):268–278, 2005.

- [190] Ian N. Sneddon. The relation between load and penetration in the axisymmetric boussinesq problem for a punch of arbitrary profile. *International Journal of Engineering Science*, 3(1):47–57, May 1965.
- [191] H. Zhang, B.E. Schuster, Q. Wei, and K.T. Ramesh. The design of accurate micro-compression experiments. *Scripta Materialia*, 54(2):181–186, Jan 2006.
- [192] Yong C. Lim, Katrina J. Altman, Dave F. Farson, and Katharine M. Flores. Micropillar fabrication on bovine cortical bone by direct-write femtosecond laser ablation. *Journal of Biomedical Optics*, 14(6):064021, 2009.
- [193] Tatiana Kochetkova, Alexander Groetsch, Michael Indermaur, Cinzia Peruzzi, Stefan Remund, Beat Neuenschwander, Benjamin Bellon, Johann Michler, Philippe Zysset, and Jakob Schwiedrzik. Assessing minipig compact jawbone quality at the microscale. *Journal of the Mechanical Behavior of Biomedical Materials*, 134:105405, Oct 2022.
- [194] P. Barry, T. Aspray, K. Briers, G. Collins, J. Compston, F. Dockery, S. Ruddick, P. Selby, D. Stephens, A. Thornhill, and J. Tobias. Osteoporosis : fragility fracture risk. *National Institute for Health and Clinical Excellence*, (August):1–97, 2012.
- [195] Stacyann Bailey and Deepak Vashishth. Mechanical Characterization of Bone: State of the Art in Experimental Approaches—What Types of Experiments Do People Do and How Does One Interpret the Results? *Current Osteoporosis Reports*, 16(4):423–433, 2018.
- [196] Klaus Engelke, Thomas Lang, Sundeep Khosla, Ling Qin, Philippe Zysset, William D. Leslie, John A. Shepherd, and John T. Schousboe. Clinical Use of Quantitative Computed Tomography (QCT) of the Hip in the Management of Osteoporosis in Adults: the 2015 ISCD Official Positions—Part I. *Journal of Clinical Densitometry*, 18(3):338–358, jul 2015.
- [197] Mohammad J. Mirzaali, J. Jakob Schwiedrzik, Suwanwadee Thaiwichai, James P. Best, Johann Michler, Philippe K. Zysset, and Uwe Wolfram. Mechanical properties of cortical bone and their relationships with age, gender, composition and microindentation properties in the elderly. *Bone*, 93:196–211, 2016.
- [198] Natalie Reznikov, Ron Shahar, and Steve Weiner. Three-dimensional structure of human lamellar bone: The presence of two different materials and new insights into the hierarchical organization. *Bone*, 59:93–104, 2014.

- [199] Ewa M Spiesz, Werner Kaminsky, and Philippe K Zysset. A quantitative collagen fibers orientation assessment using birefringence measurements : Calibration and application to human osteons. *Journal of Structural Biology*, 176(3):302–306, 2011.
- [200] Rachel Genthial, Emmanuel Beaurepaire, Marie Claire Schanne-Klein, Françoise Peyrin, Delphine Farlay, Cécile Olivier, Yohann Bala, Georges Boivin, Jean Claude Vial, Delphine Débarre, and Aurélien Gourrier. Label-free imaging of bone multi-scale porosity and interfaces using third-harmonic generation microscopy. *Scientific Reports*, 7(1):1–16, 2017.
- [201] Ahmad Golaraei, Kamdin Mirsanaye, Yeji Ro, Serguei Krouglov, Margarete K. Akens, Brian C. Wilson, and Virginijus Barzda. Collagen chirality and three-dimensional orientation studied with polarimetric second-harmonic generation microscopy. *Journal of Biophotonics*, 12(1):1–9, 2019.
- [202] Matthew A. Rubin, Iwona Jasiuk, Jeannette Taylor, Janet Rubin, Timothy Ganey, and Robert P. Apkarian. TEM analysis of the nanostructure of normal and osteoporotic human trabecular bone. *Bone*, 33(3):270–282, 2003.
- [203] Leonardo Galvis, John W.C. C Dunlop, Georg Duda, Peter Fratzl, and Admir Masic. Polarized Raman Anisotropic Response of Collagen in Tendon: Towards 3D Orientation Mapping of Collagen in Tissues. *PLoS ONE*, 8(5):1–9, 2013.
- [204] Susanne Schrof, Peter Varga, Leonardo Galvis, Kay Raum, and Admir Masic. 3D Raman mapping of the collagen fibril orientation in human osteonal lamellae. *Journal of structural biology*, 187(3):266–275, 2014.
- [205] R. B. Martin and J. Ishida. The relative effects of collagen fiber orientation, porosity, density, and mineralization on bone strength. *Journal of Biomechanics*, 22(5):419–426, 1989.
- [206] H. Oxlund, M. Barckman, G. Ørtoft, and T. T. Andreassen. Reduced concentrations of collagen cross-links are associated with reduced strength of bone. *Bone*, 17(4 SUPPL.):365–371, 1995.
- [207] Xiaodu Wang, Ruud A. Bank, Johan M. TeKoppele, and C. Mauli Agrawal. The role of collagen in determining bone mechanical properties. *Journal of Orthopaedic Research*, 19(6):1021–1026, 2001.
- [208] P. Zioupos, J. D. Currey, and A. J. Hamer. The role of collagen in the declining mechanical properties of aging human cortical bone. *Journal of biomedical materials research*, 45(2):108–116, may 1999.

- [209] Angela Sheu and Terry Diamond. Bone mineral density: Testing for osteoporosis. *Australian Prescriber*, 39(2):35–39, 2016.
- [210] Wilfrid T Dempster and Rjchahd T Liddicoat. Compact bone as non-isotropic material. *The American journal of anatomy*, 91(3):331–362, 1952.
- [211] Antonio Ascenzi and Ermanno Bonucci. The compressive properties of single osteons. *The Anatomical Record*, 161(3):377–391, 1968.
- [212] Antonio Ascenzi and Ermanno Bonucci. The tensile properties of single osteons. *The Anatomical Record*, 158(4):375–386, aug 1967.
- [213] Daniele Casari, Tatiana Kochetkova, Johann Michler, Philippe Zysset, and Jakob Schwiedrzik. Microtensile failure mechanisms in lamellar bone: Influence of fibrillar orientation, specimen size and hydration. *Acta Biomaterialia*, 131:391–402, 2021.
- [214] Jong Seto, Himadri S. Gupta, Paul Zaslansky, H. Daniel Wagner, and Peter Fratzl. Tough lessons from bone: Extreme mechanical anisotropy at the mesoscale. *Advanced Functional Materials*, 18(13):1905–1911, jul 2008.
- [215] Ewa M. Spiesz and Philippe K. Zysset. Structure-mechanics relationships in mineralized tendons. *Journal of the Mechanical Behavior of Biomedical Materials*, 52:72–84, 2015.
- [216] Ingomar Jäger and Peter Fratzl. Mineralized collagen fibrils: A mechanical model with a staggered arrangement of mineral particles. *Biophysical Journal*, 79(4):1737–1746, 2000.
- [217] Ewa M Spiesz, Paul Roschger, and Philippe K Zysset. Influence of Mineralization and Microporosity on Tissue Elasticity : Experimental and Numerical Investigation on Mineralized Turkey Leg Tendons. *Calcified Tissue International*, pages 319–329, 2012.
- [218] É. Budyn, J. Jonvaux, C. Funfschilling, and T. Hoc. Bovine cortical bone stiffness and local strain are affected by mineralization and morphology. *Journal of Applied Mechanics, Transactions ASME*, 79(1):1–12, 2012.
- [219] Georges Poumarat and Patrick Squire. Comparison of mechanical properties of human, bovine bone and a new processed bone xenograft. *Biomaterials*, 14(5):337–340, 1993.

- [220] Michiel Müller. *Introduction to Confocal and Fluorescence Microscopy*. SPIE, Bellingham, WA, second edition, 2006.
- [221] G. Van Rossum and F. L. Drake. *Python 3 Reference Manual*. Scotts Valley, CA: CreateSpace., 2009.
- [222] S. Gamsjaeger, R. Mendelsohn, A. L. Boskey, S. Gourion-Arsiquaud, K. Klaushofer, and E. P. Paschalis. Vibrational spectroscopic imaging for the evaluation of matrix and mineral chemistry. *Current Osteoporosis Reports*, 12(4):454–464, 2014.
- [223] Marek Janko, Polina Davydovskaya, Michael Bauer, Albert Zink, and Robert W. Stark. Anisotropic Raman scattering in collagen bundles. *Optics Letters*, 35(16):2765, 2010.
- [224] Stacy A. Overman and George J. Thomas. Amide modes of the α -helix: Raman spectroscopy of filamentous virus fd containing peptide 13c and 2h labels in coat protein subunits. *Biochemistry*, 37(16):5654–5665, 1998.
- [225] Hua Qiang Bao, Ru Bing Li, Hua Dan Xing, Chuan Qu, Qiu Li, and Wei Qiu. Crystalline orientation identification of phosphorene using polarized Raman spectroscopy without analyzer. *Applied Sciences (Switzerland)*, 9(11), 2019.
- [226] Andreas Roschger, Sonja Gamsjaeger, Birgit Hofstetter, Admir Masic, Stéphane Blouin, Phaedra Messmer, Andrea Berzlanovich, Eleftherios P. Paschalis, Paul Roschger, Klaus Klaushofer, and Peter Fratzl. Relationship between the ν 2PO4/amide III ratio assessed by Raman spectroscopy and the calcium content measured by quantitative backscattered electron microscopy in healthy human osteonal bone. *Journal of Biomedical Optics*, 19(6):65002, 2014.
- [227] Ozan Akkus, Fran Adar, and Mitchell B. Schaffler. Age-related changes in physicochemical properties of mineral crystals are related to impaired mechanical function of cortical bone. *Bone*, 34(3):443–453, 2004.
- [228] Y. N. Yeni, J. Yerramshetty, O. Akkus, C. Pechey, and C. M. Les. Effect of fixation and embedding on Raman spectroscopic analysis of bone tissue. *Calcified Tissue International*, 78(6):363–371, 2006.
- [229] M. Kazanci, H.D. D. Wagner, N.I. I. Manjubala, H.S. S. Gupta, E. Paschalis, P. Roschger, and P. Fratzl. Raman imaging of two orthogonal planes within cortical bone. *Bone*, 41(3):456–461, sep 2007.

- [230] Orestis L. Katsamenis, Harold M.H. H Chong, Orestis G. Andriotis, and Philipp J. Thurner. Load-bearing in cortical bone microstructure: Selective stiffening and heterogeneous strain distribution at the lamellar level. *Journal of the Mechanical Behavior of Biomedical Materials*, 17:152–165, 2013.
- [231] Anjani K. Maurya, Lukas Weidenbacher, Fabrizio Spano, Giuseppino Fortunato, René M. Rossi, Martin Frenz, Alex Dommann, Antonia Neels, and Amin Sadeghpour. Structural insights into semicrystalline states of electrospun nanofibers: A multiscale analytical approach. *Nanoscale*, 11(15):7176–7187, 2019.
- [232] S. Tadimalla, M.C. C Tourell, R. Knott, and K.I. I Momot. Quantifying collagen fibre architecture in articular cartilage using small-angle X-ray scattering. *Biomedical Spectroscopy and Imaging*, 6(1-2):37–57, 2017.
- [233] S. Ran, D. Fang, X. Zong, B. S. Hsiao, B. Chu, and P. M. Cunniff. Structural changes during deformation of Kevlar fibers via on-line synchrotron SAXS/WAXD techniques. *Polymer*, 2001.
- [234] W. Ruland. Small-angle scattering studies on carbonized cellulose fibers. *Journal of Polymer Science Part C: Polymer Symposia*, 28(1):143–151, mar 1969.
- [235] Curtis T. Rueden, Johannes Schindelin, Mark C. Hiner, Barry E. DeZonia, Alison E. Walter, Ellen T. Arena, and Kevin W. Eliceiri. ImageJ2: ImageJ for the next generation of scientific image data. *BMC Bioinformatics*, 18(1):1–26, 2017.
- [236] Michael Doube, Michał M M Kłosowski, Ignacio Arganda-carreras, and P Fabrice. BoneJ : free and extensible bone image analysis in ImageJ. *Bone*, 47(6):1076–1079, 2010.
- [237] H. Zhang, B. E. Schuster, Q. Wei, and K. T. Ramesh. The design of accurate micro-compression experiments. *Scripta Materialia*, 54(2):181–186, 2006.
- [238] Stephen W. Tsai and Edward M. Wu. A General Theory of Strength for Anisotropic Materials. *Journal of Composite Materials*, 5(1):58–80, 1971.
- [239] A. H. Burstein, J. M. Zika, K. G. Heiple, and L. Klein. Contribution of collagen and mineral to the elastic-plastic properties of bone. *The Journal of bone and joint surgery. American volume*, 57(7):956–61, oct 1975.
- [240] Mekhala Raghavan. *Investigation of Mineral and Collagen Organization in Bone Using Raman Spectroscopy*. PhD thesis, University of Michigan, 2011.

- [241] Seyyedvahid Mortazavian and Ali Fatemi. Effects of fiber orientation and anisotropy on tensile strength and elastic modulus of short fiber reinforced polymer composites. *Composites Part B: Engineering*, 72:116–129, apr 2015.
- [242] Eve Donnelly. Methods for assessing bone quality: A review. *Clinical Orthopaedics and Related Research*, 469(8):2128–2138, 2011.
- [243] L. Mosekilde. Li. Mosekilde Department of Cell Biology, Institute of Anatomy, University of Aarhus DK-8000 Aarhus, Denmark. *October*, 17(4 Supplement):343S—352S, 1995.
- [244] C. H. Turner, A. Chandran, and R. M.V. V Pidaparti. The anisotropy of osteonal bone and its ultrastructural implications. *Bone*, 17(1):85–89, 1995.
- [245] D. Carnelli, D. Gastaldi, V. Sassi, R. Contro, C. Ortiz, and P. Vena. A finite element model for direction-dependent mechanical response to nanoindentation of cortical bone allowing for anisotropic post-yield behavior of the tissue. *Journal of Biomechanical Engineering*, 132(8):1–10, 2010.
- [246] G. Guidoni, M. Swain, and I. Jäger. Nanoindentation of wet and dry compact bone: Influence of environment and indenter tip geometry on the indentation modulus. *Philosophical Magazine*, 90(5):553–565, 2010.
- [247] Susan F. Lipson and J. Lawrence Katz. The relationship between elastic properties and microstructure of bovine cortical bone. *Journal of Biomechanics*, 1984.
- [248] Simin Li, Emrah Demirci, and Vadim V. Silberschmidt. Variability and anisotropy of mechanical behavior of cortical bone in tension and compression. *Journal of the Mechanical Behavior of Biomedical Materials*, 2013.
- [249] Zherrina Manilay, Ekaterina Novitskaya, Ernest Sadovnikov, and Joanna Mckittrick. A comparative study of young and mature bovine cortical bone. *Acta Biomaterialia*, 2013.
- [250] Christian Hellmich, Andreas Fritsch, and Luc Dormieux. Multiscale Homogenization Theory: An Analysis Tool for Revealing Mechanical Design Principles in Bone and Bone Replacement Materials. In *Biomimetics—Materials, Structures and Processes*, pages 81–103. Springer Berlin Heidelberg, 2011.
- [251] Davide Carnelli, Pasquale Vena, Ming Dao, Christine Ortiz, and Roberto Contro. Orientation and size-dependent mechanical modulation within individual secondary osteons in cortical bone tissue. *Journal of the Royal Society Interface*, 10(81), apr 2013.

- [252] Giampaolo Franzoso and Philippe K. Zysset. Elastic anisotropy of human cortical bone secondary osteons measured by nanoindentation. *Journal of Biomechanical Engineering*, 131(2):1–11, 2009.
- [253] J. G. Swadener, Jae-Young Rho, and G. M. Pharr. Effects of anisotropy on elastic moduli measured by nanoindentation in human tibial cortical bone. *Journal of Biomedical Materials Research*, 57(1):108–112, oct 2001.
- [254] Jae Young Rho, Marcel E. Roy, Ting Y. Tsui, and George M. Pharr. Elastic properties of microstructural components of human bone tissue as measured by nanoindentation. *Journal of Biomedical Materials Research*, 45(1):48–54, 1999.
- [255] Orestis G. Andriotis, Sylvia Desissaire, and Philipp J. Thurner. Collagen Fibrils: Nature’s Highly Tunable Nonlinear Springs. *ACS Nano*, 12(4):3671–3680, 2018.
- [256] A. K. Bembey, A. J. Bushby, A. Boyde, V. L. Ferguson, and M. L. Oyen. Hydration effects on the micro-mechanical properties of bone. *Journal of Materials Research*, 21(8):1962–1968, 2006.
- [257] Mohammad Maghsoudi-Ganjeh, Xiaodu Wang, and Xiaowei Zeng. Computational investigation of the effect of water on the nanomechanical behavior of bone. *Journal of the Mechanical Behavior of Biomedical Materials*, 101(June 2019):103454, 2020.
- [258] L. M. Jenkins and A. M. Donald. Use of the environmental scanning electron microscope for the observation of the swelling behaviour of cellulosic fibres. *Scanning*, 19(2):92–97, 1997.
- [259] Admir Masic, Luca Bertinetti, Roman Schuetz, Shu Wei Chang, Till Hartmut Metzger, Markus J. Buehler, and Peter Fratzl. Osmotic pressure induced tensile forces in tendon collagen. *Nature Communications*, 6:1–8, 2015.
- [260] Himadri S. Gupta, Wolfgang Wagermaier, Gerald A. Zickler, Jürgen Hartmann, Sérgio S. Funari, Paul Roschger, Daniel H. Wagner, and Peter Fratzl. Fibrillar level fracture in bone beyond the yield point. *International Journal of Fracture*, 139(3-4):425–436, 2006.
- [261] Herwig Peterlik, Paul Roschger, Klaus Klaushofer, and Peter Fratzl. From brittle to ductile fracture of bone. *Nature Materials*, 5(1):52–55, 2006.
- [262] Himadri S. Gupta, Wolfgang Wagermaier, Gerald A. Zickler, D. Raz Ben Aroush, Sérgio S. Funari, Paul Roschger, H. Daniel Wagner, and Peter Fratzl. Nanoscale deformation mechanisms in bone. *Nano Letters*, 5(10):2108–2111, 2005.

- [263] Stacyann Morgan, Atharva A. Poundarik, and Deepak Vashishth. Do Non-collagenous Proteins Affect Skeletal Mechanical Properties? *Calcified Tissue International*, 97(3):281–291, 2015.
- [264] Spencer E. Szczesny and Dawn M. Elliott. Incorporating plasticity of the interfibrillar matrix in shear lag models is necessary to replicate the multiscale mechanics of tendon fascicles. *Journal of the Mechanical Behavior of Biomedical Materials*, 40:325–338, 2014.
- [265] Kuangshin Tai, Franz Josef Ulm, and Christine Ortiz. Nanogranular origins of the strength of bone. *Nano Letters*, 6(11):2520–2525, 2006.
- [266] D. M.L.L. Cooper, C. E. Kawalilak, K. Harrison, B. D. Johnston, and J. D. Johnston. Cortical Bone Porosity: What Is It, Why Is It Important, and How Can We Detect It? *Current Osteoporosis Reports*, 14(5):187–198, 2016.
- [267] D.M.L.L. Cooper, A.L. L Turinsky, C.W. W Sensen, and B. Hallgrímsson. Quantitative 3D analysis of the canal network in cortical bone by micro-computed tomography. *The Anatomical Record Part B: The New Anatomist*, 274B(1):169–179, 2003.
- [268] Juliet Compston. Bone quality: What is it and how is it measured? *Arquivos Brasileiros de Endocrinologia e Metabologia*, 50(4):579–585, 2006.
- [269] Robert Recker, Wai-nang Paul Lee, Zhang Hengwei, Robert Recker, and Wai-nang Paul Lee. Proteomics in bone research. *Expert Rev Proteomics*, 7(1):103–111, 2010.
- [270] Benjamin Voumard, Ghislain Maquer, Peter Heuberger, Philippe K. Zysset, and Uwe Wolfram. “Peroperative estimation of bone quality and primary dental implant stability”. *Journal of the Mechanical Behavior of Biomedical Materials*, 92(November 2018):24–32, 2019.
- [271] Liene Molly. Bone density and primary stability in implant therapy. *Clinical Oral Implants Research*, 17(S2):124–135, oct 2006.
- [272] Ilser Turkyilmaz, editor. *Implant Dentistry: The Most Promising Discipline of Dentistry*. InTech, 2011.
- [273] O. Nackaerts, R. Jacobs, K. Horner, F. Zhao, C. Lindh, K. Karayianni, P. van der Stelt, S. Pavitt, and H. Devlin. Bone density measurements in intra-oral radiographs. *Clinical Oral Investigations*, 11(3):225–229, sep 2007.

- [274] S.C. C. White, K.A. A. Atchison, J.A. A. Gornbein, A. Nattiv, A. Paganini-Hill, S.K. K. Service, and D.C. C. Yoon. Change in mandibular trabecular pattern and hip fracture rate in elderly women. *Dentomaxillofacial Radiology*, 34(3):168–174, may 2005.
- [275] James Graham. Detecting low bone mineral density from dental radiographs: a mini-review. *Clinical Cases in Mineral and Bone Metabolism*, 12(2):178–182, 2015.
- [276] Masih Shahlaie, Bernard Gantes, Eloy Schulz, Matt Riggs, and Max Crigger. Bone density assessments of dental implant sites: 1. Quantitative computed tomography. *The International journal of oral & maxillofacial implants*, 18(2):224–31, 2003.
- [277] N. Stoppie, V. Pattijn, T. Van Cleynenbreugel, M. Wevers, J. Vander Sloten, and I. Naert. Structural and radiological parameters for the characterization of jawbone. *Computer Methods in Biomechanics and Biomedical Engineering*, 8(sup1):261–262, sep 2005.
- [278] Prasit Aranyarachkul, Joseph Caruso, Bernard Gantes, Eloy Schulz, Matt Riggs, Ivan Dus, Jason M Yamada, and Max Crigger. Bone density assessments of dental implant sites: 2. Quantitative cone-beam computerized tomography. *The International journal of oral & maxillofacial implants*, 20(3):416–24, 2005.
- [279] William C Scarfe, Allan G Farman, and Predag Sukovic. Clinical applications of cone-beam computed tomography in dental practice. *Journal (Canadian Dental Association)*, 72(1):75–80, feb 2006.
- [280] Reinhilde Jacobs, Benjamin Salmon, Marina Codari, Bassam Hassan, and Michael M. Bornstein. Cone beam computed tomography in implant dentistry: recommendations for clinical use. *BMC Oral Health*, 18(1):88, dec 2018.
- [281] Sebastian Baumgaertel, J. Martin Palomo, Leena Palomo, and Mark G. Hans. Reliability and accuracy of cone-beam computed tomography dental measurements. *American Journal of Orthodontics and Dentofacial Orthopedics*, 136(1):19–25, jul 2009.
- [282] Yan Hua, Olivia Nackaerts, Joke Duyck, Frederik Maes, and Reinhilde Jacobs. Bone quality assessment based on cone beam computed tomography imaging. *Clinical Oral Implants Research*, 20(8):767–771, aug 2009.
- [283] Nina von Wowern. General and oral aspects of osteoporosis: a review. *Clinical Oral Investigations*, 5(2):71–82, jun 2001.

- [284] G. A. Lekholm, U. & Zarb, U Lekholm, and G A Zarb. Patient selection and preparation. In Zarb G Brånemark P.-I. and T Albrektsson, editors, *Tissue Integrated Prosthesis: Osseointegration in Clinical Dentistry*, page 199. Chicago: Quintessence publishing Co. Inc., 1985.
- [285] Maria Ángeles Fuster-Torres, María Miguel Peñarrocha-Diago, and David Peñarrocha-Oltra. Relationships between bone density values from cone beam computed tomography, maximum insertion torque, and resonance frequency analysis at implant placement: a pilot study. *The International journal of oral & maxillofacial implants*, 26(5):1051–6, 2011.
- [286] Scott Lee, Bernard Gantes, Matt Riggs, and Max Crigger. Bone density assessments of dental implant sites: 3. Bone quality evaluation during osteotomy and implant placement. *The International journal of oral & maxillofacial implants*, 22(2):208–12, 2007.
- [287] Neil Meredith. A Review of Nondestructive Test Methods and Their Application to Measure the Stability and Osseointegration of Bone Anchored Endosseous Implants. *Critical Reviews in Biomedical Engineering*, 26(4):275–291, 1998.
- [288] Ji-Su Oh and Su-Gwan Kim. Clinical study of the relationship between implant stability measurements using Periotest and Osstell mentor and bone quality assessment. *Oral Surgery, Oral Medicine, Oral Pathology and Oral Radiology*, 113(3):e35–e40, mar 2012.
- [289] Rejane Faria Ribeiro-Rotta, Christina Lindh, Andrea Castro Pereira, and Madeleine Rohlin. Ambiguity in bone tissue characteristics as presented in studies on dental implant planning and placement: A systematic review. *Clinical Oral Implants Research*, 22(8):789–801, aug 2011.
- [290] B. Van Meerbeek, G. Willems, J.P. P Celis, J.R. R Roos, M. Braem, P. Lambrechts, and G. Vanherle. Assessment by Nano-indentation of the Hardness and Elasticity of the Resin-Dentin Bonding Area. *Journal of Dental Research*, 72(10):1434–1442, oct 1993.
- [291] L. Angker and M.V. V Swain. Nanoindentation: Application to dental hard tissue investigations. *Journal of Materials Research*, 21(8):1893–1905, aug 2006.
- [292] Keiichiro Watanabe, Samantha Lewis, Xiaohan Guo, Ai Ni, Beth S. Lee, Toru Deguchi, and Do-Gyoon Gyoon Kim. Regional variations of jaw bone characteristics in an ovariectomized rat model. *Journal of the Mechanical Behavior of Biomedical Materials*, 110:103952, oct 2020.

- [293] Lee A. Feldkamp, Steven A. Goldstein, Michael A. Parfitt, Gerald Jasion, and Michael Kleerekoper. The direct examination of three-dimensional bone architecture in vitro by computed tomography. *Journal of Bone and Mineral Research*, 4(1):3–11, dec 2009.
- [294] J. L. Kuhn, S. A. Goldstein, L. A. Feldkamp, R. W. Goulet, and G. Jasion. Evaluation of a microcomputed tomography system to study trabecular bone structure. *Journal of Orthopaedic Research*, 8(6):833–842, nov 1990.
- [295] Michael V Swain and Jing Xue. State of the Art of Micro-CT Applications in Dental Research. *International Journal of Oral Science*, 1(4):177–188, dec 2009.
- [296] Alexander Groetsch, Philippe K. Zysset, Peter Varga, Alexandra Pacureanu, Françoise Peyrin, and Uwe Wolfram. An experimentally informed statistical elasto-plastic mineralised collagen fibre model at the micrometre and nanometre lengthscale. *Scientific Reports*, 11(1), dec 2021.
- [297] D.C. C O’Shea, M.L. L Bartlett, and R.A. A Young. Compositional analysis of apatites with Laser-Raman spectroscopy: (OH,F,Cl)apatites. *Archives of Oral Biology*, 19(11):995–1006, nov 1974.
- [298] G. Leroy, G. Penel, N. Leroy, and E. Brès. Human Tooth Enamel: A Raman Polarized Approach. *Applied Spectroscopy*, 56(8):1030–1034, aug 2002.
- [299] Hamideh Salehi, Elodie Terrer, Ivan Panayotov, Bernard Levallois, Bruno Jacquot, Hervé Tassery, and Frédéric Cuisinier. Functional mapping of human sound and carious enamel and dentin with Raman spectroscopy. *Journal of Biophotonics*, sep 2012.
- [300] Yong Wang, Paulette Spencer, and Mary P. Walker. Chemical profile of adhesive/caries-affected dentin interfaces using Raman microspectroscopy. *Journal of Biomedical Materials Research - Part A*, 81(2):279–286, May 2007.
- [301] Jann Hau. Animal Models for Human Diseases. In *Sourcebook of Models for Biomedical Research*. Humana Press, Totowa, NJ, 2008.
- [302] Jacqui Anne McGovern, Michelle Griffin, and Dietmar Werner Hutmacher. Animal models for bone tissue engineering and modelling disease. *Disease Models & Mechanisms*, 11(4), apr 2018.
- [303] Thomas J. Rosol, Sarah H. Tannehill-Gregg, Bruce E. LeRoy, Stefanie Mandl, and Christopher H. Contag. Animal models of bone metastasis. *Cancer*, 97(S3):748–757, feb 2003.

- [304] J. K. Simmons, B. E. Hildreth, W. Supsavhad, S. M. Elshafae, B. B. Hassan, W. P. Dirksen, R. E. Toribio, and T. J. Rosol. Animal Models of Bone Metastasis. *Veterinary Pathology*, 52(5):827–841, sep 2015.
- [305] Eiji Kobayashi, Shuji Hishikawa, Takumi Teratani, and Alan T Lefor. The pig as a model for translational research: overview of porcine animal models at Jichi Medical University. *Transplantation Research*, 1(1):8, dec 2012.
- [306] Petr Vodička, Karel Smetana Jr., Barbora Dvořánková, Teresa Emerick, Yingzhi Z. Xu, Jitka Ourednik, Václav Ourednik, and Jan Motlík. The miniature pig as an animal model in biomedical research. *Annals of the New York Academy of Sciences*, 1049(1):161–171, may 2005.
- [307] J.C. C Litten-Brown, A.M. M Corson, and L. Clarke. Porcine models for the metabolic syndrome, digestive and bone disorders: a general overview. *Animal*, 4(6):899–920, 2010.
- [308] Bělková J Rozkot M. Václavková E. and Bělková J. Rozkot M., Václavková E. Minipigs as laboratory animals - review. *Research in pig breeding*, 2015(2):10–14, 2015.
- [309] Kenneth L. Hastings Peter A. McAnulty, Anthony D. Dayan, Niels-Christian Ganderup and Niels-Christian Ganderup Kenneth L Hastings Peter A. McAnulty Anthony D. Dayan. *The Minipig in Biomedical Research*. CRC Press, 2011.
- [310] Tetsuo Nunoya, Kazumoto Shibuya, Toshiki Saitoh, Hajime Yazawa, Keigo Nakamura, Yasuko Baba, and Takuya Hirai. Use of Miniature Pig for Biomedical Research, with Reference to Toxicologic Studies. *Journal of Toxicologic Pathology*, 20(3):125–132, 2007.
- [311] M. E. Weaver, F. M. Sorenson, and E. B. Jump. The miniature pig as an experimental animal in dental research. *Archives of Oral Biology*, 7(1), 1962.
- [312] S. Wang, Y. Liu, D. Fang, and S. Shi. The miniature pig: a useful large animal model for dental and orofacial research. *Oral Diseases*, 13(6):530–537, nov 2007.
- [313] Baerbel Ruehe, Stefan Niehues, Susanne Heberer, and Katja Nelson. Miniature pigs as an animal model for implant research: bone regeneration in critical-size defects. *Oral Surgery, Oral Medicine, Oral Pathology, Oral Radiology, and Endodontology*, 108(5):699–706, nov 2009.

- [314] D. Buser, R. K. Schenk, S. Steinemann, J. P. Fiorellini, C. H. Fox, and H. Stich. Influence of surface characteristics on bone integration of titanium implants. A histomorphometric study in miniature pigs. *Journal of Biomedical Materials Research*, 25(7):889–902, Jul 1991.
- [315] Tzong-Fu Kuo, Hung-Chieh Lu, Chien-Fang Tseng, Jen-Chang Yang, Sea-Fue Wang, Thomas Chung-Kuang Yang, and Sheng-Yang Lee. Evaluation of Osseointegration in Titanium and Zirconia-Based Dental Implants with Surface Modification in a Miniature Pig Model. *Journal of Medical and Biological Engineering*, 37(3):313–320, jun 2017.
- [316] T. Imwinkelried, S. Beck, and B. Schaller. Pre-clinical testing of human size magnesium implants in miniature pigs: Implant degradation and bone fracture healing at multiple implantation sites. *Materials Science and Engineering: C*, 108:110389, mar 2020.
- [317] Cinzia Peruzzi, Rajaprakash Ramachandramoorthy, Alexander Groetsch, Daniele Casari, Philippe Grönquist, Markus Rüggeberg, Johann Michler, and Jakob Schwiedrzik. Microscale compressive behavior of hydrated lamellar bone at high strain rates. *Acta Biomaterialia*, 131:403–414, 2021.
- [318] Michael Smith. *ABAQUS/Standard User’s Manual, Version 6.9*. Dassault Systèmes Simulia Corp, Providence, RI, 2009.
- [319] Hadi S. Hosseini, Ghislain Maquer, and Philippe K. Zysset. μ CT-based trabecular anisotropy can be reproducibly computed from HR-pQCT scans using the triangulated bone surface. *Bone*, 97:114–120, apr 2017.
- [320] R core team and R Core team. *R: A Language and Environment for Statistical Computing*, 2021.
- [321] Alboukadel Kassambara. *rstatix: Pipe-Friendly Framework for Basic Statistical Tests*, 2021.
- [322] R. B. Martin and D. L. Boardman. The effects of collagen fiber orientation, porosity, density, and mineralization on bovine cortical bone bending properties. *J. Biomechanics*, 26(9):1047–1054, 1993.
- [323] Giovanna Iezzi, Carlo Mangano, Antonio Barone, Federico Tirone, Luigi Baggi, Giuliana Tromba, Adriano Piattelli, and Alessandra Giuliani. Jawbone remodeling: a

- conceptual study based on Synchrotron High-resolution Tomography. *Scientific Reports*, 10(1), dec 2020.
- [324] Jeffrey S Nyman, Alexander J Makowski, Chetan A Patil, T Philip Masui, Elizabeth C O'Quinn, Xiaohong Bi, Scott A. Guelcher, Daniel P. Nicollela, and Anita Mahadevan-Jansen. Measuring differences in compositional properties of bone tissue by confocal raman spectroscopy. *Calcified Tissue International*, 89(2):111–122, aug 2011.
- [325] Bernhard Hesse, Peter Varga, Max Langer, Alexandra Pacureanu, Susanne Schrof, Nils Männicke, Heikki Suhonen, Peter Maurer, Peter Cloetens, Francoise Peyrin, and Kay Raum. Canalicular network morphology is the major determinant of the spatial distribution of mass density in human bone tissue: Evidence by means of synchrotron radiation phase-contrast nano-CT. *Journal of Bone and Mineral Research*, 30(2):346–356, feb 2015.
- [326] Ivana Vitulli, Rocharles Cavalcante Fontenele, Eduarda Helena Leandro Nascimento, and Deborah Queiroz Freitas. Influence of artefacts generated by titanium and zirconium implants in the study of trabecular bone architecture in cone-beam CT images. *Dentomaxillofacial Radiology*, may 2022.
- [327] Sara Lofthag-Hansen, Sisko Huuonen, Kerstin Gröndahl, and Hans-Göran Gröndahl. Limited cone-beam CT and intraoral radiography for the diagnosis of periapical pathology. *Oral Surgery, Oral Medicine, Oral Pathology, Oral Radiology, and Endodontology*, 103(1):114–119, jan 2007.
- [328] John A. Chapman, Margaret Tzaphlidou, Keith M. Meek, and Karl E. Kadler. The collagen fibril—A model system for studying the staining and fixation of a protein. *Electron Microscopy Reviews*, 3(1):143–182, jan 1990.
- [329] John D. Currey, Kevin Brear, Peter Zioupos, and Gwendolen C. Reilly. Effect of formaldehyde fixation on some mechanical properties of bovine bone. *Biomaterials*, 16(16):1267–1271, jan 1995.
- [330] Klaus J. Burkhart, Tobias E. Nowak, Jochen Blum, Sebastian Kuhn, Marcel Welker, Werner Sternstein, Lars P. Mueller, and Pol M. Rommens. Influence of formalin fixation on the biomechanical properties of human diaphyseal bone. *Biomedizinische Technik/Biomedical Engineering*, 55(6):361–365, jan 2010.
- [331] S.J. Edmondston, K.P. Singer, R.E. Day, P.D. Bredahl, and R.I. Price. Formalin fixation effects on vertebral bone density and failure mechanics: an in-vitro study of human and sheep vertebrae. *Clinical Biomechanics*, 9(3):175–179, may 1994.

- [332] G. S. Keene, M. J. Parker, and G. A. Pryor. Mortality and morbidity after hip fractures. *British Medical Journal*, 307(6914):1248–1260, 1993.
- [333] Karen Hertz and Santy-Tomlinson. *Fragility Fracture Nursing Holistic Care and Management of the Orthogeriatric Patient Perspectives in Nursing Management and Care for Older Adults Series Editors*. SpringerLink, 2018.
- [334] S.C.E Schuit, M. Van Der Klift, A.E.A.M. Weel, C.E.D.H. De Laet, H. Burger, E. See-man, A. Hofman, A.G. Uitterlinden, J.P.T.M. Van Leeuwen, and H.A.P Pols. Fracture incidence and association with bone mineral density in elderly men and women: The Rotterdam Study. *Bone*, 34(1):195–202, 2004.
- [335] Jürg Andreas Gasser and Michaela Kneissel. Bone Physiology and Biology. In Susan Y Smith, Aurore Varela, and Rana Samadfam, editors, *Bone Toxicology*, pages 27–94. Springer International Publishing, Cham, 2017.
- [336] O. Johnell and J. A. Kanis. An estimate of the worldwide prevalence and disability associated with osteoporotic fractures. *Osteoporosis International*, 17(12):1726–1733, 2006.
- [337] Julie T Lin and Joseph M Lane. Osteoporosis: A review. *Clinical Orthopaedics and Related Research*, 425(425):126–134, 2004.
- [338] Randall S. Stafford, Rebecca L. Drieling, and Adam L. Hersh. National Trends in Osteoporosis Visits and Osteoporosis Treatment, 1988-2003. *Archives of Internal Medicine*, 164(14):1525, jul 2004.
- [339] Dennis M Black, Jane A Cauley, Rachel Wagman, Kristine Ensrud, Howard A Fink, Teresa A Hillier, Li-Yung Lui, Steven R Cummings, John T Schousboe, and Nicola Napoli. The ability of a single bmd and fracture history assessment to predict fracture over 25 years in postmenopausal women: The study of osteoporotic fractures. *Journal of Bone and Mineral Research*, 33(3):389–395, Jul 2017.
- [340] Derek G. Hansen, Teerapat Tutaworn, and Joseph M. Lane. What’s New in Osteoporosis and Fragility Fractures. *Journal of Bone and Joint Surgery*, 104(17):1509–1515, 2022.
- [341] Harri Sievänen, Pekka Kannus, and Teppo L N Järvinen. Bone quality: an empty term. *PLoS medicine*, 4(3):e27, mar 2007.
- [342] Robert R Recker and M Janet Barger-Lux. The Elusive Concept of Bone Quality. *Current Osteoporosis Reports*, page 97–100, 2004.

- [343] D.P. Fyhrie. Summary – measuring "bone quality". *Journal of musculoskeletal & neuronal interactions*, 5(4):318–20, 2005.
- [344] Jeffrey S. Nyman and Alexander J. Makowski. The contribution of the extracellular matrix to the fracture resistance of bone. *Current Osteoporosis Reports*, 10(2):169–177, 2012.
- [345] Jeffrey S. Nyman, Anuradha Roy, Xinmei Shen, Rae L. Acuna, Jerrod H. Tyler, and Xiaodu Wang. The influence of water removal on the strength and toughness of cortical bone. *Journal of Biomechanics*, 39(5):931–938, Jan 2006.
- [346] S Weiner and H D Wagner. The material bone: Structure-mechanical function relations. *Annual Review of Materials Science*, 28(1):271–298, 1998.
- [347] Peter Fratzl and Richard Weinkamer. Nature’s hierarchical materials. *Progress in Materials Science*, 52(8):1263–1334, 2007.
- [348] Michel K. Nieuwoudt, Rayomand Shahlori, Dorit Naot, Rhea Patel, Hannah Holtkamp, Claude Agueraray, Maureen Watson, David Musson, Cameron Brown, Nicola Dalbeth, Jillian Cornish, and M. Cather Simpson. Raman spectroscopy reveals age- and sex-related differences in cortical bone from people with osteoarthritis. *Scientific Reports*, 10(1), dec 2020.
- [349] Delphine Farlay, Gérard Panczer, Christian Rey, Pierre D. Delmas, and Georges Boivin. Mineral maturity and crystallinity index are distinct characteristics of bone mineral. *Journal of Bone and Mineral Metabolism*, pages 433–445, 2010.
- [350] Mustafa Unal, Hyungjin Jung, and Ozan Akkus. Novel Raman Spectroscopic Biomarkers Indicate That Postyield Damage Denatures Bone’s Collagen. *Journal of Bone and Mineral Research*, 31(5):1015–1025, 2016.
- [351] Mustafa Unal, Sasidhar Uppuganti, Selin Timur, Anita Mahadevan-Jansen, Ozan Akkus, and Jeffrey S. Nyman. Assessing matrix quality by Raman spectroscopy helps predict fracture toughness of human cortical bone. *Scientific Reports*, 9(1):1–13, 2019.
- [352] Erin M.B. McNerny, Bo Gong, Michael D. Morris, and David H. Kohn. Bone fracture toughness and strength correlate with collagen cross-link maturity in a dose-controlled lathyism mouse model. *Journal of Bone and Mineral Research*, 30(3):446–455, 2015.
- [353] Mustafa Unal, Rafay Ahmed, Anita Mahadevan-Jansen, and Jeffrey S Nyman. Compositional assessment of bone by Raman spectroscopy. *The Analyst*, 146:7444, 2021.

- [354] Douglas Bates, Martin Mächler, Ben Bolker, and Steve Walker. Fitting Linear Mixed-Effects Models Using lme4. *Journal of Statistical Software*, 67(1), 2015.
- [355] Charles R. Harris, K. Jarrod Millman, Stéfan J. van der Walt, Ralf Gommers, Pauli Virtanen, David Cournapeau, Eric Wieser, Julian Taylor, Sebastian Berg, Nathaniel J. Smith, Robert Kern, Matti Picus Hoyer, Stephan, Marten H. van Kerkwijk, Matthew Brett, Allan Haldane, Jaime Fernández del Río, Mark Wiebe, Pearu Peterson, Pierre Gérard-Marchant, Kevin Sheppard, Tyler Reddy, Warren Weckesser, Hameer Abbasi, Christoph Gohlke, and Travis E. Oliphant. Array programming with NumPy. *Nature*, 585(7825):357–362, sep 2020.
- [356] Fabian Pedregosa, Gaël Varoquaux, Alexandre Gramfort, Vincent Michel, Bertrand Thirion, Olivier Grisel, Mathieu Blondel, Andreas Müller, Joel Nothman, Gilles Louppe, Peter Prettenhofer, Ron Weiss, Vincent Dubourg, Jake Vanderplas, Alexandre Passos, David Cournapeau, Matthieu Brucher, Matthieu Perrot, and Édouard Duchesnay. Scikit-learn: Machine Learning in Python. *Journal of Machine Learning Research*, 12(12):2825–2830, 2011.
- [357] Stanley Lemeshow, R.X. Sturdivant, and D.W. Hosmer Jr. *Applied Logistic Regression*. John Wiley & Sons, 3 edition, 2013.
- [358] N. Fratzi-Zelman, P. Roschger, A. Gourrier, M. Weber, B. M. Misof, N. Loveridge, J. Reeve, K. Klaushofer, and P. Fratzi. Combination of nanoindentation and quantitative backscattered electron imaging revealed altered bone material properties associated with femoral neck fragility. *Calcified Tissue International*, 85(4):335–343, 2009.
- [359] Petar Milovanovic, Jelena Potocnik, Danijela Djonic, Slobodan Nikolic, Vladimir Zivkovic, Marija Djuric, and Zlatko Rakocevic. Age-related deterioration in trabecular bone mechanical properties at material level: Nanoindentation study of the femoral neck in women by using AFM. *Experimental Gerontology*, 47(2):154–159, feb 2012.
- [360] J. Y. Rho, P. Zioupos, J. D. Currey, and G. M. Pharr. Microstructural elasticity and regional heterogeneity in human femoral bone of various ages examined by nanoindentation. *Journal of Biomechanics*, 35(2):189–198, feb 2002.
- [361] Andrea Bonicelli, Tabitha Tay, Justin P Cobb, Oliver R Boughton, Ulrich Hansen, Richard L Abel, and Peter Zioupos. Association between nanoscale strains and tissue level nanoindentation properties in age-related hip-fractures. *Journal of the Mechanical Behavior of Biomedical Materials*, 138(October 2022):105573, 2023.

- [362] Benjamin Voumard, Pia Stefanek, Michael Pretterklieber, Dieter Pahr, and Philippe Zysset. Influence of aging on mechanical properties of the femoral neck using an inverse method. *Bone Reports*, 17(September):101638, 2022.
- [363] V. Sansalone, V. Bousson, S. Naili, C. Bergot, F. Peyrin, J. D. Laredo, and G. Haïat. Anatomical distribution of the degree of mineralization of bone tissue in human femoral neck: Impact on biomechanical properties. *Bone*, 50(4):876–884, apr 2012.
- [364] Janardhan S. Yerramshetty and Ozan Akkus. The associations between mineral crystallinity and the mechanical properties of human cortical bone. *Bone*, 42(3):476–482, 2008.
- [365] E. P. Paschalis, K. Verdelis, S. B. Doty, A. L. Boskey, R. Mendelsohn, and M. Yamauchi. Spectroscopic characterization of collagen cross-links in bone. *Journal of Bone and Mineral Research*, 16(10):1821–1828, Oct 2001.
- [366] Mustafa Unal, Amy Creecy, and Jeffry S. Nyman. The Role of Matrix Composition in the Mechanical Behavior of Bone. *Current Osteoporosis Reports*, 16(3):205–215, 2018.
- [367] H. Follet, G. Boivin, C. Rumelhart, and P. J. Meunier. The degree of mineralization is a determinant of bone strength: a study on human calcanei. *Bone*, 34(5):783–789, may 2004.
- [368] J. G. Liao and Khew Voon Chin. Logistic regression for disease classification using microarray data: Model selection in a large p and small n case. *Bioinformatics*, 23(15):1945–1951, 2007.
- [369] Lei Liu. Research on logistic regression algorithm of breast cancer diagnose data by machine learning. *Proceedings - 2018 International Conference on Robots and Intelligent System, ICRIS 2018*, pages 157–160, 2018.
- [370] Pahulpreet Singh Kohli and Shriya Arora. Application of machine learning in disease prediction. *2018 4th International Conference on Computing Communication and Automation, ICCCA 2018*, pages 1–4, 2018.
- [371] Julien Smets, Enisa Shevroja, Thomas Hügle, William D. Leslie, and Didier Hans. Machine Learning Solutions for Osteoporosis—A Review. *Journal of Bone and Mineral Research*, 36(5):833–851, 2021.

- [372] Insha Majeed Wani and Sakshi Arora. *Computer-aided diagnosis systems for osteoporosis detection: a comprehensive survey*, volume 58. Medical & Biological Engineering & Computing, 2020.
- [373] Jae Geum Shim, Dong Woo Kim, Kyoung Ho Ryu, Eun Ah Cho, Jin Hee Ahn, Jeong In Kim, and Sung Hyun Lee. Application of machine learning approaches for osteoporosis risk prediction in postmenopausal women. *Archives of Osteoporosis*, 15(1), 2020.
- [374] Szilard Nemes, Junmei Miao Jonasson, Anna Genell, and Gunnar Steineck. Bias in odds ratios by logistic regression modelling and sample size. *BMC Medical Research Methodology*, 9(1), Jul 2009.
- [375] Chris De Laet, Anders Odén, Helena Johansson, Olof Johnell, Bengt Jönsson, and John A. Kanis. The impact of the use of multiple risk indicators for fracture on case-finding strategies: A mathematical approach. *Osteoporosis International*, 16(3):313–318, 2005.
- [376] Jiunn H. Lin. Bisphosphonates: A review of their pharmacokinetic properties. *Bone*, 18(2):75–85, feb 1996.
- [377] Chen Deng, Jason C. Gillette, and Timothy R. Derrick. Measuring femoral neck loads in healthy young and older adults during stair ascent and descent. *PLoS ONE*, 16(1 January):1–14, 2021.
- [378] Mariana E. Kersh, Saulo Martelli, Roger Zebaze, Ego Seeman, and Marcus G. Pandy. Mechanical Loading of the Femoral Neck in Human Locomotion. *Journal of Bone and Mineral Research*, 33(11):1999–2006, 2018.
- [379] Franz Faul, Edgar Erdfelder, Albert-Georg Lang, and Axel Buchner. G*Power 3: A flexible statistical power analysis program for the social, behavioral, and biomedical sciences. *Behavior Research Methods*, 39(2):175–191, may 2007.
- [380] Heather B Hunt and Eve Donnelly. Bone Quality Assessment Techniques: Geometric, Compositional, and Mechanical Characterization from Macroscale to Nanoscale, sep 2016.
- [381] Marie Madeleine Giraud-Guille. Twisted plywood architecture of collagen fibrils in human compact bone osteons. *Calcified Tissue International*, 42(3):167–180, 1988.

- [382] Paweena U-Thainual, Yi Yang, Hanh N. D. Le, and Do-Hyun Kim. Radiant exposure level comparison between gaussian and top hat beams in various scanning patterns. *Applied Optics*, 53(36):8585, Dec 2014.
- [383] Stefan Rung, Johannes Barth, and Ralf Hellmann. Characterization of laser beam shaping optics based on their ablation geometry of thin films. *Micromachines*, 5(4):943–953, Oct 2014.
- [384] Matthew Gleeson, Kevin O’Dwyer, Sarah Guerin, Daragh Rice, Damien Thompson, Syed A. M. Tofail, Christophe Silien, and Ning Liu. Quantitative polarization-resolved second-harmonic-generation microscopy of glycine microneedles. *Advanced Materials*, 32(46):2002873, Oct 2020.
- [385] Richard Cisek, Ariana Joseph, MacAulay Harvey, and Danielle Tokarz. Polarization-sensitive second harmonic generation microscopy for investigations of diseased collagenous tissues. *Frontiers in Physics*, 9, Aug 2021.
- [386] Rajesh Kumar, Kirsten M. Grønhaug, Elisabeth I. Romijn, Andreas Finnøy, Catharina L. Davies, Jon O. Drogset, and Magnus B. Lilledahl. Polarization second harmonic generation microscopy provides quantitative enhanced molecular specificity for tissue diagnostics. *Journal of Biophotonics*, 8(9):730–739, Nov 2014.
- [387] Eve Donnelly, Adele L. Boskey, Shefford P. Baker, and Marjolein C. H. van der Meulen. Effects of tissue age on bone tissue material composition and nanomechanical properties in the rat cortex. *Journal of Biomedical Materials Research Part A*, 92(3):1048–56, 2009.
- [388] Eve Donnelly, Dan X. Chen, Adele L. Boskey, Shefford P. Baker, and Marjolein C. H. van der Meulen. Contribution of mineral to bone structural behavior and tissue mechanical properties. *Calcified Tissue International*, 87(5):450–460, Aug 2010.
- [389] Siddhartha Pathak, Shraddha J. Vachhani, Karl J. Jepsen, Haviva M. Goldman, and Surya R. Kalidindi. Assessment of lamellar level properties in mouse bone utilizing a novel spherical nanoindentation data analysis method. *Journal of the Mechanical Behavior of Biomedical Materials*, 13:102–117, Sep 2012.
- [390] Susanne Schrof, Peter Varga, Bernhard Hesse, Martin Schöne, Roman Schütz, Admir Masic, and Kay Raum. Multimodal correlative investigation of the interplaying microarchitecture, chemical composition and mechanical properties of human cortical bone tissue reveals predominant role of fibrillar organization in determining microelastic tissue properties. *Acta Biomaterialia*, 2016.

- [391] Hengwei Zhang, Robert Recker, Wai-Nang Paul Lee, and Gary Guishan Xiao. Proteomics in bone research. *Expert Review of Proteomics*, 7(1):103–111, 2010. PMID: 20121480.
- [392] Grazyna E. Sroga, Lamyia Karim, Wilfredo Colón, and Deepak Vashishth. Biochemical characterization of major bone-matrix proteins using nanoscale-size bone samples and proteomics methodology. *Molecular and Cellular Proteomics*, 10(9):1–12, 2011.
- [393] Simone Caramazza, Arianna Collina, Elena Stellino, Francesca Ripanti, Paolo Dore, and Paolo Postorino. First- and second-order Raman scattering from MoTe₂ single crystal. *The European Physical Journal B*, 91(2):35, feb 2018.
- [394] R. Loudon. The Raman effect in crystals. *Advances in Physics*, 13(52):423–482, 1964.
- [395] R. Saito, Y. Tatsumi, S. Huang, X. Ling, and M. S. Dresselhaus. Raman spectroscopy of transition metal dichalcogenides. *Journal of Physics Condensed Matter*, 28(35), 2016.
- [396] Stacy A. Overman, Masamichi Tsuboi, and George J. Thomas. Subunit orientation in the filamentous virus Ff(fd, f1, M13). *Journal of Molecular Biology*, 259(3):331–336, 1996.
- [397] Masamichi Tsuboi, James M. Benevides, and George J. Thomas. Raman Tensors and their application in structural studies of biological systems. *Proceedings of the Japan Academy Series B: Physical and Biological Sciences*, 85(3):83–97, 2009.
- [398] Takahiro Yano, Yuji Higaki, Di Tao, Daiki Murakami, Motoyasu Kobayashi, Noboru Ohta, Jun Ichiro Koike, Misao Horigome, Hiroyasu Masunaga, Hiroki Ogawa, Yuka Ikemoto, Taro Moriwaki, and Atsushi Takahara. Orientation of poly(vinyl alcohol) nanofiber and crystallites in non-woven electrospun nanofiber mats under uniaxial stretching. *Polymer*, 53(21):4702–4708, 2012.
- [399] Rudolf Weber, Thomas Graf, Peter Berger, Volkher Onuseit, Margit Wiedenmann, Christian Freitag, and Anne Feuer. Heat accumulation during pulsed laser materials processing. *Optics Express*, 22(9):11312, may 2014.
- [400] Rudolf Weber, Thomas Graf, Christian Freitag, Anne Feuer, Taras Kononenko, and Vitaly I. Konov. Processing constraints resulting from heat accumulation during pulsed and repetitive laser materials processing. *Optics Express*, 25(4):3966, feb 2017.

- [401] Samuel McPhee, Alexander Groetsch, Jonathan D. Shephard, and Uwe Wolfram. Heat impact during laser ablation extraction of mineralised tissue micropillars. *Scientific Reports*, 11(1):1–13, dec 2021.
- [402] Laurent Bozec and Marianne Odlyha. Thermal Denaturation Studies of Collagen by Microthermal Analysis and Atomic Force Microscopy. *Biophysical Journal*, 101(1):228–236, jul 2011.

Acknowledgements

First and foremost I would like to thank my supervisor at Empa **Dr. Jakob Schwierzik**, who guided me through this journey and taught me how to 'walk' in this peculiar world of academia. Thanks for believing in me, providing the freedom to explore exciting research directions, and for the constant support during my research work. Second, I am very grateful to have **Prof. Philippe Zysset** as my *University of Bern* supervisor. I truly enjoyed our regular as well as spontaneous meetings and always appreciated the valuable input and encouragement. I thank **Prof. Johann (Hannes) Michler**, head of the *Laboratory for Mechanics of Materials and Nanostructures of Empa* for the opportunity to work in his lab and the scientific advice during my stay. I thank my mentor **Prof. Dominik Obrist**, as well as the external referee **Prof. Jeffrey Nyman** and **Prof. Ralph Müller** for taking the time to provide me valuable feedback.

I gratefully acknowledge the support from the **Personalized Health and Related Technologies (PHRT)** program of the Strategic focus area of the ETH Domain. This work was generously funded by the **SFA PHRT iDoc Project 2017-304**.

The research work presented in this dissertation is the product of multiple wide-ranging collaborations. I am very grateful to many people for their scientific contributions and the privilege of working alongside them. On my Raman 'journey', I was lucky to work together with **Dr. Oliver Braun**, **Rico Muff** and **Prof. Michel Calame**, from the *Transport at Nanoscale Interfaces Laboratory (405) of Empa Duebendorf*. Thank you for the introduction to the fantastic polarized Raman setup as well as many 'tricks' on experimental and theoretical aspects of the Raman spectroscopy. During another fruitful collaboration with the *Empa Center for X-ray Analytics*, I had a chance to meet and work alongside **Prof. Antonia Neels** and **Dr. Anjani Maurya**. An undoubtfull highlight of my PhD research was a chance to work together with **Stefan Remund** and **Prof. Beat Neuenschwander** of the *BFH ALPS Institute*. I am thankful for the unique opportunity to work with the pulsed laser systems and for the constant guidance and hands-on introduction to the fascinating world of laser physics. I thank **Benjamin Bellon** and **Dr. Raphael Wagner** from the Straumann Institute, for the new research ideas and animal bone samples.

A large part of this research was evolving around sample collection and preparation. It would not have been possible to run the study on human bones without the help and assistance from **Dr. Med. Markus Hanke** and **Prof. Dr. med. Klaus Siebenrock** of the *Inselspital*, the University Hospital of Bern. I thank **Silvia Owusu** and **Prof. Dr. Dieter Bosshardt** from the *ZMK team of the University of Bern* for their help during sample prepara-

ration. I thank **Dr. Michael Indermaur**, **Dr. Benjamin Voumard** and the rest of the *MSB group of the Artorg center of the University of Bern*, where I had the opportunity to carry most of the sample preparations as well as the micro-CT measurements.

I thank **Ms. Eveline Straubhaar** for assistance with the administrative work during my PhD at Empa. I wish to show my gratitude to **Ms. Brigitte Schutte** and **Dr. Monica Schaller** for helping me by providing all the GCB administration related information and guidance.

I would like to wholeheartedly thank my colleagues from the *home-lab 206* and our neighboring *lab 204 of Empa Thun*, who made my PhD research a treat. I am afraid there won't be enough pages to write about all the people who worked and/or visited our lab but please rest assured that I enjoyed every minute we spent together over coffee breaks, hikes, lunch-runs and countless aperos. You made this journey unforgettable! A special place in my heart holds the '*bone-office-community*': **Dr. Daniele Casari**, **Dr. Cinzia Peruzzi**, **Dr. Peter Schweizer**, **Dr. Alexander (Alex) Groetsch** and (almost Dr.) **Caroline Hain**. You were always there in times of trouble and joy, and always had an appropriate meme to share. Dankele and Cinzia, thank you for teaching me everything in the lab and outside, I would not have made it without you. I also thank **Francesca Giuseppoli**, who carried her Master's thesis research with me and was a breath of fresh air at the end of my PhD.

Moving to a new country is always a challenge and I am grateful to the people who made me feel like home here in Switzerland, especially my WG-roomies **Stefanie** and **Maria** and the members of the **Schwimmclub Delphin Uetendorf**. I thank my friend from home **Olya** for her friendship throughout my studies. I must also acknowledge **Siri**, who did his best to distract me during this thesis writing. And **Patrick**, no words can describe how grateful I am to have met you and share this PhD as well as this life journey with you. Thank you for all your support and love over the past years.

Finally, I wish to thank my family. My uncle **Fedor**, from whom I inherited endless admiration for science. And my biggest gratitude goes to my parents, **Maryna** and **Sascha**, who always supported me and encouraged me to never stop learning. Thank you for being there for me and for letting me go.

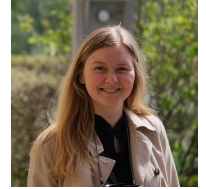
Tatiana Kochetkova
Thun, January 2023

Curriculum vitae and list of publications

Tatiana Kochetkova

Curriculum Vitae

Mittlere Str., 3600
Thun, Switzerland
✉ kochetkovatan@gmail.com
November 16th, 1995



Education

- Sept 2018- **PhD in Biomedical Engineering**
March 2023 - Empa, Swiss Federal Laboratories for Materials Science and Technology, Switzerland
- Graduate School for Cellular and Biomedical Sciences, University of Bern, Switzerland
- Sept 2013- **Diploma studies in Physics of Nanomaterials and Nanotechnologies (Physicist-Engineer, Biophysicist)**
July 2018 - Belarusian State University (BSU), Faculty of Physics, Department of Biophysics, Minsk, Belarus

Research Experiences

- Sept 2018- **PhD student**, *Empa, Swiss Federal Laboratories for Materials Science and Technology, Switzerland.*
March 2023 *Thesis title: "Quantifying bone extracellular matrix properties for improved clinical fracture risk prediction"*
Supervisors: Dr. Jakob Schwiedrzik, Prof. Philippe Zysset
- Sept 2015- **Assistant of a junior researcher**, *Laboratory of Cell Engineering and Nanobiotechnologies, Faculty of Physics, BSU, Belarus.*
July 2018 *Research project: Experimental study of the effect of electrical stimulation on cellular functional properties*
Supervisor: Dr. Pavel M. Bulai
- Aug 2017- **Research intern**, *Institute of Complex Systems (ICS-3), Forschungszentrum Jülich, Germany.*
Sept 2017 *Research project: Characterization of Red Blood Cell to Red Blood Cell interactions induced by rod-like colloids*
Supervisors: Prof. Pavlik Lettinga, Dr. Olivera Korculanin
- July 2017- **Summer student**, *Summer School in Molecular Biophysics and Systems Biology Center for Nanobiology and Structural Biology of the Academy of Sciences of the Czech Republic in Nové Hradý.*
Aug 2017 *Research project: Non-Invasive Measurements of Ion Fluxes across Cell Membranes*
Supervisors: PD Dr. Jost Ludwig, Pavel Spurný
- July 2016- **Research intern**, *The IHRS BioSoft Guest Student Programme, Forschungszentrum Jülich, ICS-3, Germany.*
Sept 2016 *Research project: Shear banding in entangled Xanthan gum polymer solution*
Supervisors: Prof. Pavlik Lettinga, Dr. Hu Tang

Links

Google Scholar
ResearchGate
Linkedin

List of publications related to this Thesis

1. **Tatiana Kochetkova**, Cinzia Peruzzi, Oliver Braun, Jan Overbeck, Anjani K Maurya, Antonia Neels, Michel Calame, Johann Michler, Philippe Zysset and Jakob Schwiedrzik. Combining polarized Raman spectroscopy and micropillar compression to study microscale structure-property relationships in mineralized tissues. *Acta Biomaterialia* 2021, 119, 390-404; DOI: 10.1016/j.actbio.2020.10.034
2. Michael Indermaur, Daniele Casari, **Tatiana Kochetkova**, Cinzia Peruzzi, Elizabeth Zimmermann, Frank Rauch, Bettina Willie, Johann Michler, Jakob Schwiedrzik and Philippe Zysset. Compressive strength of iliac bone ECM is not reduced in Osteogenesis Imperfecta and increases with mineralization. *Journal of Bone and Mineral Research* 2021, 36(7), 1364–1375; DOI: 10.1002/jbmr.4286
3. Anjani K Maurya, Anna Paola Parrilli, **Tatiana Kochetkova**, Jakob Schwiedrzik, Alex Dommann and Antonia Neels. Multiscale and multimodal X-ray analysis: Quantifying phase orientation and morphology of mineralized turkey leg tendons. *Acta Biomaterialia* 2021, 129, 169–177; DOI: 10.1016/j.actbio.2021.05.022
4. Daniele Casari, **Tatiana Kochetkova**, Johann Michler, Philippe Zysset and Jakob Schwiedrzik. Microtensile Failure Mechanisms in Lamellar Bone: Influence of Fibrillar Orientation, Specimen Size and Hydration. *Acta Biomaterialia* 2021, 131, 391–402; DOI: 10.1016/j.actbio.2021.06.032
5. **Tatiana Kochetkova**, Alexander Groetsch, Michael Indermaur, Cinzia Peruzzi, Stefan Remund, Beat Neuenschwander, Benjamin Bellon, Johann Michler, Philippe Zysset and Jakob Schwiedrzik. Assessing minipig compact jawbone quality at the microscale. *Journal of the Mechanical Behavior of Biomedical Materials* 2022, 134, 105405; DOI: 10.1016/j.jmbbm.2022.105405
6. **Tatiana Kochetkova**, Markus S. Hanke, Michael Indermaur, Alexander Groetsch, Stefan Remund, Beat Neuenschwander, Johann Michler, Klaus A. Siebenrock, Philippe Zysset, Jakob Schwiedrzik. Comparing microscale compact bone properties of patients who underwent hip arthroplasty: influence of age and gender. *In preparation*

Conference Presentations related to this Thesis

1. **Tatiana Kochetkova**, Johann Michler, Klaus Siebenrock, Philippe Zysset, Jakob Schwiedrzik. "Combining bone proteotype and multiscale extracellular matrix properties for improved clinical fracture risk prediction". *Poster presentation, Summer School: Shaping the Future of (bio)Medicine (SFM2019)*, Bellinzona, Switzerland, 12-17 May 2019.
2. **Tatiana Kochetkova**, Oliver Braun, Jan Overbeck, Cinzia Peruzzi, Johann Michler, Michel Calame, Philippe Zysset, Jakob Schwiedrzik. "Polarized Raman Spectroscopy as a method for quantitative analysis of bone fibril orientation". *Oral presentation, ETH Raman Workshop 2019*, Zurich, Switzerland, 3-5 June 2019.
3. **Tatiana Kochetkova**, Oliver Braun, Jan Overbeck, Cinzia Peruzzi, Anjani K. Maurya, Johann Michler, Michel Calame, Antonia Neels, Philippe Zysset, Jakob Schwiedrzik. "Polarized Raman Spectroscopy as a method for quantitative analysis of bone fibril orientation". *Poster presentation, Swiss Society for Biomedical Engineering (SSBE) Annual Meeting 2019*, Geneva, Switzerland, 27 August 2019.
4. **Tatiana Kochetkova**, Oliver Braun, Jan Overbeck, Cinzia Peruzzi, Anjani K. Maurya, Johann Michler, Michel Calame, Antonia Neels, Philippe Zysset, Jakob Schwiedrzik. "Polarized Raman Spectroscopy as a method for quantitative analysis of bone fibril orientation". *Oral presentation, EMPA PhD Students' Symposium 2019*, St. Gallen, Switzerland, 28 November 2019.
5. **Tatiana Kochetkova**, Oliver Braun, Jan Overbeck, Cinzia Peruzzi, Anjani K. Maurya, Johann Michler, Michel Calame, Antonia Neels, Philippe Zysset, Jakob Schwiedrzik. "Polarized Raman Spectroscopy as a method for quantitative analysis of bone fibril orientation". *Poster presentation, GCB Symposium 2020*, University of Bern, Switzerland, 30 January 2020.
6. **Tatiana Kochetkova**, Jakob Schwiedrzik. "Microscale characterization of bone for improved clinical fracture risk prediction". *Poster presentation, EMPA PhD Students' Symposium 2020*, Switzerland, 30 November 2020 (Online).
7. **Tatiana Kochetkova**, Oliver Braun, Jan Overbeck, Cinzia Peruzzi, Anjani K. Maurya, Johann Michler, Michel Calame, Antonia Neels, Philippe Zysset, Jakob Schwiedrzik. "Combining polarized Raman spectroscopy and micropillar compression to study microscale structure-property relationships in mineralized tissues". *Oral presentation, GCB Symposium 2021*, University of Bern, Switzerland, 28 January 2021 (Online).

-
8. **Tatiana Kochetkova**. "Microscale characterization of bone". *Oral presentation, Swiss Young Researchers Network(SYRN) Seminar*, Switzerland, 28 January 2021 (Online).
 9. **Tatiana Kochetkova**, Oliver Braun, Jan Overbeck, Cinzia Peruzzi, Anjani K. Maurya, Johann Michler, Michel Calame, Antonia Neels, Philippe Zysset, Jakob Schwiedrzik. "Investigation of Microscale Bone Anisotropy by Polarized Raman Spectroscopy and Micropillar Compression". *Oral presentation, The 26th Congress of the European Society of Biomechanics (ESBiomech2021)*, Milan, Italy, 11-14 July 2021 (Online).
 10. **Tatiana Kochetkova**, Alexander Groetsch, Michael Indermaur, Stefan Remund, Beat Neuenschwander, Joelle Hofstetter, Benjamin Bellon, Johann Michler, Philippe Zysset, Jakob Schwiedrzik. "Assessing jaw bone quality at the micro- and meso-scale". *Oral Presentation, Swiss Society for Biomedical Engineering (SSBE) Annual Meeting 2021*, Bern, Switzerland, 26 August 2021.
 11. **Tatiana Kochetkova**, Silvan Englisch, Tatiana Kormilina, Janis, Wirth, Dominik Drobek, Benjamin Apeleo-Zubiri, Oliver Braun, Michel Calame, Stefan Remund, Beat Neuenschwander, Johann Michler, Philippe Zysset, Jakob Schwiedrzik. "Nanoscale structural characterization of bone by a combination of quantitative polarized Raman spectroscopy, nano X-ray computed tomography, and STEM tomography". *Oral Presentation, EUROMAT 2021*, 13-17 September 2021 (Online).
 12. **Tatiana Kochetkova**, Alexander Groetsch, Michael Indermaur, Stefan Remund, Beat Neuenschwander, Joelle Hofstetter, Benjamin Bellon, Johann Michler, Philippe Zysset, Jakob Schwiedrzik. "Assessing jaw bone quality at the micro- and meso-scale". *Poster presentation, GCB Symposium 2022*, University of Bern, Switzerland, 27 January 2022 (Online).
 13. **Tatiana Kochetkova**, Alexander Groetsch, Michael Indermaur, Stefan Remund, Beat Neuenschwander, Benjamin Bellon, Johann Michler, Philippe Zysset, Jakob Schwiedrzik. "Site-matched micropillar compression and Raman spectroscopy to assess jaw bone quality". *Oral presentation, The 27th Congress of the European Society of Biomechanics (ESBiomech2022)*, Porto, Portugal, 26-29 June 2022.
 14. **Tatiana Kochetkova**, Tatiana Kormilina, Silvan Englisch, Dominik Drobek, Janis Wirth, Benjamin Apeleo Zubiri, Oliver Braun, Michel Calame, Stefan Remund, Beat Neuenschwander, Johann Michler, Philippe Zysset, Erdmann Spiecker, Jakob Schwiedrzik. "Assessing bone ultrastructure via nanoscale x-ray computed tomography and quantitative polarized Raman spectroscopy". *Poster presentation, The 27th Congress of the European Society of Biomechanics (ESBiomech2022)*, Porto, Portugal, 26-29 June

2022.

15. **Tatiana Kochetkova**, Markus S. Hanke, Klaus A. Siebenrock, Johann Michler, Philippe Zysset, Jakob Schwiedrzik. "Quantifying bone quality in a population of aging patients who underwent total hip replacement surgery". *Oral presentation, EMPA PhD Students' Symposium 2022*, Dubendorf, Switzerland, 29 November 2022.

Declaration of Originality

Last name, first name: Kochetkova, Tatiana

Matriculation number: 18-126-664

I hereby declare that this thesis represents my original work and that I have used no other sources except as noted by citations.

All data, tables, figures and text citations which have been reproduced from any other source, including the internet, have been explicitly acknowledged as such. I am aware that in case of non-compliance, the Senate is entitled to withdraw the doctorate degree awarded to me on the basis of the present thesis, in accordance with the “Statut der Universität Bern (Universitätsstatut; UniSt)”, Art. 69, of 7 June 2011.

Place, Date

Thun, 15.03.2023

Signature

A handwritten signature in black ink, appearing to be 'T. Kochetkova', written in a cursive style.

